

# Precise characterization and modeling of particle morphology development in emulsion polymerization

Noushin Rajabalinia

Supervised by:

Prof. José M. Asua and Prof. Jose R. Leiza

Chemical Engineering Group

Euskal Herriko Unibertsitatea/Universidad del País Vasco

Donostia-San Sebastián

(2019)



**POLYMAT**



# Contents

## **Chapter 1. Introduction**

1.1. Introduction.....	1
1.2. Development of particle morphology in two-stage emulsion polymerization.....	3
1.3. Mathematical modelling of particle morphology .....	11
1.4. Characterization of particle morphology .....	17
1.5. Control of particle morphology in emulsion polymerization.....	21
1.6. Objectives of the thesis .....	23
1.7. Outline of the thesis .....	24
1.8. References.....	26

## **Chapter 2. Effect of process variables on particle morphology**

2.1. Introduction.....	41
2.2. Experimental section.....	44
2.2.1. Materials .....	44
2.2.2. Synthesis of latexes.....	45
2.2.2.1. Synthesis of seed latex .....	45
2.2.2.2. Synthesis of composite polymer particle latex .....	47

2.2.3.	Latex characterization .....	50
2.3.	Results and discussion.....	50
2.3.1.	Effect of Tg of seed on particle morphology .....	52
2.3.1.1.	Analysis of evolution of particle morphology by mathematical model .....	70
2.3.2.	Effect of Tg of second stage polymer on particle morphology .....	89
2.3.3.	Effect of reaction temperature of second stage of polymerization on particle morphology .....	97
2.3.4.	Effect of initiator of second stage of polymerization on particle morphology .....	103
2.3.5.	Effect of prolonged reaction time in the second stage of polymerization on particle morphology .....	110
2.3.6.	Effect of crosslinking of the seed on particle morphology .....	115
2.3.7.	Particle morphology changes by annealing at high temperature.....	125
2.4.	Conclusions .....	127
2.5.	Nomenclature .....	130
2.6.	References.....	133

**Chapter 3. Coupling HAADF-STEM tomography and image reconstruction for the precise characterization of particle morphology**

3.1.	Introduction.....	139
------	-------------------	-----



3.2.	Synthesis of composite polymer particle latexes .....	142
3.3.	Characterization of the particle morphology .....	142
3.4.	Results and discussion .....	144
3.4.1.	Quantitative characterization of the effect of the process variables on particle morphology.....	147
3.5.	Particle morphology analysis using an upgraded mathematical model ....	156
3.6.	Use of the upgraded model to analyze some of un-explained findings in Chapter 2 .....	170
3.7.	Conclusions.....	173
3.8.	References.....	179

**Chapter 4. Effect of unreacted concentration of monomer during the second stage of process on particle morphology**

4.1.	Introduction .....	183
4.2.	Experimental section .....	184
4.2.1.	Materials .....	184
4.2.2.	Synthesis of latexes .....	185
4.2.3.	Latex characterization.....	191
4.3.	Results and discussion .....	191
4.4.	Conclusions .....	199
4.5.	References .....	199

**Chapter 5. Effect of process disturbances on development of particle morphology**

5.1. Introduction.....	201
5.2. Experimental section.....	205
5.3. Results and discussion.....	207
5.4. Conclusion .....	213
5.5. References.....	213

**Chapter 6. Conclusions .....217**

6.1. References.....	224
----------------------	-----

**Resumen y conclusiones .....229**

**Appendix I. Materials and characterization techniques .....239**

I.1. Materials .....	239
I.2. Characterization methods .....	240
I.3. References .....	246

**Appendix II. Some Figures of Chapter 2 and Chapter 4 .....249**

# Chapter 1. Introduction

## 1.1. Introduction

Waterborne dispersions are used in a wide range of applications including coatings for decorative, protective or automotive purposes, paper, lithography, adhesives, constructions, carpet, leather and textile industries<sup>1,2</sup>. Emulsion polymerization is the main polymerization technique to produce polymeric dispersions in a continuous media, mostly water. In the last decades, the interest on the development of synthesis methods and new applications of waterborne dispersions has increased due to the environmental concerns, which limits the release of volatile organic compounds (VOC) encouraging the use of waterborne dispersions instead of solvent-based polymers. Moreover, a wide variety of products with specially-tailored properties regarding to desired applications can be synthesized in emulsion polymerization due to controllability of the operation.<sup>3,4</sup>

Waterborne polymeric dispersions are often homogenous (single polymer phase) but can also be hybrid particles that are composed of at least two incompatible phases. The hybrid particles synergistically combine the properties of their constituents, which

can be polymer-polymer or polymer-inorganic phases and present enhanced properties displaying new functionalities.<sup>5</sup> This opens a wide range of applications for waterborne dispersions including anticorrosive<sup>6,7</sup>, superhydrophobic<sup>8</sup> and anti-fungal coatings<sup>9</sup>, switchable adhesives<sup>10</sup>, photo-switchable fluorescent particles<sup>11</sup>, energy storage<sup>12,13</sup>, gene and drug delivery<sup>14-16</sup>, anti-counterfeiting<sup>17</sup> and LEDs<sup>18</sup>. Hybrid particles can be synthesized using chemical or physical methods. The common chemical method to synthesize polymer-polymer hybrid particles is seeded emulsion polymerization. In this method, the particles are synthesized in a two-stage process. In first stage, one set of monomer(s) is polymerized in emulsion and the produced latex is used as the seed in the emulsion polymerization of second group of monomer(s). Most of the time, both stages are carried out semi-continuously to achieve better thermal and polymer characteristic control.<sup>19</sup> Miniemulsion polymerization is more versatile for including polymers produced by step-growth polymerization or very hydrophobic polymers produced by free radical polymerization in the synthesis of polymer-polymer hybrid particles. Moreover, miniemulsion polymerization is used to incorporate inorganic particles both within and at the surface of the polymer particles.<sup>5,20-23</sup>

The application properties of hybrid particles depends on the characteristics of their constituents (e.g., chain structure and molar mass distribution of the polymers as well as the type and shape of the inorganic materials), the interaction between different

---

phases, the particle size distribution and the particle morphology. This Thesis focuses on the morphology, which strongly affects the properties of the hybrid particle latexes and the synthesis of particles with defined morphology is of great interest.<sup>5,19,24</sup>

## **1.2. Development of particle morphology in two-stage emulsion polymerization**

Hybrid polymer-polymer waterborne dispersions are produced by seeded emulsion polymerization and/or by polymerization of monomer miniemulsions containing a preformed polymer.<sup>19</sup> In both cases, the initial state is a dispersion of particles of Polymer 1 swollen by Monomer 2 (in miniemulsion polymerization this is regarded as droplets of Monomer 2 in which Polymer 1 is dissolved). Upon addition of initiator, new polymer chains are formed in the mixture of Polymer 1 and Monomer 2 (which will be referred as polymer matrix). As the concentration of the newly formed polymer chains increases, phase separation occurs, forming clusters that are dispersed in the polymer matrix. Monomer swells both the polymer matrix and the clusters. The size of the clusters increases because of polymerization inside the clusters, diffusion of polymer formed in the polymer matrix to the clusters and coagulation with other clusters. In addition, clusters migrate towards the equilibrium morphology. Depending of the relative rates of polymerization in the polymer matrix with respect to phase

separation and diffusion of the formed polymer chains from the matrix to the clusters, the composition of the matrix may be supersaturated in Polymer 2. The motion of the clusters is ruled by the balance between van der Waals forces (which are proportional to the interfacial tensions), Brownian motion and the resistance to flow that arises from the viscous drag. Figure 1.1 shows the evolution of particle morphology during the second stage of seeded emulsion polymerization for hemispherical equilibrium morphology.

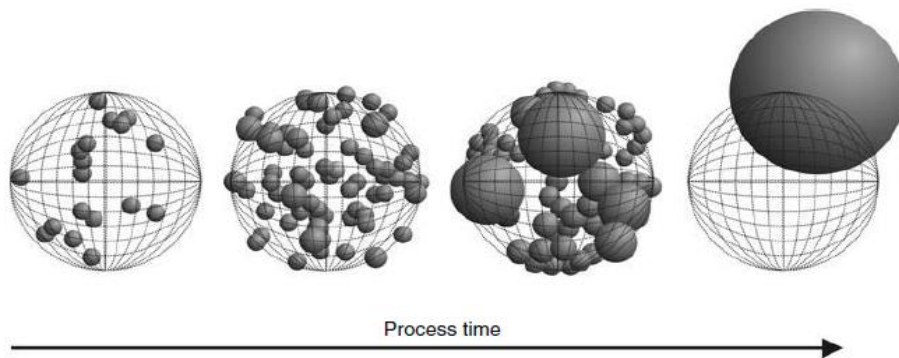


Figure 1. 1. Evolution of the particle morphology during the second stage of seeded emulsion polymerization. Dark spheres refer to the second phase clusters.<sup>3</sup> Reproduced with the permission from Wiley and Sons.

The final morphology heavily depends on the kinetics of the cluster migration. When the movement of the phases is not hindered, equilibrium morphologies are reached, otherwise, a kinetically controlled morphology is obtained. Thermodynamic

leads to equilibrium morphology that corresponds to the minimum surface free energy of the particle, which is calculated as the sum of the product of interfacial tensions ( $\gamma_{ij}$ ) and interfacial areas ( $A_{ij}$ ) being i and j the phases in the system (polymer 1, polymer 2 and water). Therefore, polymer-polymer and polymer-aqueous phase interfacial tension play key role in the morphology development as they determine the surface energy.<sup>25-29</sup> Figure 1.2 shows the limited number of equilibrium morphologies that can be synthesised in a two phase polymer-polymer system, which are core-shell<sup>30,31</sup>, inverted core-shell<sup>32,33</sup> or hemispherical<sup>34,35</sup> and it depends on the polymerization condition.<sup>36</sup> “Core-shell” morphology is favoured in the case of more hydrophilic second stage polymer, which remains at the surface of the particle while in the case of “inverted core-shell” the seed polymer is more hydrophilic and produce the shell layer in the final particle. In the case of “Hemi-spherical”, the hydrophilicities of both polymeric phases are comparable and they remain in contact with water.

Asua<sup>37</sup> reported a similar morphological map for the polymer-inorganic hybrid particle with the equilibrium morphology calculated by minimizing the surface energy of the system. The calculation accounted for the water, polymeric and inorganic phases.

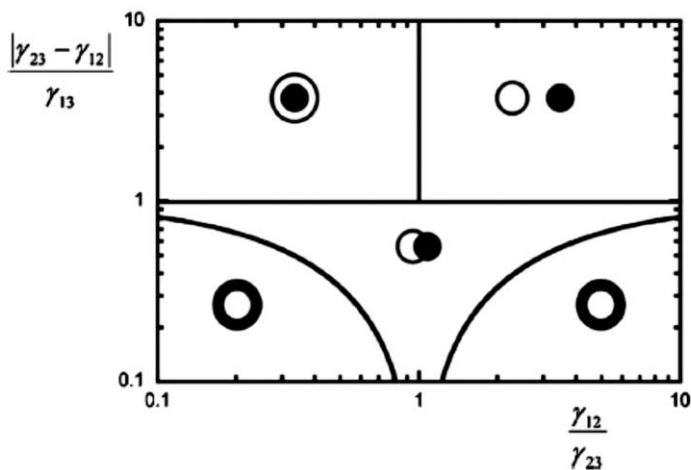


Figure 1. 2. Equilibrium morphology map for a polymer-polymer system corresponding to the minimum interfacial energy between the phases: seed polymer (1), second phase polymer (2) and water (3). Reprinted (adapted) with permission from (Gonzalez-Ortiz, L. J.; Asua, J. M. *Macromolecules* **1995**, 28 (9), 3135–3145).<sup>36</sup> Copyright (1995) American Chemical Society.

In a real system, during the second stage polymerization, clusters of second phase polymer move toward the equilibrium morphology due to van der Waals forces but the movement is hindered by viscosity drag. If the movement of second phase clusters is fast enough, equilibrium morphologies can be attained, otherwise kinetically metastable morphologies are produced.<sup>24,38–45</sup> The loci of cluster generation in the matrix strongly affects the final particle morphology and it depends on the radical and monomer concentration profiles in the polymer particles during the polymerization.



Many authors considered flat radical and monomer concentration profiles leading to homogenous distribution of cluster generation within the particles.<sup>46-51</sup> On the other hand, Grancio and Williams<sup>52</sup> proposed the existence of a decreasing concentration profile of radicals within the polymer particles when water soluble initiators were used. Later, Chern and Poehlein<sup>53</sup> showed in a Monte-Carlo simulation that anchoring the hydrophilic end-groups of growing oligo-radicals to the surface of the particles results in radical concentration profile within the particles. Decreasing radical concentration profiles can also be produced as the result of the slow diffusion of the entering radical due to its rapid growth. It was early recognized that this profile could affect particle morphology<sup>54</sup> and this has been confirmed later.<sup>55</sup> Mills *et al.*<sup>56</sup> found out that the effect of diffusion on radical concentration profile is intensified by increasing the particle size and polymerizing at high instantaneous conversion. Sundberg and co-workers<sup>57</sup> showed that the radical penetration depth is diffusion limited due to the rigidity of the seed polymer (matrix), namely, glassy seeds led to sharper radical concentration profiles.

The clusters move toward the equilibrium position during the polymerization and their movement is hindered by the internal viscosity of the matrix, which depends on the molecular weight, monomer conversion, degree of crosslinking, reaction temperature and glass transition temperature (T<sub>g</sub>) of the phases. Sundberg and co-

---

workers<sup>58-61</sup> have published a series of articles where the effect of reaction variables on particle morphology was studied. It was shown that diffusion of generated second stage polymer was limited in a glassy non-crosslinked seed and resulted in non-equilibrium morphologies in the case of polar seed and non-polar second stage polymer.<sup>59</sup> Using ionic initiator that generates radicals with charged end group, which can anchor to the surface of the particle resulting in radical concentration profile, did not induce major changes in the particle morphology compared to using non-ionic initiator in the case of diffusion-controlled system.<sup>60</sup> Chain transfer agents can make the radical concentration profile flatter allowing penetration of the radicals to the interior of the particles and therefore enhancing the distribution of the second-stage polymer throughout the latex particles.<sup>61</sup> Stubbs and Sundberg<sup>62</sup> showed that occluded non-equilibrium morphologies were obtained in the case that the penetration of the radicals and phase separation were possible and the separated phase domains were partially rearranged via coalescence. Blenner *et al.*<sup>63</sup> outlined the key factors for achieving multi-lobed polymer composite latexes with a non-crosslinked seed. The first criterion is that the radicals should not penetrate in the seed and the second stage polymer should be more hydrophobic than the seed. If these conditions are fulfilled, the particle morphology is controlled by the difference between the reaction temperature and the Tgs of the seed and second phase polymer. A guiding morphological map is provided (Figure 1.3). The

map shows that if the second stage polymer is soft at the reaction temperature, the lobes can move and coagulate between themselves to decrease the surface energy leading to the formation of large lobes. On the other hand, for a glassy second stage polymer, the polymer stays where it formed, the lobes do not coagulate and a shell of the second stage polymer with a rough surface is formed.

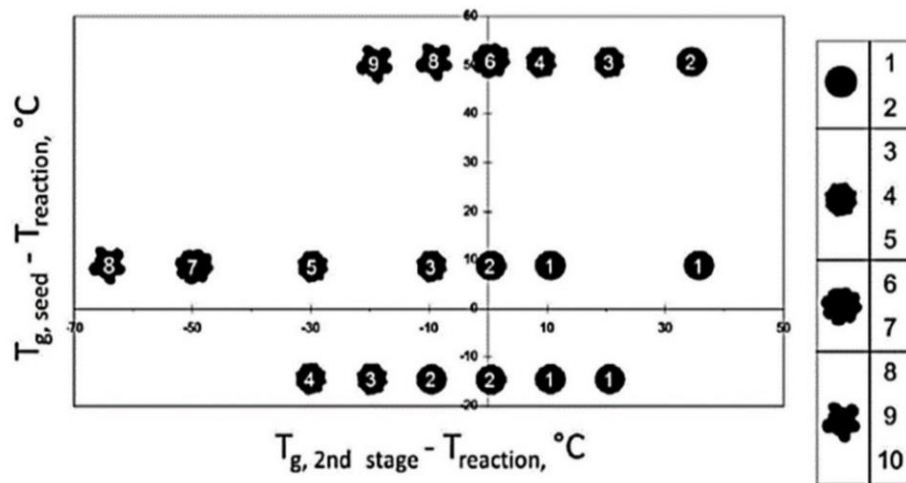


Figure 1. 3. Multi-lobed nature of composite particles with P(MMA-co-MA) seed polymers and P(Sty-co-HMA) second stage polymer, at various  $T_g$ 's as compared to reaction temperature. All representations are for stage ratios of 1:1. Non-spherical nature of the particle is ranked in the chart at the right side of the figure.<sup>63</sup> Reproduced with permission from Elsevier.

Johnsson *et al.*<sup>64</sup> studied the monomer plasticizing effect by varying monomer concentration during the polymerization of styrene using poly methyl methacrylate

(PMMA) seed in a semi-continuous process. They concluded that the higher monomer concentration, the higher radical diffusion can be achieved and the morphology could be modified from core-shell (at low monomer concentration) to a cluster distribution (at high monomer concentration) in the matrix.

Crosslinking of the polymer chains is one way to induce phase separation<sup>65</sup> and is used in the production of impact modifier<sup>66</sup> and latex interpenetrating networks (IPNs).<sup>67</sup> Crosslinking of the seed, introduces elastic forces to the total free energy of the system which compete with interfacial energy in terms of thermodynamics to determine final particle morphology.<sup>65,68</sup> Durant *et al.*<sup>69</sup> studied the effect of crosslinking of MMA seed using ethylene glycol dimethylacrylate (EGDMA) on the morphology of MMA seed/S second phase hybrid particles. The reaction was carried out in a batch emulsion polymerization using potassium persulfate as initiator and a pre-swollen seed with second stage monomer. It was shown that even with low amounts of crosslinking, the penetration of second phase styrene chains in the network of seed was restricted and the morphology changed from “inverted core-shell” to “core-shell”. Segall and co-workers synthesized a core-shell morphology using slightly crosslinked seed of BA with EDGMA and second phase of copolymer of benzyl methacrylate/styrene. They concluded that using a crosslinked seed and under starved feed conditions the core-shell morphology can be achieved.<sup>70</sup> Second phase

crosslinking has been mostly reported as a way to produce hollow particles. McDonald and Devon reviewed the production of hollow particles by synthesis of core-shell morphology using crosslinked second stage shell.<sup>71</sup> Stubbs and Sundberg studied the effect of crosslinking agent in the second stage of polymerization using monomer mixture of styrene/butyl acrylate and EGDMA as crosslinker with the seed of hydroxypropyl methacrylate (HPMA)/hexyl methacrylate (HMA). The T<sub>g</sub>s of both phases were lower than the reaction temperature and they concluded that radical penetration was not substantially affected due to softness of seed; the crosslinking of second phase did not affect the radical penetration, but limited the phase separation as the crosslinking concentration increased.<sup>72</sup>

### **1.3. Mathematical modelling of particle morphology**

Particle morphology of hybrid polymer particles plays a key role in determining the application properties of the latexes, and therefore large efforts have been devoted to develop reliable mathematical models for the prediction of particle morphology development during the synthesis of hybrid polymer particles. Many of these theoretical approaches are based on two limiting assumptions: either the polymer chains do not move from the point they are formed<sup>52,53,55,56,73</sup> or the equilibrium morphology is attained instantaneously.<sup>26,35,74,75</sup> However, in a real system, whereas the chains and clusters move towards the equilibrium morphology, the viscosity drag

---

hinders the cluster movement. Gonzalez-Ortiz and Asua<sup>36,76,77</sup> developed a model, which described the dynamics of particle morphology development. The model accounts for phase separation between Polymer 1 and Polymer 2 that leads to cluster nucleation, polymerization in both clusters and matrix (Polymer 1 rich area), polymer diffusion between matrix and clusters and cluster aggregation. The final morphology is predicted based on van der Waals forces and viscous forces. The prediction of the particle morphology of multiphase systems becomes much more complicated. The equilibrium morphology of multiphase particles was predicted using Monte Carlo simulations.<sup>75</sup> Akhmatskaya and Asua<sup>78,79</sup> simulated the dynamic evolution of the particle morphology of multiphase polymer-polymer and polymer-inorganic systems using stochastic dynamics in which the movement of phases is described by the Langevin equation. Although the models are able to describe in detail the dynamics of the morphology development, the output is the morphology of a single particle. Notwithstanding, the reality is that there is not a single morphology but a distribution of morphologies in a polymer latex. For instance, TEM image of hybrid polymer-polymer particles produced by copolymerization of styrene-butyl acrylate using a seed made of poly (methyl methacrylate-co-butyl acrylate) by emulsion polymerization in this thesis (Run R1 in Chapter 2) is shown in Figure 1.4. The image illustrates the broad number of morphologies that are encountered in a latex sample, and hence the need for

a better prediction of the morphology distribution. Indeed, better statistics can be obtained using the existing methods to simulate several particles, but as these models require long computational times, this is not practical.

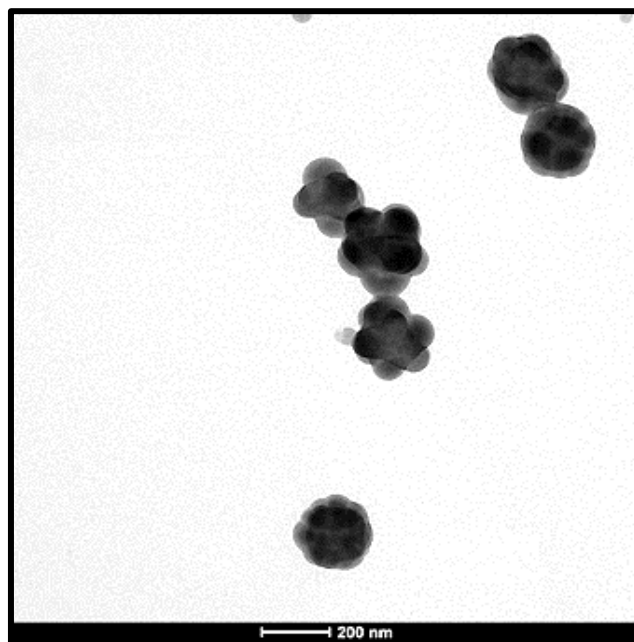


Figure 1. 4. TEM image of sample stained with the vapor of  $\text{RuO}_4$  for 1 hour from hybrid particles of styrene-butyl acrylate copolymerization in a seeded emulsion polymerization using poly (methyl methacrylate-co-butyl acrylate) seed. Image magnification is 25000.

Considering this drawback of the existing models, Hamzehlou *et al.*<sup>80</sup> have recently presented a new approach to model the dynamic development of the particle morphology of composite polymer particles produced by emulsion and miniemulsion

polymerization. The novelty of this model consists of describing the particle morphology by means of cluster size distributions (in a similar way as a polymer is characterized by the molar mass distribution and a colloid by the particle size distribution). The model was developed for polymer-polymer hybrid particles and later was validated for hybrid polymer-inorganic particles.<sup>81</sup> The model overcomes the limitations of the previous methods because it is computationally efficient as has been recently demonstrated by using the model in an optimization approach to control particle morphology in seeded semi-batch emulsion polymerization<sup>82</sup> and even more importantly, the model provides the distribution of particle morphologies.

The model will be briefly described in this section because it will be used to support and explain the evolution of the morphology of the latexes synthesized in this thesis (the reader is encouraged to get the detailed description elsewhere<sup>80</sup>). The mathematical model accounts for the development of particle morphology in the production of polymer-polymer hybrid by both seeded emulsion polymerization and miniemulsion polymerization. In both cases, the initial state is a dispersion of particles/droplets containing Polymer 1 and Monomer 2. The whole system might be described by the cluster volume distribution. However, as the position of the clusters in the particle is of importance, a single distribution does not provide a good description of the morphology. Figure 1.5 illustrates the evolution of particle morphology in a single



particle during the polymerization for a case in which the equilibrium morphology is the inverted core-shell (like the latexes synthesized in this thesis). In the non-equilibrium morphology in Figure 1.5, there are clusters at the surface of the particle, clusters within the particle and cluster at the center of the particle. For this case, the cluster at the center of the particle is at equilibrium position and the other clusters are at non-equilibrium positions. The equilibrium morphology is achieved when all the clusters at non-equilibrium positions move to the equilibrium position to aggregate and produce a single cluster at the center of the particle.

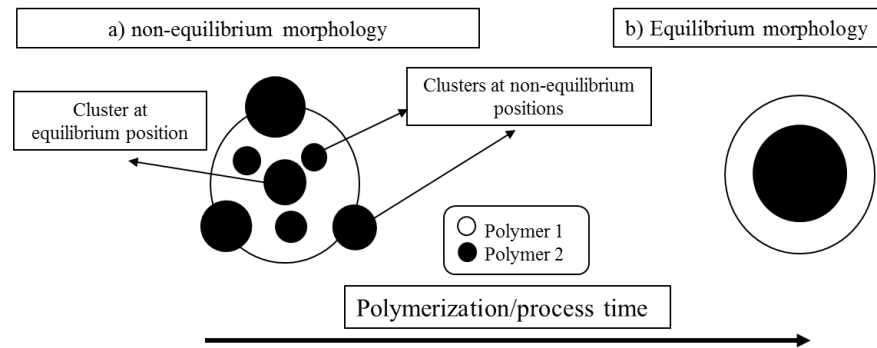


Figure 1. 5. Clusters at equilibrium and non-equilibrium positions during the polymerization.

The model is developed considering the following assumptions:

- The number of polymer particles is considered to be constant during the reaction, i.e. there is neither secondary nucleation nor coagulation.

- The amount of Polymer 1 in each particle is considered to be the same.
- The clusters contain only Polymer 2 and Monomer 2.
- The polymer matrix contains all Polymer 1, and some Polymer 2 and Monomer 2.
- There are no monomer droplets in the reactor.
- Monomer swells equally both Polymer 1 and Polymer 2.
- The amount of monomer in the aqueous phase is negligible.
- The amount of water in polymer particles is negligible.
- The radical concentration profile in the particles is flat (anchoring of the entering radicals to the particle surface is not considered).
- The radicals distributed homogeneously between clusters and polymer matrix.

Considering the assumptions listed above, the model solves the material balances for the Monomer 2 and Polymer 2 for a semicontinuous reactor considering a flat monomer concentration profile. The average number of radicals per particle was calculated in the model using the Li-Brooks approach.<sup>83</sup> The particle morphology is described by two cluster size distributions: one for clusters at the surface of the particle

and within the matrix (called clusters at non-equilibrium positions) and the other one for cluster at the center of the particles (called cluster at equilibrium position).

The population balances include the terms of the growth of the clusters by propagation and diffusion of polymer from matrix to the clusters, the terms of appearance and disappearance of clusters by aggregation, and movement of the clusters toward the equilibrium position as well as cluster nucleation. The model accounts for the effect of the operation variables (such as effective glass transition of the medium, instantaneous conversion, temperature, etc.) on the adjustable parameters of the model and hence on the particle morphology. Considering the capability of the model to predict the evolution of particle morphology for different process conditions, it will be used to support and explain the evolution of the morphology of the latexes synthesized in this thesis.

#### **1.4. Characterization of particle morphology**

A comprehensive morphological characterization of hybrid particles needs the combination of a wide range of techniques to provide information about (1) the overall shape of the hybrid particle, (2) the composition of the polymer present at the particle–water interface and (3) the internal structure of the particle.<sup>84</sup>

A wide range of techniques has been used to determine the particle morphology. Information about surface composition can be obtained with surfactant titration.<sup>85</sup> However, this technique requires an accurate determination of the surface area of the particles, which is not always available for polydispersed latexes and for non-spherical particles as the multi-lobed ones. Minimum film formation temperature (MFFT) and environmental scanning electron microscopy (ESEM) can also provide some idea about the surface composition because the temperature at which the particles start to coalesce gives an indication of the glass transition of the polymer at the surface.<sup>86</sup> However, MFFT and ESEM have only a limited value when there are different phases at the surface of the particles, e.g., for hemispherical particles.

Differential scanning calorimetry (DSC) has been used to quantify the amount of interfacial material between two polymeric phases in blends and latex films.<sup>87,88</sup> This information is contained in the plot of  $dC_p/dT$  vs. temperature obtained from the first heating cycle in the DSC experiment. The peaks in this plot are associated with the  $T_g$ s of the different polymeric phases and the region between peaks approaches to the baseline when there is no interpenetration between the polymers and presents positive values if there is polymer interpenetration.<sup>89</sup>

The microstructure of the particles is often characterized by direct observation of the particles using transmission electron microscopy (TEM). The internal morphology of the particles can be observed by cross-section of the particles embedded in a resin.<sup>84</sup> It is claimed that scanning transmission electron microscopy (STEM) with lower operation energy comparing to TEM is more suitable for analyzing the soft polymer phases which are beam-sensitive.<sup>90</sup> The contrast of the polymer phases often is not strong enough in polymer-polymer systems for a good distinction between the phases. This problem is addressed by selective staining<sup>91-94</sup> and by using techniques such as defocusing, holography and Zernike phase plate methods that increase the contrast between phases.<sup>94,95</sup> This problem is much less pronounced for polymer-inorganic systems due to the relatively higher electronic density of the inorganic material that enhances the contrast between the polymer phase and the inorganic material.<sup>96-100</sup>

Other techniques are also available. Electron energy-loss spectroscopy (EELS) uses the inelastic interaction between the energetic electrons and materials to determine their relative compositions. Combination of EELS and imaging based on spectroscopic contrast either with scanning transmission electron microscopy (STEM) or energy-filtering (EFTEM) techniques has been used to study several aspects of multiphase morphology in polymer-polymer and polymer-inorganic systems.<sup>101-109</sup> Thus, Libera and co-workers<sup>110-112</sup> have used EELS in cryo-STEM to study the composition of the

---

interface between PDMS and poly((meth)acrylates) in structured particles synthesized by seeded emulsion polymerization. However, they only analyzed a relatively simple Janus-like morphology.

High-angle annular dark field (HAADF)-STEM has emerged as a technique suitable for the detailed characterization of composite polymers. Thus, HAADF-STEM has been used to determine the distributions of nanoparticles in inhomogeneous matrices,<sup>113</sup> to study the spatial organization of thin film of various polymer systems including rubber blend and semicrystalline polyethylenes<sup>114</sup> and to image networks of nanoparticles within polymer–nanoparticle blend in photovoltaic devices.<sup>115</sup>

The precise determination of the morphology of the waterborne hybrid particles requires the assistance of wide range of characterization techniques. Whereas this can be feasible for the equilibrium morphologies (core-shell, inverted core-shell and hemispherical),<sup>116</sup> the non-equilibrium morphologies are more difficult to define as all of the particles are different. None of the experimental characterization techniques described above provides quantitative data about the 3D distribution of the phases, which is the information provided by the mathematical model described in Section 1.3. Therefore, there is a need to develop a characterization technique to determine the particle morphology in a quantitative way that would allow estimating the kinetic

parameters of the mathematical model. In this thesis, a detailed characterization method using HAADF-STEM tomography coupled with image analysis and reconstruction technique is presented to determine the morphology of composite particle latexes in a quantitative way that mimics the information provided by the mathematical model explained in Section 3.1.

### **1.5. Control of particle morphology in emulsion polymerization**

Emulsion polymers are “product by process” which means that their properties are determined during the polymerization by many microstructural characteristics of the latex including the chain composition, molecular weight distribution, particle size distribution, polymer architecture (crosslinking, chain branching and gel content) and particle morphology and the process can suffer from run-to run changes in the properties of the product.<sup>117</sup> Therefore, controlling of the polymerization process to produce the latex with desired properties in different runs is essential in the industry. Moreover, controlling the process to minimize the cost, time and raw material consumption in the process is desired. So far, in the open literature, the control has been limited to copolymer chain composition and molar mass distribution. In early attempts, open loop strategies were developed to control the copolymer chain composition in emulsion polymerization which was easy to implement and online measurement of properties was not needed in the process.<sup>118-120</sup> The drawback of the open-loop strategy

was the lack of trajectory correction during the process in the case of unexpected disturbances in the system, which leads to the deviation of product properties from the target. Further developments resulted in closed-loop control strategies. In this way, the handling of the disturbances in the system and reproducibility was achievable although online-monitoring devices, complex estimator and non-linear controllers are also needed. On-line closed-loop strategies to control the polymer chain composition using reaction calorimetry,<sup>121,122</sup> gas chromatography<sup>123</sup> and different spectroscopy techniques<sup>124,125</sup> as well as control of the molecular weight distribution of linear polymers<sup>126-128</sup> were reported in the literature. However, control of particle morphology has not been achieved yet.

The works discussed in Section 1.2 provide a nice qualitative guide for the effect of the operation variables on the final particle morphology. However, this may not be enough to successfully produce products with target morphology in an industrial process. Emulsion polymerization is an extremely competitive business where reaching the desired morphology does not guarantee success as other aspects as operation cost, safety and process time are critical. It has been already demonstrated *in silico*<sup>82</sup> that the optimal emulsion polymerization process to achieve the desired particle morphology taking into account aspects as equipment limitations, safety and process time is a complex strategy. Even if a suboptimal strategy is obtained based on extensive



experimental work with the help of the qualitative guide, the practical implementation will be restricted to open loop control, which cannot cope with unexpected uncertainties often encountered in real practice. Closed loop control would be preferable, but there are no devices available for on-line monitoring of the particle morphology and particle morphology is not observable from other online available measurements.

It is expected that both process optimization and on-line monitoring will be possible if a mathematical model for the evolution of the particle morphology is available. In this regard, the model developed by Hamzehlou *et al.*<sup>80</sup> is the most promising possibility. The model can be directly used in optimization algorithms and as a “soft” sensor in on-line monitoring. Considering that the polymerization rate can be accurately monitored on-line using available techniques such as reaction calorimetry<sup>129</sup> and Raman<sup>129–132</sup> and NIR<sup>133</sup> spectroscopies, the role of the model in the on-line control is to provide the link between the instantaneous monomer conversion and the morphology to be controlled.

## **1.6. Objectives of the thesis**

The objective of this PhD is to pave the way to process optimization and on-line control of particle morphology in emulsion polymerization process. The bottleneck in achieving this goal is the lack of proper device for on-line monitoring of particle

---

morphology. Therefore, the alternative is using a mathematical model as a soft sensor in on-line monitoring. The model needs to be capable of describing the evolution of the particle morphology during the polymerization as well as being sensitive to detect the effect of process variables on morphology changes. Experimental quantitative data of particle morphology is needed to validate the mathematical model. As it was discussed in Section 1.4, different characterization techniques are required to characterize the particle morphology of the latexes and none of them provides quantitative information currently. This implies that there is the room for developing new techniques that can characterize particle morphology in quantitative mode. Moreover, the capability of the developed control strategies to cope with the unexpected uncertainties that often occur in a real system is important. Therefore, the implemented model can be used as state-estimator to track the optimal pathway in the process.

### **1.7. Outline of the thesis**

This thesis is divided in six chapters:

In Chapter 1, a brief review of the works dealing with particle morphology is presented highlighting the aspects that are missing to achieve its control.

In Chapter 2, two-phase polymer-polymer latexes are synthesized in a seeded semibatch emulsion polymerization, using a seed of poly (methyl methacrylate-co-n-

butyl acrylate) and poly (styrene-co-n-butyl acrylate) in the second stage. The effect of different process variables on the particle morphology changes is studied and the performance of a modification of the mathematical model developed by Hamzehlou *et al.*<sup>80</sup> on the prediction of the particle morphology of synthesized latexes was evaluated.

In Chapter 3, a new technique for precise characterization of the particle morphology is presented coupling HAADF-STEM tomography with image reconstruction. Selected number of synthesized latexes in Chapter 2 were characterized using the developed technique and unexpected insights about the mechanisms involved in the process were found. This resulted in further development of the mathematical model used in Chapter 2 and the predicted particle morphology by two versions of the mathematical model for different latexes were compared.

In industrial practice, the reactions are designed to be carried out under monomer-starved conditions to have a good thermal and microstructure control during the process. Therefore, the reactions in Chapter 2 were carried out under starved condition to study the effect of process variables on the morphology. However, the range of morphologies attainable could be expanded if the constraints in the monomer concentration in the particles are relaxed. The reason is that the viscosity of matrix, which affects cluster movements, can be altered by the amount of unreacted monomers

in the polymerization process. In Chapter 4, several experiments were carried out targeting different instantaneous conversions (monomer concentrations in the polymer particles). This was achieved by means of an on-line control of the unreacted monomer concentration in a calorimetric reactor.

In Chapter 5, the effect of disturbances on development of particle morphology, which can occur in a real polymerization process, was investigated.

Finally, in Chapter 6, the most relevant conclusion of this thesis is summarized.

## 1.8. References

- (1) *Polymeric Dispersions: Principles and Applications*; Asua, J. M., Ed.; Springer Netherlands: Dordrecht, 1997.
- (2) *Polymer Dispersions and Their Industrial Applications*; Urban, D., Takamura, K., Eds.; Wiley-VCH Verlag GmbH & Co. KGaA: Weinheim, FRG, 2002.
- (3) Barandiaran, M. J.; de la Cal, J.; Asua, J. M. Emulsion Polymerization. In *Polymer reaction engineering*; Asua, J. M., Ed.; Blackwell Pub, UK, 2007; p 367.
- (4) Chern, C.-S. *Principles and Applications of Emulsion Polymerization*; John Wiley & Sons, Inc.USA, 2008.
- (5) Paulis, M.; Asua, J. M. Knowledge-Based Production of Waterborne Hybrid Polymer Materials. *Macromol. React. Eng.* **2016**, *10* (1), 8–21.
- (6) Haase, M. F.; Grigoriev, D. O.; Möhwald, H.; Shchukin, D. G. Development of Nanoparticle Stabilized Polymer Nanocontainers with High Content of the Encapsulated Active Agent and Their Application in Water-Borne Anticorrosive Coatings. *Adv. Mater.* **2012**, *24* (18), 2429–2435.

- 
- (7) Rahman, O. ur; Kashif, M.; Ahmad, S. Nanoferrite Dispersed Waterborne Epoxy-Acrylate: Anticorrosive Nanocomposite Coatings. *Prog. Org. Coatings* **2015**, *80*, 77–86.
  - (8) Yang, J.; Liang, H.; Zeng, L.; Liu, S.; Guo, T. Facile Fabrication of Superhydrophobic Nanocomposite Coatings Based on Water-Based Emulsion Latex. *Adv. Mater. Interfaces* **2018**, *5* (15), 1800207.
  - (9) Palza, H. Antimicrobial Polymers with Metal Nanoparticles. *Int. J. Mol. Sci.* **2015**, *16* (1), 2099–2116.
  - (10) Martín-Fabiani, I.; Fortini, A.; Lesage De La Haye, J.; Koh, M. L.; Taylor, S. E.; Bourgeat-Lami, E.; Lansalot, M.; D’Agosto, F.; Sear, R. P.; Keddie, J. L. PH-Switchable Stratification of Colloidal Coatings: Surfaces “on Demand.” *ACS Appl. Mater. Interfaces* **2016**, *8* (50), 34755–34761.
  - (11) Chen, J.; Zhong, W.; Tang, Y.; Wu, Z.; Li, Y.; Yi, P.; Jiang, J. Amphiphilic BODIPY-Based Photoswitchable Fluorescent Polymeric Nanoparticles for Rewritable Patterning and Dual-Color Cell Imaging. *Macromolecules* **2015**, *48* (11), 3500–3508.
  - (12) Zhu, M.; Huang, X.; Yang, K.; Zhai, X.; Zhang, J.; He, J.; Jiang, P. Energy Storage in Ferroelectric Polymer Nanocomposites Filled with Core-Shell Structured Polymer@BaTiO<sub>3</sub>nanoparticles: Understanding the Role of Polymer Shells in the Interfacial Regions. *ACS Appl. Mater. Interfaces* **2014**, *6* (22), 19644–19654.
  - (13) Wang, H.; Zhao, L.; Song, G.; Tang, G.; Shi, X. Organic-Inorganic Hybrid Shell Microencapsulated Phase Change Materials Prepared from SiO<sub>2</sub>/TiC-Stabilized Pickering Emulsion Polymerization. *Sol. Energy Mater. Sol. Cells* **2018**, *175*, 102–110.
  - (14) Wu, X. Y. Strategies for Optimizing Polymer-Lipid Hybrid Nanoparticle-Mediated Drug Delivery. *Expert Opin. Drug Deliv.* **2016**, *13* (5), 609–612.
  - (15) Zhou, Z.; Kennell, C.; Lee, J.-Y.; Leung, Y.-K.; Tarapore, P. Calcium Phosphate-Polymer Hybrid Nanoparticles for Enhanced Triple Negative Breast Cancer Treatment via Co-Delivery of Paclitaxel and MiR-221/222 Inhibitors. *Nanomedicine Nanotechnology, Biol. Med.* **2017**, *13* (2), 403–410.
  - (16) Dave, V.; Yadav, R. B.; Kushwaha, K.; Yadav, S.; Sharma, S.; Agrawal, U.
-

- Lipid-Polymer Hybrid Nanoparticles: Development & Statistical Optimization of Norfloxacin for Topical Drug Delivery System. *Bioact. Mater.* **2017**, 2 (4), 269–280.
- (17) Bae, H. J.; Bae, S.; Park, C.; Han, S.; Kim, J.; Kim, L. N.; Kim, K.; Song, S. H.; Park, W.; Kwon, S. Biomimetic Microfingerprints for Anti-Counterfeiting Strategies. *Adv. Mater.* **2015**, 27 (12), 2083–2089.
- (18) Kim, K.; Suh, M.; Choi, J.; Lee, D.; Kim, Y.; Cheong, S. H.; Kim, D.; Jeon, D. Y. Conjugated Polyelectrolyte Hybridized ZnO Nanoparticles as a Cathode Interfacial Layer for Efficient Polymer Light-Emitting Diodes. *Adv. Funct. Mater.* **2015**, 25 (48), 7450–7456.
- (19) Reyes, Y.; Akhmastkaya, E.; Leiza, J. R.; Asua, J. M. Particle Morphology. In *Chemistry and technology of emulsion polymerisation*; van Herk, A. M., Ed.; Wiley, UK, 2013; pp 145–167.
- (20) Asua, J. M. Miniemulsion Polymerization. *Prog. Polym. Sci.* **2002**, 27 (7), 1283–1346.
- (21) Schork, F. J.; Luo, Y.; Smulders, W.; Russum, J. P.; Butté, A.; Fontenot, K. Miniemulsion Polymerization. *Adv. Polym. Sci.* **2005**, 175, 129–255.
- (22) Landfester, K. Miniemulsion Polymerization and the Structure of Polymer and Hybrid Nanoparticles. *Angew. Chemie - Int. Ed.* **2009**, 48 (25), 4488–4508.
- (23) Asua, J. M. Challenges for Industrialization of Miniemulsion Polymerization. *Prog. Polym. Sci.* **2014**, 39 (10), 1797–1826.
- (24) Sundberg, D. C.; Durant, Y. G. Latex Particle Morphology, Fundamental Aspects: A Review. *Polym. React. Eng.* **2003**, 11 (3), 379–432.
- (25) Torza, S.; Mason, S. . Three-Phase Interactions in Shear and Electrical Fields. *J. Colloid Interface Sci.* **1970**, 33 (1), 67–83.
- (26) Chen, Y. C.; Dimonie, V.; El-Aasser, M. S. Effect of Interfacial Phenomena on the Development of Particle Morphology in a Polymer Latex System. *Macromolecules* **1991**, 24 (13), 3779–3787.
- (27) Winzor, C. L.; Sundberg, D. C. Conversion Dependent Morphology Predictions for Composite Emulsion Polymers: 1. Synthetic Latices. *Polymer.* **1992**, 33 (18), 3797–3810.

- 
- (28) Winzor, C. L.; Sundberg, D. C. Conversion Dependent Morphology Predictions for Composite Emulsion Polymers: 2. Artificial Latices. *Polymer*. **1992**, *33* (20), 4269–4279.
- (29) Chen, Y. C.; Dimonie, V. L.; Shaffer, O. L.; El-Aasser, M. S. Development of Morphology in Latex Particles: The Interplay between Thermodynamic and Kinetic Parameters. *Polym. Int.* **1993**, *30* (2), 185–194.
- (30) Jönsson, J. E.; Hassander, H.; Törnell, B. Polymerization Conditions and the Development of a Core-Shell Morphology in PMMA/PS Latex Particles. 1. Influence of Initiator Properties and Mode of Monomer Addition. *Macromolecules* **1994**, *27* (7), 1932–1937.
- (31) Herrera, V.; Pirri, R.; Asua, J. M.; Leiza, J. R. Morphology Control in Polystyrene/Poly(Methyl Methacrylate) Composite Latex Particles. *J. Polym. Sci. Part A Polym. Chem.* **2007**, *45*, 2484–2493.
- (32) Lee, D. I.; Ishikawa, T. The Formation of “Inverted” Core-Shell Latexes. *J. Polym. Sci. Polym. Chem. Ed.* **1983**, *21* (1), 147–154.
- (33) Herrera, V.; Pirri, R.; Leiza, J. R.; Asua, J. M. Effect of In-Situ-Produced Block Copolymer on Latex Particle Morphology. *Macromolecules* **2006**, *39* (20), 6969–6974.
- (34) Sundberg, D. C.; Casassa, A. P.; Pantazopoulos, J.; Muscato, M. R.; Kronberg, B.; Berg, J. Morphology Development of Polymeric Microparticles in Aqueous Dispersions. I. Thermodynamic Considerations. *J. Appl. Polym. Sci.* **1990**, *41* (7–8), 1425–1442.
- (35) Herrera, V.; Palmillas, Z.; Pirri, R.; Reyes, Y.; Leiza, J. R.; Asua, J. M. Morphology of Three-Phase PS/PBA Composite Latex Particles Containing in Situ Produced Block Copolymers. *Macromolecules* **2010**, *43* (3), 1356–1363.
- (36) Gonzalez-Ortiz, L. J.; Asua, J. M. Development of Particle Morphology in Emulsion Polymerization. 1. Cluster Dynamics. *Macromolecules* **1995**, *28* (9), 3135–3145.
- (37) Asua, J. M. Mapping the Morphology of Polymer-Inorganic Nanocomposites Synthesized by Miniemulsion Polymerization. *Macromol. Chem. Phys.* **2014**, *215* (5), 458–464.
-

- (38) Okubo, M.; Katsuta, Y.; Matsumoto, T. Rupture of Anomalous Composite Particles Prepared by Seeded Emulsion Polymerization in Aging Period. *J. Polym. Sci. Polym. Lett. Ed.* **1980**, *18* (7), 481–486.
- (39) Okubo, M.; Nakagawa, T. Formation of Multihollow Structures in Crosslinked Composite Polymer Particles. *Colloid Polym. Sci.* **1994**, *272* (5), 530–535.
- (40) Leal, G. P.; Asua, J. M. Evolution of the Morphology of HIPS Particles. *Polymer.* **2009**, *50* (1), 68–76.
- (41) Deng, W.; Li, R.; Zhang, M.; Gong, L.; Kan, C. Influences of MAA on the Porous Morphology of P(St-MAA) Latex Particles Produced by Batch Soap-Free Emulsion Polymerization Followed by Stepwise Alkali/Acid Post-Treatment. *J. Colloid Interface Sci.* **2010**, *349* (1), 122–126.
- (42) Li, B.; Xu, Y.; Wang, M.; Ge, X. Morphological Control of Multihollow Polymer Latex Particles through a Controlled Phase Separation in the Seeded Emulsion Polymerization. *Langmuir* **2013**, *29* (48), 14787–14794.
- (43) Zhai, W.; Wang, B.; Wang, Y.; He, Y. F.; Song, P.; Wang, R. M. An Efficient Strategy for Preparation of Polymeric Janus Particles with Controllable Morphologies and Emulsifiabilities. *Colloids Surfaces A Physicochem. Eng. Asp.* **2016**, *503*, 94–100.
- (44) Jasinski, F.; Teo, V.; Kuchel, R. P.; Mballa Mballa, M.; Thickett, S. C.; Brinkhuis, R. H. G.; Weaver, W.; Zetterlund, P. B. Synthesis and Characterisation of Gradient Polymeric Nanoparticles. *Polym. Chem.* **2017**, *8*, 495–499.
- (45) Jasinski, F.; Teo, V. L.; Kuchel, R. P.; Mballa Mballa, M.; Thickett, S. C.; Brinkhuis, R. H. G.; Weaver, W.; Zetterlund, P. B. Core–Shell and Gradient Morphology Polymer Particles Analyzed by X- Ray Photoelectron Spectroscopy: Effect of Monomer Feed Order. *J. Polym. Sci. Part A Polym. Chem.* **2017**, *55* (15), 2513–2526.
- (46) Hosseini, A.; Bouaswaig, A. E.; Engell, S. Novel Approaches to Improve the Particle Size Distribution Prediction of a Classical Emulsion Polymerization Model. *Chem. Eng. Sci.* **2013**, *88*, 108–120.
- (47) Pladis, P.; Alexopoulos, A. H.; Kiparissides, C. Mathematical Modeling and Simulation of Vinylidene Fluoride Emulsion Polymerization. *Ind. Eng. Chem.*



- 
- Res.* **2014**, 53 (18), 7352–7364.
- (48) Calvo, I.; Hester, K.; Leiza, J. R.; Asua, J. M. Mathematical Modeling of Carboxylated SB Latexes. *Macromol. React. Eng.* **2014**, 8 (4), 329–346.
- (49) Hlalele, L.; D’hooge, D. R.; Dürr, C. J.; Kaiser, A.; Brandau, S.; Barner-Kowollik, C. RAFT-Mediated *Ab Initio* Emulsion Copolymerization of 1,3-Butadiene with Acrylonitrile. *Macromolecules* **2014**, 47 (9), 2820–2829.
- (50) Hamzehlou, S.; Ballard, N.; Carretero, P.; Paulis, M.; Asua, J. M.; Reyes, Y.; Leiza, J. R. Mechanistic Investigation of the Simultaneous Addition and Free-Radical Polymerization in Batch Miniemulsion Droplets: Monte Carlo Simulation versus Experimental Data in Polyurethane/Acrylic Systems. *Polymer*. **2014**, 55 (19), 4801–4811.
- (51) Capeletto, C. A.; Costa, C.; Sayer, C.; Araújo, P. H. H. Mathematical Modeling of Molecular Weight Distribution in Miniemulsion Polymerization with Oil-Soluble Initiator. *AIChE J.* **2017**, 63 (6), 2128–2140.
- (52) Grancio, M. R.; Williams, D. J. The Morphology of the Monomer-Polymer Particle in Styrene Emulsion Polymerization. *J. Polym. Sci. Part A-1 Polym. Chem.* **1970**, 8 (9), 2617–2629.
- (53) Chern, C.-S.; Poehlein, G. W. Polymerization in Nonuniform Latex Particles: Distribution of Free Radicals. *J. Polym. Sci. Part A Polym. Chem.* **1987**, 25 (2), 617–635.
- (54) Napper, D. H. Particle Morphology in Emulsion Polymerization. *J. Polym. Sci. Part A-1 Polym. Chem.* **1971**, 9 (7), 2089–2091.
- (55) de La Cal, J. C.; Urzay, R.; Zamora, A.; Forcada, J.; Asua, J. M. Simulation of the Latex Particle Morphology. *J. Polym. Sci. Part A Polym. Chem.* **1990**, 28 (5), 1011–1031.
- (56) Mills, M. F.; Gilbert, R. G.; Napper, D. H. Effect of Polymerization Kinetics on Particle Morphology in Heterogeneous Systems. *Macromolecules* **1990**, 23 (19), 4247–4257.
- (57) Stubbs, J.; Karlsson, O.; Jönsson, J. E.; Sundberg, E.; Durant, Y.; Sundberg, D. Non-Equilibrium Particle Morphology Development in Seeded Emulsion Polymerization. 1: Penetration of Monomer and Radicals as a Function of
-

- Monomer Feed Rate during Second Stage Polymerization. *Colloids Surfaces A Physicochem. Eng. Asp.* **1999**, *153* (1–3), 255–270.
- (58) Stubbs, J. M.; Sundberg, D. C. Fundamental Studies on Morphology Control For Latex Systems with Application to Waterborne Coatings: The Effect of Polymer Radical Mobility In Latex Particles During Polymerization. *J. Coatings Technol.* **2003**, *75* (938), 59–67.
- (59) Karlsson, L. E.; Karlsson, O. J.; Sundberg, D. C. Nonequilibrium Particle Morphology Development in Seeded Emulsion Polymerization. II. Influence of Seed Polymer Tg. *J. Appl. Polym. Sci.* **2003**, *90* (4), 905–915.
- (60) Stubbs, J. M.; Sundberg, D. C. Nonequilibrium Particle Morphology Development in Seeded Emulsion Polymerization. III. Effect of Initiator End Groups. *J. Appl. Polym. Sci.* **2004**, *91*, 1538–1551.
- (61) Stubbs, J. M.; Sundberg, D. C. Nonequilibrium Morphology Development in Seeded Emulsion Polymerization. IV. Influence of Chain Transfer Agent. *J. Appl. Polym. Sci.* **2006**, *102* (2), 945–957.
- (62) Stubbs, J. M.; Sundberg, D. C. The Dynamics of Morphology Development in Multiphase Latex Particles. *Prog. Org. Coatings* **2008**, *61* (2), 156–165.
- (63) Blenner, D.; Stubbs, J.; Sundberg, D. Multi-Lobed Composite Polymer Nanoparticles Prepared by Conventional Emulsion Polymerization. *Polymer.* **2017**, *114*, 54–63.
- (64) Jönsson, J. E.; Karlsson, O. J.; Hassander, H.; Törnell, B. Semi-Continuous Emulsion Polymerization of Styrene in the Presence of Poly(Methyl Methacrylate) Seed Particles. Polymerization Conditions Giving Core-Shell Particles. *Eur. Polym. J.* **2007**, *43* (4), 1322–1332.
- (65) Sheu, H. R.; El-Aasser, M. S.; Vanderhoff, J. W. Phase Separation in Polystyrene Latex Interpenetrating Polymer Networks. *J. Polym. Sci. Part A Polym. Chem.* **1990**, *28* (3), 629–651.
- (66) Schneider, M.; Pith, T.; Lambla, M. Structured Latex Particles as Impact Modifiers for Poly(Styrene - Co-Acrylonitrile) Blends. *Polym. Adv. Technol.* **1996**, *7* (7), 577–588.
- (67) Schneider, M.; Pith, T.; Lambla, M. Preparation and Morphological

- 
- Characterization of Two- and Three-Component Natural Rubber-Based Latex Particles. *J. Appl. Polym. Sci.* **1996**, *62*, 273–290.
- (68) Durant, Y. G.; Sundberg, D. C. Effects of Cross-Linking on the Morphology of Structured Latex Particles. 1. Theoretical Considerations. *Macromolecules* **1996**, *29*, 8466–8472.
- (69) Durant, Y. G.; Sundberg, E. J.; Sundberg, D. C. Effects of Cross-Linking on the Morphology of Structured Latex Particles. 2. Experimental Evidence for Lightly Cross-Linked Systems. *Macromolecules* **1997**, *30*, 1028–1032.
- (70) Segall, I.; Dimonie, V. L.; El-Aasser, M. S.; Soskey, P. R.; Mylonakis, S. G. Core—shell Structured Latex Particles. II. Synthesis and Characterization of Poly (N-butyl Acrylate)/Poly (Benzyl Methacrylate—styrene) Structured Latex Particles. *J. Appl. Polym. Sci.* **1995**, *58* (2), 401–417.
- (71) McDonald, C. J.; Devon, M. J. Hollow Latex Particles: Synthesis and Applications. *Adv. Colloid Interface Sci.* **2002**, *99* (3), 181–213.
- (72) Stubbs, J. M.; Sundberg, D. C. Nonequilibrium Morphology Development in Seeded Emulsion Polymerization. V. The Effect of Crosslinking Agent. *J. Appl. Polym. Sci.* **2006**, *102* (3), 2043–2054.
- (73) Stubbs, J.; Carrier, R.; Sundberg, D. C. Monte Carlo Simulation of Emulsion Polymerization Kinetics and the Evolution of Latex Particle Morphology and Polymer Chain Architecture. *Macromol. Theory Simulations* **2008**, *17* (4–5), 147–162.
- (74) Chen, Y. -C; Dimonie, V.; El-Aasser, M. S. Interfacial Phenomena Controlling Particle Morphology of Composite Latexes. *J. Appl. Polym. Sci.* **1991**, *42* (4), 1049–1063.
- (75) Reyes, Y.; Asua, J. M. Modeling Multiphase Latex Particle Equilibrium Morphology. *J. Polym. Sci. Part A Polym. Chem.* **2010**, *48*, 2579–2583.
- (76) González-Ortiz, L. J.; Asua, J. M. Development of Particle Morphology in Emulsion Polymerization. 2. Cluster Dynamics in Reacting Systems. *Macromolecules* **1996**, *29* (1), 383–389.
- (77) González-Ortiz, L. J.; Asua, J. M. Development of Particle Morphology in Emulsion Polymerization. 3. Cluster Nucleation and Dynamics in Polymerizing
-

- Systems. *Macromolecules* **1996**, *29* (13), 4520–4527.
- (78) Akhmatskaya, E.; Asua, J. M. Dynamic Modeling of the Morphology of Latex Particles with In Situ Formation of Graft Copolymer. *J Polym Sci Part A Polym Chem* **2012**, *50*, 1383–1393.
- (79) Akhmatskaya, E.; Asua, J. M. Dynamic Modeling of the Morphology of Multiphase Waterborne Polymer Particles. *Colloid Polym Sci* **2013**, *291*, 87–98.
- (80) Hamzehlou, S.; Leiza, J. R.; Asua, J. M. A New Approach for Mathematical Modeling of the Dynamic Development of Particle Morphology. *Chem. Eng. J.* **2016**, *304*, 655–666.
- (81) Hamzehlou, S.; Aguirre, M.; Leiza, J. R.; Asua, J. M. Dynamics of the Particle Morphology during the Synthesis of Waterborne Polymer-Inorganic Hybrids. *Macromolecules* **2017**, *50* (18), 7190–7201.
- (82) Faust, J. M. M.; Hamzehlou, S.; Leiza, J. R.; Asua, J. M.; Mhamdi, A.; Mitsos, A. Dynamic Optimization of a Two-Stage Emulsion Polymerization to Obtain Desired Particle Morphologies. *Chem. Eng. J.* **2019**, *359*, 1035–1045.
- (83) Li, B.-G.; Brooks, B. W. Prediction of the Average Number of Radicals per Particle for Emulsion Polymerization. *J. Polym. Sci. Part A Polym. Chem.* **1993**, *31* (9), 2397–2402.
- (84) Stubbs, J. M.; Sundberg, D. C. A Round Robin Study for the Characterization of Latex Particle Morphology—multiple Analytical Techniques to Probe Specific Structural Features. *Polymer*. **2005**, *46*, 1125–1138.
- (85) Okubo, M.; Yamada, A.; Matsumoto, T. Estimation of Morphology of Composite Polymer Emulsion Particles by the Soap Titration Method. *J. Polym. Sci. Polym. Chem. Ed.* **1980**, *18* (11), 3219–3228.
- (86) Gonzalez, E.; Tollan, C.; Chuvilin, A.; Barandiaran, M. J.; Paulis, M. Determination of the Coalescence Temperature of Latexes by Environmental Scanning Electron Microscopy. *ACS Appl. Mater. Interfaces* **2012**, *4* (8), 4276–4282.
- (87) Hourston, D. J.; Song, M.; Hammiche, A.; Pollock, H. M.; Reading, M. Modulated Differential Scanning Calorimetry: 6. Thermal Characterization of

- 
- Multicomponent Polymers and Interfaces. **1997**, 38 (1), 1–7.
- (88) Song, M.; Hourston, D. J.; Reading, M.; Pollock, H. M.; Hammiche, A. Modulated Differential Scanning Calorimetry. Analysis of Interphases in Multi-Component Polymer Materials. *J. Therm. Anal. Calorim.* **1999**, 56, 991–1004.
- (89) Tripathi, A. K.; Tsavalas, J. G.; Sundberg, D. C. Quantitative Measurements of the Extent of Phase Separation during and after Polymerization in Polymer Composites Using DSC. *Thermochim. Acta* **2013**, 568, 20–30.
- (90) Geng, X.; Zhai, M. X.; Sun, T.; Meyers, G. Morphology Observation of Latex Particles with Scanning Transmission Electron Microscopy by a Hydroxyethyl Cellulose Embedding Combined with RuO<sub>4</sub> Staining Method. *Microsc. Microanal.* **2013**, 19, 319–326.
- (91) Midgley, P. A.; Weyland, M. 3D Electron Microscopy in the Physical Sciences: The Development of Z-Contrast and EFTEM Tomography. *Ultramicroscopy* **2003**, 96 (3–4), 413–431.
- (92) Smith, R. W.; Bryg, V. Staining Polymers for Microscopical Examination. *Rubber Chem. Technol.* **2006**, 79 (3), 520–540.
- (93) Sawyer, L. C.; Grubb, D. T.; Meyers, G. F. *Polymer Microscopy*, 3rd ed.; Springer: New York, 2008.
- (94) Libera, M. R.; Egerton, R. F. Advances in the Transmission Electron Microscopy of Polymers. *Polym. Rev.* **2010**, 50, 321–339.
- (95) Tosaka, M.; Danev, R.; Nagayama, K. Application of Phase Contrast Transmission Microscopic Methods to Polymer Materials. *Macromolecules* **2005**, 38 (19), 7884–7886.
- (96) Voorn, D. J.; Ming, W.; van Herk, A. M. Clay Platelets Encapsulated Inside Latex Particles. *Macromolecules* **2006**, 39, 4654–4656.
- (97) Drummy, L. F.; Wang, Y. C.; Schoenmakers, R.; May, K.; Jackson, M.; Koerner, H.; Farmer, B. L.; Mauryama, B.; Vaia, R. A. Morphology of Layered Silicate-(NanoClay-) Polymer Nanocomposites by Electron Tomography and Small-Angle X-Ray Scattering. *Macromolecules* **2008**, 41 (6), 2135–2143.
- (98) Aguirre, M.; Paulis, M.; Leiza, J. R. UV Screening Clear Coats Based on Encapsulated CeO<sub>2</sub> Hybrid Latexes. *J. Mater. Chem. A* **2013**, 1, 3155–3162.
-

- (99) Aguirre, M.; Paulis, M.; Leiza, J. R.; Guraya, T.; Iturrondobeitia, M.; Okariz, A.; Ibarretxe, J. High-Solids-Content Hybrid Acrylic/CeO<sub>2</sub> Latexes with Encapsulated Morphology Assessed by 3D-TEM. *Macromol. Chem. Phys.* **2013**, *214* (19), 2157–2164.
- (100) Aguirre, M.; Barrado, M.; Iturrondobeitia, M.; Okariz, A.; Guraya, T.; Paulis, M.; Leiza, J. R. Film Forming Hybrid Acrylic/ZnO Latexes with Excellent UV Absorption Capacity. *Chem. Eng. J.* **2015**, *270*, 300–308.
- (101) Jeanguillaume, C.; Colliex, C. Spectrum-Image: The Next Step In EELS Digital Acquisition And Processing. *Ultramicroscopy* **1989**, *28*, 252–257.
- (102) Hunt, J. A.; Williams, D. B. Electron Energy-Loss Spectrum-Imaging. *Ultramicroscopy* **1991**, *38*, 47–73.
- (103) Lieser, G.; Schmid, S. C.; Wegner, G. Electrically Conducting Polymers: Preparation and Investigation of Oxidized Poly(Acetylene) by EFTEM. *J. Microsc.* **1996**, *183* (Part 1), 53–59.
- (104) Horiuchi, S.; Kiyoshi, Y.; Kitano, T.; Higashida, N.; Ougizawa, T. EFTEM for the Characterization of Polymer Blend Morphologies. *Polymer Journal*. 1997, pp 380–383.
- (105) Horiuchi, S.; Hanada, T.; Yase, K.; Ougizawa, T. Analysis of an Interface between an Immiscible Polymer Pair by Electron Spectroscopic Imaging. *Macromolecules* **1999**, *32*, 1312–1314.
- (106) Hofer, F.; Warbichler, P. Elemental Mapping Using Energy Filtered Imaging. In *Transmission Electron Energy Loss Spectrometry in Materials Science and The EELS Atlas*; 2005.
- (107) Horiuchi, S.; Yin, D.; Ougizawa, T. Nanoscale Analysis of Polymer Interfaces by Energy-Filtering Transmission Electron Microscopy. *Macromol. Chem. Phys.* **2005**, *206* (7), 725–731.
- (108) Garcia-Meitin, E.; Bar, G.; Blackson, J.; Reuschle, D. High Resolution Polymer Imaging Using Scanning Transmission Electron Microscopy. *Microsc. Microanal.* **2008**, *14* (S2), 1380–1381.
- (109) Linares, E. M.; Leite, C. a P.; Valadares, L. F.; Silva, C. a; Rezende, C. a; Galembeck, F. Molecular Mapping by Low-Energy-Loss Energy-Filtered

- 
- Transmission Electron Microscopy Imaging. *Anal. Chem.* **2009**, *81* (6), 2317–2324.
- (110) Kim, G.; Sousa, A.; Meyers, D.; Shope, M.; Libera, M. Diffuse Polymer Interfaces in Lobed Nanoemulsions Preserved in Aqueous Media. *J. Am. Chem. Soc.* **2006**, *128*, 6570–6571.
- (111) Kim, G.; Sousa, A.; Meyers, D.; Libera, M. Nanoscale Composition of Biphasic Polymer Nanocolloids in Aqueous Suspension. *Microsc. Microanal.* **2008**, *14*, 459–468.
- (112) Yakovlev, S.; Libera, M. Dose-Limited Spectroscopic Imaging of Soft Materials by Low-Loss EELS in the Scanning Transmission Electron Microscope. *Micron* **2008**, *39* (6), 734–740.
- (113) Liu, Z.; Epicier, T.; Lefkir, Y.; Vitrant, G.; Destouches, N. HAADF-STEM Characterization and Simulation of Nanoparticle Distributions in an Inhomogeneous Matrix. *J. Microsc.* **2017**, *266* (1), 60–68.
- (114) Loos, J.; Sourty, E.; Lu, K.; de With, G.; v. Bavel, S. Imaging Polymer Systems with High-Angle Annular Dark Field Scanning Transmission Electron Microscopy (HAADF-STEM). *Macromolecules* **2009**, *42* (7), 2581–2586.
- (115) Hindson, J. C.; Saghi, Z.; Hernandez-Garrido, J.-C.; Midgley, P. A.; Greenham, N. C. Morphological Study of Nanoparticle-Polymer Solar Cells Using High-Angle Annular Dark-Field Electron Tomography. *Nano Lett.* **2011**, *11* (2), 904–909.
- (116) Stubbs, J. M.; Sundberg, D. C. Core-Shell and Other Multiphase Latex Particles-Confirming Their Morphologies and Relating Those to Synthesis Variables. *J. Coatings Technol. Res.* **2008**, *5*, 169–180.
- (117) Asua, J. M. Emulsion Polymerization: From Fundamental Mechanisms to Process Developments. *J. Polym. Sci. Part A Polym. Chem.* **2004**, *42* (5), 1025–1041.
- (118) Arzamendi, G.; Asua, J. M. Monomer Addition Policies for Copolymer Composition Control in Semicontinuous Emulsion Copolymerization. *J. Appl. Polym. Sci.* **1989**, *38*, 2019–2036.
- (119) Arzamendi, G.; Asua, J. M. Copolymer Composition Control during the Seeded
-

- Emulsion Copolymerization of Vinyl Acetate and Methyl Acrylate. *Macromol. Symp.* **1990**, 35/36, 249–268.
- (120) Arzamendi, G.; Leiza, J. R.; Asua, J. M. Semicontinuous Emulsion Copolymerization of Methyl Methacrylate and Ethyl Acrylate. *J. Polym. Sci. Part A Polym. Chem.* **1991**, 29, 1549–1559.
- (121) Saenz de Buruaga, I.; Echevarra, A.; Armitage, P. D.; de la Cal, J.; Leiza, J. R.; Asua, J. M. On-Line Control of a Semibatch Emulsion Polymerization Reactor Based on Calorimetry. *AIChE J.* **1997**, 43 (4), 1069–1081.
- (122) Saenz de Buruaga, I.; Armitage, P. D.; Leiza, J. R.; Asua, J. M. Nonlinear Control for Maximum Production Rate of Latexes of Well-Defined Polymer Composition. *Ind. Eng. Chem. Res.* **1997**, 36 (1992), 4243–4254.
- (123) Leiza, J. R.; de la Cal, J. C.; Meira, G. R.; Asua, J. M. On-Line Copolymer Composition Control in the Semicontinuous Emulsion Copolymerization of Ethyl Acrylate and Methyl Methacrylate. *Polym. React. Eng.* **1993**, 1 (4), 461–497.
- (124) Fonseca, G. E.; Dubé, M. A.; Penlidis, A. A Critical Overview of Sensors for Monitoring Polymerizations. *Macromol. React. Eng.* **2009**, 3 (7), 327–373.
- (125) *Monitoring Polymerization Reactions: From Fundamentals to Applications.*; Reed, W. F., Alb, A. M., Eds.; John Wiley & Sons, Inc., 2014.
- (126) Echevarría, A.; Leiza, J. R.; de la Cal, J. C.; Asua, J. M. Molecular-Weight Distribution Control in Emulsion Polymerization. *AIChE J.* **1998**, 44 (7), 1667–1679.
- (127) Vicente, M.; Benamor, S.; Gugliotta, L. M.; Leiza, J. R.; Asua, J. M. Control of Molecular Weight Distribution in Emulsion Polymerization Using On-Line Reaction Calorimetry. *Ind. Eng. Chem. Res.* **2001**, 40 (1), 218–227.
- (128) Vicente, M.; Leiza, J. R.; Asua, J. M. Simultaneous Control of Copolymer Composition and MWD in Emulsion Copolymerization. *AIChE J.* **2001**, 47 (7), 1594–1606.
- (129) Elizalde, O.; Azpeitia, M.; Reis, M. M.; Asua, J. M.; Leiza, J. R. Monitoring Emulsion Polymerization Reactors: Calorimetry versus Raman Spectroscopy. *Ind. Eng. Chem. Res.* **2005**, 44 (18), 7200–7207.



- (130) Van, M.; Brink, D.; Hansen, J.; De Peinder, P.; Van Herk, A. M.; German, A. L. Measurement of Partial Conversions during the Solution Copolymerization of Styrene and Butyl Acrylate Using On-line Raman Spectroscopy. *J. Appl. Polym. Sci.* **2001**, *79* (3), 426–436.
- (131) Elizalde, O.; Arzamendi, G.; Leiza, J. R.; Asua, J. M. Seeded Semibatch Emulsion Copolymerization of *n*-Butyl Acrylate and Methyl Methacrylate. *Ind. Eng. Chem. Res.* **2004**, *43* (23), 7401–7409.
- (132) Reis, M. M.; Araújo, P. H. H.; Sayer, C.; Giudici, R. Spectroscopic On-Line Monitoring of Reactions in Dispersed Medium: Chemometric Challenges. *Anal. Chim. Acta* **2007**, *595* (1–2), 257–265.
- (133) Santos, A. F.; Silva, F. M.; Lenzi, M. K.; Pinto, J. C. Monitoring and Control of Polymerization Reactors Using NIR Spectroscopy. *Polym. Plast. Technol. Eng.* **2005**, *44* (1), 1–61.



## **Chapter 2. Effect of process variables on particle morphology**

### **2.1. Introduction**

As explained in the literature survey in Chapter 1, the most common method to synthesize polymer-polymer composite particles is seeded semi-batch emulsion polymerization. During the polymerization, the particle morphology forms as a result of phase separation of the second stage polymer that is usually incompatible with the polymer in the seed. Thermodynamics defines the equilibrium morphology, which corresponds to the minimum surface energy, and in a two-phase polymer-polymer system the morphology can be either core-shell, inverted core-shell or hemispherical<sup>1-4</sup> and experimental proof is available in the literature.<sup>5-8</sup> Kinetically metastable morphologies (non-equilibrium) are reached as a result of the hindered movement of the clusters due to the high internal viscosity of the particles.<sup>9-16</sup> The internal viscosity

depends on the molecular weight, crosslinking density and glass transition temperature (T<sub>g</sub>) of the seed polymer, the polymerization temperature, the amount of free monomer in the reactor (monomer acts as plasticizer) and also the type of monomer (is important on the effect of hydro-plasticization).

The effect of the internal viscosity is reinforced when the second stage polymer is produced in a position that is far from where it will be under equilibrium conditions. The position where the polymer is formed depends on the radical and monomer concentration profiles in the particles. Often flat concentration profiles of monomer(s) and radicals within the polymer particles are considered in emulsion polymerization.<sup>17–22</sup> However, in processes carried out at temperatures lower than the T<sub>g</sub> of the seed and under severe starved conditions, the concentration of monomer near the particle surface may be greater than in the interior part of the particles.<sup>23,24</sup> On the other hand, Grancio and Williams<sup>25</sup> proposed the existence of a decreasing concentration profile of radicals within the polymer particles when water soluble initiators were used. The rationale behind this is that the radicals entering into the particle have a hydrophilic segment (many contain a charged inorganic moiety) that can anchor to the surface of the particle and therefore their movement towards the center of the particle is restricted.<sup>26</sup>

The effect of the decreasing profiles of radical concentration is expected to be stronger for inverted core-shell equilibrium morphology where the second stage polymer is substantially more hydrophobic than the seed. In this case, the radical concentration profile restricts the formation of the second stage polymer to a region close to the surface of the particle and hence the hydrophobic polymer is produced far from the equilibrium position (center of the particle).

In this chapter, a series of latexes were synthesized in a two-step seeded semi-batch emulsion polymerization with a hydrophilic seed composed of methyl methacrylate/n-butyl acrylate (MMA/BA) as main monomers and small amount of acrylic acid (AA) and acrylamide (AM) to enhance colloidal stability. The second stage copolymer was more hydrophobic and it was composed of styrene/n-butyl acrylate (S/BA) and some AA and AM. According to the thermodynamics, the equilibrium morphology of the system is “inverted core-shell” with the hydrophobic second phase as the core of the particle. The polymerization reactions were carried out varying different reaction variables including Tg and crosslinking of the seed, reaction temperature, type of initiator, reaction time in the second stage of polymerization and Tg of second stage polymer. The aim of these experiments was to understand the effect of process variables on the produced particle morphology and the performance of the

mathematical model developed by Hamzehlou *et al.*<sup>27</sup> on the prediction of the evolution of the particle morphology of composite polymer particles was evaluated.

## **2.2. Experimental section**

### **2.2.1. Materials**

Technical grade monomers, methyl methacrylate (MMA, Quimidroga), styrene (S, Quimidroga), butyl acrylate (BA, Quimidroga), acrylic acid (AA, Aldrich), acrylamide (AM, Aldrich), ethylene glycol dimethacrylate (EGDMA, Aldrich) and allyl methacrylate (AMA, Aldrich) were used as received. Sodium persulfate (NaPS, Fluka) as water-soluble thermal radical initiator, 2,2'-azobis (2-methylpropionitrile) (AIBN, Aldrich) as oil-soluble thermal radical initiator, tert-Butyl hydroperoxide (TBHP, Aldrich) and sodium acetone bisulfite (ACBS, BASF) as water-soluble REDOX pair radical initiator were used in the formulation of different latex synthesis. Sodium lauryl sulfate (SLS, Aldrich) and Emulan-OG (BASF, Germany) were used as ionic and non-ionic emulsifiers, respectively. Deionized water (DI-water) was used in the formulation and hydroquinone (HQ, Aldrich) was used to stop the reaction in the samples withdrawn from the reactor. Tetrahydrofuran (GPC grade-THF, Aldrich) and ethanol (analytical standard grade, Aldrich) were used as solvent and internal standard in GC characterization, respectively.

## **2.2.2. Synthesis of latexes**

### **2.2.2.1. Synthesis of seed latex**

The seed latexes were synthesized in a 1 L jacketed glass reactor equipped with an anchor impeller rotating at 160 rpm, platinum resistance thermometer, nitrogen inlet, reflux condenser, feeding inlets and sampling tube. The formulation and the reaction conditions used to synthesize the seeds are summarized in Table 2.1. The seeds with different Tgs were prepared by varying the monomer composition<sup>28</sup> and all seeds contained functional monomers (acrylic acid and acrylamide) to improve the colloidal stability of the particles. In seeds M4 to M8, either ethylene glycol dimethylacrylate (EGDMA) or allyl methacrylate (AMA) was added as crosslinking agent.

The procedure for the synthesis of seeds is summarized in Table 2.2. In the process, the reactor was charged with 350 g DI-water and heated up to 80 °C. Then, 44.5 g of pre-emulsion (monomers, surfactant, and water) and 5 g of sodium persulfate (NaPS) initiator solution were injected to the reactor as initial load and were polymerized for 15 minutes to produce a pre-seed. The process continued by pre-emulsion feeding with the feed rate of 3.8 g/min in the first 15 minutes and with 6.06 g/min in the next 75 minutes. The initiator solution was fed at constant flow rate of 13.4 g/h during 90 minutes. The monomers composition was the same for the initial load and the feeding.

Finally, the latexes were allowed to react batchwise for one hour at the reaction temperature to reduce the unreacted monomers. The DI-water in the initial load was purged with nitrogen and the whole process was carried out under nitrogen. The final seeds were coagulum free with 38.1-38.5 wt% solids content.

Table 2. 1. Formulation used in the synthesis of seed latexes

Seed	Monomers	Weight percent in monomer mixture	T <sub>g</sub> ,calculated (°C)	Initiator	T <sub>reaction</sub> (°C)
M1	MMA/BA/AA/AM	88/10/1/1	90	NaPS	80
M2	MMA/BA/AA/AM	75/23/1/1	60	NaPS	80
M3	MMA/BA/AA/AM	64/34/1/1	40	NaPS	80
M4	MMA/BA/AA/AM+EGDMA	62/36/1/1+ (0.5 mol% total monomer)	40	NaPS	80
M5	MMA/BA/AA/AM+EGDMA	62/36/1/1+ (1 mol% total monomer)	40	NaPS	80
M6	MMA/BA/AA/AM+AMA	62/36/1/1+ (0.1 mol% total monomer)	40	NaPS	80
M7	MMA/BA/AA/AM+AMA	62/36/1/1+ (0.5 mol% total monomer)	40	NaPS	80
M8	MMA/BA/AA/AM+AMA	62/36/1/1+ (1 mol% total monomer)	40	NaPS	80



Table 2. 2. Procedure used in the synthesis of seed latexes M1-M8

Material	Initial load (g)			Feed stream (g)	
		Pre-emulsion	Initiator solution	Pre-emulsion	Initiator solution
<b>DI-water</b>	350	15.9		183.1	
<b>Emulan OG</b>		0.3		3.2	
<b>SDS</b>		0.3		3.2	
<b>Monomers</b>		28		322.0	
<b>NaPS solution ,7wt%</b>			5		20.1

### 2.2.2.2. Synthesis of composite polymer particle latex

The second stage of the process was a seeded semi-batch emulsion polymerization carried out in a 0.5 L jacketed glass reactor. The reaction conditions and monomer compositions of synthesized latexes are summarized in Table 2.3. The S/BA co-monomer composition was varied to modify the Tg.<sup>28</sup> Functional monomers (AA and AM) were used to improve the colloidal stability. The seeds form 50 wt% of the final polymer particles in all cases. The synthesis procedures are illustrated in Table 2.4 for Run R1, N1 and A1.

The reactor was filled with the seed latex, heated to the reaction temperature in each run (Table 2.3) and purged with nitrogen. Then, in the case of using redox initiator, the TBHP solution was injected to the reactor as a shot and the pre-emulsion and aqueous solution of ACBS were fed to the reactor at constant flow rate in 90 minutes.

## Chapter 2

---

In the case of using thermal initiator, the pre-emulsion and initiator solution (NaPS or AIBN) were fed to the reactor in 90 minutes.

Table 2. 3. Formulation and reaction conditions used in the synthesis of composite polymer latexes

Run	Seed		Second stage				
	Latex	T <sub>g</sub> calculated (°C)	Monomers (wt %): S/BA/AA/AM	T <sub>g</sub> calculated (°C)	Initiator	T <sub>reaction</sub> (°C)	Reaction time (min)
<b>R1</b>	M1	90	67/31/1/1	40	TBHP+ACBS	80	210
<b>R2</b>	M2	60	67/31/1/1	40	TBHP+ACBS	80	210
<b>R3</b>	M3	40	67/31/1/1	40	TBHP+ACBS	80	210
<b>R4</b>	M3	40	93/5/1/1	90	TBHP+ACBS	80	210
<b>R5</b>	M1	90	93/5/1/1	90	TBHP+ACBS	80	210
<b>R6</b>	M2	60	67/31/1/1	40	TBHP+ACBS	65	210
<b>R7</b>	M3	40	93/5/1/1	90	TBHP+ACBS	60	210
<b>R8</b>	M3	40	67/31/1/1	40	TBHP+ACBS	80	480
<b>N1</b>	M3	40	93/5/1/1	90	NaPS	80	210
<b>A1</b>	M1	90	67/31/1/1	40	AIBN	80	210
<b>R9</b>	M4 <sup>a</sup>	40	92/6/1/1	90	TBHP+ACBS	60	210
<b>R10</b>	M5 <sup>a</sup>	40	92/6/1/1	90	TBHP+ACBS	60	210
<b>R11</b>	M6 <sup>a</sup>	40	92/6/1/1	90	TBHP+ACBS	60	210
<b>R12</b>	M7 <sup>a</sup>	40	92/6/1/1	90	TBHP+ACBS	60	210
<b>R13</b>	M8 <sup>a</sup>	40	92/6/1/1	90	TBHP+ACBS	60	210

<sup>a</sup> The seeds containing crosslinker ( See Table 2.1 for details)

Post-polymerization was carried out at the end of feeding to minimize the amount of residual monomers. TBHP was injected as a shot to the reactor and ACBS was fed for two hours at 80 °C. In Run A1, the latex was left to react batchwise at the end of feeding for 2 hours at 80 °C instead of post-polymerization with TBHP/ACBS. The whole process was carried out under atmospheric pressure of nitrogen. The final conversions were higher than 99.9% and coagulum free latexes with 47.4-47.7 wt% solids content were obtained.

Table 2. 4. Procedure used in the synthesis of composite polymer particle latex of Run R1 as representative formulation for cases synthesised with TBHP+ACBS, Run N1 synthesised with NaPS and Run A1 synthesised with AIBN.

Material	Initial load (g)	Pre-emulsion(g)			Initiator solution (g) (Main polymerization)			Initiator solution (g) (Post polymerization)		
		R1	N1	A1	R1	N1	A1	R1	N1	A1
MMA rich seed	232.8									
DI-water		45.75	45.75	53.25						
Emulan OG		0.875	0.875	0.875						
SDS		0.875	0.875	0.875						
Monomers		87.5	87.5	80						
NaPS solution, 7 wt%						6.25				
AIBN solution in styrene, 5.36 wt%							7.95			
TBHP solution, 24 wt%					1.825					
ACBS solution, 13 wt%					6			2.4	2.4	
tBHP solution, 10 wt%								1.75	1.75	

### **2.2.3. Latex characterization**

The global and instantaneous conversion of samples was measured by gravimetry and gas chromatography (GC), respectively. Polymer particle size was measured by dynamic light scattering (DLS) and particle size distribution was characterized by capillary hydrodynamic fractionation (CHDF). Gel fraction and swelling degree of samples was measured by soxhlet extraction in THF. The absolute molar mass distribution of polymers was measured by asymmetric-flow field flow fractionation (AF4) equipped with a multi angle light scattering laser photometer (MALS) and a differential refractometer. The morphology of the latex particles was studied by transmission electron microscopy (TEM) in conventional and cryo, scanning electron microscopy (SEM) and environmental scanning electron microscopy (ESEM). Modulated differential scanning calorimetry (M-DSC) was used to estimate the extent of interpenetration of the two phases of polymers in the particles. Minimum film-forming temperature (MFFT) of the latexes was measured in an MFFT bar. A detailed description of the characterization methods is provided in Appendix I.

### **2.3. Results and discussion**

The study that is going to be presented in this section, would be reliable if the particles maintained their identity during the second stage of polymerization, namely if there were neither much secondary nucleation nor substantial coagulation. Table 2.5

Effect of process variables on particle morphology

---

presents the particle sizes of the seed and final latexes for all cases measured by DLS and as illustrated in Figure 2.1, CHDF measurements showed that weight percent of the small particles in different cases was less than 5 percent; therefore the effect of the secondary nucleation on the morphology was negligible.

Table 2. 5. z-average particle diameter measured by DLS for seed and final latexes of Runs mentioned in Table 2.4

Run		d <sub>particle</sub> (nm)	Run		d <sub>particle</sub> (nm)	Run		d <sub>particle</sub> (nm)
<b>R1</b>	Seed	218	R6	Seed	238	R9	Seed	240
	Final latex	250		Final latex	299		Final latex	280
<b>R2</b>	Seed	222	R7	Seed	230	R10	Seed	218
	Final latex	266		Final latex	271		Final latex	271
<b>R3</b>	Seed	243	R8	Seed	243	R11	Seed	231
	Final latex	288		Final latex	298		Final latex	275
<b>R4</b>	Seed	243	N1	Seed	243	R12	Seed	219
	Final latex	298		Final latex	300		Final latex	282
<b>R5</b>	Seed	218	A1	Seed	218	R13	Seed	212
	Final latex	275		Final latex	255		Final latex	281

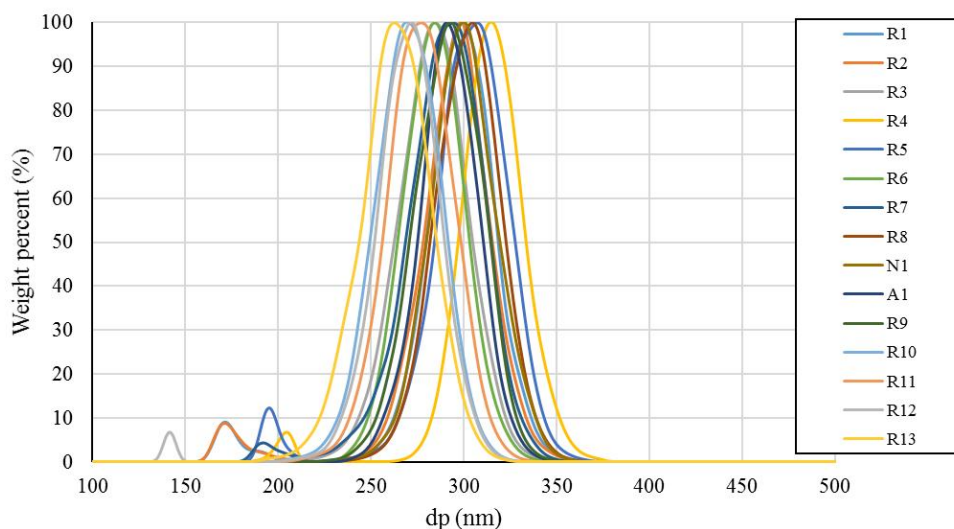


Figure 2. 1. Particle size distribution measured by CHDF for Runs mentioned in Table 2.4.

### 2.3.1. Effect of T<sub>g</sub> of seed on particle morphology

Latexes R1, R2 and R3 (Table 2.3) were synthesized using seeds M1, M2 and M3 with T<sub>g</sub>s of 86 °C, 63 °C and 46 °C, respectively as measured by modulated DSC. The T<sub>g</sub> of the second stage copolymer was measured to be 45-49 °C (Table 2.6). The molar mass distributions (MMD) were measured by (AF4/MALS). The MMD of the seeds and final latexes of Runs R1, R2 and R3 are shown in Figure 2.2 (a) and (b), respectively. The MMDs of the three seeds are bimodal and by increasing the amount of BA in the formulation of the seed (from Run R1 to Run R3), the molar masses shifted to higher value, likely because of the increased probability for intermolecular chain

transfer to polymer.<sup>29–33</sup> The gel measured by soxhlet extraction using THF was almost negligible (less than 5 weight percent, Table 2.7) for all three seeds, which suggests that branched but not cross-linked chains are produced and hence they are soluble in THF.

Table 2. 6. Measured  $T_g$  of Runs R1, R2 and R3 by modulated DSC.

Run		$T_{g, \text{calculated}} (^{\circ}\text{C})$	$T_{g, \text{measured}} (^{\circ}\text{C})$
R1	seed	90	86
	2 <sup>nd</sup> stage	40	49
R2	Seed	60	63
	2 <sup>nd</sup> stage	40	45
R3	Seed	40	46
	2 <sup>nd</sup> stage	40	46

Table 2. 7. Characterization data of Runs R1, R2 and R3.

Run		Gel <sup>a</sup> (w%)	$\overline{M}_w$ <sup>b</sup> (KDa)	$\overline{D}$ <sup>c</sup>	MFFT ( $^{\circ}\text{C}$ )
R1	Seed	0	715.4	3.5	Not available
	Final latex	0	4370.2	29.4	80
R2	Seed	2.0±1.7	11920	10.2	Not available
	Final latex	14.9±0.0	72756.8	107.1	60
R3	Seed	3.9±0.3	50967	12.5	Not available
	Final latex	26.0±0.4	94594	195.1	46

a. Gel measured by soxhlet extraction. b. Weight-average molar mass measured by AF4/MALS. c. Dispersity of molar mass distribution.

The MMDs of final latexes are plotted in Figure 2.2 (b) and the gel content measured for these latexes are presented in Table 2.7. Interestingly, latex R1 did not contain any insoluble polymer. The MMDs are bimodal in all three cases with a peak in the range of  $10^5$ - $10^6$  Da (a bit broader for latex R1) and a broad peak at molar masses higher than  $10^6$  Da. The kinetic length of the second stage polymerization was the same for the three cases. Comparison of the MMDs of seeds R2 and R3 with that of the corresponding final latexes shows that the polymer formed in the second stage of polymerization is the one that formed the peak at around  $2 \times 10^5$  Da . The reason for the relatively low molar mass was the high content of styrene (67 w% in monomer mixture). On the other hand, the fraction of polymer higher than  $10^6$  Da shifted to higher values during the seeded semi-continuous process indicating grafting of the second stage polymer (by intermolecular chain transfer to polymer) onto the MMA/BA polymer chains. The likelihood of this mechanism is expected to increase with the amount of BA in the seed ( $R3 > R2 > R1$ ) and this is seen in the MMDs (Figure 2.2 b). This is also in agreement with the increased amount of gel content for reactions R2 and R3.

Figures 2.3, 2.8 and 2.9 present the evolution of the instantaneous conversions and particle morphology during the seeded emulsion copolymerization of Runs R1, R2 and R3. (Figures with larger images are presented in Appendix II).



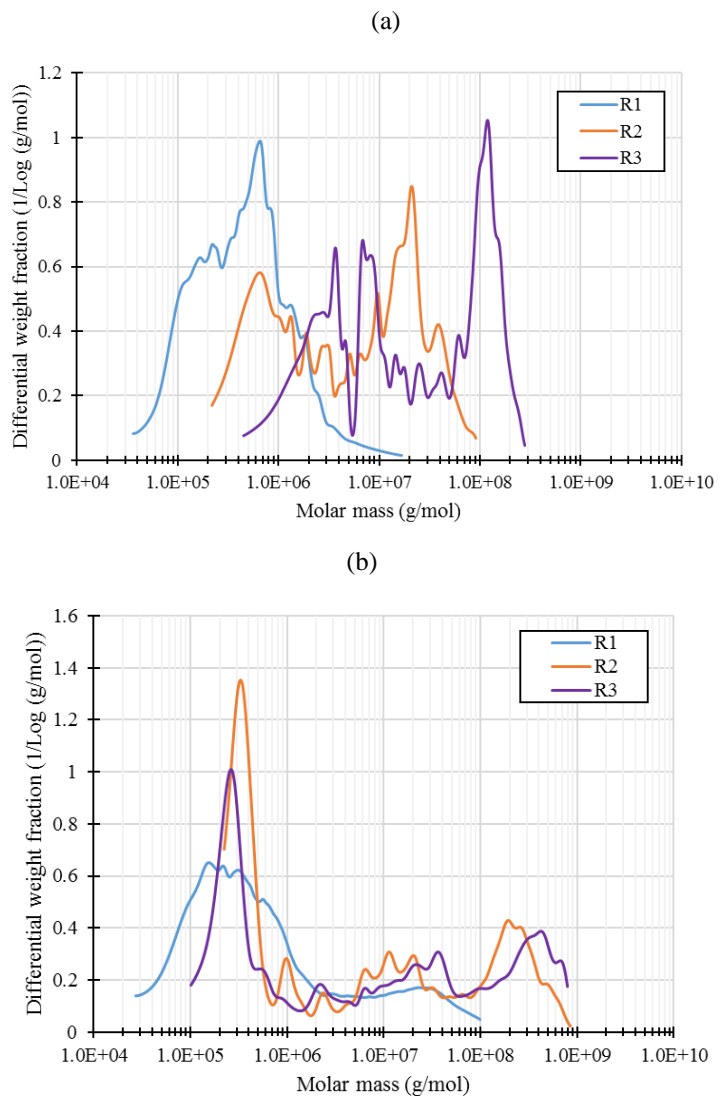


Figure 2. 2. Molar mass distribution of Runs R1, R2 and R3 measured by AF4/MALS; (a) seeds and (b) final latexes. The seeds of Runs R2 and R3 were characterized using a sample concentration of 16 mg/ml in THF. The other samples were analysed at 8 mg/ml.

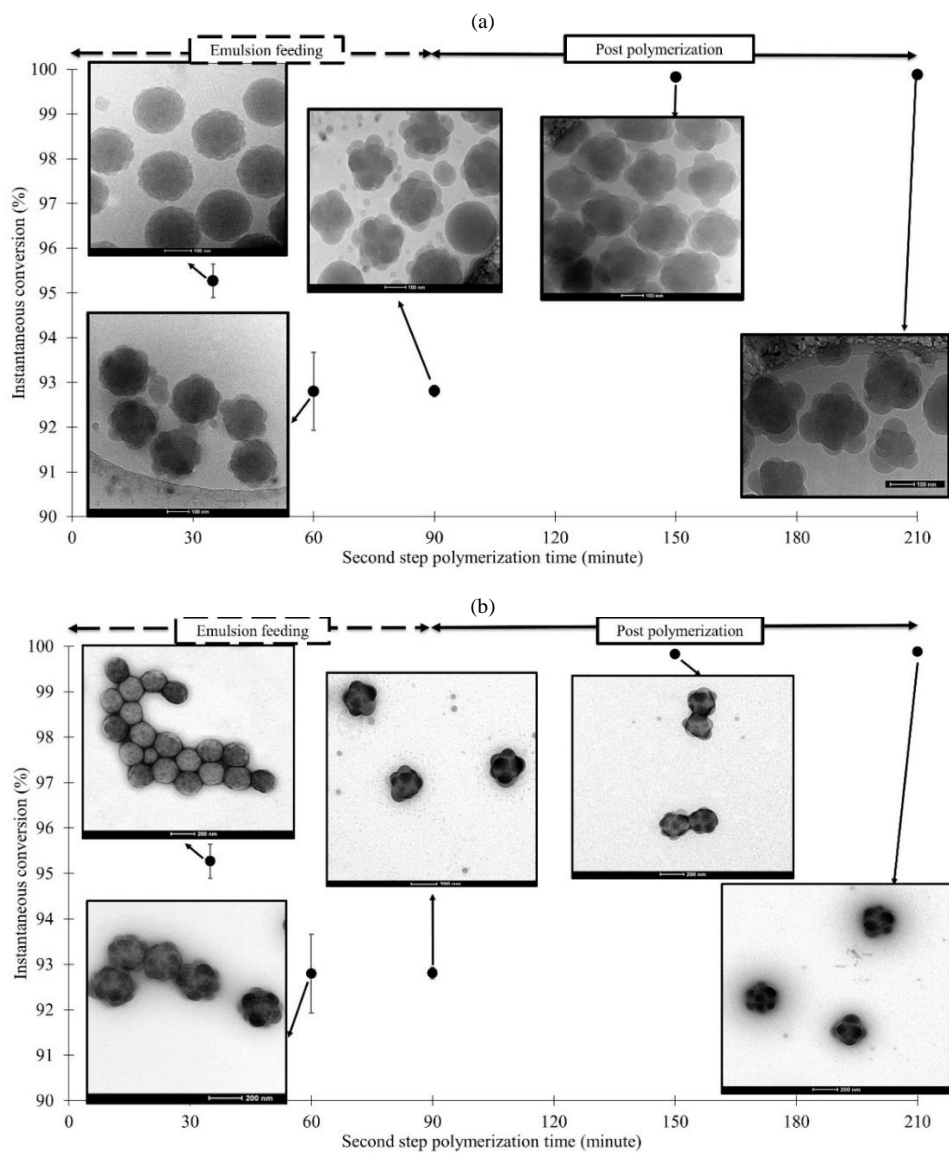


Figure 2. 3. Evolution of the instantaneous conversion and particle morphology during the seeded emulsion polymerization of Run R1 ( $T_{g_{seed}} = 86$  °C): (a) Cryo-TEM images, scale bar: 100 nm (image magnification: 50000); (b) TEM image of RuO<sub>4</sub> stained samples, scale bar: 200 nm (image magnification: 25000).

Comparison of the conversions achieved in these polymerizations shows that the three reactions were carried out under starved conditions (instantaneous conversions greater than 90%) and that within this range, different average conversions were obtained in the three cases, even though the same formulation was used during the semi-continuous operation. The differences were attributed to variations in the residual initiator in the seeds and to small differences in the efficiency of the oxygen removal.

The small amount of monomer present in the system strongly affected the effective glass transition temperature ( $T_{g_{effective}}$ ) of the polymer. For example, it can be seen in Figure 2.3 that the average instantaneous conversion during the pre-emulsion feeding was about 94 % for Run R1, namely that the polymer particles contained about 6% of monomer. The amount of monomer in the polymer particles determined  $T_{g_{effective}}$  as the monomer plasticized the polymers.  $T_{g_{effective}}$  can be estimated as follows:<sup>34</sup>

$$T_{g_{effective}} = \frac{T_{g_p} + (\kappa T_{g_M} - T_{g_p})\phi_M}{1 + (\kappa - 1)\phi_M} \quad (2.1)$$

where  $T_{g_p}$  and  $T_{g_M}$  are glass transition temperatures of polymer and monomer 2,  $\phi_M$  is the monomer volume fraction in the polymer and  $\kappa$  is a constant varying from 1 to 3<sup>34</sup> that was taken to be 2.  $T_{g_M}$  can be estimated as  $\frac{2}{3}T_{meltM}$ , where  $T_{meltM}$  is the melting point of the monomer<sup>35</sup>. The  $T_{g_M}$  of the S/BA monomer mixture was calculated using

the  $T_{\text{melt}}$  of monomers<sup>36</sup> and the Flory-Fox equation.<sup>28</sup> Considering that,  $\phi_M = 0.06$ ,  $T_{g_p} = 359$  K and  $T_{g_M} = 154$  K, the estimated  $T_{g_{\text{effective}}}$  of the seed for Run R1 was 62.8 °C, namely below the reaction temperature. Figure 2.3 presents the evolution of the particle morphology as measured by cryo-TEM (Figure 2.3 a) and by TEM of samples stained with  $\text{RuO}_4$  (Figure 2.3 b). Figure 2.3 (a) gives a good image of the surface topography mainly at the beginning of the process and particle morphology is better seen in Figure 2.3 (b) (the dark areas in the images correspond to the styrene rich second stage polymer). Figure 2.3 shows that at the early stages of the reaction (30 min sample), many small lobes were formed on the surface of the particles (this is more clearly seen in Figure 2.3 a). The size of the lobes increased and their number decreased with time during the semi-continuous operation. The lobes grew by the combined effect of polymerization and coagulation. No significant changes of the particle morphologies were observed during post-polymerization. It is worth mentioning that the post-polymerization process was performed at a temperature lower than the  $T_g$  of the hardest phase in the composite latex particles. The images in Figure 2.3 suggest that the lobes accounted for most of the second stage polymer, namely, that even though the inverted core-shell (i.e. with the PS rich polymer in the core) was the equilibrium morphology, there was only a modest penetration of the second stage polymer in the seed. This can be due to strong concentration profiles of radicals and/or monomer.

The monomer concentration profile in the polymer particle was calculated via solving the following partial differential equations by orthogonal collocation<sup>37</sup>:

$$\frac{\partial[M](t,r)}{\partial t} = \nabla^2 D_M [M](t,r) - k_p [R](t,r)[M](t,r) \quad (2.2)$$

$$\frac{\partial[M](t,0)}{\partial t} = 0; [M](0,0) = 0; [M](t,rp) = [M]_s \quad (2.3)$$

where  $[M](t,r)$  and  $[R](t,r)$  are the monomer and radical concentrations at time  $t$  and radius of  $r$ , respectively.  $D_M$  is the monomer diffusion coefficient and  $k_p$  is the propagation rate coefficient.  $[M]_s$  is the monomer concentration at the surface of the particle. The diffusion constant of the monomer  $D_M$  was calculated using a modified Vrentas-Duda free-volume model of small molecule diffusion in binary polymer solutions<sup>38</sup>:

$$\log D_M = \log D^\circ - \frac{E}{2.303RT} - \frac{1}{2.303} \left[ \frac{(1-w_2)\hat{V}_1^* + \epsilon w_2 \hat{V}_2^*}{\frac{\hat{V}_f}{\gamma}} \right] \quad (2.4)$$

$$\frac{\hat{V}_f}{\gamma} = (1-w_2) \left( \frac{K_{11}}{\gamma} \right) (K_{21} + T - Tg_1) + w_2 \left( \frac{K_{12}}{\gamma} \right) [K_{22} + a(T - Tg_p)] \quad (2.5)$$

where  $D^\circ$  and  $E$  are the pre-exponential factor and activation energy of the monomer diffusion coefficient, respectively.  $a$  is the ratio between the coefficients of thermal expansion of the polymer below and above Tg of polymer.  $\frac{K_{11}}{\gamma}$ ,  $\frac{K_{12}}{\gamma}$ ,  $K_{21}$ ,  $K_{22}$  are free

---

volume parameters.  $Tg_1$  and  $Tg_p$  are monomer and polymer glass transition temperatures, respectively.  $T$  is the reaction temperature.  $\hat{V}_1^*$  and  $\hat{V}_2^*$  are specific volumes of monomer and polymer, respectively.  $w_2$  is the weight fraction of polymer.  $\mathcal{E}$  is the size parameter<sup>38</sup> and  $\frac{\hat{V}_f}{\gamma}$  is the solution free volume. The values of the parameters used are given in Table 2.8. Figure 2.4 shows a representative monomer concentration profile in the particle with a  $[M](t, r_p) = 0.377$  mol/L (which corresponds to  $\phi_{pol} = 0.96$ ) and  $Tg_{seed} = 90$  °C at  $T_{reaction} = 80$  °C. It can be seen that the monomer was homogeneously distributed in the particle.

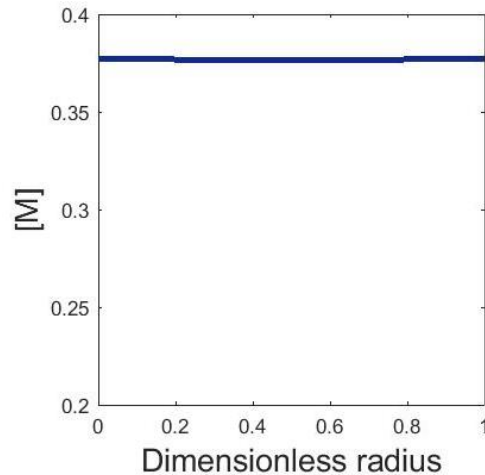


Figure 2. 4. Monomer concentration profile snapshot at  $t=8$ s in the particle (mol/L) with  $D_M = 3.17 \times 10^{-14}$  m<sup>2</sup>/s. ( $[M](t, r_p) = 0.377$  mol/L (which corresponds to  $\phi_{pol} = 0.96$ ) and  $Tg_{seed} = 90$  °C at  $T_{reaction} = 80$  °C).

The radical concentration profile in the polymer particle was calculated via solving the following partial differential equation by orthogonal collocation on finite elements.<sup>37</sup>

$$\frac{\partial[R](t, r)}{\partial t} = \nabla^2 D_R [R](t, r) - k_t [R]^2(t, r) \quad (2.6)$$

$$\frac{\partial[R](t, 0)}{\partial t} = 0; [R](t, r_p) = [R]_s \quad (2.7)$$

$$\int_0^{r_p} [R] 4\pi r^2 dr_p = \bar{n} / N_A \quad (2.8)$$

where  $D_R$  is the radical diffusion coefficient and  $k_t$  is the termination rate coefficient.  $[R]_s$  is the radical concentration at the surface of the particle. It is worth mentioning that the redox initiator used in the semibatch process produced non-charged hydrophobic radicals in the aqueous phase. Therefore, anchoring of the entering radical to the surface of the particle was not considered. The diffusion coefficient for radicals was reported to show a power-law variation with chain length<sup>39</sup>. In this work a constant kinetic chain length for the growing radical was assumed in the simulations (half of the degree of the polymerization of polymer 2,  $(\bar{x}_m)$  considering that termination reaction occurs by combination) and dependency parameter ( $\beta$ ) was considered as adjustable:

$$D_R = \frac{D_M}{(\bar{x}_m/2)^\beta} \quad (2.9)$$

The value of the parameters are presented in Table 2.8. Figure 2.5 shows a representative radical concentration profile in the particle with  $[M](t, r) = 0.377$  mol/L (corresponds to the  $\phi_{Pol} = 0.96$ ) and  $T_{g_{seed}} = 90$  °C at  $T_{reaction} = 80$  °C. It can be shown that a sharp radical profile was generated, with the radical concentration decreasing rapidly towards the interior of the particle.

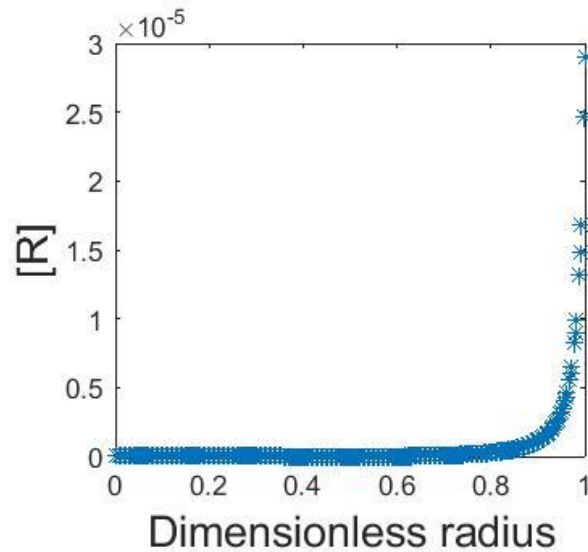


Figure 2. 5. Radical concentration profile snapshot at  $t=5400$ s in the particle (mol/L) with  $D_R = 2.04 \times 10^{-16}$  m<sup>2</sup>/s. ( $[M](t, r) = 0.377$  mol/L (corresponds to the  $\phi_{Pol} = 0.96$ ) and  $T_{g_{seed}} = 90$  °C at  $T_{reaction} = 80$  °C) PDE was solved using 100 elements and 4 collocation points at each element.



The simulations presented show that the monomer was homogeneously distributed within the polymer particles. Therefore, the observed effect should be due to a rapidly decreasing radical concentration profile. It is worth mentioning that the redox initiator used in the semibatch process produced non-charged hydrophobic radicals in the aqueous phase. Therefore, the radical concentration profile was not due to anchoring of the entering radical to the surface of the particle, but to the slow diffusion of the growing polymer chain through the particles.

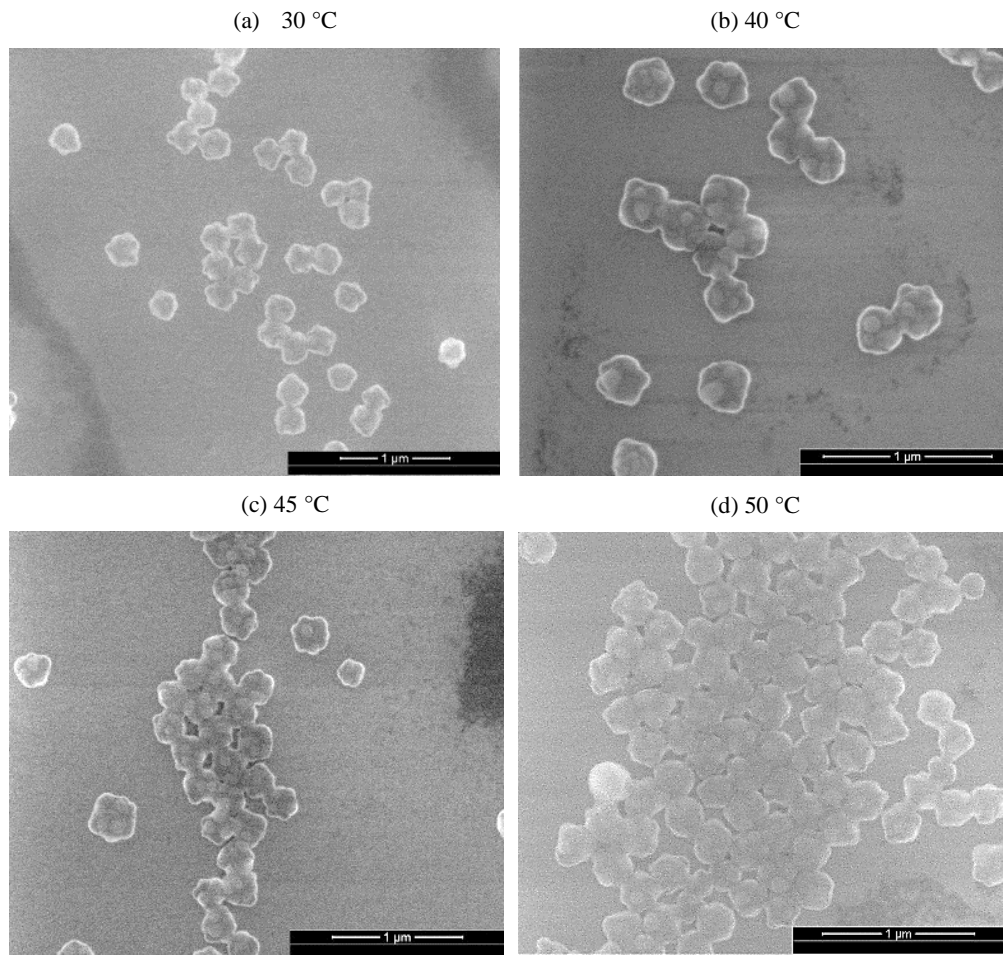
Table 2. 8. Parameters for monomer and radical diffusion coefficient calculations (The parameters are for diffusion of MMA monomer in PMMA)

Parameter	value	Reference
$D^\circ$ (cm <sup>2</sup> /s)	$1.61 \times 10^{-3}$	38
$E$ (cal/mol)	778	38
$\epsilon$	0.6	38
$\hat{V}_1^*$ (cm <sup>3</sup> /g)	0.87	38
$\hat{V}_2^*$ (cm <sup>3</sup> /g)	0.757	38
$\frac{K_{11}}{\gamma}$ (cm <sup>3</sup> /g.K)	$0.815 \times 10^{-3}$	38
$K_{21}$ (K)	143	38
$\frac{K_{12}}{\gamma}$ (cm <sup>3</sup> /g.K)	$0.477 \times 10^{-3}$	38
$K_{22}$ (K)	52.38	38
$\alpha$	0.44	38
$\beta$	0.645	This work

The results presented in Figure 2.3 suggest that the surface of the particles was covered by lobes of the PS rich polymer. However, the MFFT of this latex was 80 °C, which is much higher than the T<sub>g</sub> of the lobes (49 °C) and closer to the T<sub>g</sub> of the polymer forming the seed. This seems inconsistent with a particle morphology with 50% of the polymer forming soft lobes on the particle surface. Particle coalescence was further checked by ESEM measurements at different temperatures. Figure 2.6 shows that the multi-lobed composite particles started to coalesce after 10 minutes at a temperature between 60 °C and 70 °C.

The high temperature needed to form a film could be due to lower effective fraction of the soft polymer on the surface due to a high level of interpenetration between two polymers. However, no proof for this interpenetration was found in the modulated DSC experiments for Case R1. Figure 2.7 shows two clear peaks and that the value of  $dC_p/dT$  in the region between peaks was close to the baseline, which indicates that there was not intermixing between the polymers. This is further supported by the fact that there was no difference between the first and second cycles. It is worth pointing out that the differences in the baseline in the glassy and the rubbery regions are due to the difference in temperature sensitivity of the  $C_p$  of the polymer in glass and melt states<sup>40</sup>. A possible reason for the high MFFT is that as the PS-rich clusters were partially embedded in the hard polymer forming the seed, the effective volume fraction

of the hard phase was higher than 50% and therefore the hard phase controlled film formation.



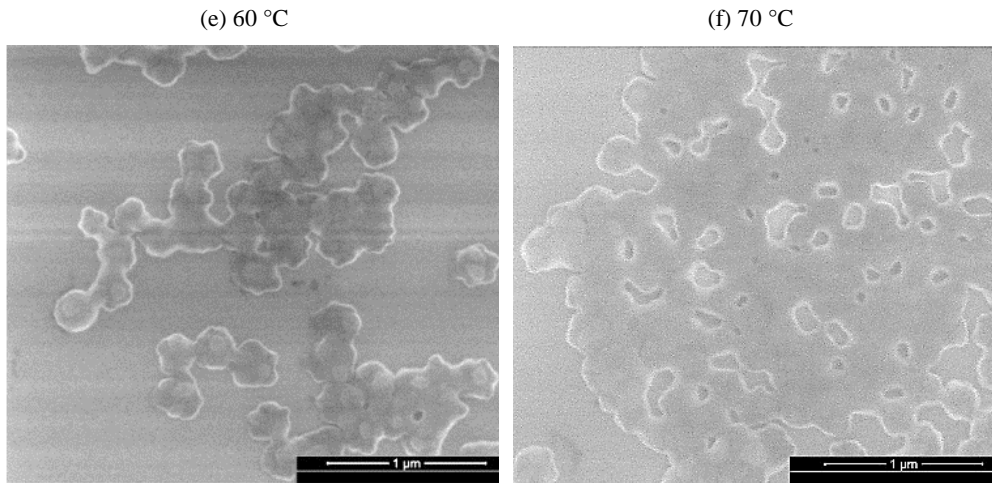


Figure 2. 3. Coalescence of polymer particles of Run R1 in the ESEM at different temperatures: (a) 30 °C; (b) 40 °C; (c) 45 °C; (d) 50 °C; (e) 60 °C; (f)70 °C. Heating ramp between temperatures: 10 °C/min. Time at each constant temperature: 10 min.

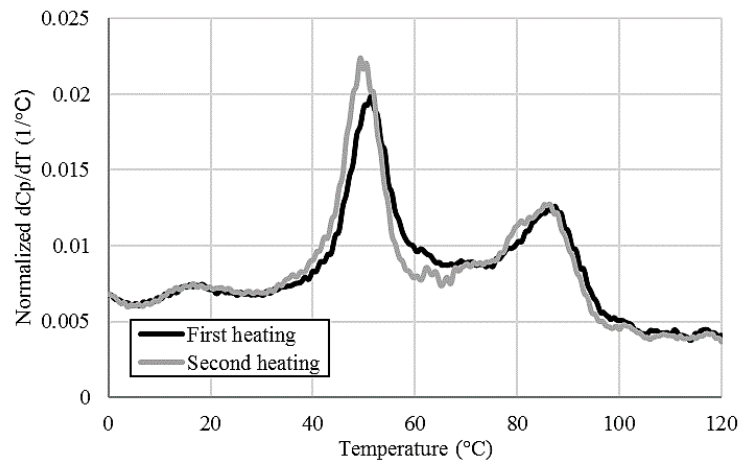


Figure 2. 4.  $dC_p/dT$  from M-DSC for Run R1.

Figure 2.8. presents the evolution of the instantaneous conversion and the particle morphology for Run R2 that used a seed with a  $T_g = 63\text{ }^\circ\text{C}$ . The process was carried out under very starved conditions (the average instantaneous conversion was 98.5%). Taking into account the free monomer in the system,  $T_{g\text{effective}}$  of the seed calculated with equation 2.1 was  $57.6\text{ }^\circ\text{C}$ , namely below the reaction temperature.

Figure 2.8 shows that at the beginning of the process, clusters of the second stage polymer were formed near the surface of the particles, but they were more embedded than in Run R1 (Figure 2.5). During the reaction, the size of clusters increased and their number decreased, likely due to the combined effect of polymerization within the clusters and coagulation between them. At the end of the process, multi-lobed polymer particles were obtained although the clusters forming the lobes were better embedded in the particle than for Run R1. The difference was attributed to the lower  $T_g$  of the seed that allowed more migration of the clusters toward the inverted core-shell equilibrium morphology. Meanwhile, the higher molar mass of the seed in Run R2 compared to Run R1 (Figure 2.2 a) led to higher viscosity of the polymerization matrix in the second stage of polymerization and resulted in the lowering of the cluster movement. Considering the effect of lower  $T_g$  and higher molar mass of the seed which act contrary to each other on changing the viscosity, it seems that lowering the glassy effect of the polymerization matrix by altering the  $T_g$  of seed, overcame the slower

---

movement of the clusters due to the higher viscosity induced by the higher molar mass. The minimum film forming temperature for this latex was 60 °C, which was very close to  $T_g$  of the seed (63 °C). As in Run R1, here also the penetration of the soft clusters in the harder seed increased the effective volume fraction of the hard phase and the MFFT was close to the  $T_g$  of the seed.

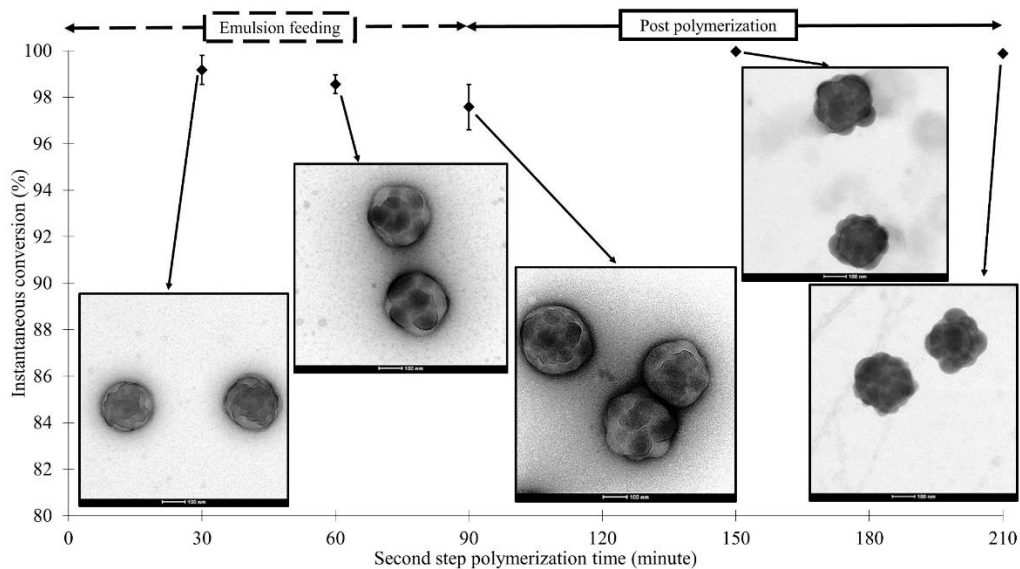


Figure 2. 5. Evolution of instantaneous conversion and particle morphology (TEM images of stained sample with vapor of  $\text{RuO}_4$ ) during the second stage of polymerization of Run R2 ( $T_{g\text{seed}} = 63 \text{ }^\circ\text{C}$ ). Images magnification: 50000.

Figure 2.9 presents the evolution of the instantaneous conversion and particle morphology of Run R3 where a seed with a  $T_g = 46 \text{ }^\circ\text{C}$  was used. Taking into account

the free monomer,  $T_{g\text{effective}}$  of the seed was estimated to be 26.5 °C. As in Run R1 and R2, initially many small clusters were formed that later evolved to larger and fewer ones. The main difference with respect to the previous cases is that the clusters penetrated more within the particle and relatively spherical particles were obtained at the end of the process. The reason was the low  $T_{g\text{effective}}$  of the seed that allowed migration of the clusters and perhaps a faster diffusion of the radicals that might result in a flatter radical concentration in the particles.

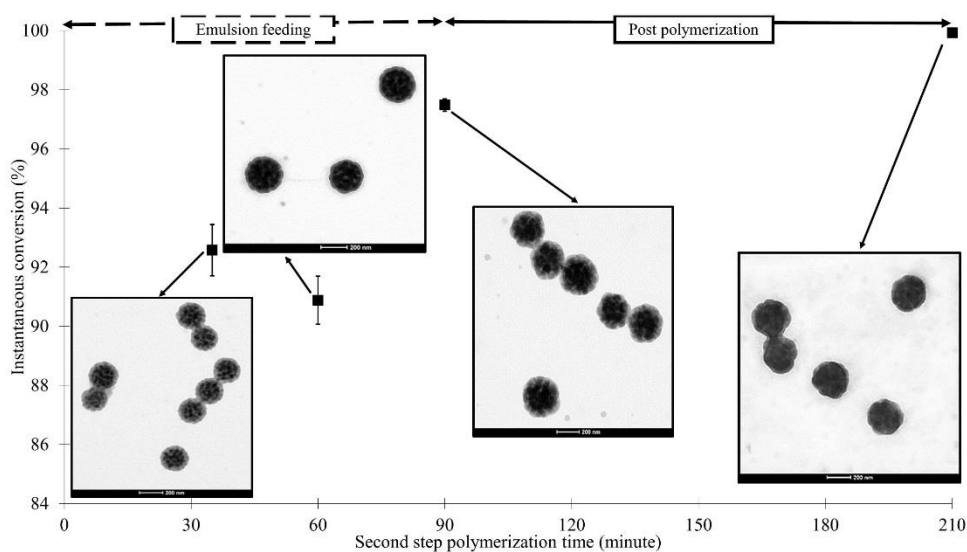


Figure 2. 6. Evolution of (a) instantaneous conversion and (b) particle morphology (TEM images of stained sample with vapor of  $\text{RuO}_4$ ) during the second stage of polymerization of Run R3 ( $T_{g\text{seed}} = 46$  °C). Images magnification: 50000.

In this case, the MMFT does not provide any information about the morphology because both polymers have the same Tg. The higher molar mass of the seed in Run R3 compared to Run R2 and Run R1 (Figure 2.2 a) which imply a higher viscosity of the polymerization matrix in the second stage of polymerization did not overcome the softening of the matrix and hence the clusters penetrated even more in Run R3.

### 2.3.1.1. Analysis of evolution of particle morphology by mathematical model

The evolutions of the particle morphology presented above were analyzed using a mathematical model developed by Hamzehlou *et al.*<sup>27</sup> The model includes the material balances for the monomers and polymer formed during the second stage of polymerization (*pol2*) and the population balance for the clusters.

$$\frac{dM_i}{dt} = -\bar{k}_{pi} \frac{\bar{n}N_p}{N_A} \frac{M_i}{V_p} + F_{mi} \quad \left(\frac{mol}{s}\right) ; M_i(t=0) = M_{i0} \quad (2.10)$$

$$\frac{dpol2}{dt} = \sum -\frac{dM_i}{dt} \quad \left(\frac{mol}{s}\right) ; pol2(t=0) = 0 \quad (2.11)$$

where  $\bar{k}_{pi}$  is the average propagation rate coefficient which is calculated using the reactivity ratios of monomers,  $\bar{n}$  the average number of radicals per particle,  $N_p$  number



of particles,  $N_A$  is the Avogadro's number and  $V_p$  the total volume of polymer particles given by:

$$V_p = pol2 \bar{V}_{pol2} + \sum_i M_i \bar{V}_{m_i} + V_{pol1} \quad (2.12)$$

where  $\bar{V}_{pol2}$  and  $\bar{V}_{m_i}$  are the molar volumes of the Polymer 2 and Monomers, respectively, and  $V_{pol1}$  is the volume of Polymer 1. The volume of one particle is  $V_p/N_p$ .

The material balances for the monomers require the calculation of the number of radicals per particle which was calculated by using the following equations<sup>41</sup>:

$$\bar{n} = \frac{2k_{abs}[R]_w}{k_{des} + (k_{des}^2 + 4k_{abs}[R]_w c f)^{0.5}} \quad (2.13)$$

$$f = \frac{2 * (2k_{ads}[R]_w + k_{des})}{2k_{abs}[R]_w + k_{des} + c} \quad (2.14)$$

$$c = \frac{k_t}{2v_p N_A} \quad (2.15)$$

where  $k_{abs}$  is the radical entry rate coefficient (L/mol.s),  $k_{des}$  is the radical exit rate coefficient (1/s),  $k_t$  is the termination rate coefficient (L/mol.s),  $N_A$  is Avogadro number,  $v_p$  is the volume of particle (L) and  $[R]_w$  is the radical concentration in water

---

phase (mol/L). Equation 2.13 shows that to calculate  $\bar{n}$  the concentration of radicals in the aqueous phase ( $[R]_w$ ) is needed. The latter can be calculated assuming pseudo-steady state conditions as follow:

$$\frac{[R]_w}{dt} = 0 = 2k_i[Red][Ox] + k_{des}\bar{n} \frac{N_p}{N_A V_w} - k_{tw}[R]_w^2 - k_{abs}[R]_w \frac{N_p}{N_A V_w} \quad (2.16)$$

where  $k_i$  is rate coefficient for the redox reaction rate (L/mol.s),  $N_p$  is the number of polymer particles,  $V_w$  is the volume of water phase (L),  $[Red]$  and  $[Ox]$  are the reductant and oxidant concentrations in the aqueous phase (mol/L), respectively and  $k_{tw}$  is the termination rate coefficient in water phase (L/mol.s). Equation 2.16 is also dependent to the value of  $\bar{n}$ . Equations 2.13 and 2.16 are solved iteratively. Note that one effective rate coefficient of termination ( $\bar{k}_t$ ) was used in the simulation to reduce the number of the parameters. Equations 2.13 to 2.16 show that calculation of the number of radicals per particle depends on the rate coefficients for radical entry, exit and termination. Working values of these coefficients were estimated by fitting the evolution of the experimental conversion for Run R1-R3. The estimated values are given in Table 2.9. In this model, the particle morphology is characterized by means of cluster size distributions (in a similar way as a polymer is characterized by the molar mass distribution). The experimental data discussed in Section 2.3.1 clearly indicate that there is a radical concentration profile in the polymer particles. The radical

---

concentration profiles were calculated at early stage in the polymerization using equations 2.6 - 2.8. The profiles were arbitrarily reduced to two regions, one close to the surface and the other representing the rest of the particle as illustrated in Figure 2.10. The volume ratio of the regions was considered constant during the process. The model distinguishes between clusters at equilibrium positions (for the cases studied in this thesis, the equilibrium position was the center of the particle) and non-equilibrium positions (see Figure 2.10). In addition, the discretization of the radical concentration profile divides the clusters at non-equilibrium into two distributions. Therefore, the particle morphology is characterized by three distributions as illustrated in Figure 2.10. The population balances of the non-equilibrium clusters in the exterior region ( $m_1$ ), non-equilibrium clusters in the interior region ( $m_2$ ) and equilibrium clusters at the core of the particles ( $n$ ) are presented in equations 2.17, 2.27 and 2.28, respectively. It is worth mentioning that the penetration of the external clusters is not included in the model and all the clusters within the external non-equilibrium zone are counted in one distribution ( $m_1(x)$ ).

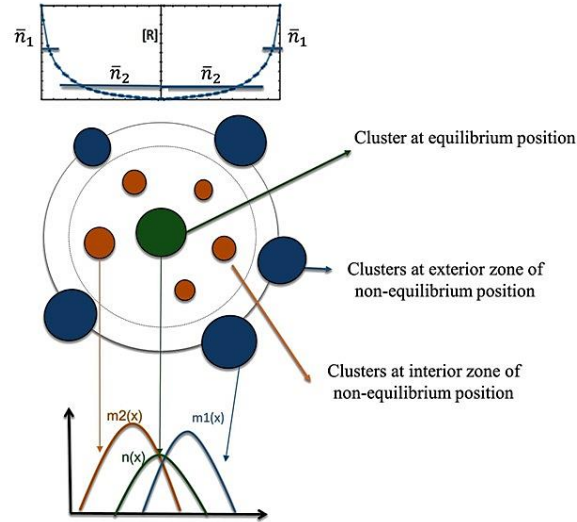


Figure 2. 7. Illustration of the equilibrium and non-equilibrium positions considered in the mathematical model.

The first line in the right hand side of equation 2.17 refers to cluster growth by polymerization with a rate of  $r_p^{m1}$  (rate coefficient of  $\bar{k}_p$ ) and the second line corresponds to the growth of the clusters by diffusion of Polymer 2 from the polymer matrix which occurs at the rate of  $r_d^{m1}$  (mass transfer rate coefficient of  $k_d^{pol2}$ ). The next two integral terms accounts for cluster coagulation with rate coefficient of  $k_a$ . Clusters movement to interior non-equilibrium region due to cluster-water van der Waals forces with rate coefficients of  $k_{mov1}$  is accounted in the model. The last term

in equation 2.17 refers to cluster nucleation at the rate of  $r_{nuc}$  (with rate coefficient of  $k_n$ ). Note that  $\delta$  is equal to one if the condition in its subscript is fulfilled.

**Population balance of clusters at exterior non-equilibrium positions:**

$$\begin{aligned}
 \frac{dm_1(x)}{dt} = & (1 - \delta_{x_c})r_p^{m_1}(x-1)m_1(x-1) - r_p^{m_1}(x)m_1(x) \\
 & + (1 - \delta_{x_c})r_d^{m_1}(x - \bar{x}_m) m_1(x - \bar{x}_m) - r_d^{m_1}(x)m_1(x) \\
 & + (1 - \delta_{x \leq 2x_c})\alpha_m(x) \frac{k_a}{V_p} \left(1 - \frac{1}{m_1^{av}}\right) \int_{x_c}^{x-x_c} m_1(z)m_1(x-z) dz \\
 & - 2m_1(x) \frac{k_a}{V_p} \left(1 - \frac{1}{m_1^{av}}\right) \int_{x_c}^{x_{max}-x} \alpha_m(x+z)m_1(z) dz \\
 & - k_{mov1}m_1(x) + \delta_{x_c}r_{nuc}
 \end{aligned} \tag{2.17}$$

Rates of  $r_p^{m_1}(x)$ ,  $r_d^{m_1}(x)$  and  $r_{nuc}$  are given by:

$$r_p^{m_1}(x) = \bar{k}_p \frac{\bar{n}_1 N_p M}{N_a V_1} \phi_x \tag{2.18}$$

$$\phi_x = \frac{x}{(pol1 + pol2)N_A} \tag{2.19}$$

$$r_d^{m1}(x) = \frac{k_d^{pol2} \phi a_{m1}(x) N_A}{\bar{x}_m} \quad (2.20)$$

$$r_{nuc} = \frac{k_n \phi N_A}{x_c} \quad (2.21)$$

where  $\bar{x}_m$  being the kinetic chain length of Polymer 2,  $V_1$  is the volume of region 1,  $a_{m1}$  is the surface area of the clusters in region 1,  $x_c$  is the size of the newly nucleated cluster that within a certain range, this size does not affect the particle morphology.<sup>27</sup>  $\phi$  is excess of Polymer 2 in the polymer matrix with respect to the equilibrium condition given by:

$$\phi = \phi_2^H - \phi_2^c = \begin{cases} \phi_2^H - \phi_2^c & \text{if } \phi_2^H > \phi_2^c \\ 0 & \text{otherwise} \end{cases} \quad (2.22)$$

where  $\phi_2^H$  is the actual volume fraction of Polymer 2 in the matrix and  $\phi_2^c$  is the volume fraction of the Polymer 2 in the matrix under equilibrium conditions.

$k_d^{pol2}$ ,  $k_{mov1}$ ,  $k_{mov2}$  and  $k_a$  are considered inversely proportional to the viscosity of the medium of polymerization that according to the van-Krevelen-Hoftyzen model, depends on the fraction of the polymer and the ratio of reaction temperature to the Tg of the medium of polymerization.<sup>42</sup> Therefore the coefficients were defined in the model with following expressions:

$$k_a = \frac{k_{a0}}{\phi_P^5 * A * \exp\left(\frac{B}{\left(\frac{T}{T_{g\text{effective}}} - 0.866\right)}\right)} \quad (2.23)$$

$$k_{mov1} = \frac{k_{mov1_0}}{\phi_P^5 * A * \exp\left(\frac{B}{\left(\frac{T}{T_{g\text{effective}}} - 0.866\right)}\right)} \quad (2.24)$$

$$k_{mov2} = \frac{k_{mov2_0}}{\phi_P^5 * A * \exp\left(\frac{B}{\left(\frac{T}{T_{g\text{effective}}} - 0.866\right)}\right)} \quad (2.25)$$

$$k_d^{pol2} = \frac{k_{d0}^{pol2}}{\phi_P^5 * A * \exp\left(\frac{B}{\left(\frac{T}{T_{g\text{effective}}} - 0.866\right)}\right)} \quad (2.26)$$

where A, B,  $k_{a0}$ ,  $k_{mov1_0}$ ,  $k_{mov2_0}$ ,  $k_{d0}^{pol2}$  are adjustable parameters of the model and  $T_{g\text{effective}}$  of the polymerization medium is calculated using equation 2.1. In the model

---

calculation,  $Tg_p$  in equation 2.1 is considered as the volume average of  $Tg$  of polymers from seed and second stage.

The population balances for clusters at interior non-equilibrium position (equation 2.27) and for clusters at equilibrium position (2.28) are similar to equation 2.17 and the explanation for the terms are given above. Noteworthy, in these equations the term of cluster movement to equilibrium position is also considered with  $k_{mov2}$  that is a second order rate coefficient of the movement whereas  $k_{mov1}$  is the first order one. It is worth mentioning that only one equilibrium cluster can be presented in each particle at the core of the particle. Therefore, the movement of the clusters from exterior regions toward the core of the particle leads to the aggregation of these clusters with the equilibrium cluster. The model was implemented in MATLAB and the discrete cluster distributions were calculated using 100 pivots.

As explained above, the model accounts for the effect of the operation variables (such as effective glass transition of the medium, instantaneous conversion, temperature, etc.) on the adjustable parameters of the model and hence on the particle morphology.



**Population balance of clusters at interior non-equilibrium positions:**

$$\begin{aligned}
 \frac{dm_2(x)}{dt} = & (1 - \delta_{x_c})r_p^{m_2}(x-1)m_2(x-1) - r_p^{m_2}(x)m_2(x) \\
 & + (1 - \delta_{x_c})r_d^{m_2}(x - \bar{x}_m) m_2(x - \bar{x}_m) - r_d^{m_2}(x)m_2(x) \\
 & + (1 - \delta_{x \leq 2x_c})\alpha_m(x) \frac{k_a}{V_p} \left(1 - \frac{1}{m_2^{av}}\right) \int_{x_c}^{x-x_c} m_2(z)m_2(x-z) dz \\
 & - 2m_2(x) \frac{k_a}{V_p} \left(1 - \frac{1}{m_2^{av}}\right) \int_{x_c}^{x_{max}-x} \alpha_m(x+z)m_2(z) dz \\
 & + k_{mov1}m_1(x) - m_2(x) \frac{k_{mov2}}{V_p} \int_{x_c}^{x_{max}-x} \alpha_m(x+z)n(z) dz + \delta_{x_c}r_{nuc} \quad (2.27)
 \end{aligned}$$

**Population balance of clusters at equilibrium position:**

$$\begin{aligned}
 \frac{dn(x)}{dt} = & (1 - \delta_{x_c})r_p^n(x-1)n(x-1) - r_p^n(x)n(x) \\
 & + (1 - \delta_{x_c})r_d^n(x - \bar{x}_m) n(x - \bar{x}_m) - r_d^n(x)n(x) \\
 & + (1 - \delta_{x \leq 2x_c})\alpha_n(x) \frac{k_{mov2}}{V_p} \int_{x_c}^{x-x_c} m_2(z)n(x-z) dz \\
 & - n(x) \frac{k_{mov2}}{V_p} \int_{x_c}^{x_{max}-x} \alpha_n(x+z)m_2(z) dz \quad (2.28)
 \end{aligned}$$

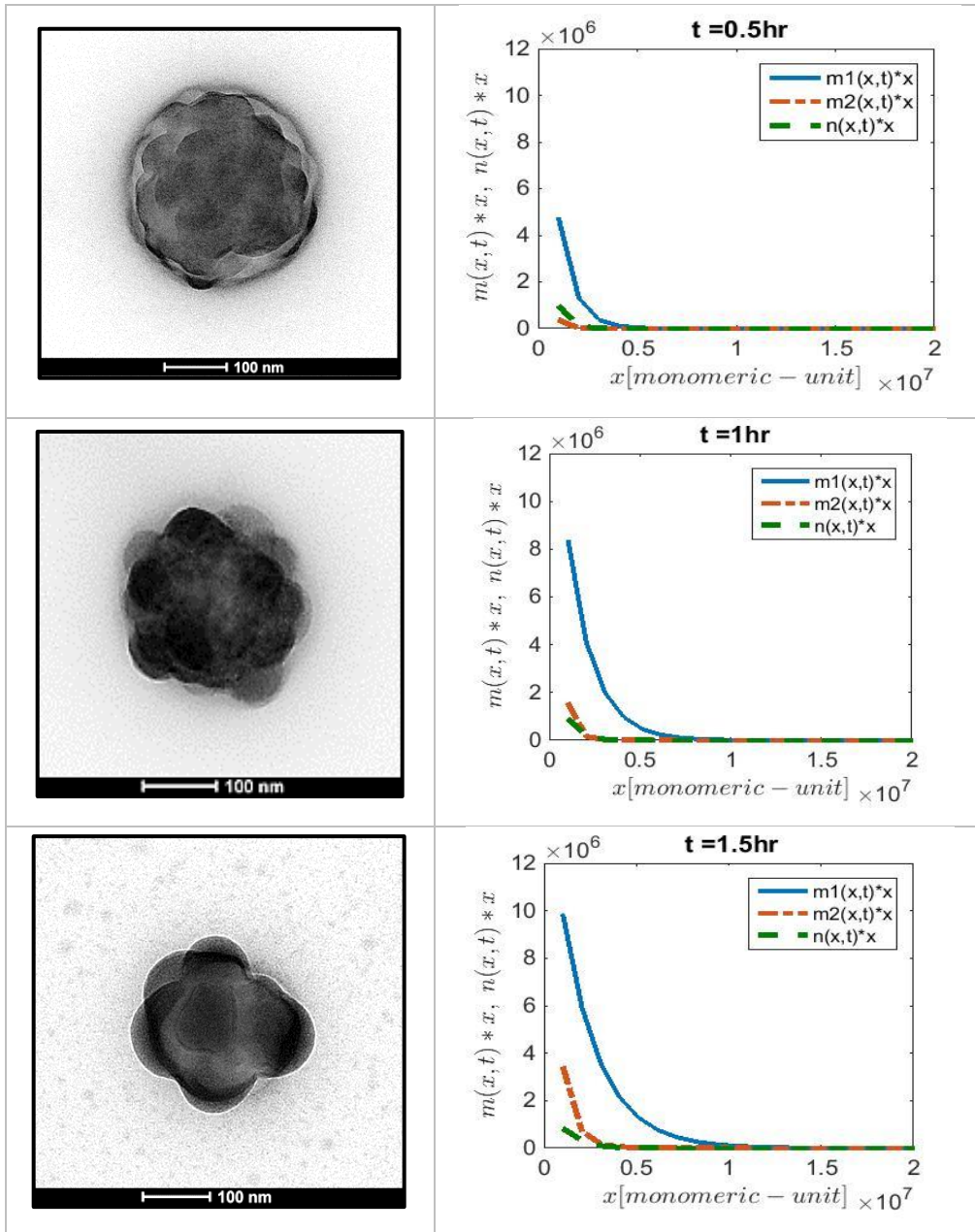
Table 2. 9. Values of the parameters used in the model

Parameter	value	Reference
$k_{p,BA}$ (L/mol.s)	$2.21 \times 10^7 \exp(-17.9/RT)$	43
$k_{p,St}$ (L/mol.s)	$4.27 \times 10^7 \exp(-32.5/RT)$	44
$r_{St}$	0.95	45
$r_{BA}$	0.18	45
$\kappa$	1	34
$k_{a0}$ (L/s)	$1 \times 10^{-22}$	This work
$k_{mov1,0}$ (1/s)	$1 \times 10^{-3}$	This work
$k_{mov2,0}$ (L/s)	$8 \times 10^{-5}$	This work
$k_{d0}^{pol2}$ (mol/dm <sup>2</sup> .s)	$5 \times 10^{-10}$	This work
$k_n$ (mol/s)	$5 \times 10^{-2}$	This work
$\Phi_2^c$	$5 \times 10^{-4}$	27
$x_c$ (monomeric units)	$4 \times 10^4$	27
$\bar{x}_m$ (monomeric units)	$5 \times 10^3$	27
$k_i$ (L/mol.s)	0.076	46
$k_{ads}$ (L/mol.s)	$3 \times 10^6$	This work
$k_{des}$ (1/s)	$1 \times 10^{-5}$	This work
$\bar{k}_t$ (L/mol.s)	$2.09 \times 10^6$	This work
A	$1.36 \times 10^{-5}$	This work
B	3.2	This work

It is worth mentioning that due to the limited available experimental images and the fact that the TEM provides 2D images with no clear indication of the location of the clusters, transferring of the morphologies of the TEM images to a distribution was

not possible and the comparison between simulated and experimental morphologies was made visually.

Figures 2.11 - 2.13 present a comparison of the experimental evolution of the particle morphology and the mass cluster distribution predicted by the model with the parameters given in Table 2.9 for Runs R1-R3. It can be seen that the model captured well the evolution of the particle morphology. Figure 2.11 shows that for Run R1 where a high T<sub>g</sub> seed (86 °C) was used, the model predicted that most of the second stage polymer was in the outer part of the non-equilibrium positions. Figure 2.12 shows that for Run R2 (T<sub>g,seed</sub> = 63 °C), most of the second stage polymer was at non-equilibrium positions, and the main part of it was in the inner region of the non-equilibrium positions. This is in good agreement with the TEM images that show that the clusters are more embedded in the particle than in Run R1. For Run R3 (Figure 2.13) where the softest seed (T<sub>g,seed</sub> = 46 °C) was used, the amount of second stage polymer in the outer shell of the non-equilibrium position was very small and the styrene rich polymer was distributed between the clusters in the inner region of the non-equilibrium positions and the core (equilibrium position). This is in a nice agreement with the TEM images of the particles that show that at the end of the process there were no clusters at the surface of the particles.



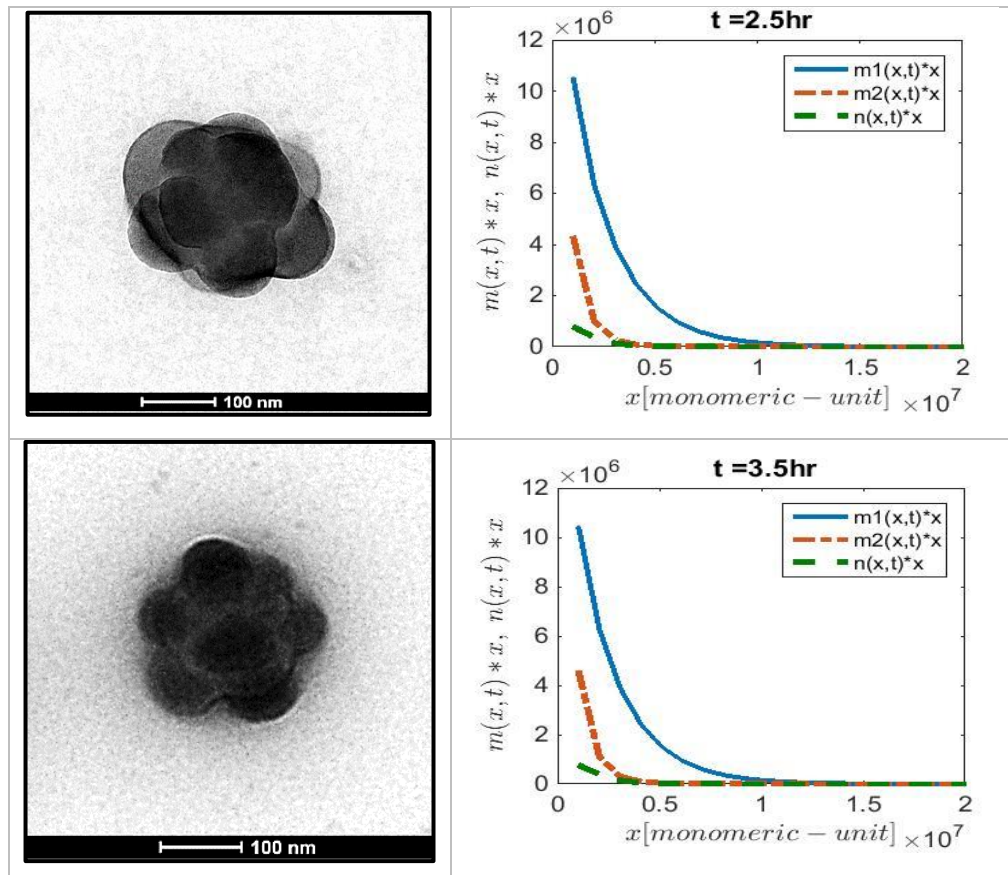
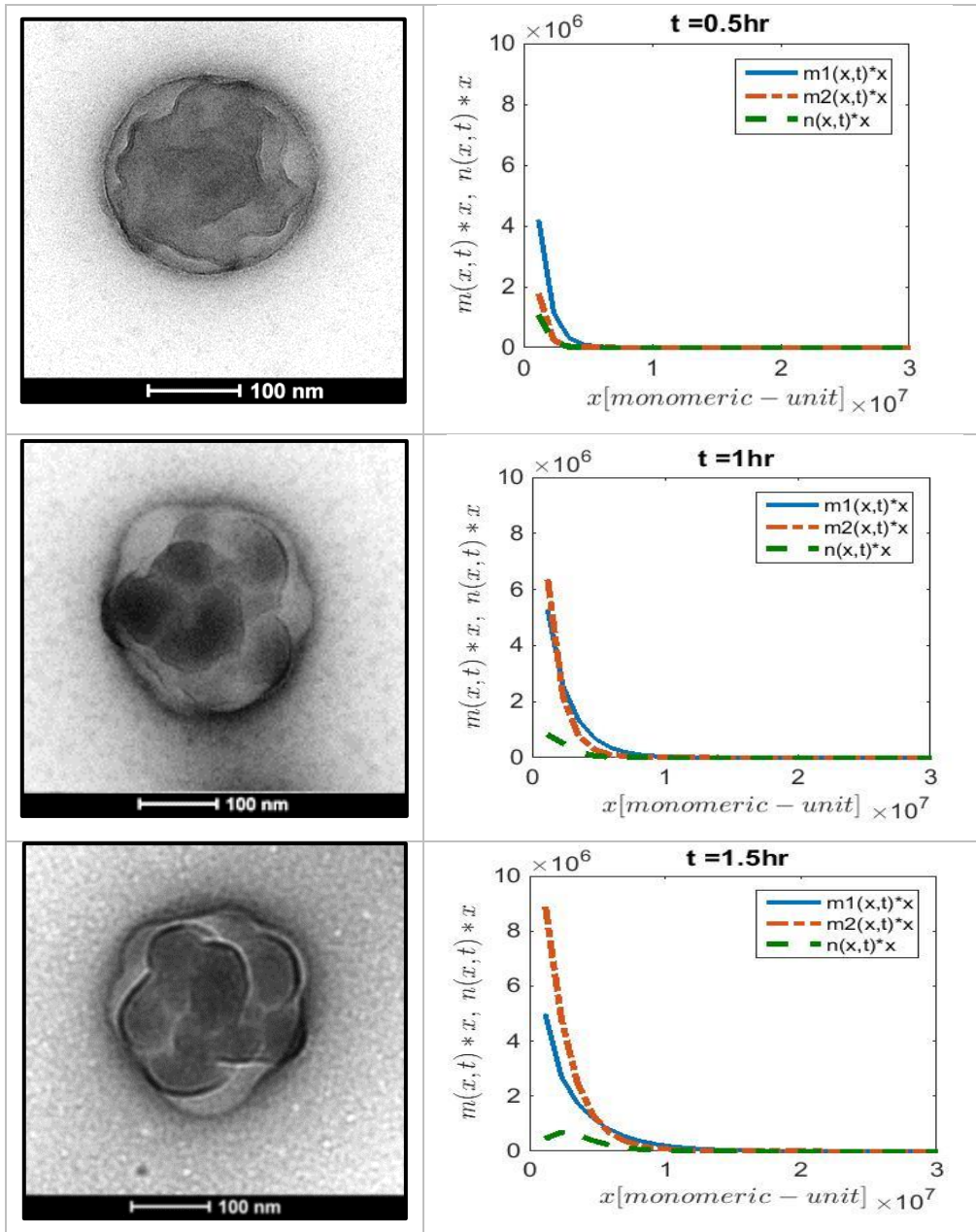


Figure 2. 8. Comparison between the evolution of the experimental particle morphology (TEM images of stained sample with vapor of  $\text{RuO}_4$  for 1 hour) and the predicted mass cluster distributions for Run R1. ( $m_1$  (blue): clusters in the outer shell of the non-equilibrium positions;  $m_2$  (orange): clusters in the inner region of the non-equilibrium positions;  $n$  (yellow): clusters at equilibrium positions). TEM image magnification: 50000.



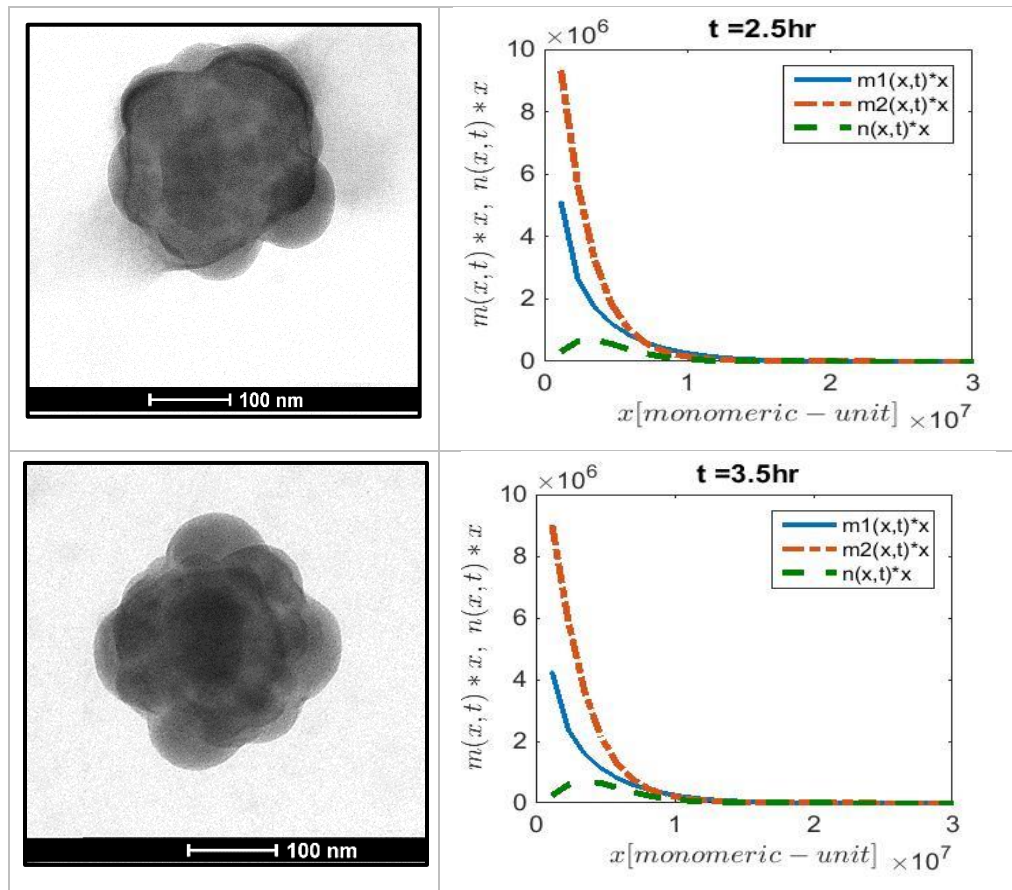
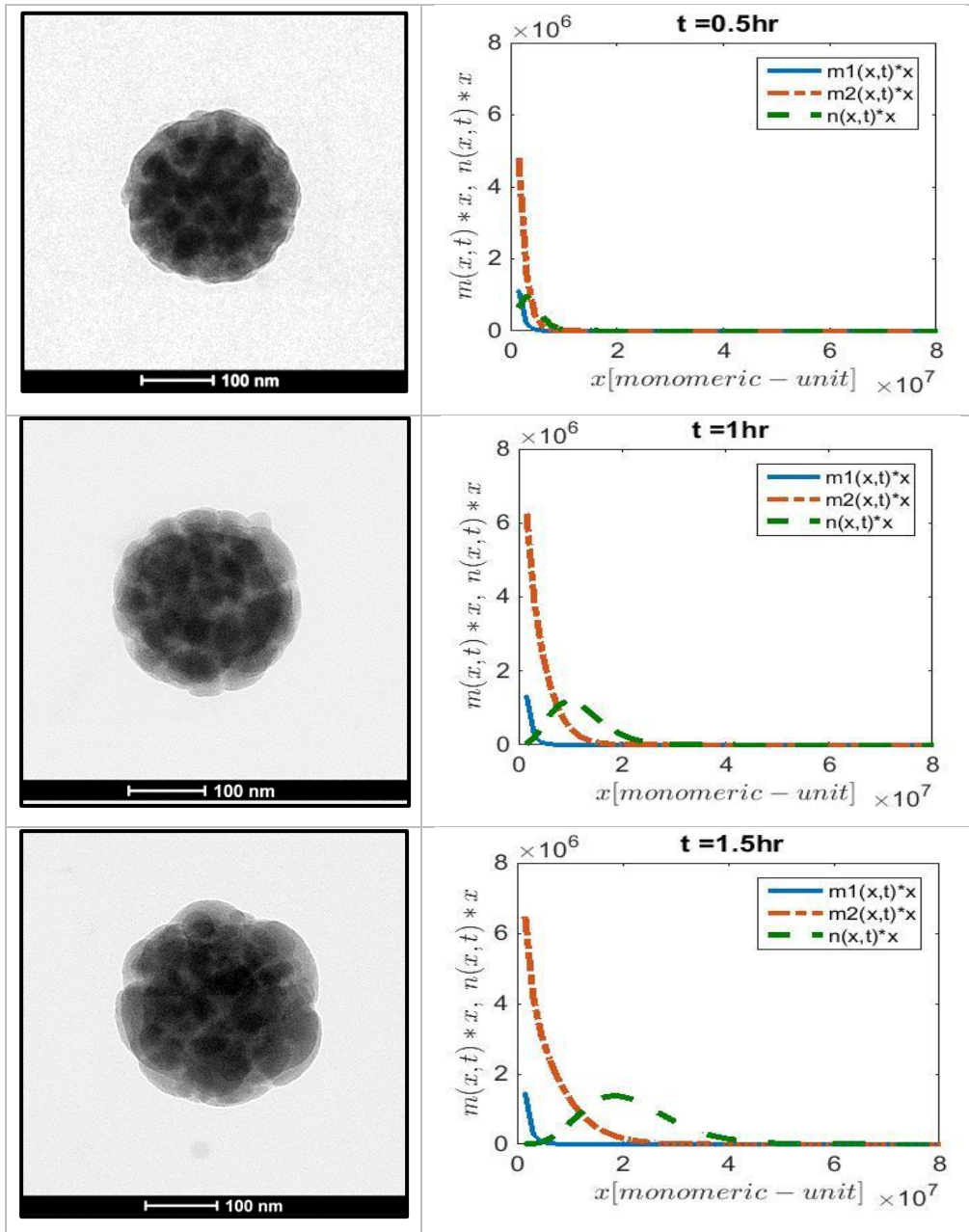


Figure 2. 9. Comparison between the evolution of the experimental particle morphology (TEM images of stained sample with vapor of  $\text{RuO}_4$  for 1 hour) and the predicted mass cluster distributions for Run R2. ( $m1$  (blue): clusters in the outer shell of the non-equilibrium positions;  $m2$  (orange): clusters in the inner region of the non-equilibrium positions;  $n$  (yellow): clusters at equilibrium positions). TEM image magnification: 50000.







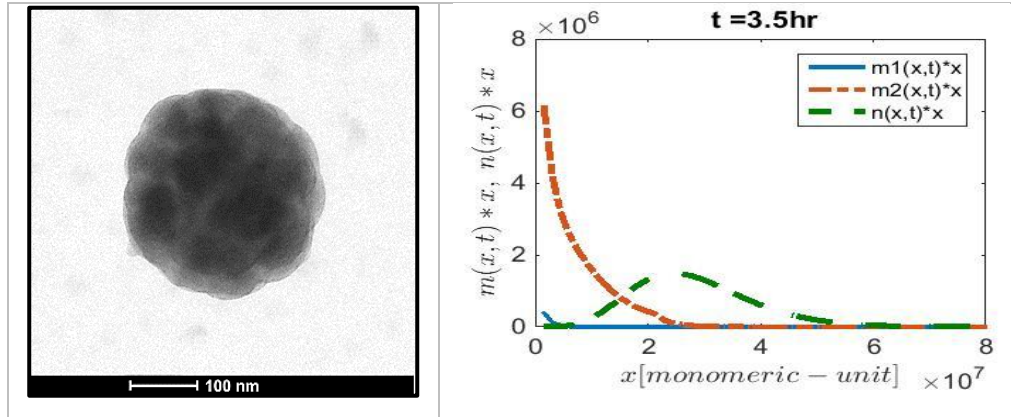


Figure 2. 10. Comparison between the evolution of the experimental particle morphology (TEM images of stained sample with vapor of  $\text{RuO}_4$  for 1 hour) and the predicted mass cluster distributions for Run R3. (m1 (blue): clusters in the outer shell of the non-equilibrium positions; m2 (orange): clusters in the inner region of the non-equilibrium positions; n (yellow): clusters at equilibrium positions). TEM images magnification: 50000.

Figure 2.14 gives a visual comparison of the TEM images of the final samples and the TEM-like images generated from the distributions in Figures 2.11- 2.13 by random sampling using the algorithm implemented by Hamzehlou *et al.*<sup>27</sup> It can be seen that the model captured very well the experimental observations. This opens the way to both process optimization and online control of the particle morphology.

For the sake of comparison, a simulation of Run R1 was carried out assuming a flat profile of radicals. It can be seen in Figure 2.15 that the predicted morphology was strongly different from the experimental ones. This demonstrates that the radical concentration profile determined the observed morphologies.

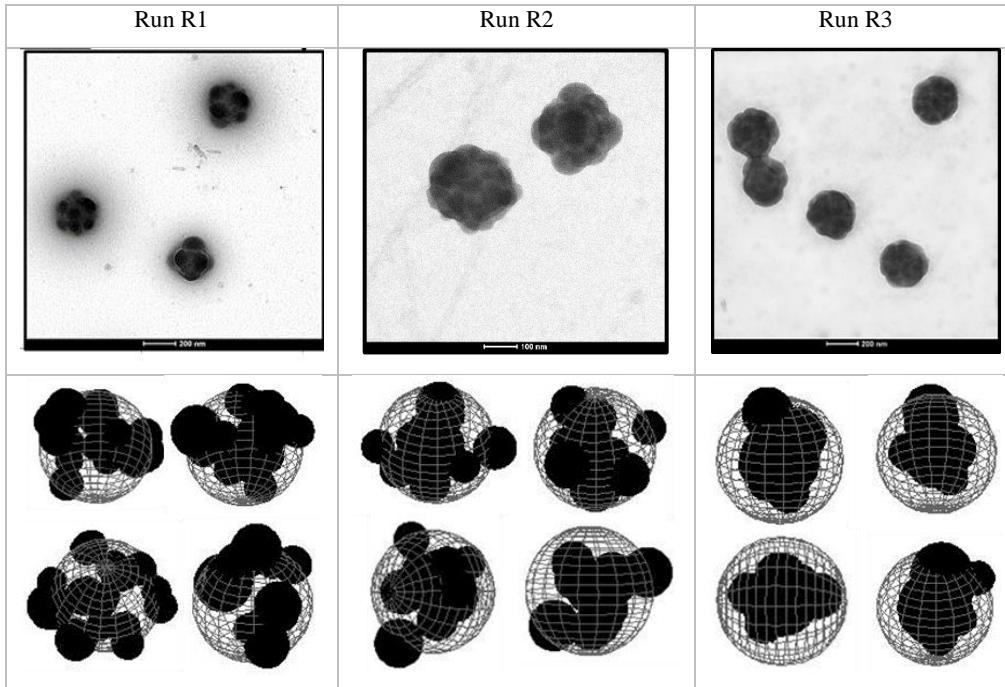


Figure 2. 11. Comparison between the TEM images of the final samples and the TEM-like particles generated from the cluster distributions.

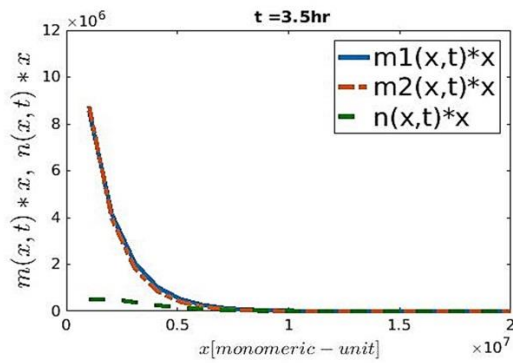


Figure 2. 12. Predicted mass cluster distributions for Run R1 considering flat profile of the radical.

### 2.3.2. Effect of T<sub>g</sub> of second stage polymer on particle morphology

The effect of T<sub>g</sub> of the second stage polymer on particle morphology was studied by comparing Runs R4 and R5 (Table 2.3) with Runs R3 and R1 (Table 2.10).

Table 2. 10. Measured T<sub>g</sub> of Runs R1, R3, R4 and R5 by modulated DSC.

Run	T <sub>g</sub> seed (°C)	T <sub>g</sub> 2 <sup>nd</sup> stage (°C)
<b>R4</b>	45	95
<b>R3</b>	46	46
<b>R5</b>	90	90
<b>R1</b>	86	49

Table 2. 11. Characterization data of Runs R1, R3, R4 and R5.

Run		Gel <sup>a</sup> (%)	MFFT (°C)
<b>R4</b>	Seed	3.9±0.3	Not available
	Final latex	25.9±0.3	96
<b>R3</b>	Seed	3.9±0.3	Not available
	Final latex	26.0±0.4	46
<b>R5</b>	Seed	0	Not available
	Final latex	0	96
<b>R1</b>	Seed	0	Not available
	Final latex	0	80

a. Gel measured by soxhlet extraction

The average instantaneous conversion in these experiments were 93.6 % for Run R3 and 98% for Run R4 (Figure 2.16) which led to  $T_{g\text{effective}}$  of 26.5 °C for Run R3 and 38.3 °C for Run R4, both well below the polymerization temperature. Figures 2.17 presents the experimental particle morphology and the mass cluster distributions predicted by the mathematical model explained in Section 2.3.1.1 for the final latexes of Run R3 and Run R4 which were synthesized using seeds of similar  $T_g$  (46 °C and 45 °C, respectively). TEM images show that increasing the  $T_g$  of second stage polymer from 46 °C in Run R3 to 93 °C in Run R4, the number of clusters (darker regions in TEM image) is higher and their size is smaller than for Run R3. Furthermore, the particles are more spherical.

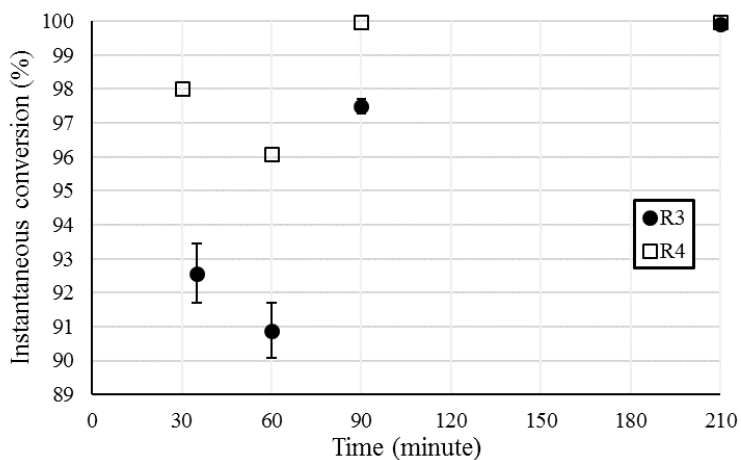


Figure 2. 13. Evolution of instantaneous conversion of Runs R3 and R4 in the second stage of polymerization

Effect of process variables on particle morphology

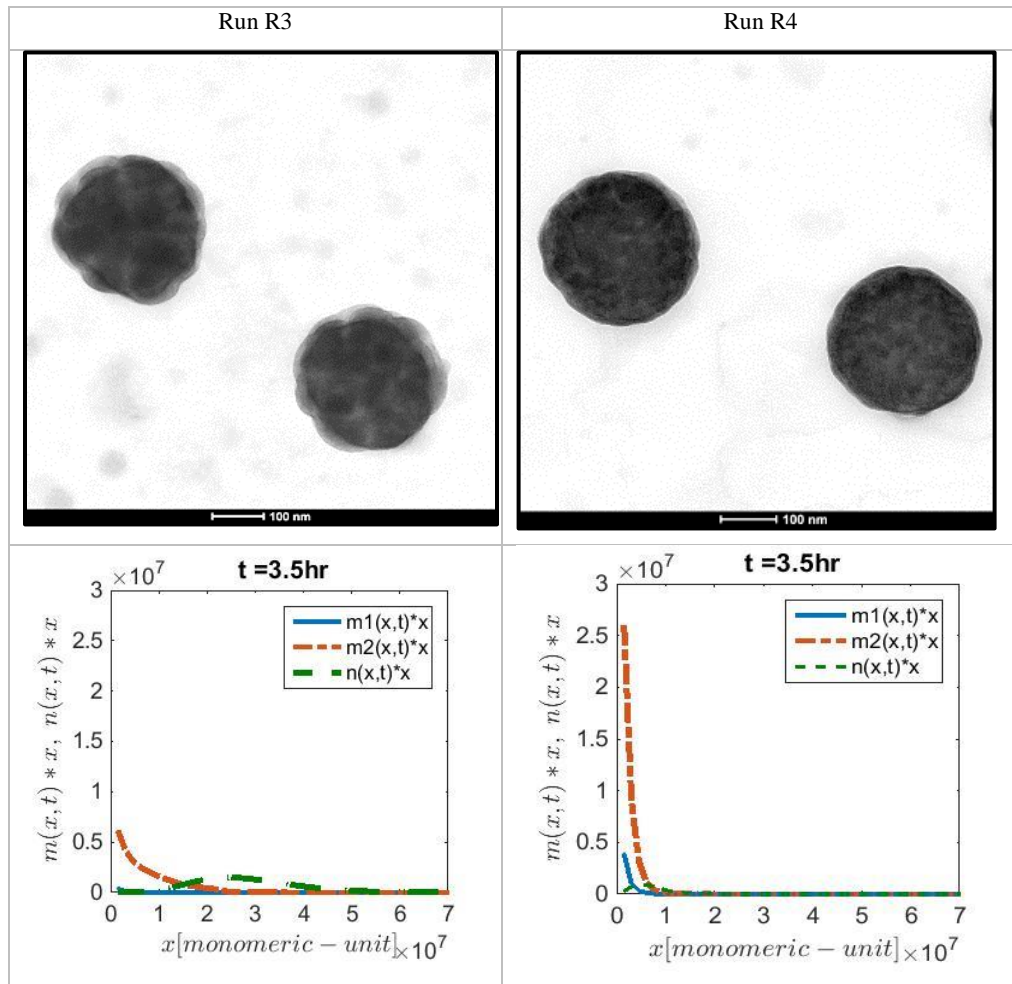


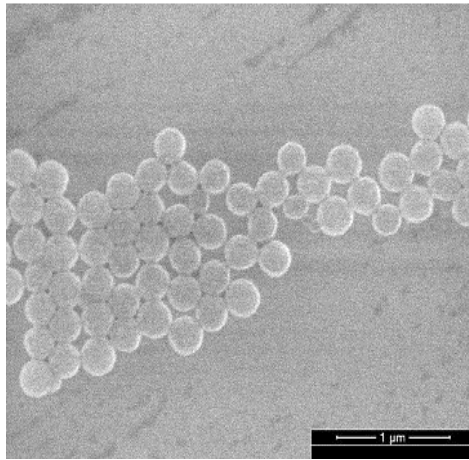
Figure 2. 14. Comparison between the TEM images of stained sample with vapor of  $\text{RuO}_4$  for 1 hour and the predicted mass cluster distributions ( $m_1$  (blue): clusters in the outer shell of the non-equilibrium positions;  $m_2$  (orange): clusters in the inner region of the non-equilibrium positions;  $n$  (yellow): clusters at equilibrium positions) of Runs R3 and R4. Magnification of TEM images is 50000.

The model predicted that increasing the  $T_g$  of second stage polymer from 46 °C in Run R3 to 95 °C in Run R4, the number of clusters at inner region of non-equilibrium positions increased while their size decreased. In addition, almost no cluster reached the equilibrium position (center of the particle) in Run R4, whereas a significant fraction of second stage polymer was at the center in Run R3. The differences are due to the fact that in the model, the  $T_{g\text{effective}}$  that affected the coefficients controlling the movement of clusters (equations 2.23-2.26), was calculated taking into account the contribution of the two polymers and that of the monomer. Therefore,  $T_{g\text{effective}}$  in Run R4 was higher than in Run R3 and hence the clusters moved less reducing coalescence and migration to the center of the particle (equilibrium position). This way of including the effect of the  $T_g$  of the second stage polymer is likely good for the cluster coalescence, but it seems that affects too much the cluster migration towards the equilibrium position. However, the TEM images do not allow to reach a conclusion at this point and the reader is referred to Chapter 3 where a better experimental characterization method to determine the morphology is presented.

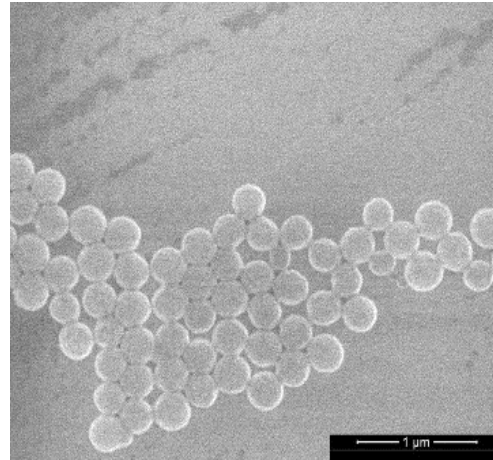
The MFFT of the Run R4 was measured to be 96 °C that was close to the  $T_g$  of the second stage polymer. Moreover, particle coalescence was checked by ESEM at different temperatures and as it is shown in Figure 2.18; particles started to coalesce

around 80 °C which was close to the Tg of the second stage polymer and indicates the presence of second stage polymer on the surface of the particles.

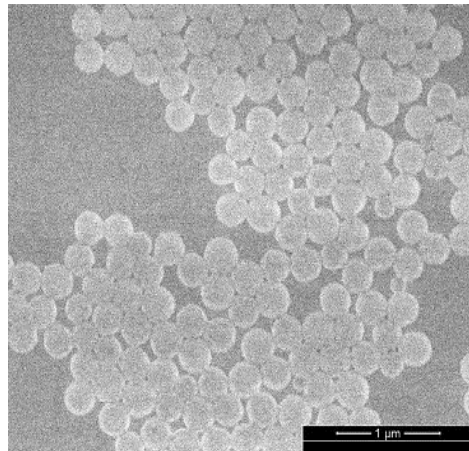
(a) 30 °C



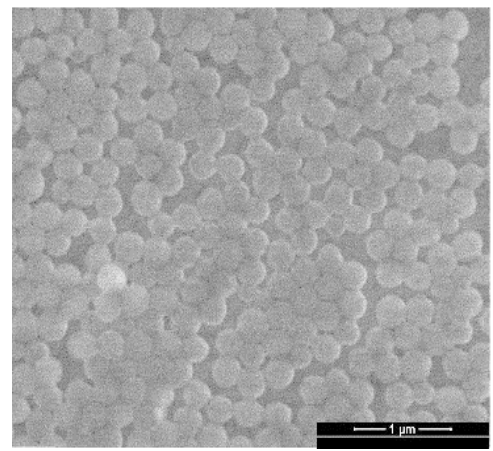
(b) 40 °C



(c) 50 °C



(d) 60 °C



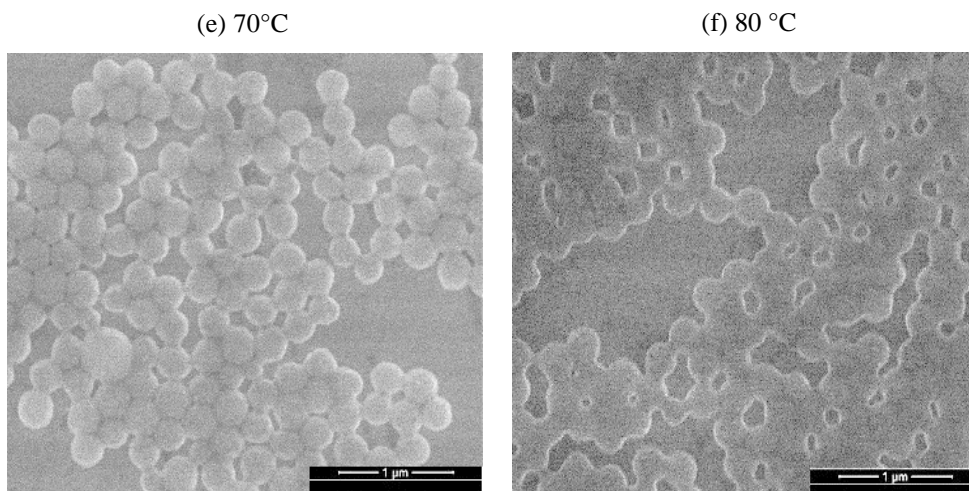


Figure 2. 15. Coalescence of polymer particles of Run R4 in the ESEM at different temperatures: (a) 30 °C; (b) 40 °C; (c) 50 °C; (d) 60 °C; (e) 70 °C; (f) 80 °C. Heating ramp between temperatures: 10°C/min. Time at each constant temperature: 10 min.

In Run R5, the average instantaneous monomer conversion during feeding time was 92.6% (Figure 2.19). Using the equation 2.1, the  $T_{g_{\text{effective}}}$  of the matrix during the polymerization was calculated 61.7 °C which was very close to that in run R1 (62.8 °C), both lower than the reaction temperature, namely the clusters could move in the non-glassy matrix. Figure 2.20 presents the TEM images of particle morphology and the mass cluster distributions predicted by the mathematical model for final latexes of Runs R1 and R5. Particles were rather spherical in Run R5 with the surface covered by many small clusters. In this case, the MFFT did not give any information because both



phases have the same Tg. On the other hand, large clusters located near the surface of the particles are presented in Run R1. The model prediction deviates from the experimental observations. It seems that the size of the clusters (that in the discussion has been referred to as coalescence) is mainly determined by the Tg of the second stage polymer, whereas the migration towards the equilibrium morphology is controlled by the Tg of the matrix.

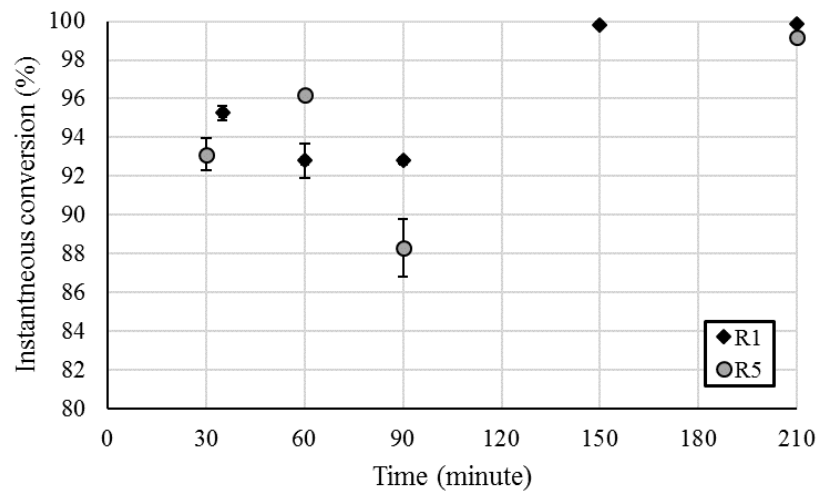


Figure 2. 16. Evolution of instantaneous conversion of Runs R1 and R5 in the second stage of polymerization.

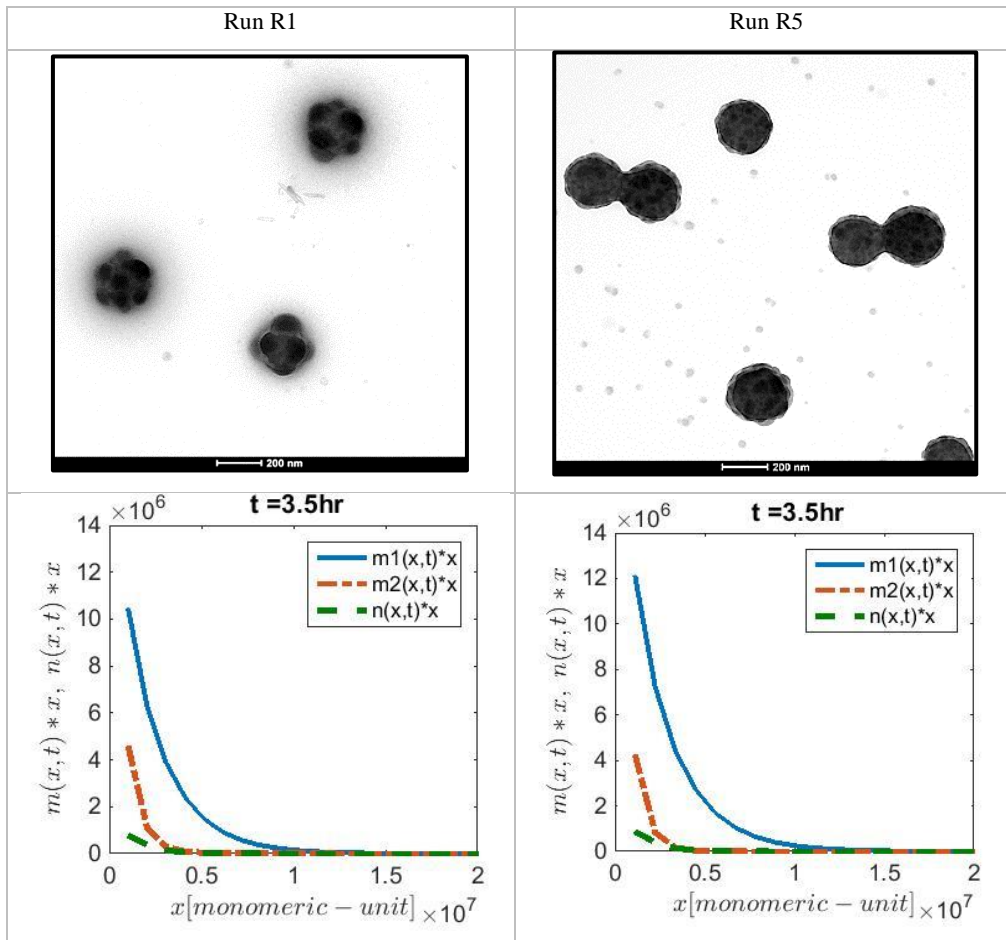


Figure 2. 17. Comparison between the TEM images of stained sample with vapor of  $\text{RuO}_4$  for 1 hour and the predicted mass cluster distributions ( $m_1$  (blue): clusters in the outer shell of the non-equilibrium positions;  $m_2$  (orange): clusters in the inner region of the non-equilibrium positions;  $n$  (yellow): clusters at equilibrium positions) of Runs R1 and R5. Magnification of TEM images is 25000.

### 2.3.3. Effect of reaction temperature of second stage of polymerization on particle morphology

The effect of reaction temperature of second stage of polymerization on the particle morphology was studied by comparing Runs R6 and R7 to Runs R2 and R4, respectively (Table 2.12). Runs R2 and R6 used the same formulation but different polymerization temperature (80 °C for R2 and 65 °C for R6). Similarly, Runs R4 and R7 differed only in the reaction temperature (80 °C for R4 and 60 °C for R7). As it is shown in Figure 2.21 where reactions R2 and R6 are compared, the instantaneous conversion was lower at the lower reaction temperature, but still the process was carried out under highly starved conditions. The calculated  $T_{g\text{effective}}$  of the seeds using equation 2.1 were 57.6 °C for Run R2 and 49 °C for Run R6, both below the reaction temperature.

Table 2. 12. Measured  $T_g$  of Runs R2, R4, R6 and R7 by modulated DSC and the reaction temperature of the second stage of polymerization process.

Run	$T_{g\text{seed}}$ (°C)	$T_{g\text{2nd stage}}$ (°C)	$T_{\text{reaction, 2nd stage}}$ (°C)
<b>R6</b>	63	49	65
<b>R2</b>	63	45	80
<b>R7</b>	46	95	60
<b>R4</b>	45	95	80

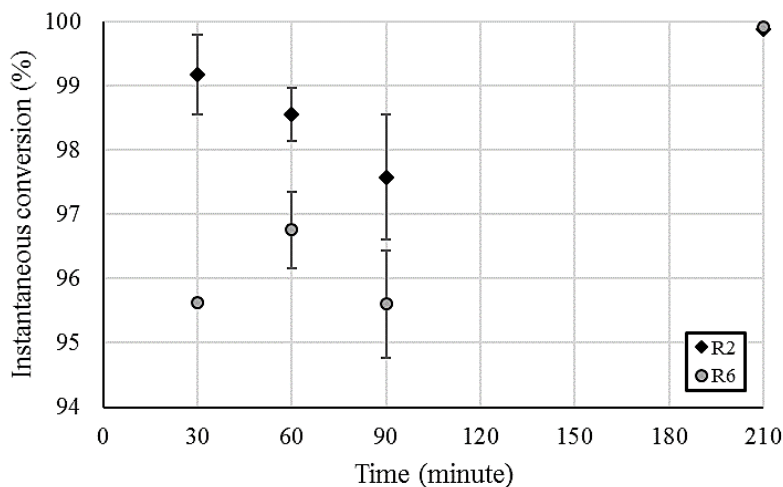


Figure 2. 18. Evolution of instantaneous conversion in the second stage of polymerization of R2 and R6 measured by GC.

Figure 2.22 presents the TEM images of the final latex particles and the predicted mass cluster distributions by the mathematical model for Runs R2 and R6. In both images, the lobes are seen on the surface of the particle but their size is smaller and their number is slightly higher for the experiment carried out at lower temperature (Run R6). The model predicted a higher number of the clusters at the outer shell of the non-equilibrium positions (m1, blue line) for the polymerization that was carried out at lower temperature (Run R6). The clusters are mainly in the non-equilibrium positions and the amount of clusters at equilibrium position was less than in Run R2. This was the result of the more glassy state of the matrix in Run R6 due to the smaller difference between the reaction temperature of second stage of polymerization and the  $T_{g\text{effective}}$

of seed (65-49=16 °C) compared to Run R2 (80-57.6=22.4 °C) which led to the slower movement and less coagulation of the clusters.

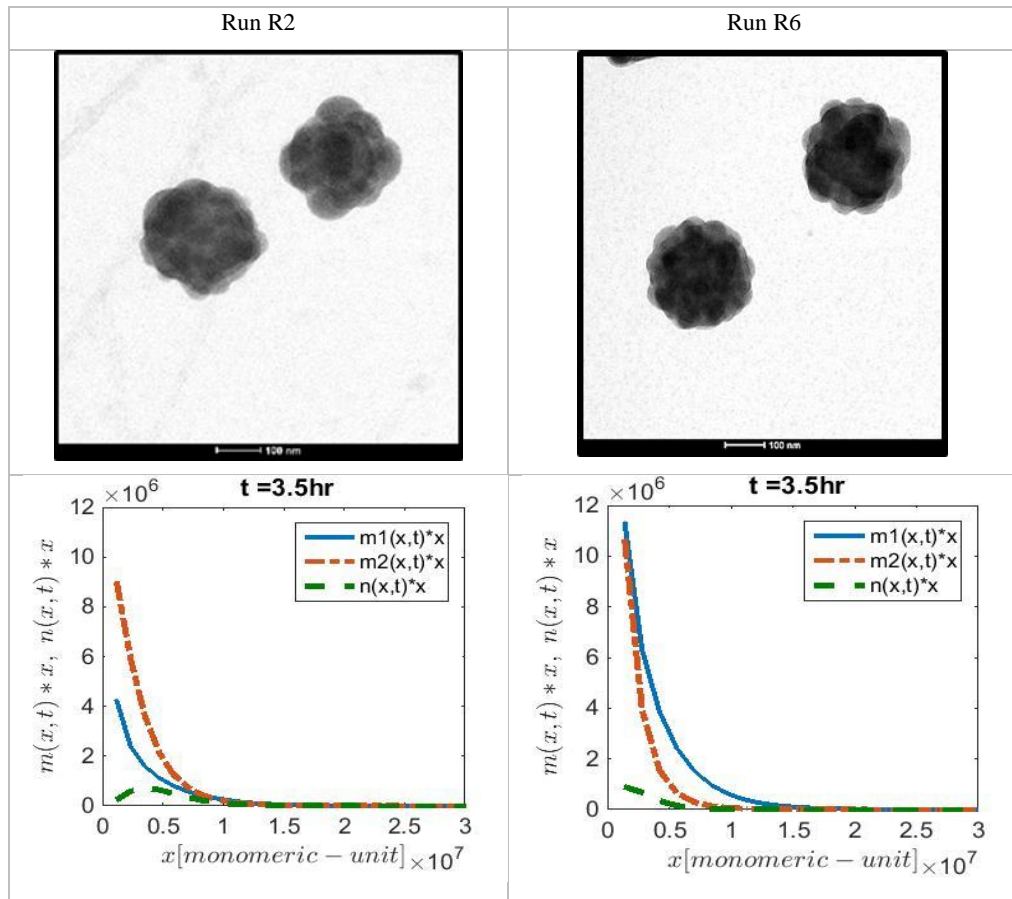


Figure 2. 19. Comparison of TEM images of stained sample with vapor of RuO<sub>4</sub> for 1 hour and the predicted mass cluster distributions (m1 (blue): clusters in the outer shell of the non-equilibrium positions; m2 (orange): clusters in the inner region of the non-equilibrium positions; n (yellow): clusters at equilibrium positions) of Run R2 and R6. Magnification of TEM images is 50000.

Run R7 was synthesized using the same formulation than for Run R4, but at a lower reaction temperature (60 °C instead of 80 °C). TEM images and the model predicted mass cluster distributions of Run R4 and R7 are shown in Figure 2.23. The particles were spherical with less phase separation in Run R7. The MMFT of 86 °C, which was smaller than the T<sub>g</sub> of the second stage polymer suggesting intermixing of the phases. This was checked by M-DSC measurements.

Figure 2.24 shows the first and second heating M-DSC cycles for Runs R4 and R7. In the first heating of R7, a broad peak can be seen between the two T<sub>g</sub>s of the pure phases, indicating high level of intermixing. This is confirmed in the second heating cycle where two distinct peaks are observed for Run R7 because phase separation was achieved after one hour of annealing at 150 °C for 60 minutes at the end of first heating. On the other hand, Run R4 did not show any substantial intermixing (similar DSC curves in both heating cycles). Although the evolution of instantaneous conversion by GC is not available for Run R7, the instantaneous conversion was measured above 99% by gravimetry during the second stage of process. Therefore, relatively glassy clusters were formed in Run R7. These clusters were small as they did not grow by coalescence. As they were small, they were able to migrate towards the interior of the particle. The large cluster-matrix interfacial area was the reason for the substantial intermixing observed in Figure 2.24. The model was not able to capture these findings.

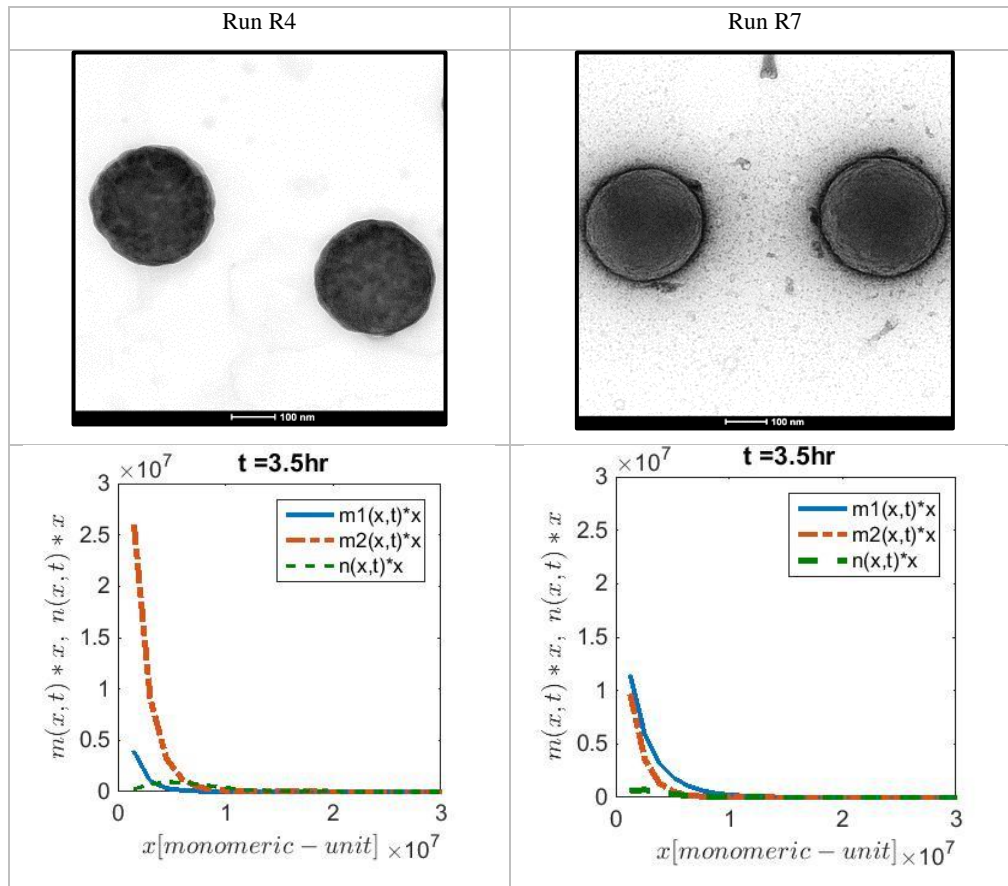


Figure 2. 20. Comparison between the TEM images of stained sample with vapor of  $\text{RuO}_4$  for 1 hour and the predicted mass cluster distributions ( $m_1$  (blue): clusters in the outer shell of the non-equilibrium positions;  $m_2$  (orange): clusters in the inner region of the non-equilibrium positions;  $n$  (yellow): clusters at equilibrium positions) of Runs R4 and R7. Magnification of TEM images is 50000.

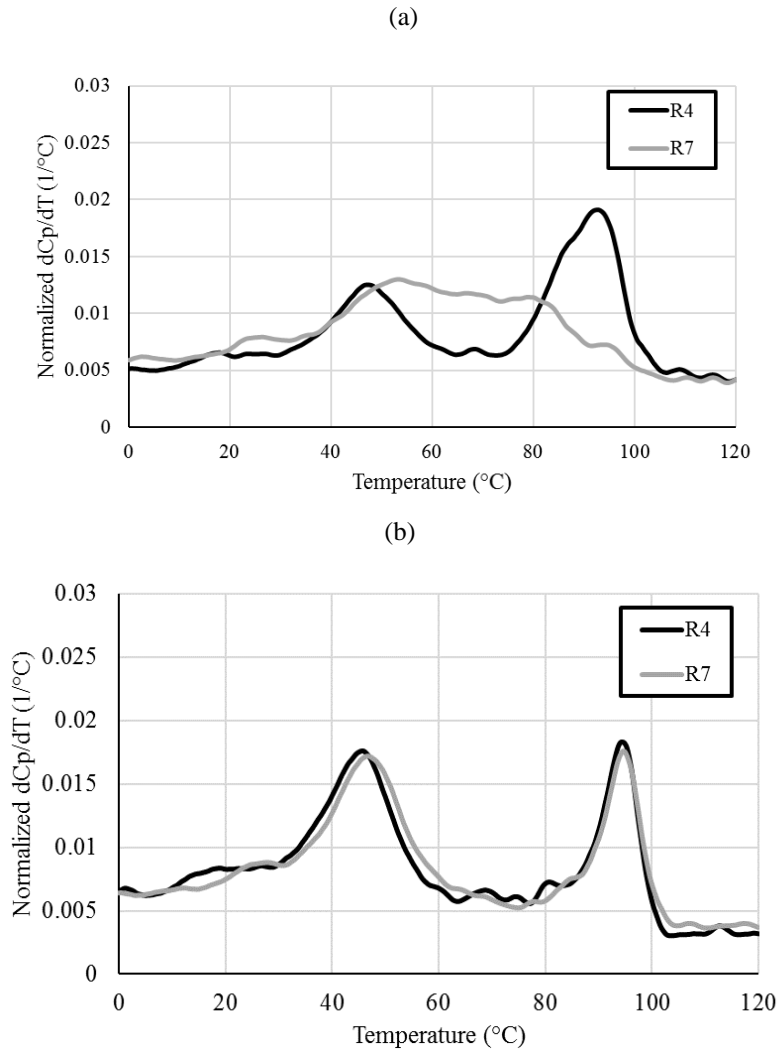


Figure 2. 21. Normalized  $dC_p/dT$  from M-DSC of Runs R4 and R7: (a) first heating and (b) second heating. Data are smoothed by 3 °C.



#### **2.3.4. Effect of initiator of second stage of polymerization on particle morphology**

The second stage of polymerization of Run N1 was carried out using thermal initiator (NaPS) instead of the redox initiator employed in the experiments discussed above. The goal was to investigate if the charged entering radicals from NaPS, which are expected to create a sharper radical concentration profile in the particles, affected the particle morphology. Figure 2.25 presents the evolution of the instantaneous conversions for Runs N1 and R4 (which was carried out with the same formulation with  $T_{g_{seed}} = 45\text{ }^{\circ}\text{C}$  and  $T_{g_{second\ stage}} = 95\text{ }^{\circ}\text{C}$ , but using TBHP/ACBS as initiator). It can be seen that both of the Runs were carried out under starved condition with slightly lower instantaneous conversion for Run N1.

Figure 2.26 compares the TEM images of stained final latexes for Run R4 and N1. It can be seen that both latexes showed similar morphologies although the surface of N1 looks slightly bumpier that could be attributed to a sharper radical concentration profile. MFFT of  $96\text{ }^{\circ}\text{C}$  for both cases, which is the  $T_g$  of the second stage polymer, proved the presence of the second stage clusters on the surface of the particles.

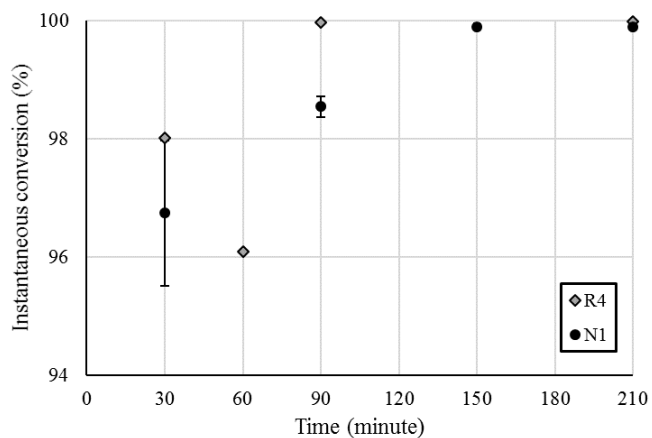


Figure 2. 22. Evolution of instantaneous conversion in the second stage of polymerization of R4 and N1 measured by GC

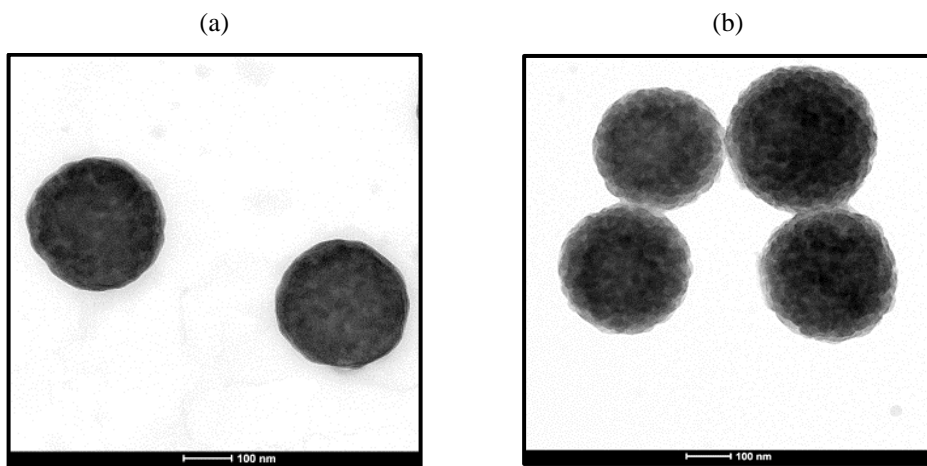


Figure 2. 23. Conventional TEM images of stained samples with vapor of  $\text{RuO}_4$  for 1 hour of (a) Run R4 and (b) Run N1. Image magnification: 50000.

A way to obtain a flatter radical concentration profile is to use an oil soluble initiator. This was done in Run A1 that was synthesized with the same composition of

the seed and the second stage monomer mixture as Run R1, but with AIBN instead TBHP/ACBS in the second stage of polymerization (Table 2.13). The condition of Run R1 was chosen because this latex gave the morphology that was farther from the equilibrium one. Figure 2.27 compares the instantaneous conversion for both reactions. It can be seen that high conversion was achieved and  $T_{g_{\text{effective}}}$  were 62.8 °C and 60.3 °C for Run R1 and A1, respectively.

Table 2. 13. Measured Tg of Runs R1 and A1 in modulated DSC.

Run	T <sub>g<sub>seed</sub></sub> (°C)	T <sub>g<sub>2<sup>nd</sup> stage</sub></sub> (°C)
R1	86	49
A1	86	48

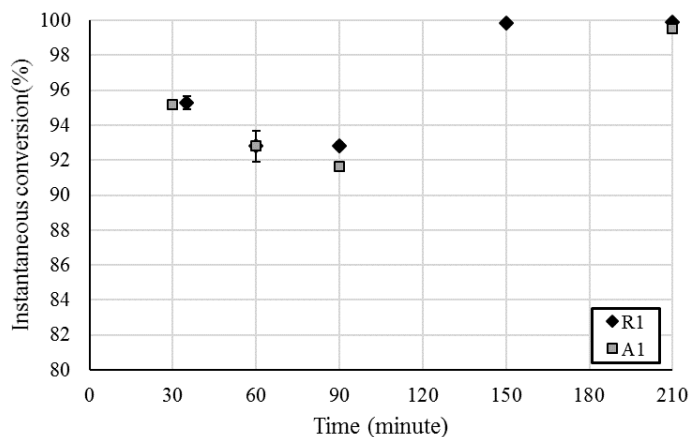


Figure 2. 24. Evolution of instantaneous conversion in the second stage of polymerization of R1 and A1 measured by GC.

Figure 2.28 presents the TEM images of particle morphology and the mass cluster distributions predicted by the mathematical model for Runs R1 and A1. Morphology changed from multi-lobed with styrene rich clusters on the surface to a morphology in which due to the flat radical concentration profile, the styrene rich clusters are distributed within the particle. This resulted in spherical particles. It is interesting to see that even if the radicals are generated within the particles and hence second stage polymer is produced inside the particle, the equilibrium morphology was not attained, because the high viscosity of the matrix reduced the movement of the styrene rich clusters.

The minimum film forming temperature of A1 was 75 °C, which was slightly lower than that of Run R1 (80 °C). On the other hand, ESEM experiment (Figure 2.29) showed that particles started to coalesce at a temperature close to the T<sub>g</sub> of the second stage polymer (50 °C). These results are double surprising. First, with the morphologies presented in Figure 2.28, one would expect that the MFFT of Run A1 was at least as higher than that of Run R1 because it seems that the outer layer in the particles of Run A1 is formed by the hard polymer of the seed. It can be said that 5 °C of difference in MFFT might be due to small differences in the film formation process. However, the differences between Run R1 and A1 observed in ESEM experiments are bigger. The particles of Run A1 coalesced at about 50 °C (Figure 2.29) whereas the particles of Run

R1 needed higher temperature (60-70 °C, Figure 2.6). Therefore, against the expectation particles of Run A1 formed film easier than particles of Run R1.

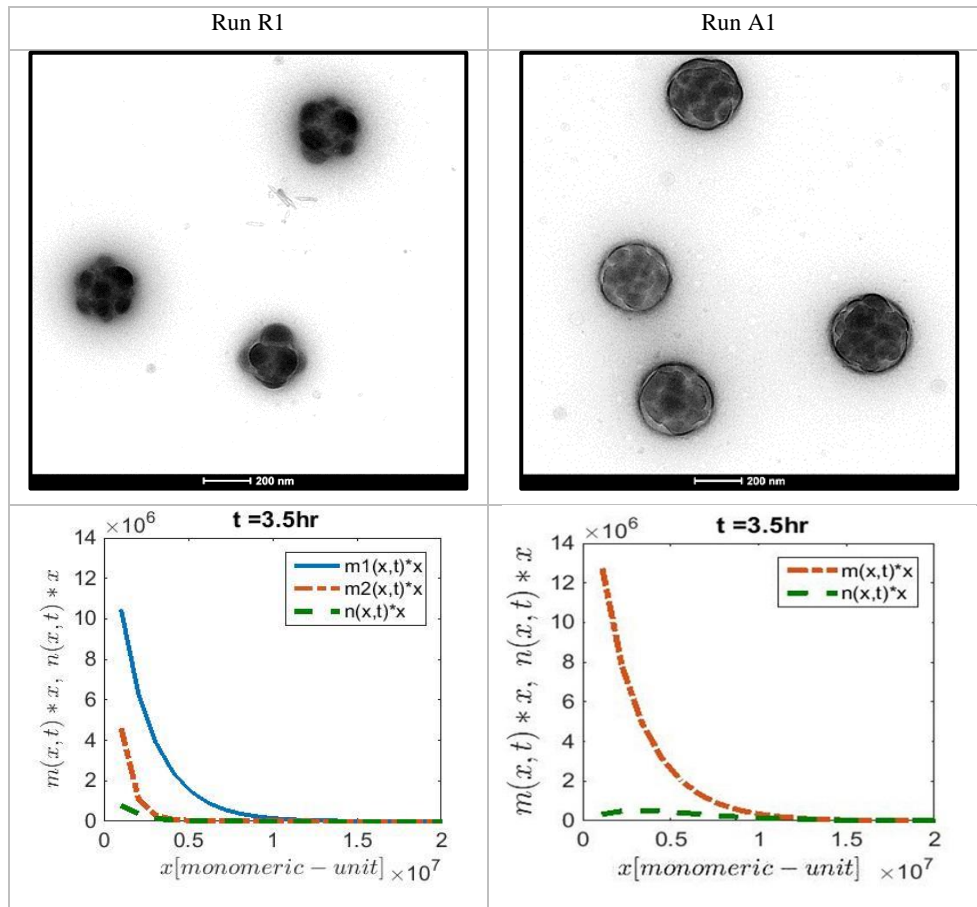


Figure 2. 25. Comparison between the TEM images of stained sample with vapor of RuO<sub>4</sub> for 1 hour and the predicted mass cluster distributions ( $m_1$  (blue): clusters in the outer shell of the non-equilibrium positions;  $m_2$  (orange): clusters in the inner region of the non-equilibrium positions;  $n$  (yellow): clusters at equilibrium positions) of Runs R1 and A1. Magnification of TEM images is 25000.

A possible reason is the mechanical strength of the structure of the hybrid polymer-polymer particle. This is illustrated in the reconstructed 3D images of the matrix of polymer particle of Runs R1 and A1 from tomographic analysis of the samples by high angle annular dark field-scanning transmission electron microscopy (HAADF-STEM) and image reconstruction in Figure 2.30 that the technique will be explained in detail in Chapter 3. It can be seen that the object formed by the matrix of Run R1 does not present weak points whereas that of Run A1 has several. Actually, hard polymers forming structures with weak points are the bases of the ability to form films of soft seed-hard second stage polymer latexes, which presents much better properties than the corresponding hard core-soft second stage polymer latexes.<sup>47</sup> The second surprise in the results presented above is the difference between the MFFT of Run A1 (75 °C) and the temperature at which the coalesced occurred in the ESEM experiment (50 °C). A possible reason is the effect of film thickness on crack formation. This is a phenomenon that has been studied only for homogenous latex particles<sup>48</sup>, but for which the information is available shows that by forming a film, a vertical profile of stresses is formed and the stress is being maximum at the air-film surface. The stress difference between the substrate interface and the air interface increases with the rigidity of the particles and the thickness of the film. Therefore, for relatively rigid particles as those

of A1, the vertical stress in ESEM is virtually zero, whereas a significant stress can be developed for thicker films giving a higher MFFT.

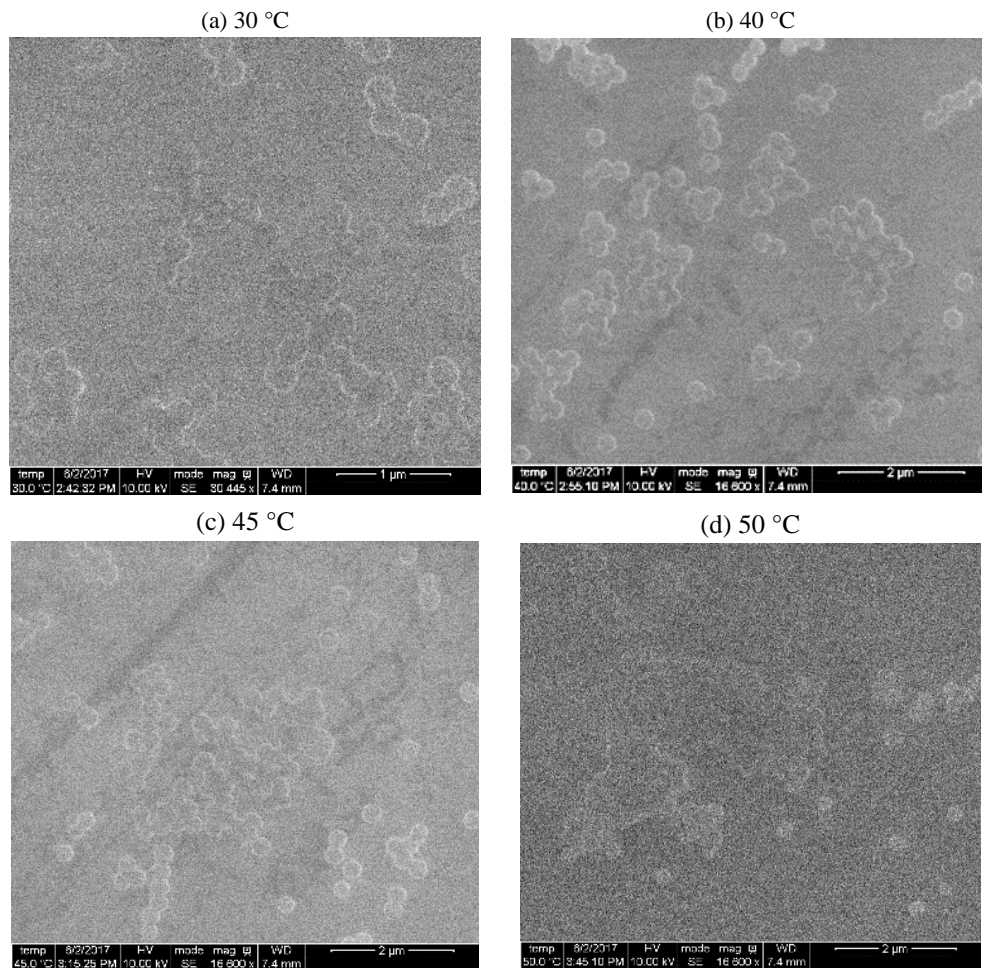


Figure 2. 26. Images from ESEM at different Temperature for Run A1: (a) 30 °C; (b) 40 °C; (c) 45 °C; (d) 50 °C. Heating ramp between temperatures: 10 °C/min. Time at each constant temperature: 10 min.

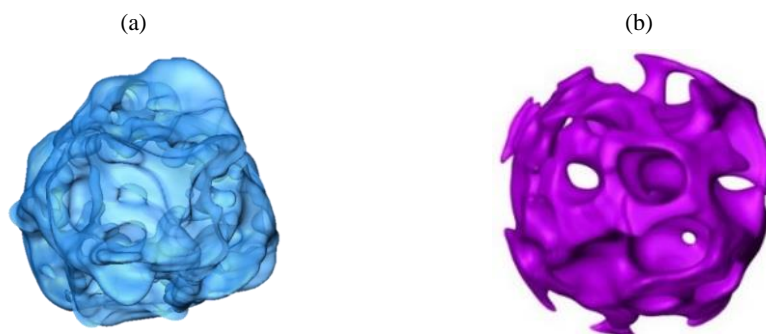


Figure 2. 27. Reconstructed 3D images of the matrix of polymer particle for Runs R1 (a) and A1 (b) by tomographic analysis of samples by HAADF-STEM and image reconstruction

### **2.3.5. Effect of prolonged reaction time in the second stage of polymerization on particle morphology**

It was discussed in Section 2.3.1 that using a water-soluble redox initiator resulted in a sharp radical concentration profile and the majority of the clusters were produced at the exterior zone of the particles away from the equilibrium position (the center of the particles in the synthesized cases). Lowering the  $T_g$  of the seed resulted in a higher penetration of the second stage polymer in the matrix. However, the equilibrium position was not attained. Run R8 was designed to evaluate that whether not reaching to equilibrium morphology when the  $T_g$  of the matrix was soft and reaction temperature was well above the  $T_g$  of the matrix was a kinetic issue (namely, there was not enough time for the clusters to move). Run R8 was a replica of Run R3 (seed M3 with  $T_{g_{calculated}}$



= 40 °C and second stage polymer of  $T_{g_{\text{calculated}}} = 40 \text{ °C}$ ), but the feedings of the second stage of polymerization were discontinued for 3 hours after feeding of 33% of the pre-emulsion and initiator to the reactor (in 30 minutes). The remaining 67% were fed in 60 minutes afterwards. Figure 2.31 compares the evolution of the instantaneous conversion for Runs R8 and R3. The difference at minute 30 is attributed to the differences in the amount of residual initiator in the seed and to the difference in the oxygen concentration in different Runs. It can be seen the conversion at minute 60 of Run R3 was lower than that of Run R8 at minute 240 that corresponds to the feeding of 67% of total pre-emulsion and at the end of feeding in both cases the conversion reaches to 97% (minute 90 in Run R3 and minute 270 in Run R8). For a soft seed, these differences in conversion are not expected to significantly affect the viscosity of the matrix.

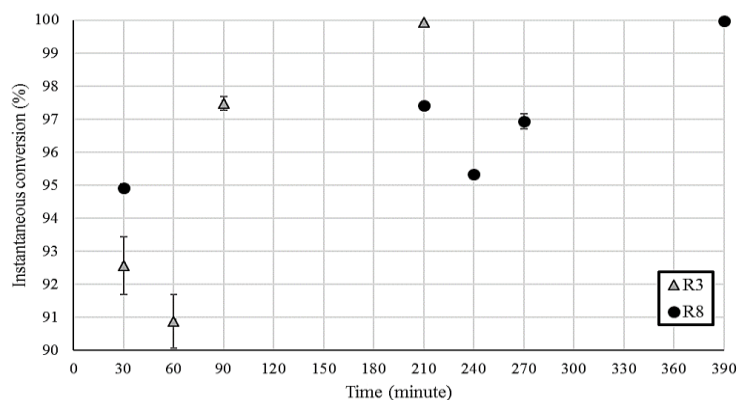
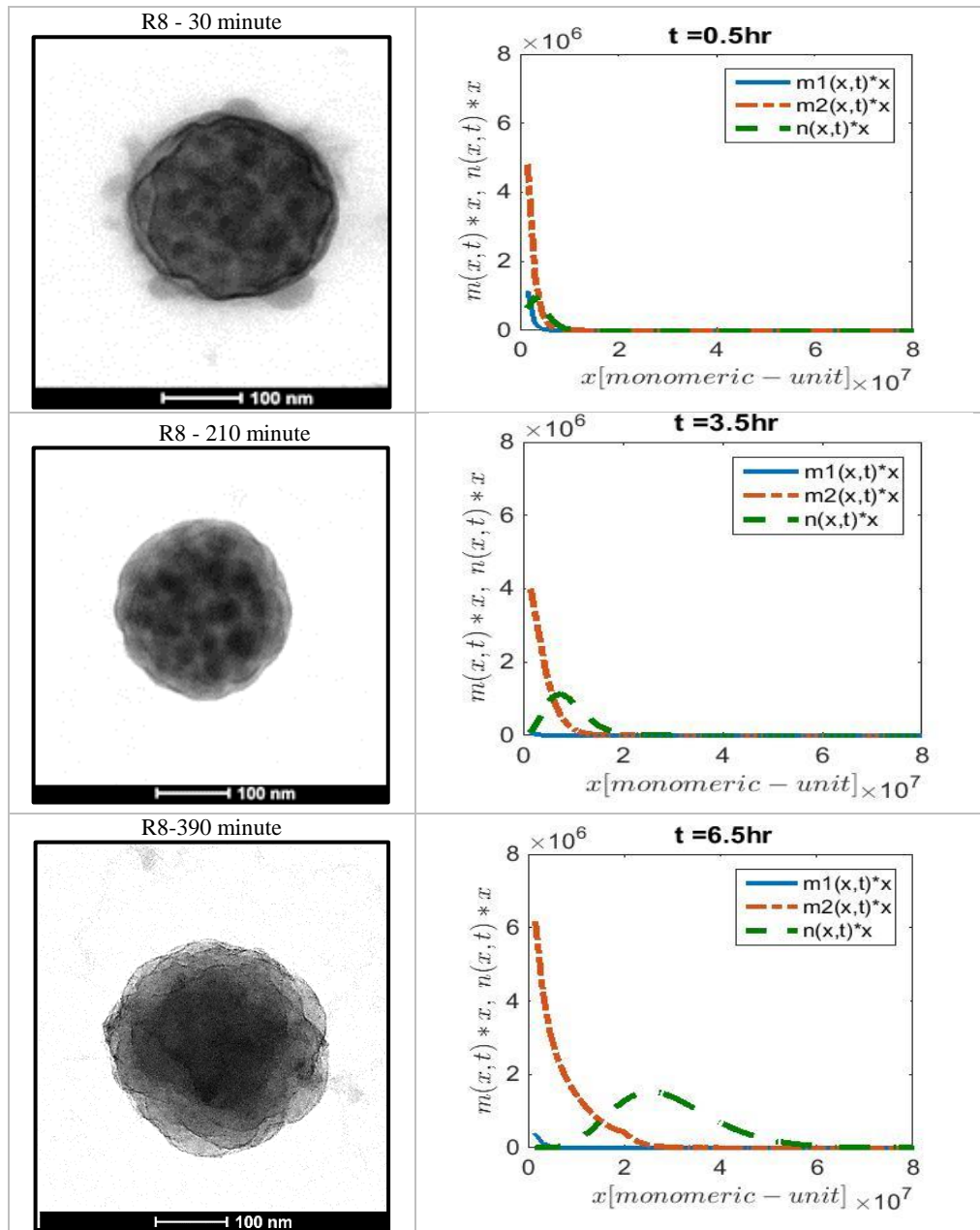


Figure 2. 28. Evolution of instantaneous conversion for Runs R3 and R8 measured by GC.

Figure 2.32 presents the evolution of morphology and mass cluster distribution predicted by the mathematical model for Runs R8 and R3. The morphology at minute 30 is similar to that obtained in Run R3. Small clusters with substantial penetration in the matrix can be distinguished in the image. The morphology did not change noticeable at 210 minutes (after 3 hours of batchwise reaction) while the model predicted the penetration of the clusters toward the equilibrium position. The sample at 390 minutes (after the addition of the remaining 67 % of feeding streams and then two hours of post-polymerization) shows a morphology where the small clusters are not clearly seen. The main difference between the two images for the final latex morphologies of Runs R3 and R8 is that the clusters can be distinguished in Run R3 (larger than during the process) and the particles show bumps on the surface whereas in Run R8 the clusters have collapsed and only a dark central one was visible. The surface of the particles is smoother. The model predicts similar final morphologies for both runs with considerable amount of clusters at equilibrium position and does not predict any substantial change in the final morphology considering 3 hours without feeding in the process while it can be interpreted from the TEM images that the clusters in Run R8 is bigger than in Run R3.

Effect of process variables on particle morphology



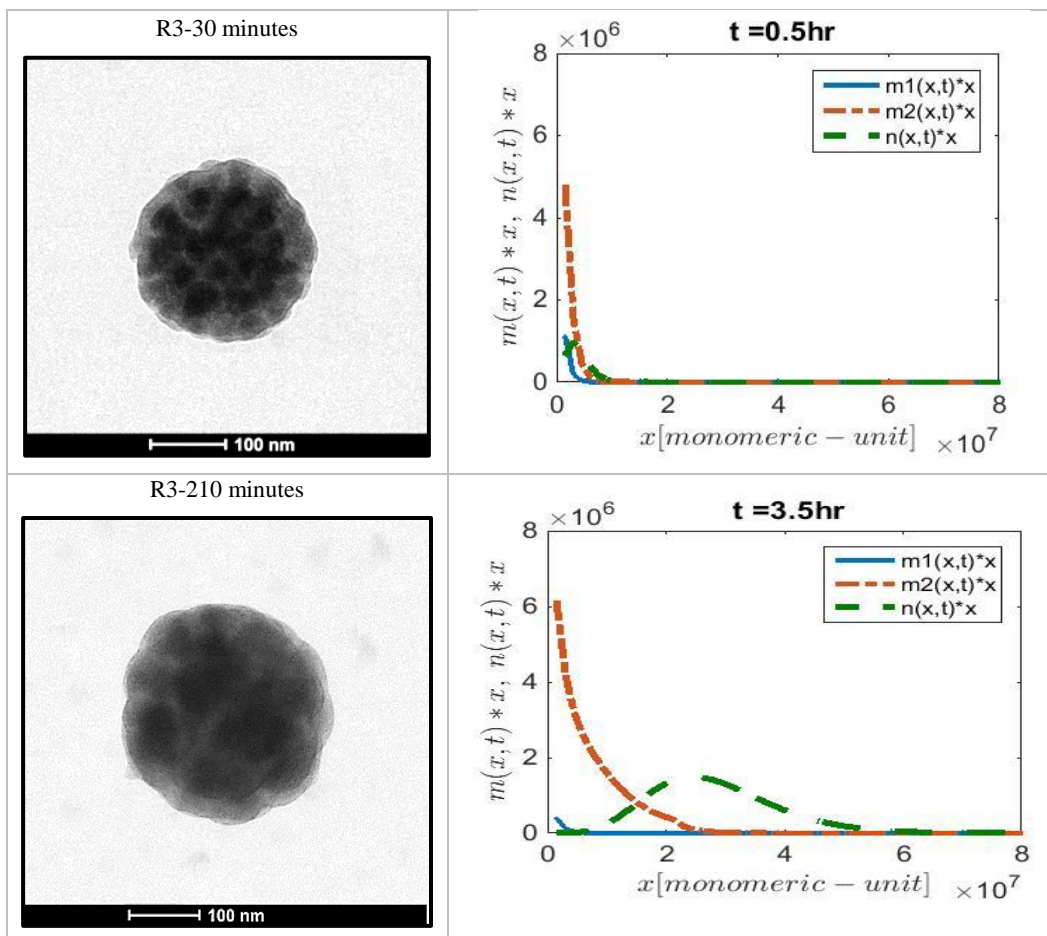


Figure 2. 29. TEM images of samples stained with vapor of  $\text{RuO}_4$  compared to the predicted mass cluster distributions during the second stage of polymerization for Run R8 and Run R3. (m1 (blue): clusters in the outer shell of the non-equilibrium positions; m2 (orange): clusters in the inner region of the non-equilibrium positions; n (yellow): clusters at equilibrium positions). Images magnification is 50000.

### **2.3.6. Effect of crosslinking of the seed on particle morphology**

The effect of nature and amount of crosslinking agents used in the synthesis of seed on the particle morphology was explored using two different crosslinking agents with different molar percentages based on the total amount of monomers in the seed. Table 2.14 shows the characteristics of the latexes synthesized with seeds crosslinked with EGDMA and AMA as compared to Run R7, which was synthesized using a not-crosslinked seed. EGDMA is a symmetric crosslinker with two methacrylate double bonds whereas AMA is an asymmetric crosslinker with the allyl double bond being substantially less reactive than methacrylate one.<sup>49</sup> These experiments were carried out at 60 °C at the second stage of polymerization.

The instantaneous conversion data during the polymerization of these cases is not available from GC but it was measured greater than 99 % by gravimetry. Therefore, it can be accepted that these experiments were carried out at high instantaneous conversion. The gel contents of the seeds increased from Run R7 to Run R10 with 1 mol% of EGDMA. Similarly, the gel content in the seed of Run R11 was higher than in Run R7 and increased with the concentration of AMA from Run R11 to Run R13. For the same molar concentration of crosslinker, the amount of insoluble polymer was higher for AMA than for EGDMA (Run R13 compared to Run R10). This was already reported in the literature<sup>50,51</sup> and was attributed to the higher likelihood of EGDMA for

intramolecular cyclization reactions that waste pendant double bonds and produce cycles that do not contribute in the formation of the network.

Table 2. 14. Characteristic of synthesized latexes with cross-linked seed and Run R7 (with non-crosslinked seed)

Run	Gel <sup>a</sup> (w%)	Swelling <sup>b</sup>	MFFT (°C)
R7	Seed (M3: not cross-linked)	2.7±0.1	Not available
	Final latex	31.9±0.1	9.4±0.5
R9	Seed (M4: 0.5mol% EGDMA)	Not available	Not available
	Final latex	51.3±0.2	8.4±4.3
R10	Seed (M5: 1mol% EGDMA)	70.7±0.1	5.5±0.1
	Final latex	54.4±0.0	3.8±0.3
R11	Seed (M6: 0.1mol% AMA)	82.3±0.2	5.8±0.2
	Final latex	62.9±0.1	3.9±0.3
R12	Seed (M7: 0.5mol% AMA)	94.9±0.7	2.9±0.7
	Final latex	76.6±0.1	2.3±0.0
R13	Seed (M8: 1mol% AMA)	96.3±0.0	2.3±0.4
	Final latex	82.8±0.1	1.4±0.1

a. Gel measured by soxhlet extraction. b. Swelling parameter represents the inverse of crosslinking density.

The gel content of final latex of composite particles was higher than 50 wt% (considering that each polymer phase is 50 wt% of composite particles) in all runs using crosslinked seeds and increased with the amount of crosslinker used in the seed. The increase was more evident for AMA (from 76.6 % in R12 to 82.8% in R13) than for EGDMA (from 51.3% in R9 to 54.4% in R10). The increase of the gel content during

the polymerization of a styrene-rich monomer mixture can only be explained by grafting reactions of second stage polymer on the cross-linked seed polymer. In particular on the unreacted pendant double bonds available in the seed polymer. Since AMA presents allylic double bond that is less reactive than the methacrylic one, the effect for the runs with AMA was prominent, whereas for the runs with EGDMA was less because fewer pendant double bonds were available. Swelling data also reflect the changes in the microstructure discussed above. The crosslinking density (inverse of swelling measurement) increased from the seed to the final latex in all runs, indicating that the second stage chains became part of the cross-linked network by reacting with the pendant double bonds and increasing the density of the network.

Figure 2.33 shows the TEM images of the stained samples for Runs R7 (non-crosslinked seed), R9 (seed with 0.5 mol% EGDMA) and R10 (seed with 1 mol% EGDMA). Using the seed prepared with 0.5 mol% of EGDMA, the composite particles were mostly spherical whereas for 1 mol%, non-spherical and multi-lobed particles were formed. In addition, the composition of the lobes deduced from the color of the images seems to be rich in MMA, which differs from what was observed in the particles without crosslinker. The gel data suggests the grafting of second stage polymer on the polymer of seeds. This was checked by M-DSC.

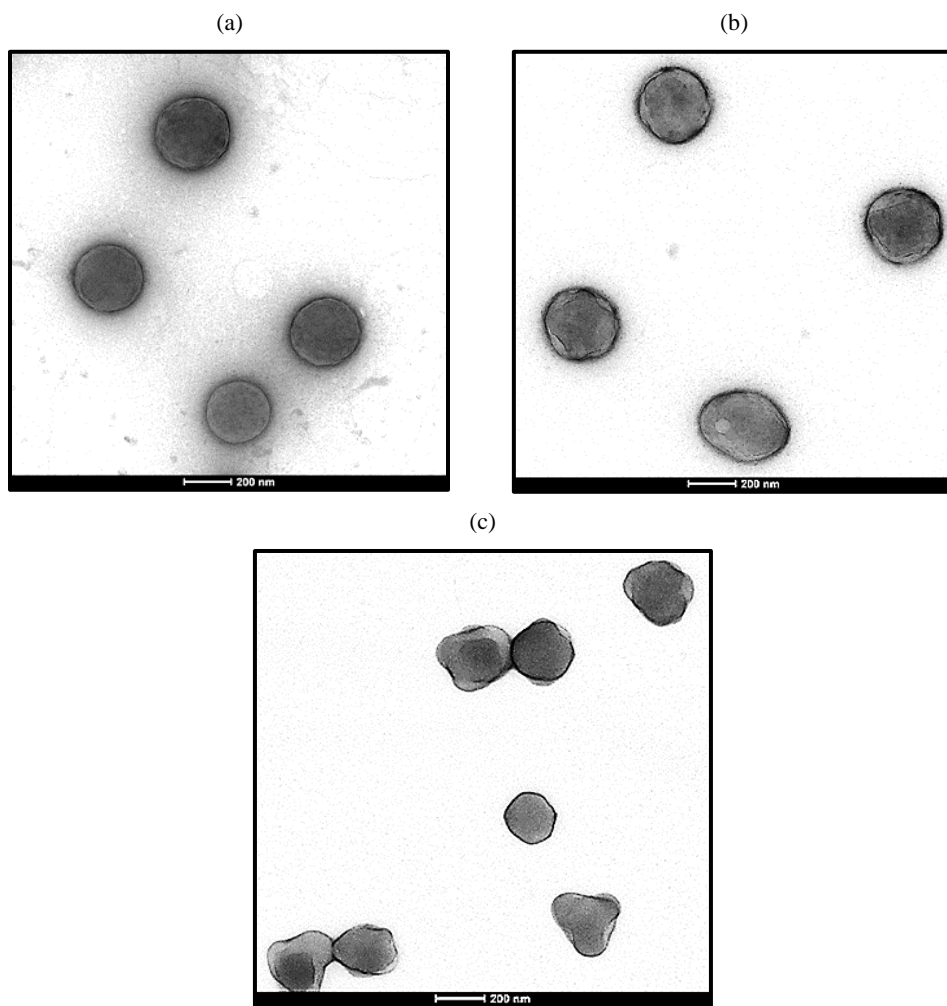


Figure 2. 30. Conventional TEM image of stained sample with  $\text{RuO}_4$  for 1 hour for (a) Run R7, (b) Run R9 and (c) Run R10. Images magnification is 25000.

Figure 2.34 shows the first and second heating cycles in M-DSC for Runs R7, R9 and R10. In the first heating, a single broad peak is observed indicating a large fraction



of intermixed material in all runs while the second heating shows two well-separated peaks circa the Tgs of seed and second stage.

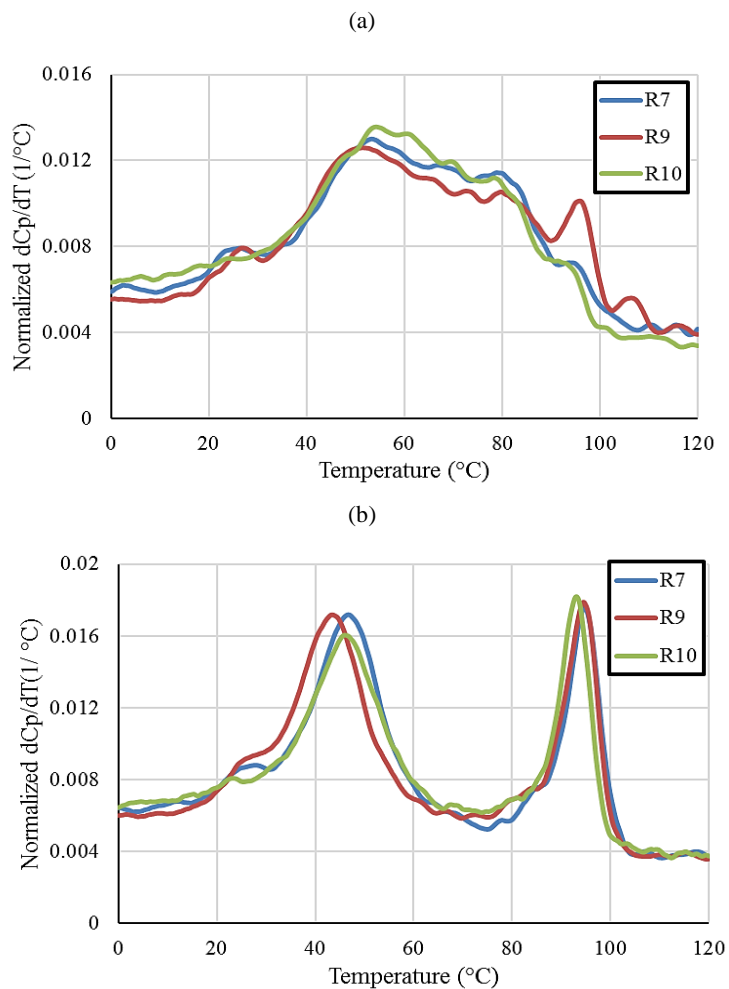


Figure 2. 31.  $dC_p/dT$  of cases with cross-linked seed with EGDMA and Run R7 (not cross-linked seed) from M-DSC: (a) first heating and (b) second heating. Data are smoothed by 3 °C.

A close look at the measured T<sub>g</sub>s for Run R9 and R10 in the second heating (Table 2.15) shows that the difference between T<sub>g</sub> of seed and second stage polymer is decreasing with the concentration of the EGDMA (51 °C for R9 and 47 °C for R10). The observation is likely due to some grafting of high T<sub>g</sub> second stage chains on the pendant double bond of the matrix. The slightly higher T<sub>g</sub> of seed and second stage polymer in Run R7 (non-crosslinked seed) compared to Run R9 and R10 is due to higher weight percent of MMA in the co-monomer compositions. However, the difference between the T<sub>g</sub> of seed and second stage polymer is 49 °C which is more than the difference in Run R10 (47 °C).

Table 2. 15. The measured T<sub>g</sub> of the seed and second state polymers in the studied Runs for the effect of crosslinking agent in the seed

Run		Monomer composition (w%)		T <sub>g, measured</sub> (°C)
R7	seed	MM/BA/AA/AM	64/34/1/1	46
	2 <sup>nd</sup> stage	S/BA/AA/AM	93/5/1/1	95
R9	seed	MM/BA/AA/AM	62/36/1/1 (+ 0.5 mol% EGDMA)	43
	2 <sup>nd</sup> stage	S/BA/AA/AM	92/6/1/1	94
R10	seed	MM/BA/AA/AM	62/36/1/1 (+ 1 mol% EGDMA)	46
	2 <sup>nd</sup> stage	S/BA/AA/AM	92/6/1/1	93
R12	seed	MM/BA/AA/AM	62/36/1/1 (+ 0.5 mol% AMA)	53
	2 <sup>nd</sup> stage	S/BA/AA/AM	92/6/1/1	92
R13	seed	MM/BA/AA/AM	62/36/1/1 (+ 1 mol% AMA)	59
	2 <sup>nd</sup> stage	S/BA/AA/AM	92/6/1/1	90

Figure 2.35 presents the morphologies for final latexes obtained in Runs R7 (non-crosslinked seed), R11 (seed with 0.1 mol% AMA), R12 (seed with 0.5 mol% AMA) and R13 (Seed with 1 mol% AMA). SEM images for Runs R12 and R13 are presented in Figure 2.36. TEM and SEM images show that by increasing the amount of AMA in the seed, the particles change from an almost spherical shape (Runs R7 and R11) to a multi-lobed one (Runs R12 and R13). The images suggest that the number of lobes increased with the increased concentration of AMA. A higher degree of crosslinking of the seed (even if the T<sub>g</sub> of the seed is below the reaction temperature) hinders the movement of the newly produced clusters that preferentially are produced near the surface of the particle. In addition, in Runs R11-R13 there was a substantial number of pendant double bonds in the matrix able to react with the second stage polymer increasing the compatibility of the phases. This is clearly seen in M-DSC results (Figure 2.37). Substantial intermixing of phases is detected for all runs in the first heating data and the observed peak becomes narrower increasing the amount of AMA in the seed, which implies on the more intermixing. The second heating demonstrated that grafting occurred in the presence of AMA and it increased with the concentration of AMA in the seed. For Run R7, the M-DSC of second heating showed two peaks with T<sub>g</sub> of 46 °C and 95 °C that corresponds to the T<sub>g</sub>s of the seed and second stage polymer. This means that the polymers are separated upon heating. However, the peaks

of Run R12 and R13 shifted so that they become closer as the concentration of AMA increased, which is a proof of higher grafting.

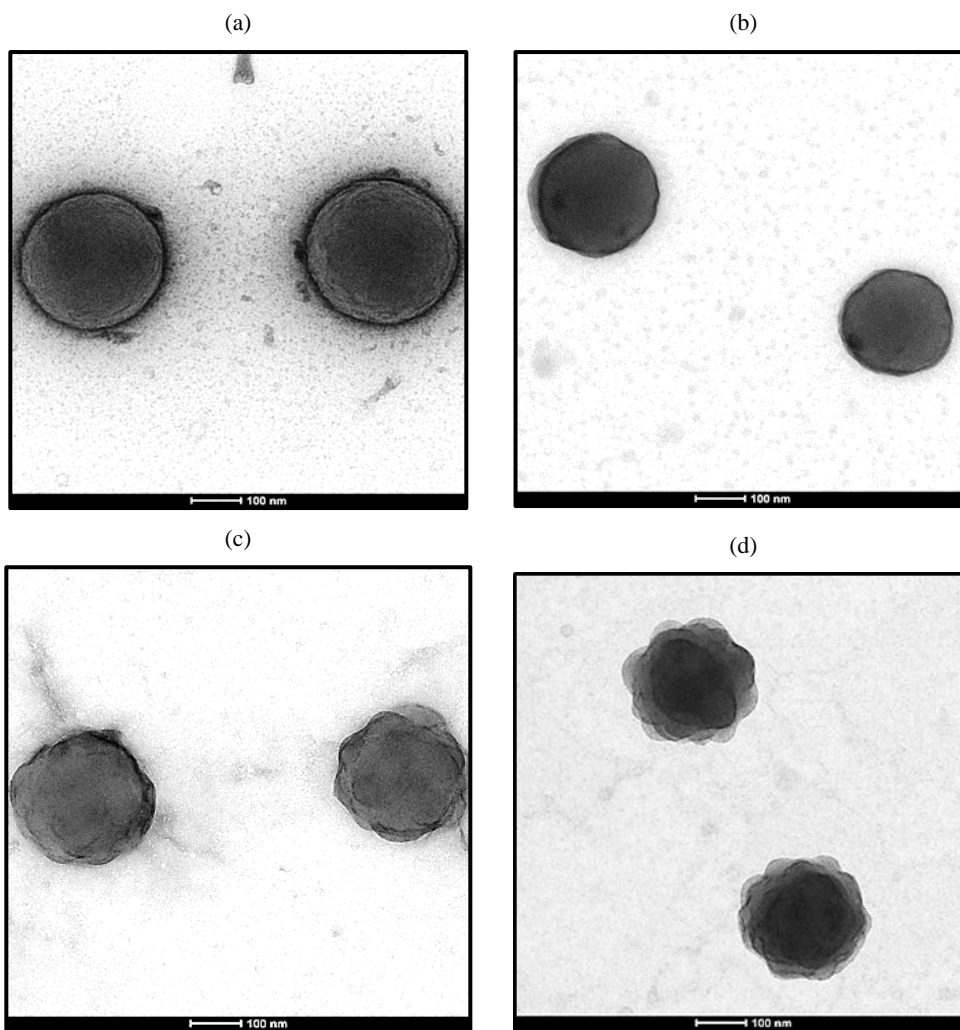
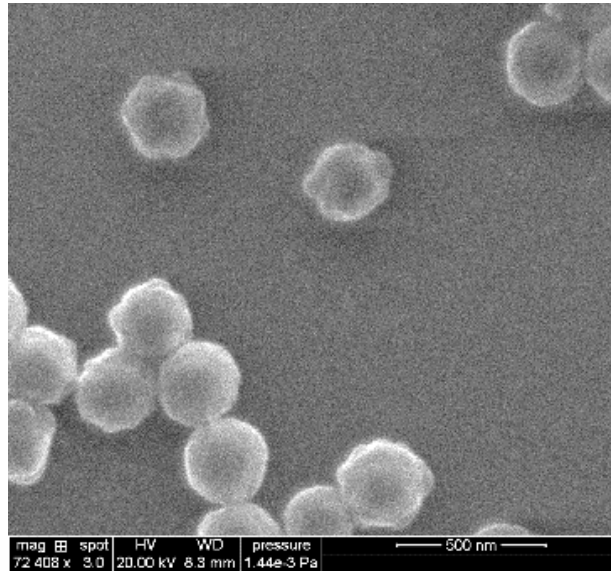


Figure 2. 32. Conventional TEM image of stained sample with  $\text{RuO}_4$  for 1 hour for (a) Run 7; (b) Run 11(c); Run 12 and (d) Run 13. Images magnification is 50000.

(a)



(b)

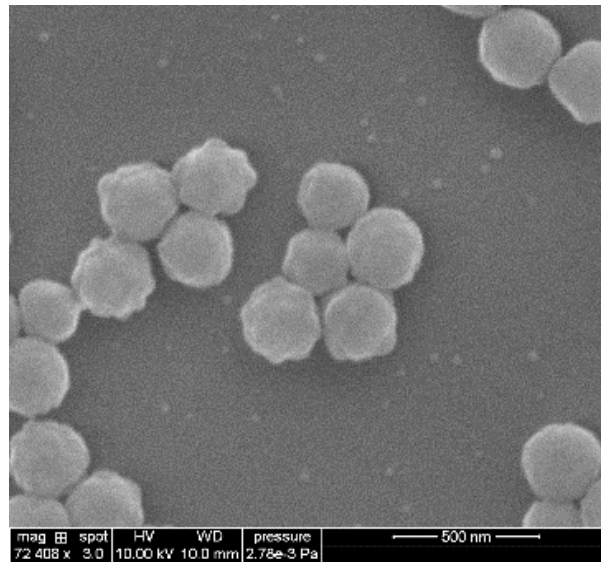


Figure 2. 33. SEM images of (a) Run R12 and (b) Run R13.

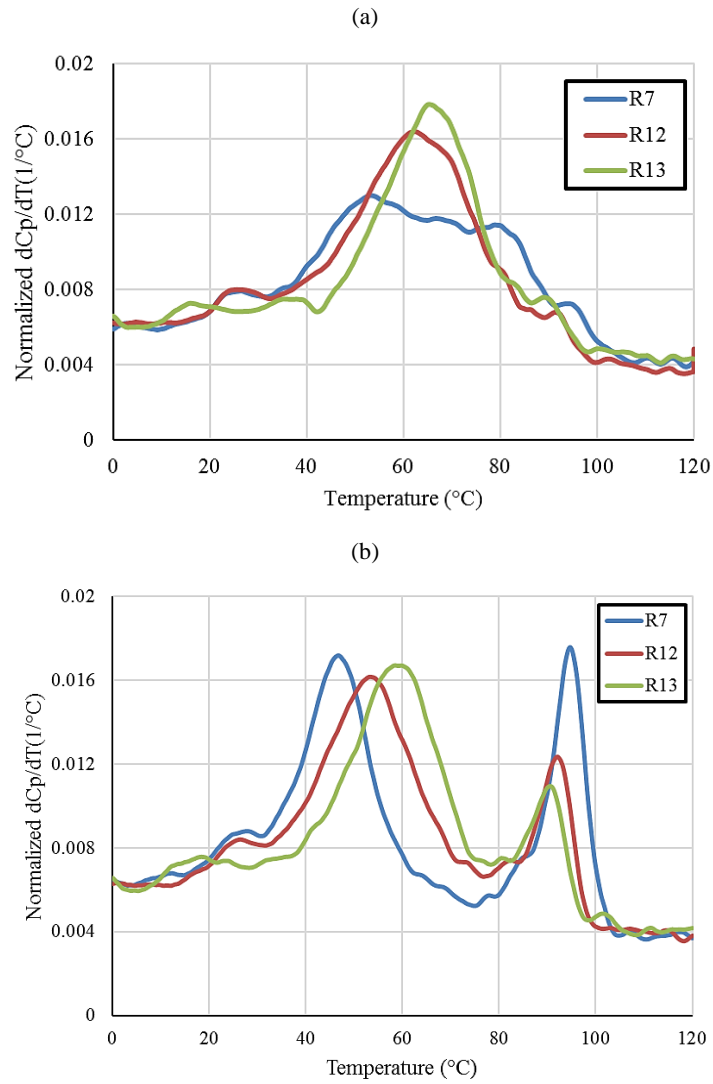


Figure 2. 34.  $dC_p/dT$  of cases with cross-linked seed with AMA and Run R7 (not cross-linked seed) from M-DSC: first heating (a); second heating (b). Data are smoothed by 3  $^\circ\text{C}$ .

### **2.3.7. Particle morphology changes by annealing at high temperature**

It was discussed in Section 2.3.5 that prolonging the reaction time at the reaction temperature (80 °C) did not induce a significant change in the morphology. To study the effect of time and temperature on the clusters migration, the latexes of Runs R1, Run R2 and Run R3 were heated in a sealed high-pressure metal reactor at 150 °C for 24 hours. The experiments were carried out to investigate whether facilitating of the migration of the clusters at high temperature during a long time will lead the clusters toward the equilibrium position. The latexes were diluted to 10 w% solids contents to prevent the coagulation during the heating in the reactor under high pressure conditions.

TEM images of stained samples with the vapor of RuO<sub>4</sub> for 1 hour are shown in Figure 2.38. In Run R1, the clusters migrated due to cluster-cluster van der Waals forces and coagulated into the bigger clusters. It happened due to facilitated movement of clusters at much higher temperature than the T<sub>g</sub> of both phases. However, the clusters did not move toward the equilibrium position at the center of the particle, because for these large clusters the repulsive water-cluster van der Waals forces were not enough to overcome the resistance of the matrix in the time available. In Runs R2 and R3, as the seeds were more soft compared to Run R1, the clusters penetrated more in particles. Although the particles were more round, they did not fully reach the inverted core-shell equilibrium morphology after heating.

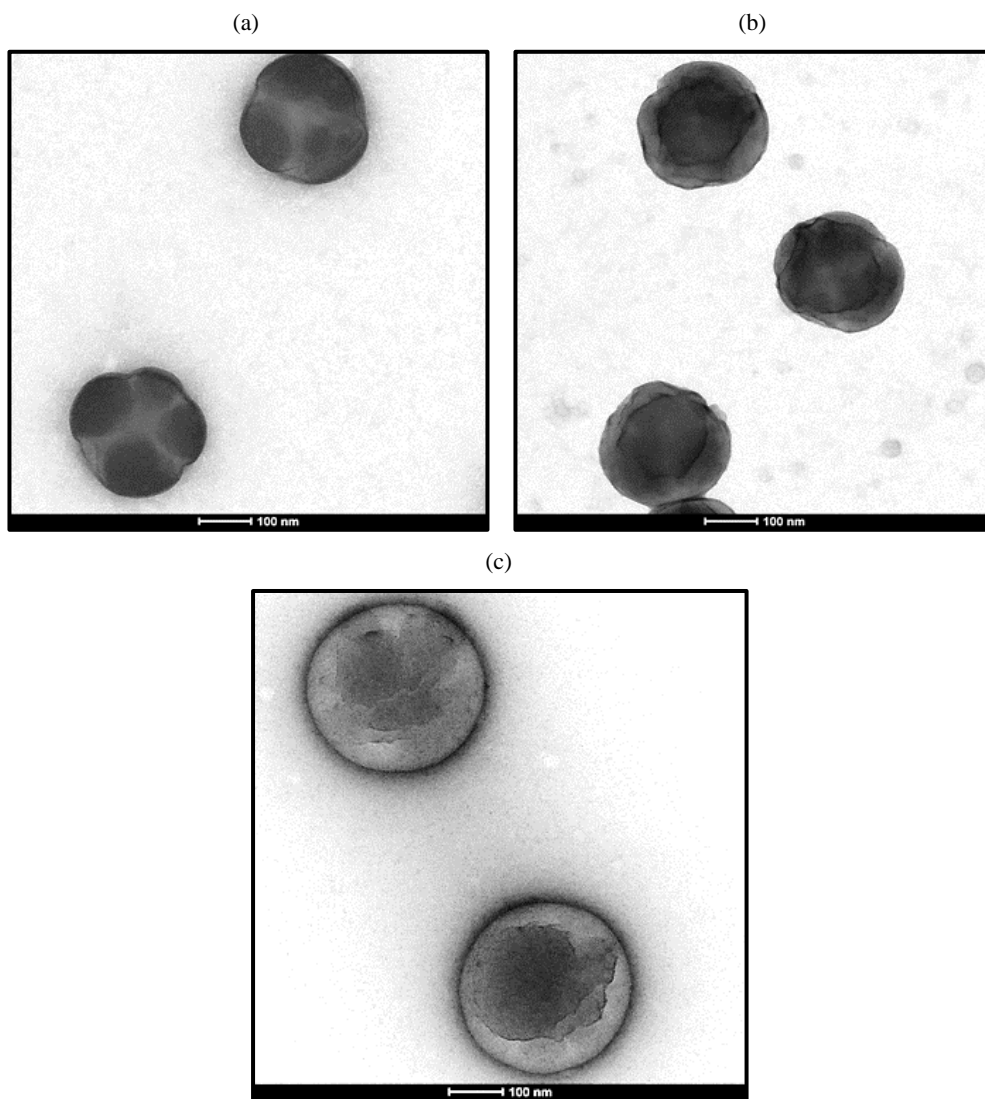


Figure 2. 35. TEM image of stained sample with vapor of  $\text{RuO}_4$  for 1 hour from diluted latex (SC=10 w%) heated at 150 °C for 24 hour for (a) Run R1, (b) Run R2 and (c) RunR3. Image magnification: 50000.



## 2.4. Conclusions

In this chapter, composite polymer-polymer particle latexes were synthesized in a two-step seeded semi-batch emulsion polymerization. More hydrophobic comonomers (Styrene/n-butyl acrylate) were polymerized in the second stage of polymerization using a more hydrophilic seed of poly (methyl methacrylate-co-n-butyl acrylate). According to thermodynamics, the equilibrium morphology for the studied cases was "inverted core-shell" while in all synthesized cases in this chapter; kinetically meta-stable morphologies were achieved due to determining effect of radical concentration profile on the development of the particle morphology. The effect of different reaction variables to alter the movement of synthesized clusters at the exterior zone of the particles toward to the equilibrium position in the center of the particles was studied.

In the studied cases for the effect of T<sub>g</sub> of seed on particle morphology, the evolution of the morphology was determined by Cryo TEM and TEM of samples stained with RuO<sub>4</sub>. It was found that in the second stage of the process many small lobes were formed initially at the surface of the seed. The size of the lobes increased and their number decreased by the combined effect of polymerization and coagulation. Molar mass distribution of the seed increased by increase in the amount of BA in the softer seed, likely because of increased probability of intermolecular chain transfer to

polymer and therefore led to higher viscosity of the matrix. It was observed that lowering the  $T_g$  of the seed was prominent on reducing the viscosity of the matrix than its increase due to higher molar mass of polymer chains and the softer the seed, the more penetration of the clusters in the particles was achieved. In agreement with the experimental observation, the mathematical model predicted more penetration of the clusters toward the equilibrium position at the center of the particle by softening the seed.

More spherical particles were synthesized changing the  $T_g$  of second stage polymer from lower than reaction temperature to above it using a soft seed. It was difficult to conclude the position of the clusters inside the particles from conventional TEM images while the mathematical model predicted less cluster penetration toward the center of the particle and smaller clusters were captured in the inner non-equilibrium positions. The differences in the model predictions were due to the fact that in the model, the  $T_{g\text{effective}}$  that affected the coefficients controlling the movement of clusters was calculated taking into account the contribution of the polymers from seed and second stage and that of the monomer. On the other hand, increasing the  $T_g$  of second stage polymer using a hard seed, spherical particles with small clusters was achieved instead of multi-lobed protruding one while the model predictions deviated from the experimental observations. Therefore, it seems that contrary to the assumed

dependency of movement and coagulation of the clusters on the Tg of seed and second stage polymer in the mathematical model, the size of the clusters was mainly determined by the Tg of the second stage polymer, whereas the migration towards the equilibrium morphology was controlled by the Tg of the matrix.

In the studied cases for the effect of reaction temperature in the second stage of polymerization, it was observed that at higher reaction temperature clusters coagulated more and the model predicted more cluster penetration toward the equilibrium position.

The nature of initiator in the second stage of polymerization, strongly affects the final morphology. Changing from water-soluble initiator to an oil soluble one, led to flatter radical concentration profile in the particles and the morphology changed from multi-lobed protruding morphology to the cluster occluded one. Although in that case, the inverted core-shell morphology was not achieved due to high viscosity of the matrix.

The effect of crosslinking of the seed on the morphology strongly depends on the reactivity of the double bonds in the crosslinking molecule compared to the used monomer. In a cross-linked seed, the elastic forces compete with van der Waals forces in the network of polymerization and result in the hindering of the cluster movements.

The predicted cluster distributions by mathematical model compared to experimental data revealed that the dependency of the parameters controlling the movement and coagulation of the clusters needed to be modified. Moreover, it was recognized that although the combination of different characterization techniques can provide reliable knowledge about the particle morphology development, it was difficult to reach the conclusion on the effect of process variables on the morphology changes in some cases. To overcome this limit, a new method for the precise characterization of particle morphology will be presented in Chapter 3.

## 2.5. Nomenclature

A: Adjustable parameter in the equation 2.23

B: Adjustable parameter in the equation 2.23

$a$  : Ratio of the coefficients of thermal expansion of the polymer below and above  $T_g$  of polymer

$D^\circ$ : Pre-exponential factor of monomer diffusion coefficient ( $\text{cm}^2/\text{s}$ )

$D_M$ : Diffusion constant of the monomer ( $\text{cm}^2/\text{s}$ )

$D_R$ : Diffusion constant of the radical ( $\text{cm}^2/\text{s}$ )

E: Activation energy of monomer diffusion coefficient (cal/mol)

$\frac{K_{11}}{\gamma}, \frac{K_{12}}{\gamma}$  : Free volume parameters ( $\text{cm}^3/\text{g.K}$ )

$K_{21}, K_{22}$ : Free volume parameters(K)

$k_d^{pol2}$ : Mass transfer rate coefficient of Polymer 2(mol/dm<sup>2</sup>.s)

$k_p$ : Propagation rate constant (L/mol.s)

$k_a$ : Rate coefficient for cluster coagulation (L/s)

$k_{abs}$ : Rate coefficient for radical entry (L/mol.s)

$k_{des}$ : Rate coefficient for radical exit (1/s)

$k_i$ : Rate coefficient for the redox reaction rate (L/mol.s)

$k_{mov1}$ : Rate coefficient movement to non-equilibrium interior position (1/s)

$k_{mov2}$ : Rate coefficient for movement to equilibrium position (L/s)

$k_n$ : Rate coefficient for nucleation (mol/s)

$\bar{k}_t$ : Effective termination rate coefficient (L/mol.s)

$m1(x)$ : Number of clusters with size  $x$  at non-equilibrium exterior positions

$m2(x)$ : Number of clusters with size  $x$  at non-equilibrium interior positions

$m_{av}$ : Average number of clusters at non-equilibrium positions per particle

$M_i$ : Monomer  $i$  (mol)

$n(x)$ : Number of clusters with size  $x$  at equilibrium positions

$n_{av}$ : Average number of clusters at equilibrium position per particle

$\bar{n}$ : Average number of radicals per particle

## Chapter 2

---

$N_p$  : Number of particles

$N_A$  : Avogadro's number

R: Gas constant (cal/K.mol)

$[R]_w$ : Radical concentration in water phase (mol/L)

$r_p$ : Radius of polymer particle (m)

$r_p^m(x)$ : Polymerization rate of non-equilibrium clusters with x monomer units (1/s)

$r_p^n(x)$ : Polymerization rate of equilibrium clusters with x monomer units (1/s)

$r_{nuc}$ : Rate of nucleation (1/s)

T : Reaction temperature (K)

$T_{g1}$ : Monomer glass transition temperature (K)

$T_{gp}$ : Polymer glass transition temperature (K)

$\hat{V}_1^*$ : Specific volume of monomer (cm<sup>3</sup>/g)

$\hat{V}_2^*$ : Specific volume of polymer (cm<sup>3</sup>/g)

$V_p$ : Total volume of polymer particles (L)

$\bar{V}_{pol2}$ : Molar volume of the Polymer 2 (L/mol)

$\bar{V}_{mi}$  : Molar volume of monomer  $i$  (L/mol)

$V_{pol1}$  :Volume of Polymer 1 (L)

$\frac{\bar{V}_f}{\gamma}$  : Solution free volume (cm<sup>3</sup>/g)

$w_1$ : Weight fraction of monomer

$w_2$ : Weight fraction of polymer

$x$ : Number of polymerized monomer units

$x_c$ : Initial size (number of monomeric units) of the clusters formed by phase separation

$x_{max}$ : Maximum size (number of monomeric units) of clusters

$\bar{x}_m$ : Average degree of polymerization of polymer 2

$\phi_2^H$ : Volume fraction of Polymer 2 in the matrix

$\phi_2^C$ : Volume fraction of the Polymer 2 in the matrix under equilibrium conditions

$\phi_P$ : Polymer fraction

$\alpha_{m,n}(x)$ : Probability of coagulation of clusters with sizes higher than the average value

$\beta$ : Parameter of the diffusion constant of radicals

$\mathcal{E}$ : Size parameter

## 2.6. References

- (1) Torza, S.; Mason, S. . Three-Phase Interactions in Shear and Electrical Fields. *J. Colloid Interface Sci.* **1970**, *33* (1), 67–83.
- (2) Chen, Y. C.; Dimonie, V.; El-Aasser, M. S. Effect of Interfacial Phenomena on the Development of Particle Morphology in a Polymer Latex System.

*Macromolecules* **1991**, *24* (13), 3779–3787.

- (3) Chen, Y. C.; Dimonie, V. L.; Shaffer, O. L.; El-Aasser, M. S. Development of Morphology in Latex Particles: The Interplay between Thermodynamic and Kinetic Parameters. *Polym. Int.* **1993**, *30* (2), 185–194.
- (4) Gonzalez-Ortiz, L. J.; Asua, J. M. Development of Particle Morphology in Emulsion Polymerization. 1. Cluster Dynamics. *Macromolecules* **1995**, *28* (9), 3135–3145.
- (5) Lee, D. I.; Ishikawa, T. The Formation of “Inverted” Core-Shell Latexes. *J. Polym. Sci. Polym. Chem. Ed.* **1983**, *21* (1), 147–154.
- (6) Sundberg, D. C.; Casassa, A. P.; Pantazopoulos, J.; Muscato, M. R.; Kronberg, B.; Berg, J. Morphology Development of Polymeric Microparticles in Aqueous Dispersions. I. Thermodynamic Considerations. *J. Appl. Polym. Sci.* **1990**, *41* (7–8), 1425–1442.
- (7) Jönsson, J. E.; Hassander, H.; Törnell, B. Polymerization Conditions and the Development of a Core-Shell Morphology in PMMA/PS Latex Particles. 1. Influence of Initiator Properties and Mode of Monomer Addition. *Macromolecules* **1994**, *27* (7), 1932–1937.
- (8) Herrera, V.; Palmillas, Z.; Pirri, R.; Reyes, Y.; Leiza, J. R.; Asua, J. M. Morphology of Three-Phase PS/PBA Composite Latex Particles Containing in Situ Produced Block Copolymers. *Macromolecules* **2010**, *43* (3), 1356–1363.
- (9) Okubo, M.; Katsuta, Y.; Matsumoto, T. Rupture of Anomalous Composite Particles Prepared by Seeded Emulsion Polymerization in Aging Period. *J. Polym. Sci. Polym. Lett. Ed.* **1980**, *18* (7), 481–486.
- (10) Okubo, M.; Nakagawa, T. Formation of Multihollow Structures in Crosslinked Composite Polymer Particles. *Colloid Polym. Sci.* **1994**, *272* (5), 530–535.
- (11) Sundberg, D. C.; Durant, Y. G. Latex Particle Morphology, Fundamental Aspects: A Review. *Polym. React. Eng.* **2003**, *11* (3), 379–432.
- (12) Deng, W.; Li, R.; Zhang, M.; Gong, L.; Kan, C. Influences of MAA on the Porous Morphology of P(St-MAA) Latex Particles Produced by Batch Soap-Free Emulsion Polymerization Followed by Stepwise Alkali/Acid Post-Treatment. *J. Colloid Interface Sci.* **2010**, *349* (1), 122–126.



- (13) Li, B.; Xu, Y.; Wang, M.; Ge, X. Morphological Control of Multihollow Polymer Latex Particles through a Controlled Phase Separation in the Seeded Emulsion Polymerization. *Langmuir* **2013**, *29* (48), 14787–14794.
- (14) Zhai, W.; Wang, B.; Wang, Y.; He, Y. F.; Song, P.; Wang, R. M. An Efficient Strategy for Preparation of Polymeric Janus Particles with Controllable Morphologies and Emulsifiabilities. *Colloids Surfaces A Physicochem. Eng. Asp.* **2016**, *503*, 94–100.
- (15) Jasinski, F.; Teo, V.; Kuchel, R. P.; Mballa Mballa, M.; Thickett, S. C.; Brinkhuis, R. H. G.; Weaver, W.; Zetterlund, P. B. Synthesis and Characterisation of Gradient Polymeric Nanoparticles. *Polym. Chem.* **2017**, *8*, 495–499.
- (16) Jasinski, F.; Teo, V. L.; Kuchel, R. P.; Mballa Mballa, M.; Thickett, S. C.; Brinkhuis, R. H. G.; Weaver, W.; Zetterlund, P. B. Core–Shell and Gradient Morphology Polymer Particles Analyzed by X- Ray Photoelectron Spectroscopy: Effect of Monomer Feed Order. *J. Polym. Sci. Part A Polym. Chem.* **2017**, *55* (15), 2513–2526.
- (17) Hosseini, A.; Bouaswaig, A. E.; Engell, S. Novel Approaches to Improve the Particle Size Distribution Prediction of a Classical Emulsion Polymerization Model. *Chem. Eng. Sci.* **2013**, *88*, 108–120.
- (18) Pladis, P.; Alexopoulos, A. H.; Kiparissides, C. Mathematical Modeling and Simulation of Vinylidene Fluoride Emulsion Polymerization. *Ind. Eng. Chem. Res.* **2014**, *53* (18), 7352–7364.
- (19) Calvo, I.; Hester, K.; Leiza, J. R.; Asua, J. M. Mathematical Modeling of Carboxylated SB Latexes. *Macromol. React. Eng.* **2014**, *8* (4), 329–346.
- (20) Hlalele, L.; D’hooge, D. R.; Dürr, C. J.; Kaiser, A.; Brandau, S.; Barner-Kowollik, C. RAFT-Mediated *Ab Initio* Emulsion Copolymerization of 1,3-Butadiene with Acrylonitrile. *Macromolecules* **2014**, *47* (9), 2820–2829.
- (21) Hamzehlou, S.; Ballard, N.; Carretero, P.; Paulis, M.; Asua, J. M.; Reyes, Y.; Leiza, J. R. Mechanistic Investigation of the Simultaneous Addition and Free-Radical Polymerization in Batch Miniemulsion Droplets: Monte Carlo Simulation versus Experimental Data in Polyurethane/Acrylic Systems. *Polymer*. **2014**, *55* (19), 4801–4811.

- (22) Capeletto, C. A.; Costa, C.; Sayer, C.; Araújo, P. H. H. Mathematical Modeling of Molecular Weight Distribution in Miniemulsion Polymerization with Oil-Soluble Initiator. *AIChE J.* **2017**, *63* (6), 2128–2140.
- (23) Mills, M. F.; Gilbert, R. G.; Napper, D. H. Effect of Polymerization Kinetics on Particle Morphology in Heterogeneous Systems. *Macromolecules* **1990**, *23* (19), 4247–4257.
- (24) Stubbs, J.; Karlsson, O.; Jönsson, J. E.; Sundberg, E.; Durant, Y.; Sundberg, D. Non-Equilibrium Particle Morphology Development in Seeded Emulsion Polymerization. 1: Penetration of Monomer and Radicals as a Function of Monomer Feed Rate during Second Stage Polymerization. *Colloids Surfaces A Physicochem. Eng. Asp.* **1999**, *153* (1–3), 255–270.
- (25) Grancio, M. R.; Williams, D. J. The Morphology of the Monomer-Polymer Particle in Styrene Emulsion Polymerization. *J. Polym. Sci. Part A-1 Polym. Chem.* **1970**, *8* (9), 2617–2629.
- (26) Chern, C.-S.; Poehlein, G. W. Polymerization in Nonuniform Latex Particles: Distribution of Free Radicals. *J. Polym. Sci. Part A Polym. Chem.* **1987**, *25* (2), 617–635.
- (27) Hamzehlou, S.; Leiza, J. R.; Asua, J. M. A New Approach for Mathematical Modeling of the Dynamic Development of Particle Morphology. *Chem. Eng. J.* **2016**, *304*, 655–666.
- (28) Fox, T. G. Influence of Diluent and of Copolymer Composition on the Glass Temperature of a Polymer System. *Bull. Am. Phys. Soc.* **1956**, *1*, 123–132.
- (29) Plessis, C.; Arzamendi, G.; Leiza, J. R.; Schoonbrood, H. A. S.; Charmot, D.; Asua, J. M. Seeded Semibatch Emulsion Polymerization of N-Butyl Acrylate. Kinetics and Structural Properties. *Macromolecules* **2000**, *33* (14), 5041–5047.
- (30) Elizalde, O.; Arzamendi, G.; Leiza, J. R.; Asua, J. M. Seeded Semibatch Emulsion Copolymerization of *n*-Butyl Acrylate and Methyl Methacrylate. *Ind. Eng. Chem. Res.* **2004**, *43* (23), 7401–7409.
- (31) González, I.; Asua, J. M.; Leiza, J. R. The Role of Methyl Methacrylate on Branching and Gel Formation in the Emulsion Copolymerization of BA/MMA. *Polymer*. **2007**, *48* (9), 2542–2547.

- (32) Ballard, N.; Hamzehlou, S.; Asua, J. M. Intermolecular Transfer to Polymer in the Radical Polymerization of *n*-Butyl Acrylate. *Macromolecules* **2016**, *49* (15), 5418–5426.
- (33) Ballard, N.; Asua, J. M. Radical Polymerization of Acrylic Monomers: An Overview. *Prog. Polym. Sci.* **2018**, *79*, 40–60.
- (34) Bueche, F. Rate and Pressure Effects in Polymers and Other GlassForming Substances. *J. Chem. Phys.* **1962**, *36* (11), 2940.
- (35) Vonka, M.; Soos, M.; Storti, G. Viscosity and Drop Size Evolution During Suspension Polymerization. *AIChE J.* **2016**, *62* (12), 4229–4239.
- (36) *Polymer Handbook*, Forth ed.; Brandrup, J., Immergut, E. H., Grulke, E. A., Eds.; Wiley-Interscience, 2004.
- (37) Finlayson, B. A.; Biegler, L. T.; Grossmann, I. E. *Mathematics in Chemical Engineering*; Wiley-VCH Verlag GmbH & Co. KGaA, 2006.
- (38) Faldi, A.; Tirrell, M.; Lodge, T. P.; Meerwall, E. Von. Monomer Diffusion and the Kinetics of Methyl Methacrylate Radical Polymerization at Intermediate to High Conversion. *Macromolecules* **1994**, *27*, 4184–4192.
- (39) Smith, G. B.; Russell, G. T.; Heuts, J. P. A. Termination in Dilute-Solution Free-Radical Polymerization: A Composite Model. *Macromol. Theory Simulations* **2003**, *12* (5), 299–314.
- (40) Tripathi, A. K.; Tsavalas, J. G.; Sundberg, D. C. Quantitative Measurements of the Extent of Phase Separation during and after Polymerization in Polymer Composites Using DSC. *Thermochim. Acta* **2013**, *568*, 20–30.
- (41) Li, B.-G.; Brooks, B. W. Prediction of the Average Number of Radicals per Particle for Emulsion Polymerization. *J. Polym. Sci. Part A Polym. Chem.* **1993**, *31* (9), 2397–2402.
- (42) van Krevelen, D. W.; te Nijenhuis, K. *Properties of Polymers: Their Correlation with Chemical Structure; Their Numerical Estimation and Prediction from Additive Group Contributions*, 4th ed.; Elsevier Ltd, Oxford, UK, 2009.
- (43) Asua, J. M.; Beuermann, S.; Buback, M.; Castignolles, P.; Charleux, B.; Gilbert, R. G.; Hutchinson, R. A.; Leiza, J. R.; Nikitin, A. N.; Vairon, J.-P.; et al.

- Critically Evaluated Rate Coefficients for Free-Radical Polymerization, 5 Propagation Rate Coefficient for Butyl Acrylate. *Macromol. Chem. Phys.* **2004**, 205 (16), 2151–2160.
- (44) Beuermann, S.; Buback, M. Rate Coefficients of Free-Radical Polymerization Deduced from Pulsed Laser Experiments. *Prog. Polym. Sci.* **2002**, 27 (2), 191–254.
- (45) Dube, M. A.; Penlidis, A.; O'Driscoll, K. F. A Kinetic Investigation of Styrene/Butyl Acrylate Copolymerization. *Can. J. Chem. Eng.* **1990**, 68, 974–987.
- (46) Agirre, A.; Calvo, I.; Weitzel, H. P.; Hergeth, W. D.; Asua, J. M. Semicontinuous Emulsion Co-Polymerization of Vinyl Acetate and VeoVa10. *Ind. Eng. Chem. Res.* **2014**, 53 (22), 9282–9295.
- (47) Limousin, E.; Ballard, N.; Asua, J. M. Soft Core-Hard Shell Latex Particles for Mechanically Strong VOC-Free Polymer Films. *J. Appl. Polym. Sci.* **2019**, 136, 47608.
- (48) Islam, O.; Dragnevski, K. I.; Siviour, C. R. On Some Aspects of Latex Drying – ESEM Observations. *Prog. Org. Coatings* **2012**, 75 (4), 444–448.
- (49) Bouvier-Fontes, L.; Pirri, R.; Asua, J. M.; Leiza, J. R. Seeded Semicontinuous Emulsion Copolymerization of Butyl Acrylate with Cross-Linkers. *Macromolecules* **2005**, 38 (4), 1164–1171.
- (50) Tobita, H.; Yoshihara, Y. Microgel Formation in Emulsion Copolymerization .2. Seeded Polymerization. *J. Polym. Sci. Part B-Polymer Phys.* **1996**, 34 (8), 1415–1422.
- (51) Bouvier-Fontes, L.; Pirri, R.; Asua, J. M.; Leiza, J. R. Cross-Linking Emulsion Copolymerization of Butyl Acrylate with Diallyl Maleate. *J. Polym. Sci. Part A Polym. Chem.* **2005**, 43 (20), 4684–4694.

## **Chapter 3. Coupling HAADF-STEM tomography and image reconstruction for the precise characterization of particle morphology**

### **3.1. Introduction**

As it was discussed in Section 1.4, an accurate characterization of the morphology of composite polymer particles is challenging and involves determining the shape, surface composition and internal structure of the particles. Stubbs and Sundberg<sup>1</sup> concluded in a relatively old (year 2005) round robin study that there was no single technique that can give an unambiguous determination of the morphology of the particles and several techniques should be combined to get a more detailed information on the morphology of the polymer particles. On the other hand, uncertainties due to sample preparation or damage during the measurement can lead to erroneous and different interpretation of the particle morphology. Despite of all efforts devoted to the development of characterization techniques for particle morphology assessment, the work presented in Chapter 2 shows that still the available techniques do not provide

quantitative information about the distribution of the phases in the particles. Therefore, this chapter presents a characterization method that can overcome the limitations of the previous techniques providing a detailed and quantitative information about the distribution of the phases in the particles.

Electron tomography (ET) is a technique that retrieves 3D structural information from a tilt series of 2D projections. Two different nanoscale imaging techniques typically used in the physical sciences, transmission electron microscopy (TEM) and scanning transmission electron microscopy (STEM), utilize different illumination modes, which result in very different contrast mechanisms. Both techniques can be used for electron tomography.<sup>2</sup> TEM tomography was used to analyze the morphology of organic/inorganic nanocomposites in bulk state<sup>3,4</sup> and hybrid polymer/inorganic particle latexes.<sup>5,6</sup> It is claimed that STEM that uses a lower operation energy comparing to TEM is more suitable for analyzing the soft polymer phases which are beam-sensitive.<sup>7</sup> High-angle annular dark field (HAADF)-STEM tomography formerly used to determine the 3D structure of inorganic specimens<sup>8</sup> and started to find its application in the characterization of complex polymer systems. Thus, it has been used to determine the distributions of nanoparticles in inhomogeneous matrices,<sup>9</sup> to study the spatial organization of thin film of various polymer systems including rubber blend

and semicrystalline polyethylenes<sup>10</sup> and to image networks of nanoparticles within polymer–nanoparticle blends in photovoltaic devices.<sup>11</sup>

A novel approach for quantitative characterization of polymer-polymer particle morphology in 3D by means of electron tomography using HAADF-STEM is presented in this chapter. The fiducial-less tilt-series alignment and tomographic reconstructions with weighted back-projection (WBP) and simultaneous iterative reconstruction (SIRT) techniques<sup>12</sup> were done using in-house developed software. This novel characterization technique was then used to quantitatively characterize the particle morphology of selected latexes synthesized and characterized with the conventional TEM in Chapter 2. The precise characterization allowed getting unexpected insights about the mechanisms involved in the development of particle morphology during the second stage of polymerization. Further improvements on the mathematical model presented in Chapter 2 were achieved based on the information provided by this technique and the results of model prediction using the upgraded version of model are also presented in this chapter. In addition, the upgraded model was used to analyze the effect of Tg of the second stage polymer that could not be accounted for by the model used in Chapter 2.

### 3.2. Synthesis of composite polymer particle latexes

The material and the procedure used in the synthesis of composite polymer particle latexes are given in Sections 2.2.1 and 2.2.2, respectively. The latexes characterized in this chapter are summarized in Table 3.1.

Table 3. 1.The summary of latexes characterized in Chapter 3.

Run	Seed monomers	T <sub>g, measured</sub> (°C)	2 <sup>nd</sup> stage monomer	T <sub>g, measured</sub> (°C)	T <sub>reaction</sub> (°C)	Initiator
R1	MMA/BA/AA/AM	86	S/BA/AA/AM	49	80	TBHP+ACBS
R2	MMA/BA/AA/AM	63	S/BA/AA/AM	46	80	TBHP+ACBS
R3	MMA/BA/AA/AM	46	S/BA/AA/AM	46	80	TBHP+ACBS
R5	MMA/BA/AA/AM	90	S/BA/AA/AM	90	80	TBHP+ACBS
A1	MMA/BA/AA/AM	86	S/BA/AA/AM	48	80	AIBN

### 3.3. Characterization of the particle morphology

Three-dimensional (3D) particle morphology of latexes summarized in Table 3.1 was characterized by HAADF-STEM electron tomography technique using Titan 60-300 electron microscope (FEI Company, Netherlands) operated at acceleration voltage of 300 kV. HAADF-STEM imaging mode provides the contrast that is strongly dependent on the atomic number ( $\sim Z^2$ ) and thus stained polymer phase looks much brighter at HAADF-STEM images.



Tilt series were acquired automatically at angles between  $-74^\circ$  and  $+74^\circ$  at  $2^\circ$  tilt step. To reduce beam-damage effects, reasonably low-dose conditions were set up, and some sensitive samples were imaged at cryogenic temperature using a cryotomographic sample holder (Gatan, model 914) cooled by liquid nitrogen. Images were taken with a FEI Tomography 4.0 software in automatic mode; dwell time for acquisition was set to 20  $\mu\text{s}$  for the images of  $1024 \times 1024$  pixels.

The fiducial-less tilt-series alignment and tomographic reconstructions with weighted back-projection (WBP) and simultaneous iterative reconstruction (SIRT) techniques were done using in-house DigitalMicrograph (Gatan, USA) scripts. Reconstructed volumes had a voxel size of  $\sim 2 \times 2 \times 2 \text{ nm}^3$ . For the stained phase separation, the intensity-based segmentation (local thresholding criteria) was used. Depending on the intensity of pixels, they were assumed as belonging to the feature of interest which is stained phase (bright) or belonging to the matrix (dark). Segmentation of different phases in the particles, subsequent 3-D rendering, and statistical calculations were done using FEI Avizo 8.1 software.

Conventional TEM was also used to highlight the differences between the two techniques. Transmission electron microscopy (TEM) was carried out with Tecnai<sup>TM</sup> G2 electron microscope (FEI Company, Netherlands) at 200 kV. One droplet

of diluted latex with deionized water with 0.05 wt% solids content was placed on a carbon coated copper grid and dried at ambient temperature. TEM samples were stained with  $\text{RuO}_4$  vapor for 1 hour to increase the contrast of styrene containing component. To obtain cross-sections, dried latexes at ambient temperature were embedded in epoxy resin and were cured at room temperature for 12 hours. The crosscut slices with 70 nm thickness prepared by microtome were collected on carbon coated copper grids and stained with vapor of  $\text{RuO}_4$  for 1 hour to increase the image contrast.

### **3.4. Results and discussion**

Figure 3.1 presents a series of slices of the reconstructed composite polymer for Run R1 (Table 3.1). Note that in HAADF STEM, the styrene rich phase appears brighter than the methyl methacrylate rich phase as discussed earlier. It can be clearly seen that the polymer particle presents styrene-rich lobes close to the surface of the particle. In addition, smaller clusters present in the interior zone of the polymer particles.

Figure 3.2 shows the reconstructed 3D image of the polymer particle and matrix and clusters. Each PS-rich cluster is shown with a different color to simplify their visual recognition. Segmentation confirms that the latex particle consists of big polystyrene lobes at the surface of the particle and a number of small clusters in the interior region

of the particle. Figure 3.2 (b) shows the clusters at the surface and in the interior region in separate images.

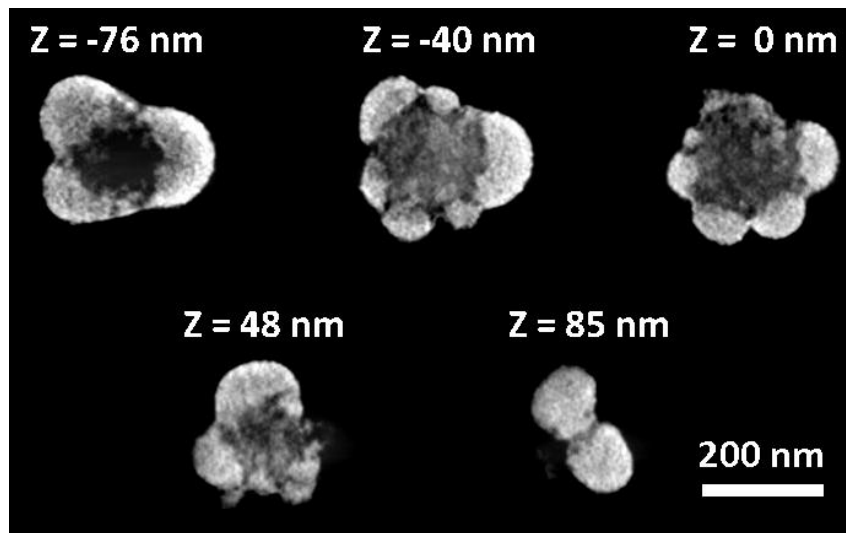


Figure 3. 1. Tomographic cross-sections of Run R1 from upper surface of the sample to the bottom obtained from HAADF-STEM.

For the sake of comparison, the morphologies determined by TEM for Run R1 are presented in Figure 3.3. It can be seen that although they clearly show the presence of clusters near the surface of the particle, the observed morphology is just the 2D projection of the actual morphology in which the location of these clusters inside the particles is difficult to determine and the statistical evaluation is hardly possible even with the cross-sections of the particles (Figure 3.3 b).

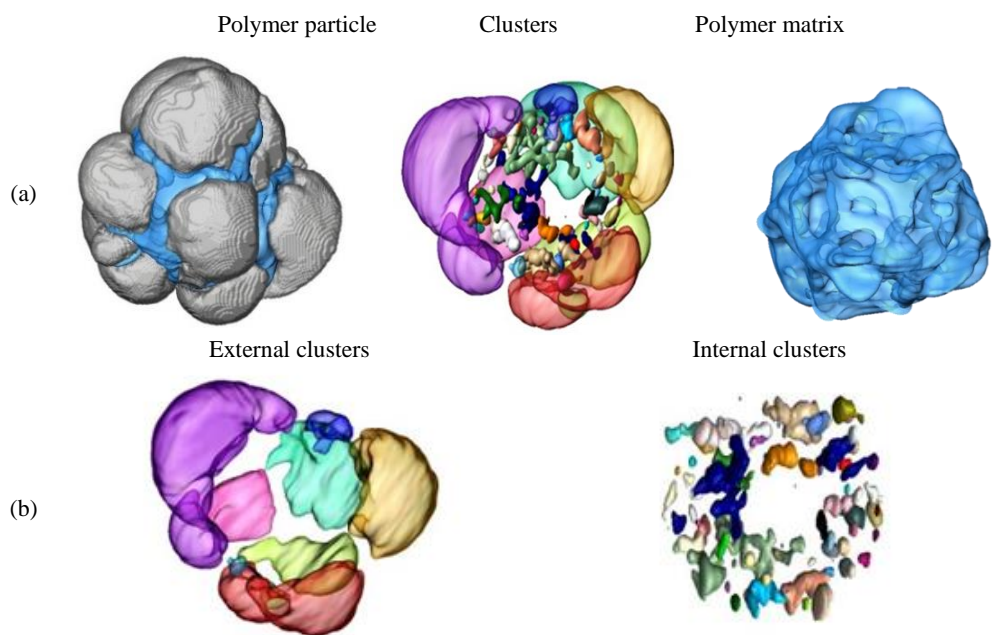


Figure 3. 2. Reconstructed 3D images of polymer particle of Run R1. Segmentation of the clusters is made on the base of local threshold criteria.

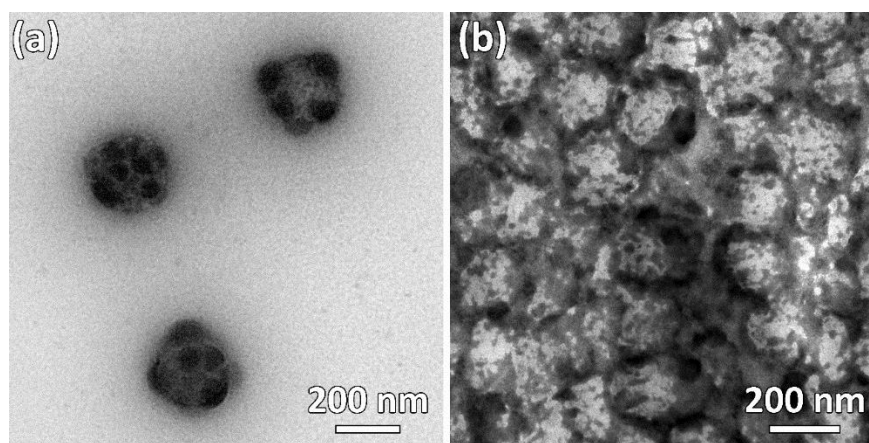


Figure 3. 3. TEM analysis of Run R1: (a) TEM of sample stained with RuO<sub>4</sub>, (b) RuO<sub>4</sub> stained crosscut image. The scale bar is 200 nm (image magnification: 25000).

The results in Figure 3.2 show that the equilibrium “inverted core-shell” morphology is not attained. The most likely reason of the large fraction of styrene-rich clusters near the surface of the particle is the formation of a profile of radicals in the particle.<sup>13</sup> The redox initiator used in the second stage polymerization was TBHP-ACBS that is known to form hydrophobic tertbutoxyl radicals in the aqueous phase. These radicals can directly enter into the polymer particles, where they rapidly react with the monomer present there, forming growing polymer chains that cannot further diffuse towards the center of the particle due to the high viscosity of the matrix. The later is the result of the combination of the high Tg of the seed polymer (Tg = 86 °C), high molar mass of the forming chains and low concentration of the monomer in the particles (starved process with an average instantaneous conversion of 94% during the monomer feeding time in the second stage of polymerization).

#### **3.4.1. Quantitative characterization of the effect of the process variables on particle morphology**

The potential of the method described above was exploited in the quantitative characterization of selected latexes produced varying process conditions that showed a substantial effect on the particle morphology as presented in Chapter 2. In Runs R1, R2 and R3, the co-monomer composition used in the seed (MMA/BA) was changed to reduce the Tg of seed from 86 °C in Run R1 to 63 °C and 46 °C in Runs R2 and R3,

respectively (Table 3.1) . As discussed in Chapter 2, the aim of these experiments was to facilitate the movement of the styrene-rich clusters towards the center of the particle (equilibrium morphology).

Figure 3.4 shows the 3D reconstructed images of the Runs R1, R2 and R3 as well as conventional TEM images of the stained samples. It can be seen that by decreasing the glass transition temperature of the matrix, from 86°C to 63°C and 46°C, the whole particle became more spherical and the clusters penetrated more toward the center. This change in the particle morphology was due to the lower internal viscosity of the matrix in the softer systems, which led to an easier movement of the clusters toward the equilibrium morphology. In addition, a less sharp profile of radicals is expected in softer matrices because the diffusion of the growing chains was less hindered.

The detailed particle morphologies in Figure 3.4 were further analyzed by 3D statistics and independent size distributions of the inner clusters and outside lobes were obtained. Figure 3.5 presents the cluster size distributions for Runs R1, R2 and R3 for internal and external clusters, which is the type of information that is comparable with the predictions of the model. Unfortunately, because HAADF-STEM tomography is very time consuming only one particle per sample was analyzed, and therefore the distributions were not statistically significant. Nevertheless, Figure 3.5 shows that as

the hardness of the seed polymer decreased, the size of the external clusters increased because cluster aggregation became easier.

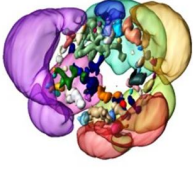
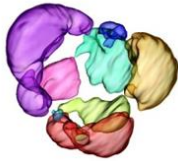

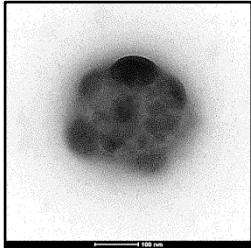
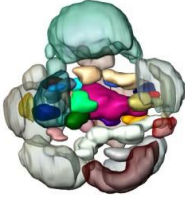


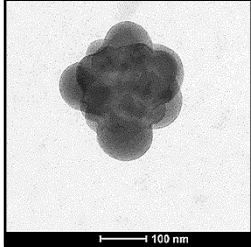
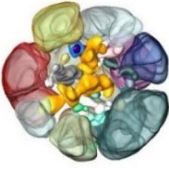

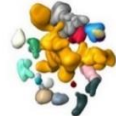
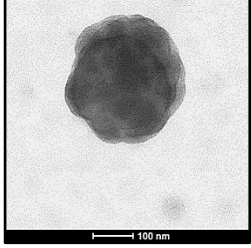
Run	Reconstructed image	External clusters	Internal clusters	TEM
R1				
R2				
R3				

Figure 3. 4. Reconstructed 3D images of polymer particle of Run R1, R2 and R3 by tomographic analysis of samples by HAADF-STEM and the corresponding TEM images (the scale is 100 nm).

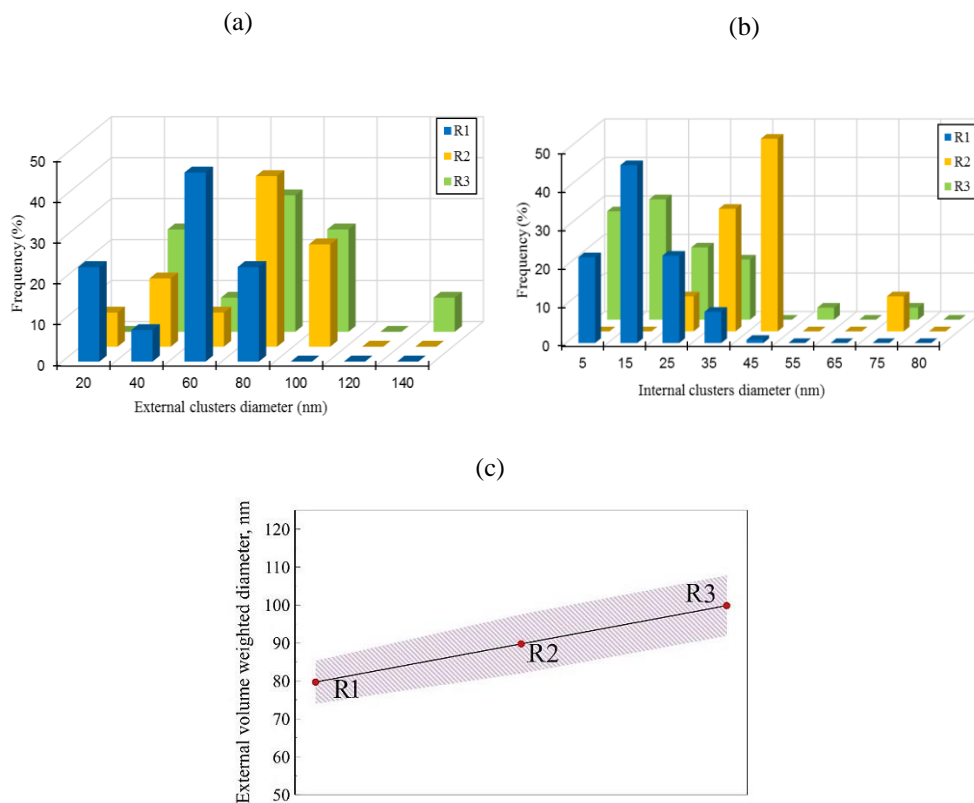


Figure 3. 5. Cluster size distributions for latexes of Runs R1, R2 and R3: (a) sizes of external clusters calculated as diameters of equivalent sphere for the experimentally measured volumes; (b) sizes of internal clusters, calculated in the same way; (c) volume weighted average size of external clusters vs sample cases - the softness of the matrix increases in a row  $R1 < R2 < R3$ .

A close look at the morphologies of Runs R2 and R3 reveals an unexpected result. According to the existing views, the morphology of the softer system (Run R3) is expected to be closer to the equilibrium morphology (inverted core-shell with the



styrene-rich polymer in the core of the particle,) than that of harder R2. However, this is not the case and there is no visible difference in clusters distribution in the latex particle volume, besides more pronounced lobes on a harder seed polymer in Run R2. In order to verify the difference numerically, the distribution of the amount of the second stage polymer along the radius  $r$  of the particles was calculated as:

$$F(r) = \frac{\sum_{r \leq \sqrt{x^2+y^2+z^2} < r+\Delta r} P(x, y, z)}{\sum_{0 \leq \sqrt{x^2+y^2+z^2} < \infty} P(x, y, z)} \quad (3.1)$$

where  $P=1$  in the voxels of the clusters and  $P=0$  in the voxels of the matrix,  $\Delta r$  was selected to be equal to the linear size of one voxel. Figure 3.6 presents the radial distribution of the second stage polymer for Runs R1-R3. In this figure, the reference radius for normalization was that of the matrix surface. It can be seen that against the expectations, the fraction of polymer located in the interior of the particle ( $r < 0.6$ ) was maximum for Run R2. Implicit in this expectation is that clusters migrate towards the center of the particle due to repulsive van der Waals forces with the aqueous phase.<sup>14</sup> However, whereas this was the case for the big clusters in the outer part of the particle and therefore they became more embedded in the particle as the Tg of the seed was lower, the situation of the smaller inner clusters was different. These clusters were partially isolated from the aqueous phase by big clusters of hydrophobic

---

styrene-rich polymer and they suffered two opposite van der Waals forces. One repulsive from the water that pushes them towards the center of the particle and another one attractive towards the hydrophobic large clusters near the surface of the particle, namely away from the center of the particle. The results in Figures 3.4 and 3.6 suggest that the attractive one was predominant and that the effect was more acute in the case of the softer system.

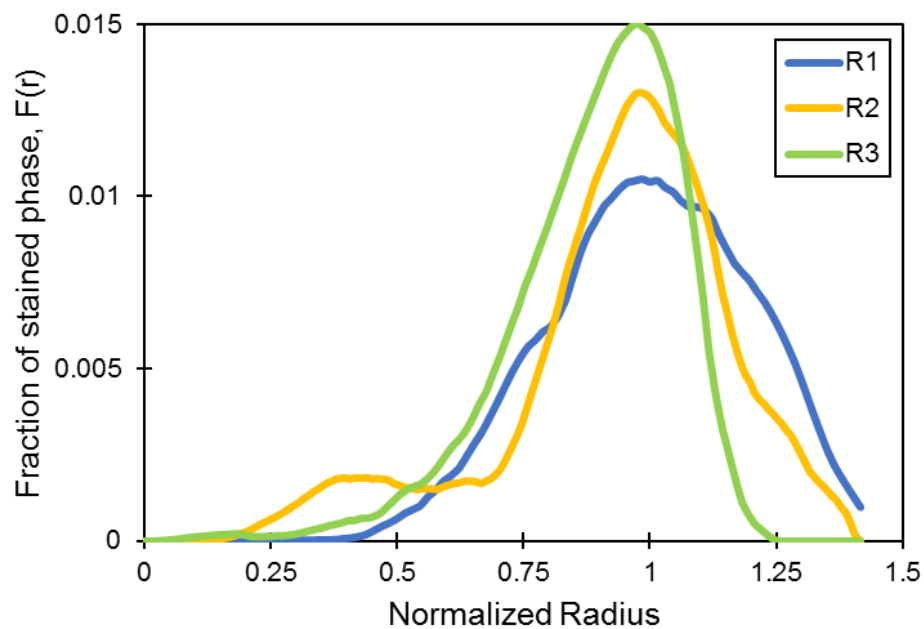


Figure 3. 6. Radial distribution of the second stage polymer for Runs R1, R2 and R3.  $F$  is defined by equation 1.

The effect of  $T_g$  of second stage polymer on the particle morphology was explored by determining the particle morphology of latex R5, which was synthesized with the  $T_g$  of 90 °C in the seed as well as in the second stage polymer (Table 3.1). Figure 3.7 shows the reconstructed particle image for this case as well as a series of slices of the reconstructed composite polymer.

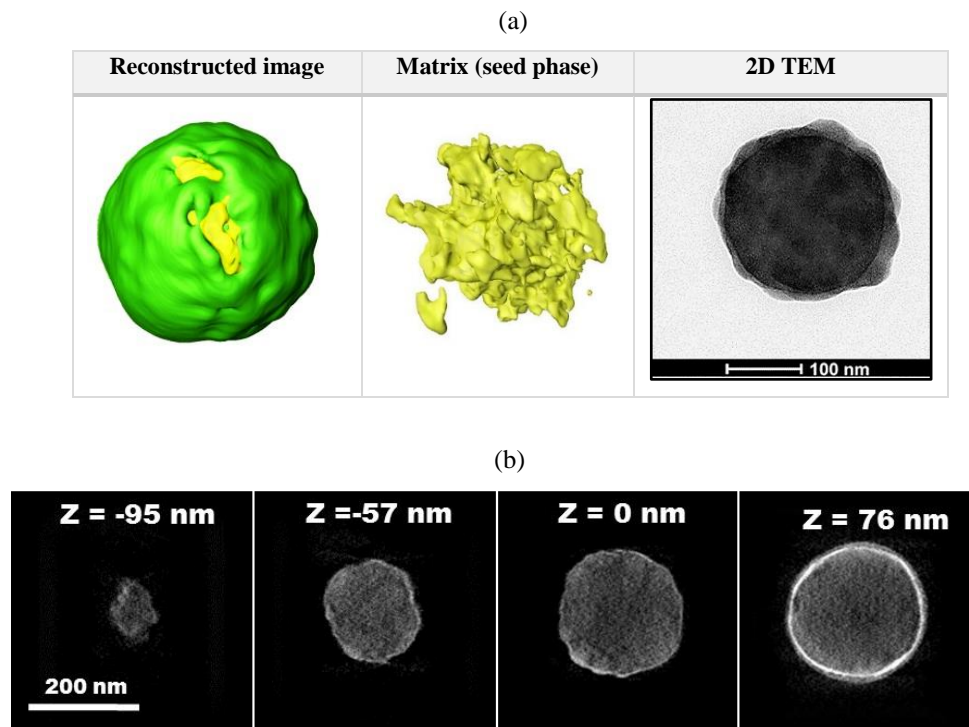


Figure 3. 7. (a) Reconstructed 3D images of polymer particle for Run R5 by tomographic analysis of samples by HAADF-STEM and the corresponding TEM images (the scale is 100 nm); (b) Tomographic cross-sections of Run R5 from upper surface of the sample to the bottom obtained from HAADF-STEM.

It can be seen that the second phase polymer (in green in Figure 3.7 a) is located on the surface of the particle and the composite particle is mostly spherical with the second stage polymer covering an irregular polymer matrix. The penetration of the second stage polymer was small due to the high  $T_g$  of the seed. On the other hand, the second stage polymer did not form large clusters at the surface of the particle.

The particle morphologies discussed so far were largely determined by the use of a water-soluble initiator that led to a steep radical concentration profile. A way of obtaining a flatter radical concentration profile is to use an oil-soluble initiator. The harder seed ( $T_g = 90\text{ }^\circ\text{C}$ ) that led to the morphology that was farthest from the equilibrium was chosen to study the effect of the radical concentration profile. Run A1 was carried out using the same seed and the same second stage monomer mixture as for Run R1, but using AIBN instead of TBHP/ACBS. Figure 3.8 (a) presents the particle morphology of Run A1, and the radial concentration of the second stage polymer for Runs R1 and A1 is compared in Figure 3.8 (b). It can be seen that a rather uniform concentration of the second stage polymer was obtained with the oil soluble initiator (Figure 3.8 b) and that the clusters of the second stage polymer were embedded in the particle (Figure 3.8 a), but the equilibrium morphology was not reached because the viscosity of the particle was too high to allow further movement of the clusters.

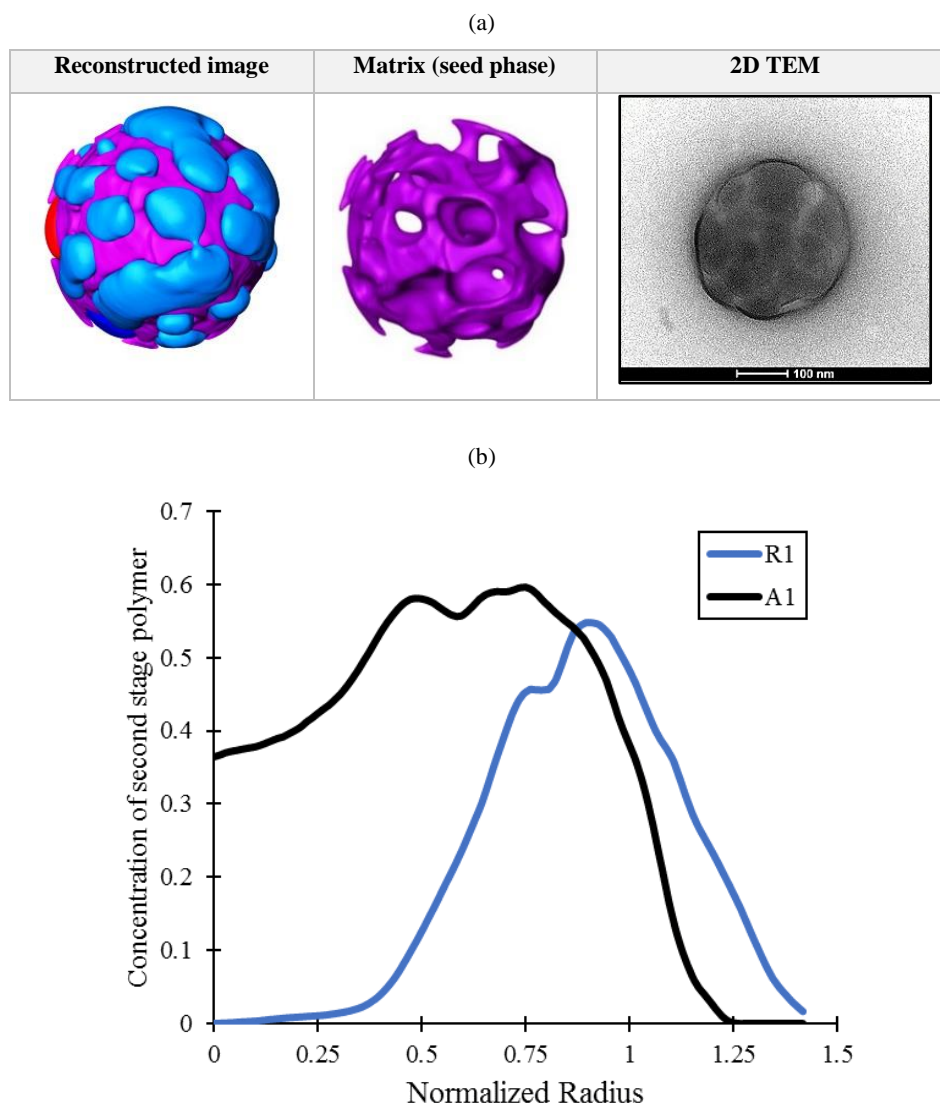


Figure 3. 8. (a) Reconstructed 3D images of polymer particle for Run A1 and a representative TEM image (the scale bar is 100 nm); (b) concentration profile of second stage polymer in Run A1 compared to R1.

### **3.5. Particle morphology analysis using an upgraded mathematical model**

In Section 2.3.1.1, the predictions of the mathematical model for development of particle morphology<sup>15</sup> were compared with the experimental results of the particle morphology measured by conventional TEM. The model was used to explain the effect of different process variables on the development of particle morphology. The cluster size distributions predicted by the model (with the estimated parameters) were in good agreement with the experimental results in most of the cases. However, the results presented in Figure 3.4 show that this conclusion was biased by the fact that in conventional TEM, only the big clusters were observed in the 2D images obtained.

Consideration of the results for Runs R2 and R3 (Figure 3.4 and 3.6) clearly shows that the model should include an additional term to account for the migration of the internal hydrophobic clusters towards the surface of the particles, which is driven by the attraction between the small internal clusters and the large lobes near the surface of the particle. Therefore, a term for the backward movement was added to the population balances and therefore, the population balances for the clusters of size  $x$  (number of polymerized monomer units) at non-equilibrium positions ( $m_1$  and  $m_2$ ) and clusters at equilibrium position ( $n$ ) were modified as follows:

**Population balance for clusters at exterior non-equilibrium positions:**

$$\frac{dm_1(x)}{dt} = (1 - \delta_{x_c})r_p^{m_1}(x-1)m_1(x-1) - r_p^{m_1}(x)m_1(x)$$

Propagation

$$+ (1 - \delta_{x_c})r_d^{m_1}(x - \bar{x}_m) m_1(x - \bar{x}_m) - r_d^{m_1}(x)m_1(x)$$

Polymer diffusion from polymer matrix

$$+ (1 - \delta_{x \leq 2x_c})\alpha_m(x) \frac{k_a}{V_p} \left(1 - \frac{1}{m_{1_{av}}}\right) \int_{x_c}^{x-x_c} m_1(z)m_1(x-z)dz$$

$$- 2m_1(x) \frac{k_a}{V_p} \left(1 - \frac{1}{m_{1_{av}}}\right) \int_{x_c}^{x_{max}-x} \alpha_m(x+z)m_1(z) dz$$

Cluster coalescence

$$- k_{mov1}m_1(x)$$

Movement to interior non-equilibrium region

$$+ k_{mov3}m_2(x)$$

**Backward movement to exterior non-equilibrium region**

$$+ \delta_{x_c}r_{nuc}$$

$$\text{Cluster nucleation} \quad (3.2)$$

Compared to equation 2.17, in equation 3.2 it is considered that due to cluster-cluster van der Waals forces, clusters at the interior non-equilibrium region can also

---

move backward to the exterior non-equilibrium region with a rate coefficient  $k_{mov3}$ .

The other terms are as explained for equation 2.17.

The parameters controlling the movement and coalescence of the clusters ( $k_d^{pol2}$ ,  $k_{mov1}$ ,  $k_{mov2}$ ,  $k_{mov3}$  and  $k_a$ ) deserve some discussion. In Chapter 2, when the effect of the Tg of second stage polymer on the particle morphology was discussed, it was concluded that the movement of the clusters towards the equilibrium morphology seemed to be determined by the Tg of the matrix, whereas the Tg of second stage polymer played an important role in the coalescence. This last observation is intriguing because movement seems to be a prerequisite for coalescence of the clusters. It is important to point out that these conclusions were drawn out from conventional TEM images where the main characteristic was the size of the clusters that were located near or at the surface of the particles (because water soluble initiator was used). On the other hand, HAADF-STEM images available for this effect are only those of Runs R1 and R5 and they do not allow to discuss if this effect was also observed in the interior of the particles. Therefore, the discussion below is limited to the clusters that are located near/at the surface of the particle. For this case, the cluster size increased as the Tg of second stage polymer decreased and it seems that the Tg of the matrix does not significantly influence the process.



The situation has some resemblance with the sintering in heterogeneous catalysis that led to deactivation<sup>16</sup>, where there has been a long debate about the mechanisms involved.<sup>17</sup> The mechanisms proposed are the Ostwald ripening and the coalescence, and it appears that Ostwald ripening involving both the transport by the surface and through the gas phase is the dominant process in catalysis.<sup>17</sup>

The situation in the present case is different as illustrated in Figure 3.9 where the mechanisms for cluster aggregation are presented (here aggregation is used to include the result of both coalescence and Ostwald ripening).

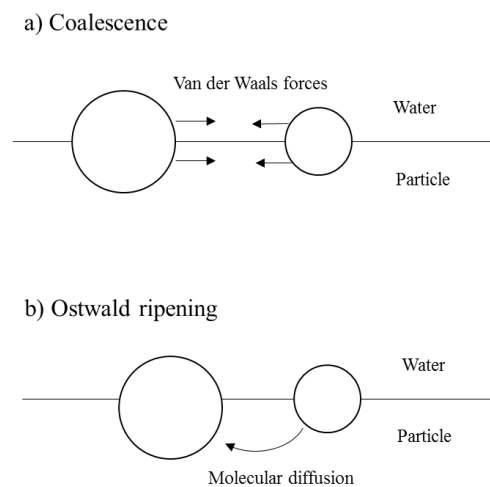


Figure 3. 9. Cluster aggregation at the surface of the particle

Ostwald ripening involves the molecular diffusion of polymer chains from small to large clusters due to the higher chemical potential of the polymer in the small

clusters, which is created by the higher surface energy per unit volume. For this process, transport should occur through the polymer particle and the diffusion is more likely for low T<sub>g</sub> polymer.

Coalescence involves the movement of the clusters. For the situation depicted in Figure 3.9 (a), the driving forces are the van der Waals forces, which are different for the fractions of the clusters that are in the particles and those that are in the aqueous phase. As the van der Waals forces between two objects of the same material separated by another material increase with the interfacial tension between the materials, the van der Waals forces are higher through the aqueous phase.<sup>18</sup> In addition, the viscosity of the aqueous phase is very low. Therefore, the coalescence will most likely occur through the aqueous phase and the only resistance is the viscosity of the second stage polymer, namely the lower T<sub>g</sub> the easier will be the coalescence.

With the data available, it is not possible to accurately conclude which is the mechanism (coalescence or Ostwald ripening). Nevertheless, the fact that small clusters (for which Ostwald ripening would be substantial) were observed in HAADF-STEM images suggests that Ostwald ripening was not the main mechanism for the clusters aggregation.

The discussion above explains the reasons for the observations that the T<sub>g</sub> of matrix controls the migration of the clusters towards the equilibrium morphology and the T<sub>g</sub>

---

of the second stage polymer controls the coalescence of the clusters. In order to include these ideas in the model,  $k_d^{pol2}$ ,  $k_{mov1}$ ,  $k_{mov2}$  and  $k_{mov3}$  were considered inversely proportional to the viscosity of the medium of polymerization that according to the van-Krevelen-Hoftyzen model, depends on the fraction of the polymer and the ratio of reaction temperature to the Tg of the medium of polymerization.<sup>19</sup> On the other hand, as the movement of the clusters towards or away the surface of the particles is driven by the attraction between the internal and external clusters, these parameters were considered dependent on the fraction of second stage polymer in the exterior region of particles in a way that if there is more second stage polymer located on the surface, the backward movement is more predominant and vice versa. Therefore, the coefficients were defined in the model with following expressions:

$$k_{mov1} = \frac{k_{mov1_0}}{\phi_P^5 * A * \exp\left(\frac{B}{\left(\frac{T}{T_{g\,effective,matrix}} - 0.866\right)}\right)} * \frac{V_{pol1,region1}}{V_{pol2,region1} + V_{pol1,region1}} \quad (3.3)$$

$$k_{mov2} = \frac{k_{mov2_0}}{\phi_P^5 * A * \exp\left(\frac{B}{\left(\frac{T}{T_{g\,effective,matrix}} - 0.866\right)}\right)} \quad (3.4)$$

$$k_{mov3} = \frac{k_{mov3,0}}{\phi_p^5 * A * \exp\left(\frac{B}{\left(\frac{T}{T_{g_{effective,matrix}}} - 0.866\right)}\right)} * \frac{V_{pol2,region1}}{V_{pol2,region1} + V_{pol1,region1}} \quad (3.5)$$

$$k_d^{pol2} = \frac{k_{d0}^{pol2}}{\phi_p^5 * A * \exp\left(\frac{B}{\left(\frac{T}{T_{g_{effective,matrix}}} - 0.866\right)}\right)} \quad (3.6)$$

where A, B,  $k_{mov1,0}$ ,  $k_{mov2,0}$ ,  $k_{mov3,0}$  and  $k_{d0}^{pol2}$  are adjustable parameters of the model.  $V_{pol2,region1}$  is the volume of the second phase polymer in the exterior region of the particle (region 1),  $V_{pol1,region1}$  is the volume of the seed in region 1 and  $T_{g_{effective}}$  of the matrix is calculated as:

$$T_{g_{effective,matrix}} = \frac{Tg_p + (\kappa Tg_M - Tg_p)\phi_M}{1 + (\kappa - 1)\phi_M} \quad (3.7)$$

where  $Tg_p$  is considered as the  $Tg$  of polymer from seed and  $\kappa$  is 1. On the other hand, in order to account for the effects discussed above for the aggregation of clusters maintaining at the same time the structure of the model, a coalescence coefficients ( $k_a$ ) was used, but the  $T_{g_{effective}}$  was calculated assuming a mixture of monomer and second stage polymer:

$$k_a = \frac{k_{a0}}{\phi_p^5 * A * \exp\left(\frac{B}{\left(\frac{T}{T_{g\text{ effective, 2nd polymer}}} - 0.866\right)}\right)} \quad (3.8)$$

where,  $k_{a0}$  is adjustable parameter of the model.

The population balances for clusters at interior non-equilibrium position and for clusters at equilibrium positions are given in equations 3.9 and 3.10, respectively. The values of estimated parameters for the upgraded version of the mathematical model are given in the Table 3.2.

**Population balance for clusters at interior non-equilibrium position:**

$$\frac{dm_2(x)}{dt} = (1 - \delta_{x_c})r_p^{m_2}(x-1)m_2(x-1) - r_p^{m_2}(x)m_2(x)$$

Propagation

$$+ (1 - \delta_{x_c})r_d^{m_2}(x - \bar{x}_m) m_2(x - \bar{x}_m) - r_d^{m_2}(x)m_2(x)$$

Polymer diffusion from polymer matrix

$$+ (1 - \delta_{x \leq 2x_c})\alpha_m(x) \frac{k_a}{V_p} \left(1 - \frac{1}{m_{2av}}\right) \int_{x_c}^{x-x_c} m_2(z)m_2(x-z)dz$$

$$- 2m_2(x) \frac{k_a}{V_p} \left(1 - \frac{1}{m_{2av}}\right) \int_{x_c}^{x_{max}-x} \alpha_m(x+z)m_2(z) dz$$

Cluster coalescence

$$+k_{\text{mov}1}m1(x)$$

Movement to interior non-equilibrium position

$$-k_{\text{mov}3}m2(x)$$

**Backward movement to exterior non-equilibrium region**

$$-m2(x) \frac{k_{\text{mov}2}}{V_p} \int_{x_c}^{x_{\text{max}} - x} \alpha_m(x+z)n(z) dz$$

Movement to equilibrium position

$$+ \delta_{x_c} r_{\text{nuc}} \quad \text{Cluster nucleation} \quad (3.9)$$

**Population balance for cluster at equilibrium position**

$$\frac{dn(x)}{dt} = (1 - \delta_{x_c}) r_p^n(x-1)n(x-1) - r_p^n(x)n(x)$$

Propagation

$$+ (1 - \delta_{x_c}) r_d^n(x - \bar{x}_m) n(x - \bar{x}_m) - r_d^n(x)n(x)$$

Polymer diffusion from polymer matrix

$$+ (1 - \delta_{x \leq 2x_c}) \alpha_n(x) \frac{k_{\text{mov}2}}{V_p} \int_{x_c}^{x-x_c} m2(z)n(x-z) dz$$

$$- n(x) \frac{k_{\text{mov}2}}{V_p} \int_{x_c}^{x_{\text{max}} - x} \alpha_n(x+z)m2(z) dz$$

$$\text{Movement to equilibrium position} \quad (3.10)$$


---

In the upgraded model, the calculated discrete mass cluster distributions using 100 pivot were converted to continuous mass cluster distributions following the method explained by Calvo.<sup>20</sup> The upgraded model was first used to simulate the particle morphologies of the latexes presented in Table 3.1. Figure 3.10 presents the predictions for Runs R1, R2 and R3, where the Tg of the seed was varied (the predictions of the model made in Chapter 2 were converted to continuous distributions and are included for the sake of comparison).

Table 3. 2. Values of estimated parameters in the upgraded version of the mathematical model

Parameter	Value	Reference
<b>A</b>	$1.36 \times 10^{-5}$	This work
<b>B</b>	3.2	This work
<b><math>k_{p,BA}</math> (L/mol.s)</b>	$2.21 \times 10^7 \exp(-17.9/RT)$	21
<b><math>k_{p,St}</math> (L/mol.s)</b>	$4.27 \times 10^7 \exp(-32.5/RT)$	22
<b><math>r_{St}</math></b>	0.95	23
<b><math>r_{BA}</math></b>	0.18	23
<b><math>k_{a0}</math> (L/s)</b>	$1 \times 10^{-22}$	This work
<b><math>k_{mov01}</math> (1/s)</b>	$1 \times 10^{-7}$	This work
<b><math>k_{mov02}</math> (L/s)</b>	$8 \times 10^{-10}$	This work
<b><math>k_{mov03}</math> (1/s)</b>	$2 \times 10^{-4}$	This work
<b><math>k_{d0}^{pol2}</math> (mol/dm<sup>2</sup>.s)</b>	$5 \times 10^{-22}$	This work
<b><math>k_n</math> (mol/s)</b>	$5 \times 10^{-2}$	This work
<b><math>x_c</math> (monomeric units)</b>	$4 \times 10^4$	15
<b><math>\bar{x}_m</math> (monomeric units)</b>	$5 \times 10^3$	15

It can be seen that in agreement with experimental results, the consideration of the backward movement considerably reduced the amount of second stage polymer in the interior of Run R3.

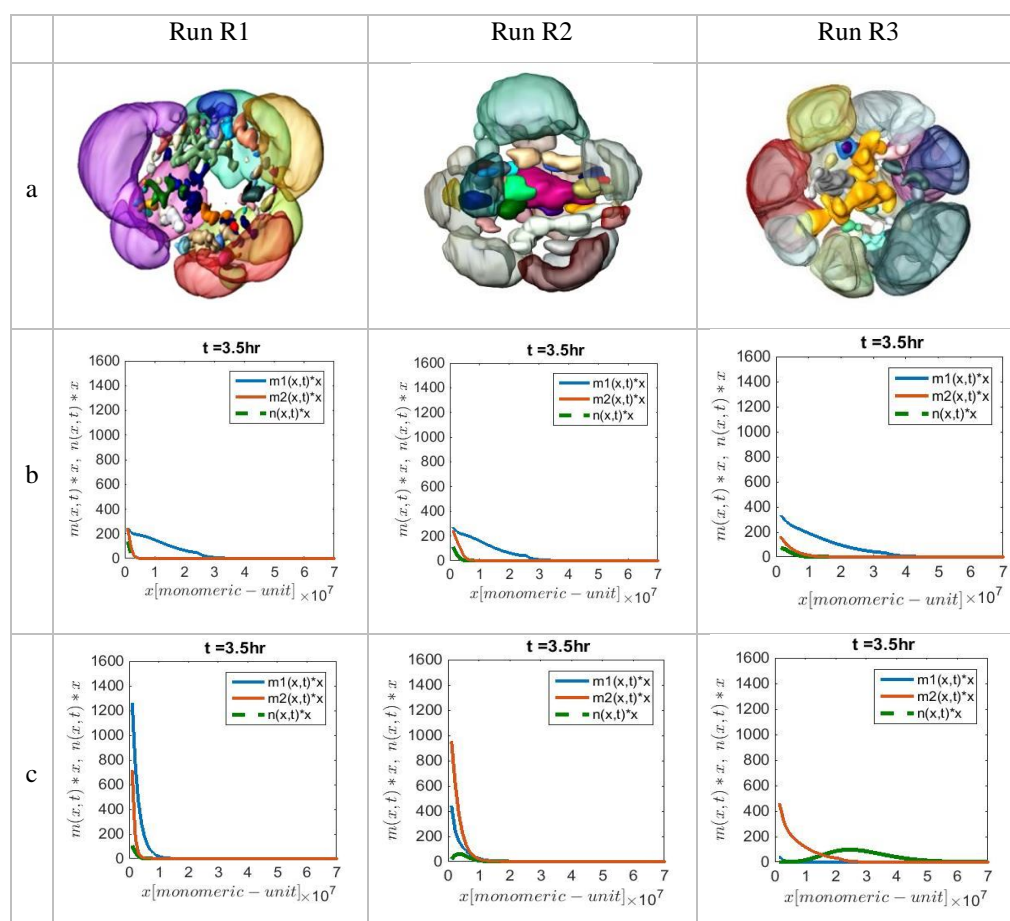


Figure 3. 10. Comparison of Runs R1-R3 in a) Tomographic reconstruction images, b) continuous mass-cluster distributions using upgraded version of the model in this chapter, c) continuous mass-cluster distributions using the presented version of the model in Chapter 2.<sup>13</sup>



The upgraded model was also applied to Runs R5 and A1 for which HAADF-STEM images were available. Run R5 was designed to study the effect of the Tg of the second stage polymer when a hard seed was used.

Figure 3.11 presents the tomographic reconstructions of the morphology of the particles in Runs R1 and R5, as well as the model predictions. For sake of comparison, the predictions obtained with the model in Chapter 2 are included. It can be seen that the upgraded model closely agreed with the experimental observations in that the size of the clusters near the surface of the particle was substantially larger for R1 than for R5. The model used in Chapter 2 did not account for this difference.

The upgraded model was also used to analyze the effect of the type of initiator on particle morphology (Runs R1 and A1). The results are presented in Figure 3.12. It can be seen that in agreement with the experiments, the upgraded model predicted that in Run R1 the majority of the second stage polymer was at the surface of the particles forming large clusters, whereas in Run A1 formed smaller clusters in the non-equilibrium positions. The model used in Chapter 2 predicted smaller clusters than the predicted ones by the upgraded version of the model in the non-equilibrium positions in Run A1.

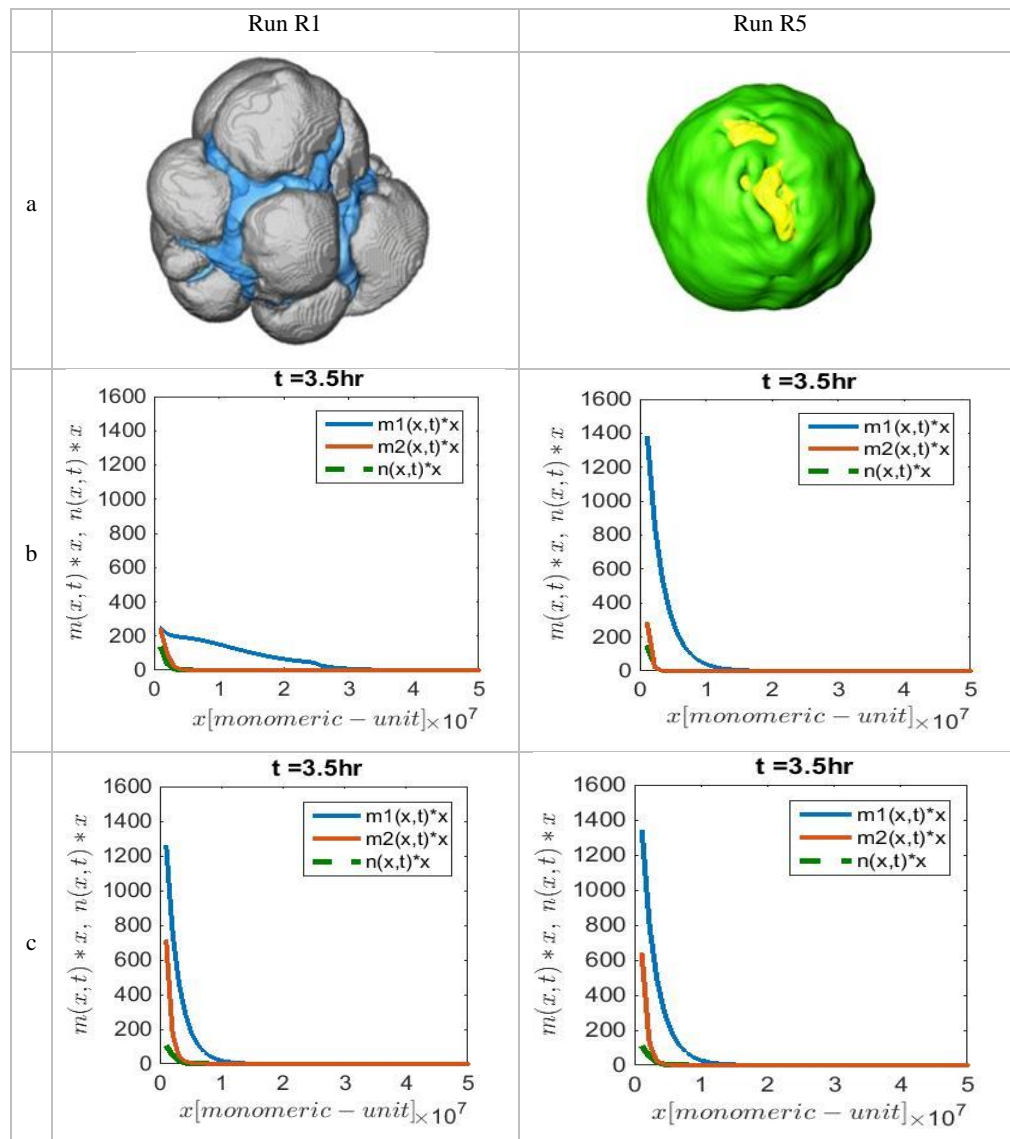


Figure 3. 11. Comparison of Runs R1 and R5 in a) Tomographic reconstruction image, b) continuous mass-cluster distributions using upgraded version of the model in this chapter, c) continuous mass-cluster distributions using the presented version of the model in Chapter 2.

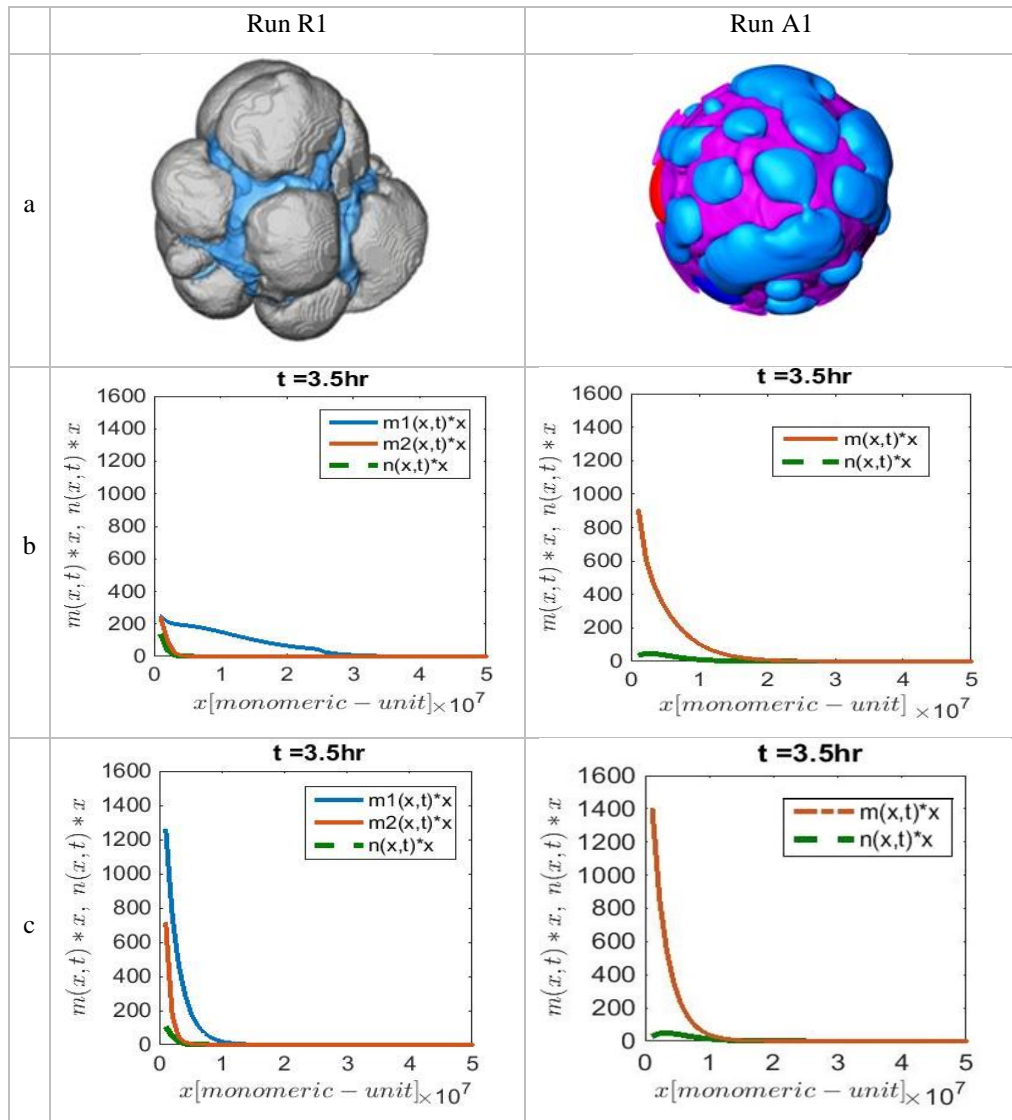


Figure 3. 12. Comparison of Runs R1 and A1 in a) Tomographic reconstruction image, b) continuous mass-cluster distribution using upgraded version of the model in this chapter, c) continuous mass-cluster distribution using the presented version of the model in Chapter 2.

### 3.6. Use of the upgraded model to analyze some of un-explained findings in Chapter 2

In Chapter 2, Runs R3 and R4 were carried out to study the effect of the T<sub>g</sub> of the second stage polymer on particle morphology when a soft seed was used (summarized in Table 3.3). It was found that the model used in that chapter was not able to justify the experimental observations. Therefore, the upgraded model was used to simulate those experiments and the predictions are presented in Figure 3.13. It can be seen that the upgraded model accounts for the effect of the T<sub>g</sub> of the second stage polymer when soft seeds were used. In particular, it shows that for both Runs R3 and R4, most of the clusters stayed near the surface of the particle and that the size of the clusters in Run R3 was larger than that of Run R4. The prediction for Run R4 nicely agreed with the measured MFFT (96 °C) which strongly points out that the hard polymer was at the surface of the particles.

Table 3. 3. Modulated DSC measured T<sub>g</sub>s for Runs R4 and R5.

Run	T <sub>g</sub> seed (°C)	T <sub>g</sub> 2 <sup>nd</sup> stage (°C)
R4	45	95
R3	46	46

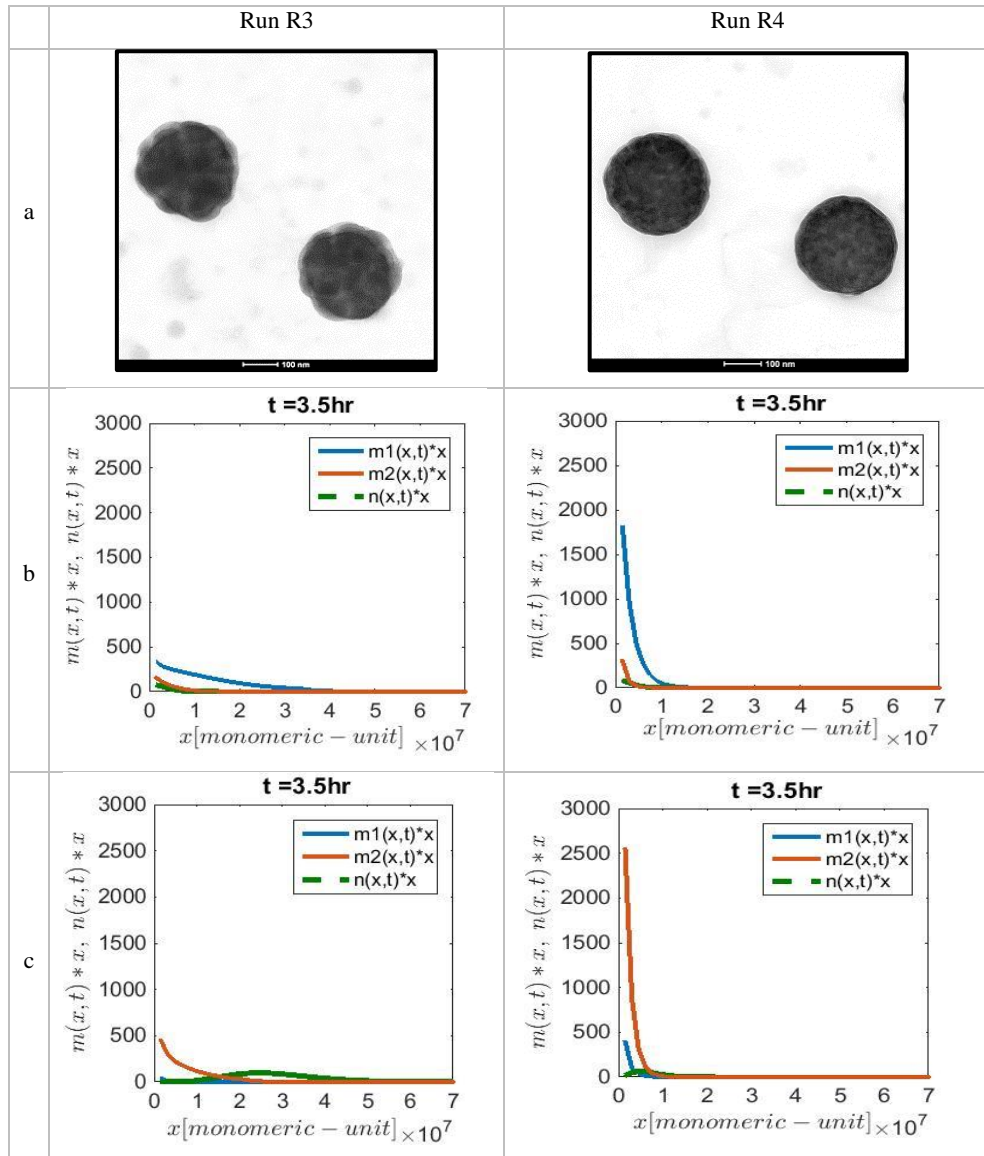


Figure 3. 13. Comparison of Runs R3 and R4 in a) TEM image, b) continuous mass-cluster distributions using upgraded version of the model in this chapter, c) continuous mass-cluster distributions using the presented version of the model in Chapter 2.

In Chapter 2, the effect of reaction temperature in the second stage of the polymerization on particle morphology was studied by means of Runs R2, R4, R6 and R7 (Summarized in Table 3.4). The model used in Chapter 2, was not able to account for the experimental observations. Therefore, the upgraded model was applied to these experiments. The results are given in Figure 3.14 for Runs R2 and R6. It can be seen that the model predicts that for both reactions, the majority of the clusters were near the surface of the particle and that the main effect of the reaction temperature was to increase the size of the external clusters when the reaction temperature was higher (Run R2).

Table 3. 4. Modulated DSC measured  $T_g$  of Runs R2, R4, R6 and R7 and the reaction temperature of the second stage of polymerization process.

Run	$T_{g_{seed}}$ ( $^{\circ}\text{C}$ )	$T_{g_{2^{nd} \text{ stage}}}$ ( $^{\circ}\text{C}$ )	$T_{\text{reaction, 2}^{nd} \text{ stage}}$ ( $^{\circ}\text{C}$ )
<b>R2</b>	63	45	80
<b>R6</b>	63	49	65
<b>R4</b>	45	95	80
<b>R7</b>	46	95	60

Figure 3.15 presents the predictions of the upgraded model for Runs R4 and R7. For the sake of discussion, the evolutions of the outputs of the model for the instantaneous conversion and for the effective  $T_g$ s for the matrix and second stage

polymer are presented in Figure 3.16. In this figure, it can be seen that the slightly lower instantaneous conversion in Run R7 led to a small difference in the effective T<sub>g</sub>s, but the difference of T<sub>reaction</sub> and T<sub>g effective</sub> of matrix was significantly higher in Run R4 than in Run R7. Therefore, one would expect deeper penetration of clusters in Run R4. However, the model predicted that in agreement with the experimental findings the clusters penetrated more in Run R7. The reason was that in Run R4, the attractive van der Waals forces between the inner and outer clusters moved the smaller inner clusters towards the exterior of the particle. It is worth pointing out that in Run R7 because of the fact that the reaction temperature was lower than the effective T<sub>g</sub> of the clusters, the clusters did not coalesce and their growth was due to polymerization and polymer diffusion from the matrix.

### **3.7. Conclusions**

In this chapter, a method for the precise quantitative 3D characterization of polymer-polymer composite waterborne particles based on tomographic analysis using high angular dark field -scanning transmission electron microscopy (HAADF-STEM) coupled with image reconstruction is presented.

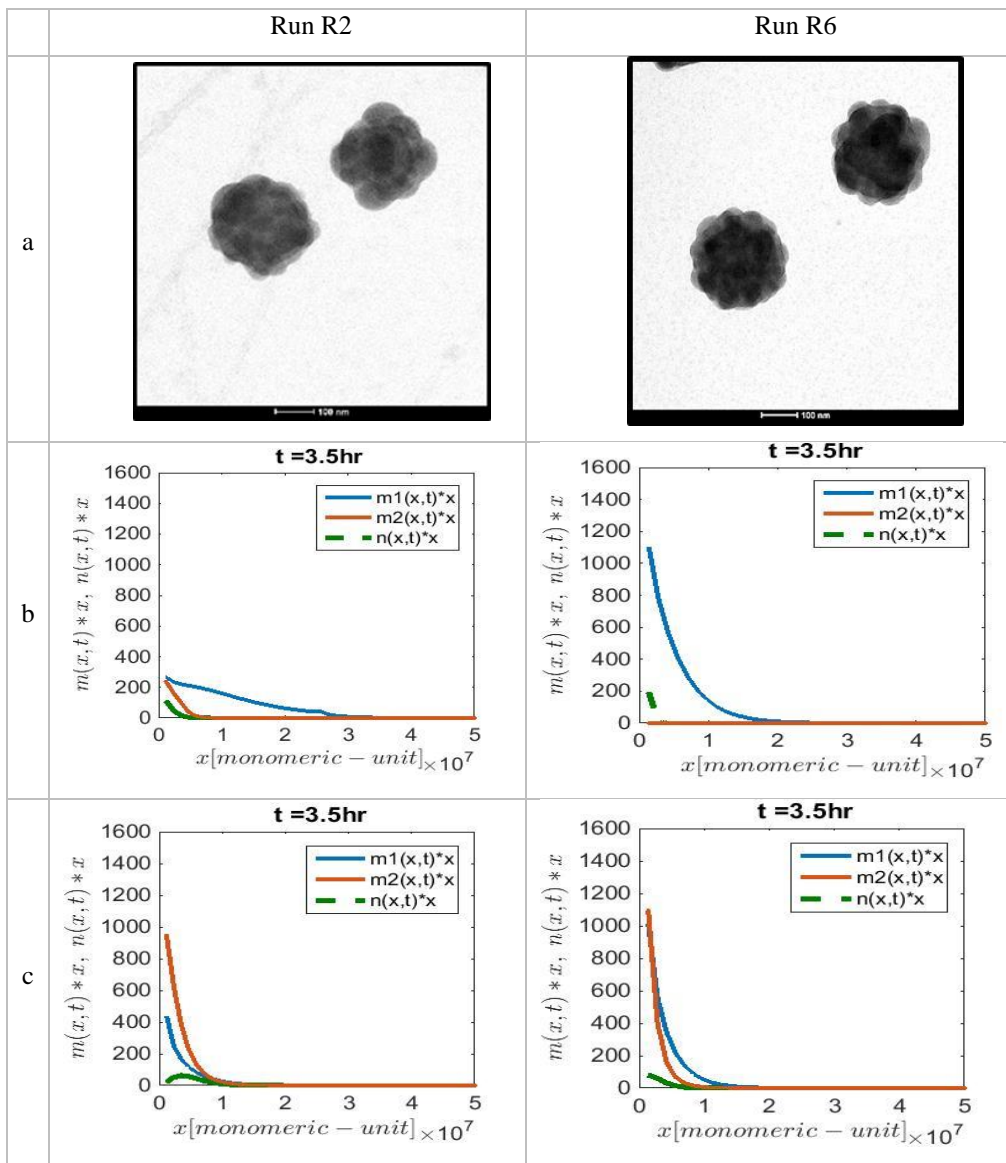


Figure 3. 14. Comparison of Runs R2 and R6 in a) TEM image, b) continuous mass-cluster distribution using upgraded version of the model in this chapter, c) continuous mass-cluster distribution using the presented version of the model in Chapter 2.



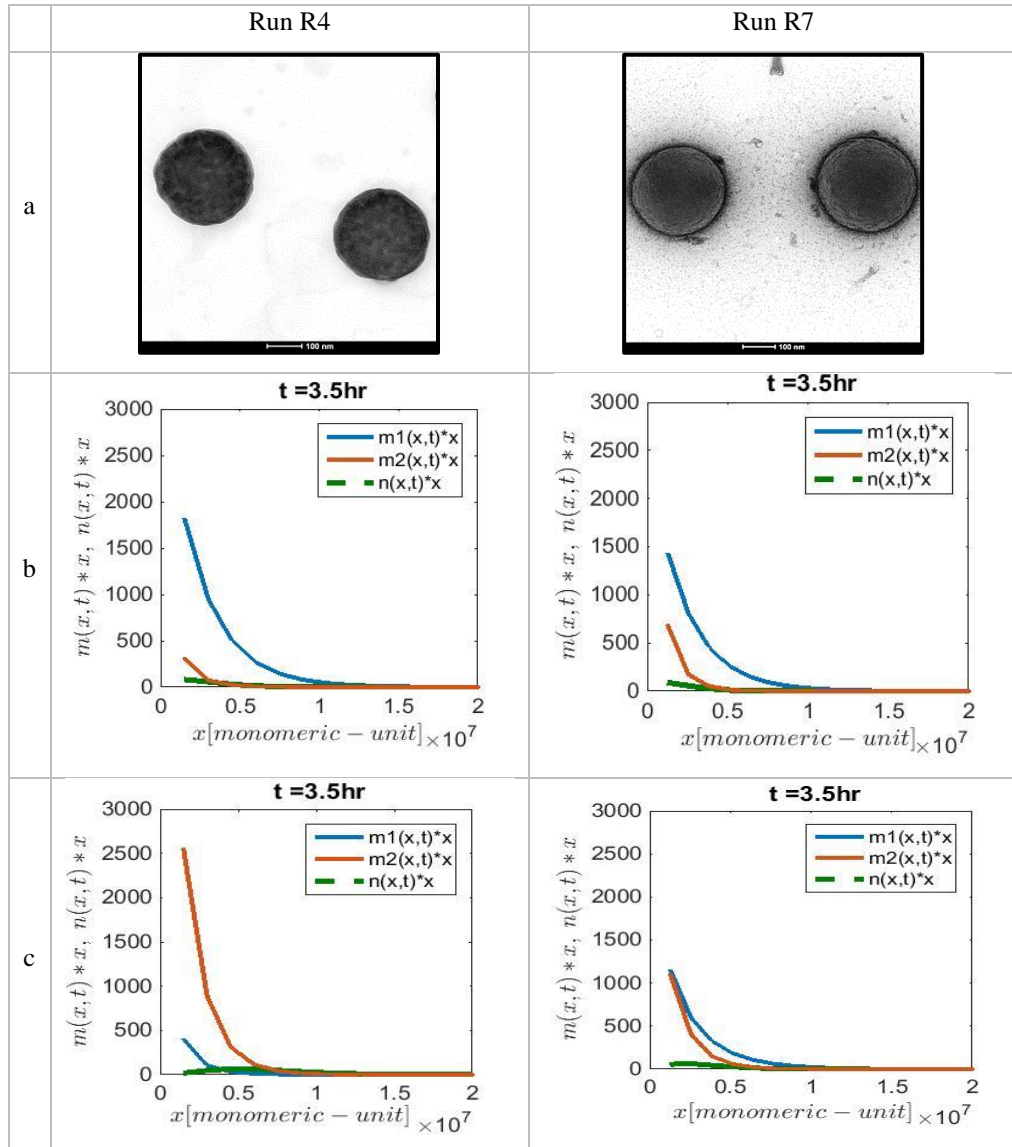


Figure 3. 15. Comparison of Runs R4 and R7 in a) TEM image, b) continuous mass-cluster distribution using modified version of the model in this chapter, c) continuous mass-cluster distribution using the presented version of the model in Chapter 2.

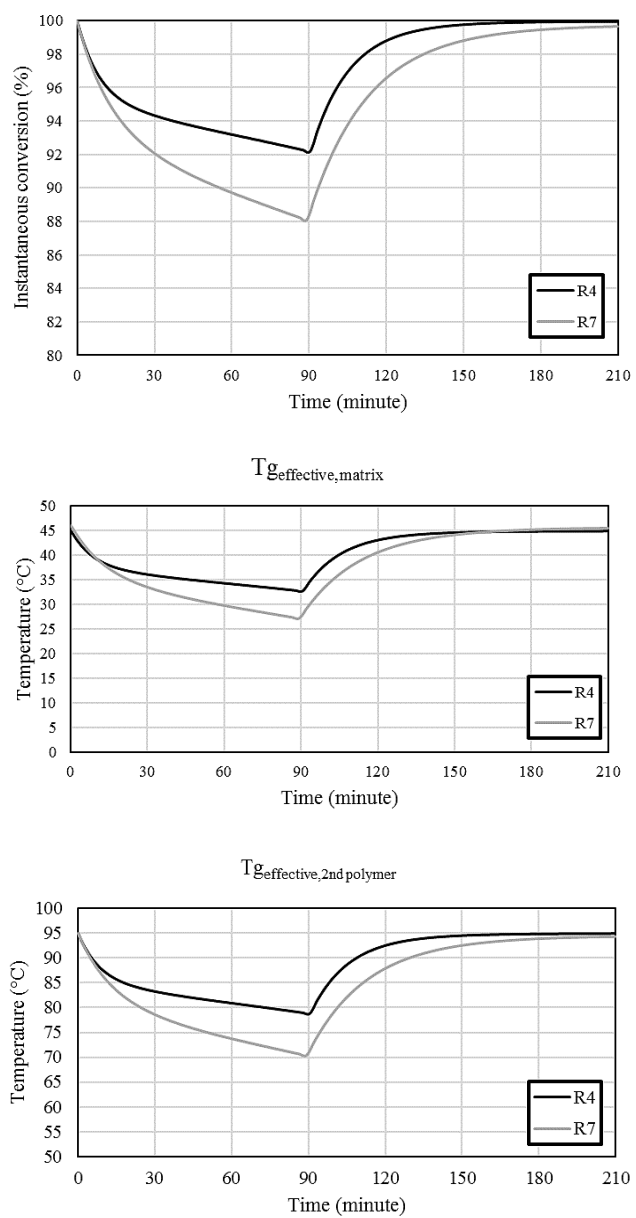


Figure 3. 16. Evolution of Instantaneous conversion and the effective Tgs of the matrix and clusters calculated by the upgraded mathematical model for Runs R4 and R7.

---

The potential of this technique was demonstrated in the study of the effect of process variables ( $T_g$  of both the seed and second stage polymer and type of initiator) on particle morphology development of some of studied and characterized latexes in Chapter 2. As it was discussed in Chapter 2, the  $T_g$  of the seed determines the viscosity of the particle, which in turn hinders the movement of the clusters. The driving forces for this movement are the van der Waals forces among the clusters (attractive) and between the clusters and the aqueous phase (repulsive). The latter force pushed the clusters toward the center of the particle (equilibrium morphology). Therefore, for the water-soluble initiator, the large clusters of poly(S-BA) formed lobes protruding from the surface of the particle when a hard seed ( $T_g = 86\text{ }^\circ\text{C}$ ) was used, and these clusters were more embedded in the particle for lower  $T_g$  seeds. The presence of these large clusters at the outer region of the particle caused an unexpected effect on the position of the smaller inner clusters, which were affected by two opposite van der Waals forces. The repulsive force with the aqueous phase pushed the clusters toward the center of the particle and the attractive one with the large clusters that directed them toward the outer part of the particle. The detailed characterization shows that the attractive one was the predominant force, which suggested the introduction of backward movement in the model discussed in Chapter 2. The observed small internal clusters from HAADF-STEM tomography suggests that among different aggregation mechanism (Ostwald

ripening and coalescence due to van der Waals forces) involved in the coalescence of the clusters, the Ostwald ripening was not the main mechanism. Therefore, it could be concluded that the movement of the clusters was controlled by the Tg of the matrix and Tg of second stage polymer controlled the coalescence of the clusters located at the exterior of the particle. The mathematical model was upgraded including the backward movement and dependency of the cluster movement and coalescence on the Tgs of the matrix and the second stage polymer, respectively. The cluster size distributions predicted by the upgraded model for the effect of Tg of seed on the particle morphology development were in agreement with experimental observations.

Although the presented method is the only available characterization technique capable of providing accurate information about the morphology of complex polymer-polymer composite particle latexes, it is extremely time consuming and therefore it is worthy to have experimental cluster distribution statistically meaningful.

Nevertheless, the information about the morphology gathered by this technique revealed mechanistic features on the development of the particle morphology that could not be captured by the conventional TEM images and hence it allowed upgrading the mathematical model presented in Chapter 2. All overall, the upgraded model provides a better prediction of the effect of process variables on the morphology of composite

polymer particles and this opens the way to use the model in optimization and on-line control strategies.

### 3.8. References

- (1) Stubbs, J. M.; Sundberg, D. C. A Round Robin Study for the Characterization of Latex Particle Morphology—multiple Analytical Techniques to Probe Specific Structural Features. *Polyme.* **2005**, *46*, 1125–1138.
- (2) Ercius, P.; Alaidi, O.; Rames, M. J.; Ren, G. Electron Tomography: A Three-Dimensional Analytic Tool for Hard and Soft Materials Research. *Adv. Mater.* **2015**, *27* (38), 5638–5663.
- (3) Kohjiya, S.; Kato, A.; Ikeda, Y. Visualization of Nanostructure of Soft Matter by 3D-TEM: Nanoparticles in a Natural Rubber Matrix. *Prog. Polym. Sci.* **2008**, *33* (10), 979–997.
- (4) Kato, A.; Shimanuki, J.; Kohjiya, S.; Ikeda, Y. Three-Dimensional Morphology of Carbon Black in NR Vulcanizates as Revealed by 3D-TEM and Dielectric Measurements. *Rubber Chem. Technol.* **2006**, *79* (4), 653–673.
- (5) Aguirre, M.; Paulis, M.; Leiza, J. R.; Guraya, T.; Iturrondobeitia, M.; Okariz, A.; Ibarretxe, J. High-Solids-Content Hybrid Acrylic/CeO<sub>2</sub> Latexes with Encapsulated Morphology Assessed by 3D-TEM. *Macromol. Chem. Phys.* **2013**, *214* (19), 2157–2164.
- (6) Mori, Y.; Kawaguchi, H. Impact of Initiators in Preparing Magnetic Polymer Particles by Miniemulsion Polymerization. *Colloids Surfaces B Biointerfaces* **2007**, *56* (1–2), 246–254.
- (7) Geng, X.; Zhai, M. X.; Sun, T.; Meyers, G. Morphology Observation of Latex Particles with Scanning Transmission Electron Microscopy by a Hydroxyethyl Cellulose Embedding Combined with RuO<sub>4</sub> Staining Method. *Microsc. Microanal.* **2013**, *19*, 319–326.
- (8) Midgley, P. A.; Weyland, M.; Meurig Thomas, J.; Johnson, B. F. G. Z-Contrast Tomography: A Technique in Three-Dimensional Nanostructural Analysis Based on Rutherford Scattering. *Chem. Commun.* **2001**, No. 10, 907–908.

- (9) Liu, Z.; Epicier, T.; Lefkir, Y.; Vitrant, G.; Destouches, N. HAADF-STEM Characterization and Simulation of Nanoparticle Distributions in an Inhomogeneous Matrix. *J. Microsc.* **2017**, *266* (1), 60–68.
- (10) Loos, J.; Sourty, E.; Lu, K.; de With, G.; v. Bavel, S. Imaging Polymer Systems with High-Angle Annular Dark Field Scanning Transmission Electron Microscopy (HAADF-STEM). *Macromolecules* **2009**, *42* (7), 2581–2586.
- (11) Hindson, J. C.; Saghi, Z.; Hernandez-Garrido, J.-C.; Midgley, P. A.; Greenham, N. C. Morphological Study of Nanoparticle-Polymer Solar Cells Using High-Angle Annular Dark-Field Electron Tomography. *Nano Lett.* **2011**, *11* (2), 904–909.
- (12) Wolf, D.; Lubk, A.; Lichte, H. Weighted Simultaneous Iterative Reconstruction Technique for Single-Axis Tomography. *Ultramicroscopy* **2014**, *136*, 15–25.
- (13) Rajabalinia, N.; Hamzehlou, S.; Leiza, J. R.; Asua, J. M. Experimental Validation of a Mathematical Model for the Evolution of the Particle Morphology of Waterborne Polymer-Polymer Hybrids: Paving the Way to the Design and Implementation of Optimal Polymerization Strategies. *Chem. Eng. J.* **2019**, *363*, 259–269.
- (14) González-Ortiz, L. J.; Asua, J. M. Development of Particle Morphology in Emulsion Polymerization. 2. Cluster Dynamics in Reacting Systems. *Macromolecules* **1996**, *29* (1), 383–389.
- (15) Hamzehlou, S.; Leiza, J. R.; Asua, J. M. A New Approach for Mathematical Modeling of the Dynamic Development of Particle Morphology. *Chem. Eng. J.* **2016**, *304*, 655–666.
- (16) Deraz, N. M. Sintering Process and Catalysis. *Int. J. Nanomater. Nanotechnol. Nanomedicine* **2018**, 001–003.
- (17) Hansen, T. W.; DeLaRiva, A. T.; Challa, S. R.; Datye, A. K. Sintering of Catalytic Nanoparticles: Particle Migration or Ostwald Ripening? *Acc. Chem. Res.* **2013**, *46* (8), 1720–1730.
- (18) Gonzalez-Ortiz, L. J.; Asua, J. M. Development of Particle Morphology in Emulsion Polymerization. 1. Cluster Dynamics. *Macromolecules* **1995**, *28* (9), 3135–3145.
- (19) van Krevelen, D. W.; te Nijenhuis, K. *Properties of Polymers: Their*

*Correlation with Chemical Structure; Their Numerical Estimation and Prediction from Additive Group Contributions*, 4th ed.; Elsevier Ltd, Oxford, UK, 2009.

- (20) Calvo, I. *Mathematical Modeling of Emulsion Polymerization of Styrene Butadiene Acidic Monomers*, Euskal Herriko Unibertsitatea/ Universidad del País Vasco, 2012.
- (21) Asua, J. M.; Beuermann, S.; Buback, M.; Castignolles, P.; Charleux, B.; Gilbert, R. G.; Hutchinson, R. A.; Leiza, J. R.; Nikitin, A. N.; Vairon, J.-P.; et al. Critically Evaluated Rate Coefficients for Free-Radical Polymerization, 5 Propagation Rate Coefficient for Butyl Acrylate. *Macromol. Chem. Phys.* **2004**, *205* (16), 2151–2160.
- (22) Beuermann, S.; Buback, M. Rate Coefficients of Free-Radical Polymerization Deduced from Pulsed Laser Experiments. *Prog. Polym. Sci.* **2002**, *27* (2), 191–254.
- (23) Dube, M. A.; Penlidis, A.; O'Driscoll, K. F. A Kinetic Investigation of Styrene/Butyl Acrylate Copolymerization. *Can. J. Chem. Eng.* **1990**, *68*, 974–987.





## **Chapter 4. Effect of unreacted concentration of monomer during the second stage of process on particle morphology**

### **4.1. Introduction**

It was shown in Chapters 2 and 3 that the viscosity of the matrix (seed) during polymerization influences the development of particle morphology. Different process variables affect the viscosity including the T<sub>g</sub> of the seed, reaction temperature, amount of unreacted monomers, molecule weight and cross-linking density of the seed. In industrial practice, the polymerization processes are carried out under monomer-starved conditions to have a good thermal and microstructural control and therefore, all the experiments in Chapter 2 were carried out under monomer-starved conditions and the effect of other process variables affecting particle morphology were investigated. It was found that T<sub>g</sub> of the seed strongly influenced particle morphology. During the polymerization, the effective glass transition temperatures of both the matrix and the second stage polymer are affected by the amount of unreacted monomers. Therefore,

the instantaneous conversion affects cluster movement and coalescence, and consequently particle morphology.

This chapter explores the use of the instantaneous conversion (concentration of unreacted monomer in the reactor) as a mean to modify the particle morphology. The experiments of this chapter were designed to control the viscosity of the reaction medium by regulating the free monomer that plasticizes the polymer (instantaneous conversion) during the reaction. Hence, the viscosity of the matrix was altered and in turn, the mobility of the clusters and the radical profile in the polymer particles was varied. Experiments were carried out with target instantaneous conversion evolutions that were tracked by manipulating the monomer feed flow rate based on on-line determined heat of polymerization. For this purpose, a RTCal<sup>TM</sup> calorimeter reactor was used.

## **4.2. Experimental section**

### **4.2.1. Materials**

Technical grade monomers, methyl methacrylate (MMA, Quimidroga), styrene (S, Quimidroga), butyl acrylate (BA, Quimidroga), acrylic acid (AA, Aldrich), acrylamide (AM, Aldrich) were used as received. tert-Butyl hydroperoxide (TBHP, Aldrich) and sodium acetone bisulfite (ACBS, BASF) were used as water-soluble redox pair radical

initiator. Sodium lauryl sulfate (SLS, Aldrich) and Emulan-OG (BASF, Germany) were used as ionic and non-ionic emulsifiers, respectively. Deionized water (DI-water) was used in the formulation and hydroquinone (HQ, Aldrich) was used to stop the reaction in the samples withdrawn from the reactor. Tetrahydrofuran (GPC grade-THF, Aldrich) and ethanol (analytical standard grade, Aldrich) were used as solvent and internal standard in GC characterization, respectively.

#### 4.2.2. Synthesis of latexes

Composite polymer particle latexes were synthesized in a two stage seeded semi-batch emulsion polymerization process.

The monomer composition and the reaction conditions used in the synthesis of seeds M1 and M2 are summarized in Table 4.1. The reaction description and the formulation used in the synthesis of the seeds are given in Section 2.2.2.1.

Table 4. 1. Monomer composition and reaction conditions used in the synthesis of seeds

Seed	Monomers	Weight percent in monomer mixture	T <sub>g</sub> ,calculated (°C)	Initiator	T <sub>reaction</sub> (°C)
M1	MMA/BA/AA/AM	88/10/1/1	90	NaPS	80
M2	MMA/BA/AA/AM	75/23/1/1	60	NaPS	80

In the second stage of the process, the composite polymer particle latexes were synthesized in a commercial calorimeter reactor (RTCal™, Mettler-Toledo) equipped

with a one-liter glass reactor tank, an anchor impeller, platinum resistance thermometer, nitrogen and feeding inlets and sampling tube. RTCal™ is a leading edge technology that provides easy access to heat flow data online in real time without calibrations.<sup>1</sup> The overall monomer conversion in the second stage of polymerization in the RTCal™ was monitored continuously by measuring the heat released by polymerization,  $Q_r(t)$ , and it was calculated as follows:<sup>2,3</sup>

$$X_{overall}(t) = \frac{\int_0^t Q_r(t) dt}{\int_0^\infty Q_r(t) dt} = \frac{\int_0^t Q_r(t) dt}{\Delta H_p \cdot M_{total}} \quad (4.1)$$

where  $\Delta H_p \cdot M_{total}$  is the overall heat of polymerization for the corresponding amount of monomer in the formulation of second stage polymerization.

The information of the seed, monomer composition and reaction conditions in the second stage of polymerization for latexes studied in this chapter is summarized in Table 4.2 where the target instantaneous conversion is based on polymer and monomer produced during the second stage of the process. The comonomer (S/BA) composition was calculated to have a Tg of 40 °C using the Fox equation<sup>4</sup> and functional monomers (acrylic acid and acrylamide) were used in the formulation to provide colloidal stability. Table 4.2 also includes Run R1 from Chapter 2 that had the same seed and the same the second stage polymer than C1, but it was carried out at higher instantaneous conversion. In addition, Run R6 from Chapter 2 is also presented. This reaction used

---

the same formulation than Runs C2 and C3, but was carried out under more starved conditions.

Table 4. 2. The summary of studied composite polymer latexes.

Run	Seed		Second stage				
	Latex	T <sub>g</sub> <sup>calculated</sup> (°C)	Monomers (wt%): S/BA/AA/AM	T <sub>g</sub> <sup>calculated</sup> (°C)	T <sub>reaction</sub> (°C)	Initiator	Instantaneous conversion (%) *
R1	M1	90	67/31/1/1	40	80	TBHP+ACBS	> 84
C1	M1	90	67/31/1/1	40	80	TBHP+ACBS	70
R6	M2	60	67/31/1/1	40	65	TBHP+ACBS	> 89
C2	M2	60	67/31/1/1	40	65	TBHP+ACBS	80
C3	M2	60	67/31/1/1	40	65	TBHP+ACBS	70

\* Instantaneous conversion based on the second stage co-monomers.

Table 4. 3. Formulation used in the synthesis of composite polymer particle latexes in the second stage of polymerization in RTCa1<sup>TM</sup> (Runs C1, C2 and C3).

Material	Initial Load (g)	Feeding streams (g)		
		Pre-emulsion	Initiator solution (Main polymerization)	Initiator solution (Post polymerization)
MMA rich Seed	338			
TBHP solution, 7.65 wt%	10			
DI-water		72.450		
Emulan OG		1.275		
SDS		1.275		
AM		1.275		
AA		1.275		
BA		39.525		
S		85.425		
ACBS solution, 2.62 wt%			43.8	8.75

The formulation used in the synthesis of the composite polymer particle latexes is presented in Table 4.3.  $\Delta H_P \cdot M_{total}$  was measured in an experiment carried out using the formulation presented in Table 4.3 feeding the pre-emulsion and the initiator with constant flow rates for 90 minutes (similar to Run R1 in Chapter 2). A value of 94 KJ was measured for  $\Delta H_P \cdot M_{total}$  and employed in the other experiments to determine  $X_{overall}$  using equation 4.1.

In the experiments, the trajectory for the instantaneous conversion was tracked as a function of the overall conversion. The overall and instantaneous conversion were referred to the second stage monomer in a seeded semi-batch polymerization and are defined as follows:

$$X_{Overall} = \frac{Polymer(t)}{Monomer_{total}} \quad (4.2)$$

$$X_{Instantaneous} = \frac{Polymer(t)}{Monomer(t)} \quad (4.3)$$

where  $Monomer_{total}$  is the total amount of second stage monomer,  $Monomer(t)$  the monomer fed until time t, and  $Polymer(t)$  the second stage polymer formed until time t. From equations 4.2 and 4.3,  $Monomer(t)$ , can be expressed as a function of the total monomer in the formulation, the instantaneous conversion and the overall conversion:

$$Monomer(t) = Monomer_{total} * \frac{X_{Overall}(t)}{X_{Instantaneous}(t)} \quad (4.4)$$

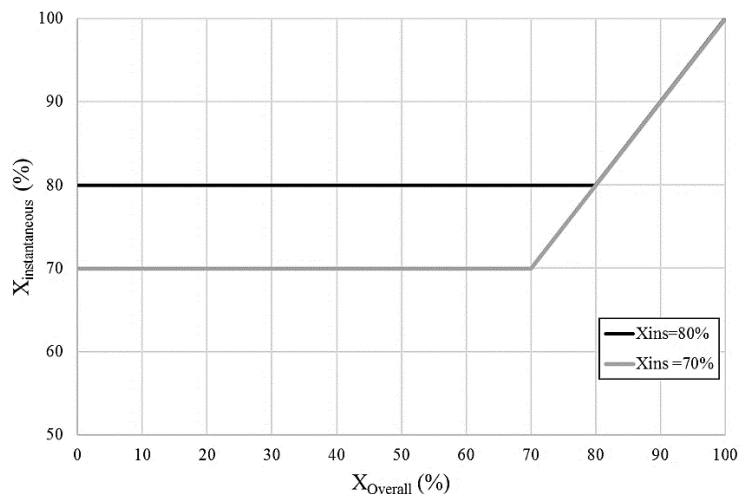


Figure 4. 1. The trajectory profiles for instantaneous conversion versus the overall conversion with target constant value during the feeding time.

Two trajectory profiles of constant values at 80% and 70% for the instantaneous conversion (of the second stage co-monomer) were considered as a function of overall conversion (Figure 4.1). These profiles were tracked measuring on-line,  $X_{Overall}(t)$ , determining  $X_{Instantaneous}(t)$  with Figure 4.1 and calculating  $Monomer(t)$  with equation 4.4. The monomer was fed as a pre-emulsion and the reductant (ACBS) of the redox initiator solution was fed as an aqueous solution, maintaining constant the ratio of reductant/ monomer.

The reactor was charged with the seed latex and TBHP aqueous solution and heated up to the reaction temperature with the impeller rotating at 160 rpm. The whole process was carried out under nitrogen. RTCal<sup>TM</sup> was programmed to set the detected  $Q_r(t)$  to zero after temperature stabilization. 2.5 wt% of pre-emulsion in 2 min and then 2.5 wt % of initiator solution in 1 min were fed to the reactor to generate the heat of polymerization, which was used to calculate overall conversion of the starting point of the defined feeding trajectories. The process continued by feeding the 97.5 wt% of pre-emulsion and the ACBS solution following the feeding trajectories defined by equation 4.4 and maintaining constant the ACBS/monomer ratio. At the end of the feeding, the reaction continued batchwise till  $Q_r(t)$  decreased to zero. Then two hours of post-polymerization were implemented by feeding the ACBS solution to remove unreacted monomers.

Figure 4.2 presents the target feeding trajectories for pre-emulsion and ACBS for Run R1 that targeted an instantaneous conversion of 70% and the actual trajectories followed during the experiment in the RTCal<sup>TM</sup>. The plot shows that the target trajectories were successfully tracked as a function of the measured overall conversion.



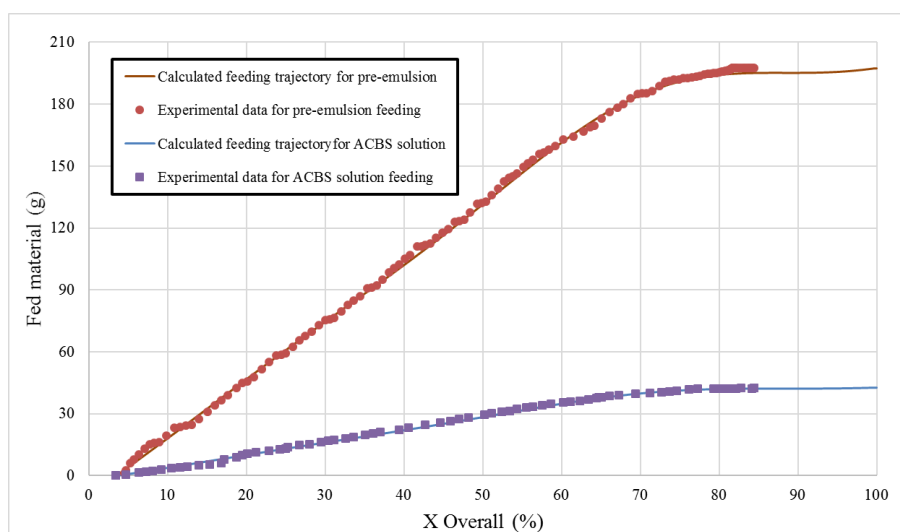


Figure 4. 2. Experimental data from RC1 vs. target feeding trajectories of pre-emulsion and ACBS solution during the feeding time of second stage of polymerization for Run C1. The target instantaneous conversion was 70% based on the monomers from second stage of polymerization.

#### 4.2.3. Latex characterization

The monomer conversions was measured by GC and particle morphologies by TEM as explained in Appendix I. Moreover, Runs R1 and C1 were characterized using coupled HAADF-STEM tomography and image reconstruction as explained in Chapter 3.

### 4.3. Results and discussion

The evolution of the instantaneous conversion based on second stage monomers for a target of 70% for Runs C1 and C3 and 80% for Run C2 is presented in Figure 4.3.

Notably, the instantaneous conversions measured by gas chromatography of samples withdrawn from the reactor are in good agreement with the instantaneous conversion measured on-line by calorimetry.

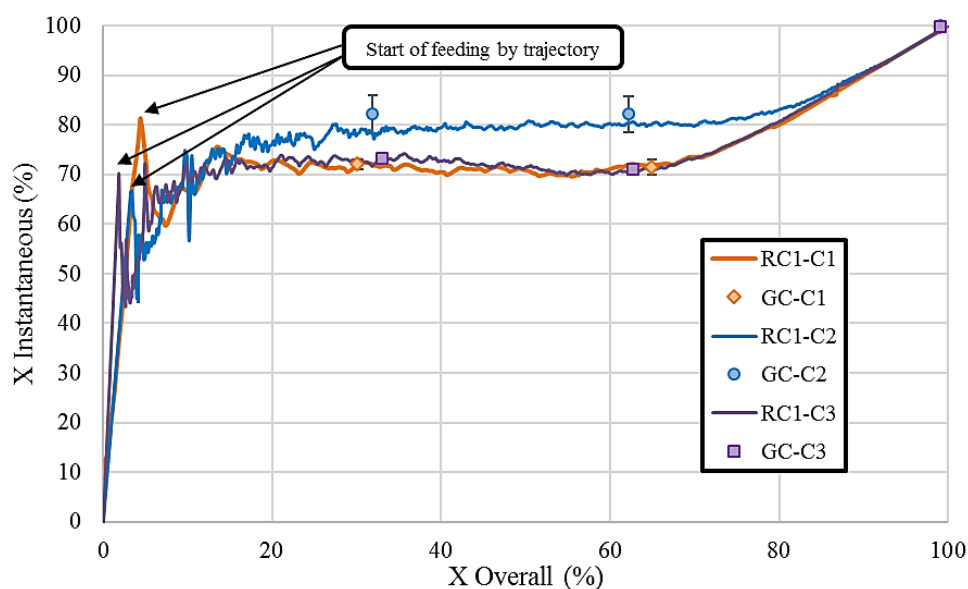


Figure 4. 3. Evolution of instantaneous conversion over the overall conversion for Runs C1, C2 and C3. Lines are instantaneous conversion measured on-line by calorimetry and points measured by gas chromatography.

Figure 4.4 presents the 3D reconstructed images of Runs R1 and C1, as well as conventional TEM images of the stained samples for comparison. It can be seen that even though the instantaneous conversion in Run C1 was low, still most of the second stage polymer formed large clusters at near the surface of the particle, although they

were more embedded in the particle than for Run R1. On the other hand, the size of the clusters was larger for C1 (the cluster size distributions for Runs R1 and C1 are shown in Appendix II).

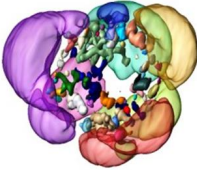
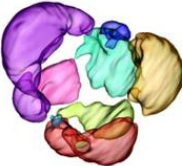
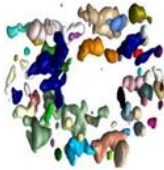
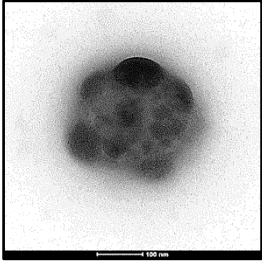
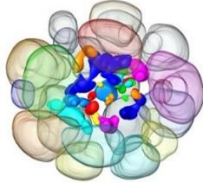

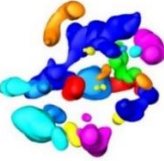
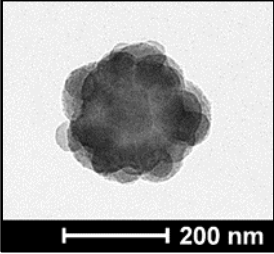
Run	Reconstructed image	External clusters	Internal clusters	TEM
R1				
C1				

Figure 4. 4. Reconstructed 3D image of polymer particle of Runs R1 and C1 by tomographic analysis of samples by HAADF-STEM and the corresponding TEM images (the scale is 100 nm).

The analysis of these data is not simple because the lower instantaneous conversion in Run C1 resulted in a higher polymerization rate (as a consequence of the higher monomer concentration) and therefore, in substantially shorter process time. Figure 4.5

presents the time evolution of the estimated effective Tgs of the matrix and clusters for Runs R1 and C1. It can be seen that up to about 35 min, the difference between the reaction temperature and the effective Tg of the matrix was larger for Run C1, namely the clusters could move easier. After 35 min, the opposite situation occurred, but the difference ( $T_{reaction} - T_{effective,matrix}$ ) was that small that movement was unlikely in both cases.

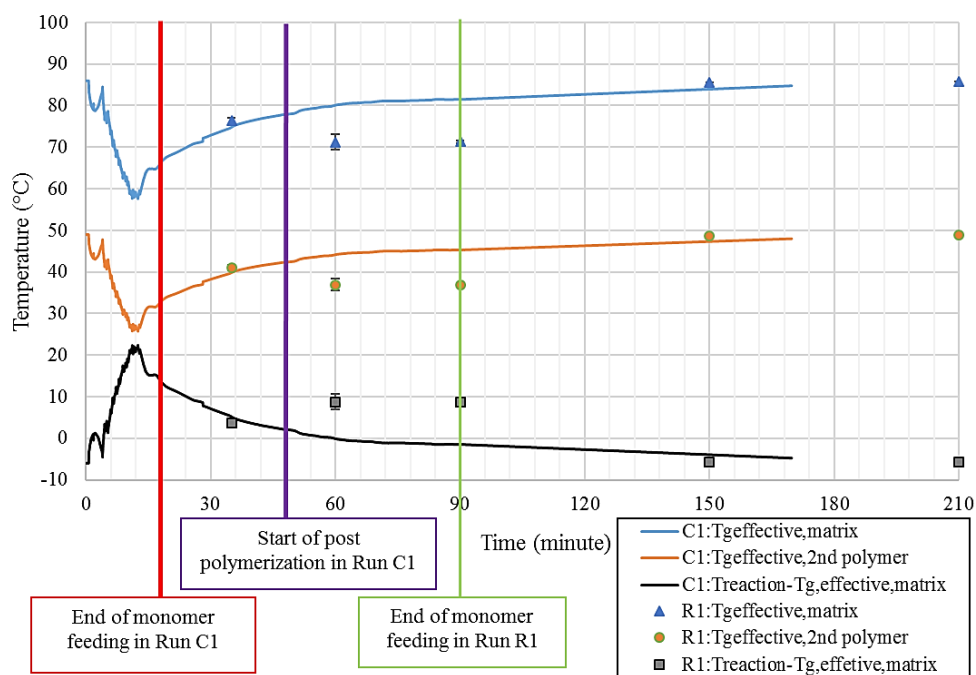


Figure 4. 5. Evolution of  $T_{g, effective}$  for matrix and second polymer calculated from equation 3.7 and the difference of reaction temperature with  $T_{g, effective}$  of matrix during the second stage of polymerization for Runs R1 and C1.

Figure 4.6 presents the predictions of the upgraded model for Runs R1 and C1. It can be seen that in agreement with the experimental finding the model predicted that the inner clusters were larger for Run C1. On the other hand, the differences in the size distribution of the outer clusters predicted by the model could not be appreciated in the reconstructed morphologies, although it should be pointed out that the number of clusters in a single particle (only a single particle was characterized by HAADF-STEM due to the time consuming technique) is not enough to have statistically significant distributions.

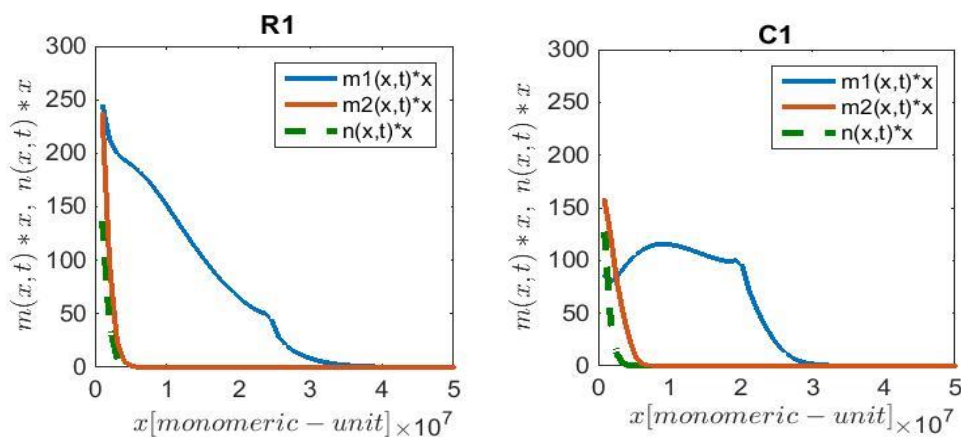


Figure 4. 6. Continuous mass cluster distribution predicted by the upgraded mathematical model for Runs R1 and C1.

Run C2 and C3 were carried out using same seed and second stage polymer and reaction temperature than R6, but at lower instantaneous conversions. As HAADF-STEM image was only available for Run C2, comparison of regular TEM images were

done in these cases. Figure 4.7 presents the TEM images of Runs R6, C2 and C3 as well as the cluster distributions predicted by the upgraded mathematical model. The evolution of the instantaneous conversions and the effective  $T_g$  of the matrix in these experiments is given in Figure 4.8. It can be seen that the TEM images clearly show that the external clusters were progressively more embedded as the instantaneous conversion decreased because the difference between the reaction temperature and the effective  $T_g$  of matrix increased. It was explained in Section 2.3.1.1, that the degree of penetration of the external clusters was not included in the model and all the clusters within the external zone are counted in one distribution ( $m_1(x)$ ). In addition, the model predicted that the fraction of interior clusters increased as the instantaneous conversion decreased because the matrix was softer. This effect was too subtle to be observed in the TEM images. At first sight, surprising result is that the size of the external clusters predicted by the model was larger for Run R6. There are two reason for that. The first one is that the particles in Run R1 were bigger (as larger seed was used) and therefore there was more second stage polymer per particle. The second is that the process time of Run R6 was substantially longer and for an important part of the process, the amount of unreacted monomer was not negligible. This monomer plasticized the second stage polymer and coalescence of the external clusters occurred leading to larger external clusters.

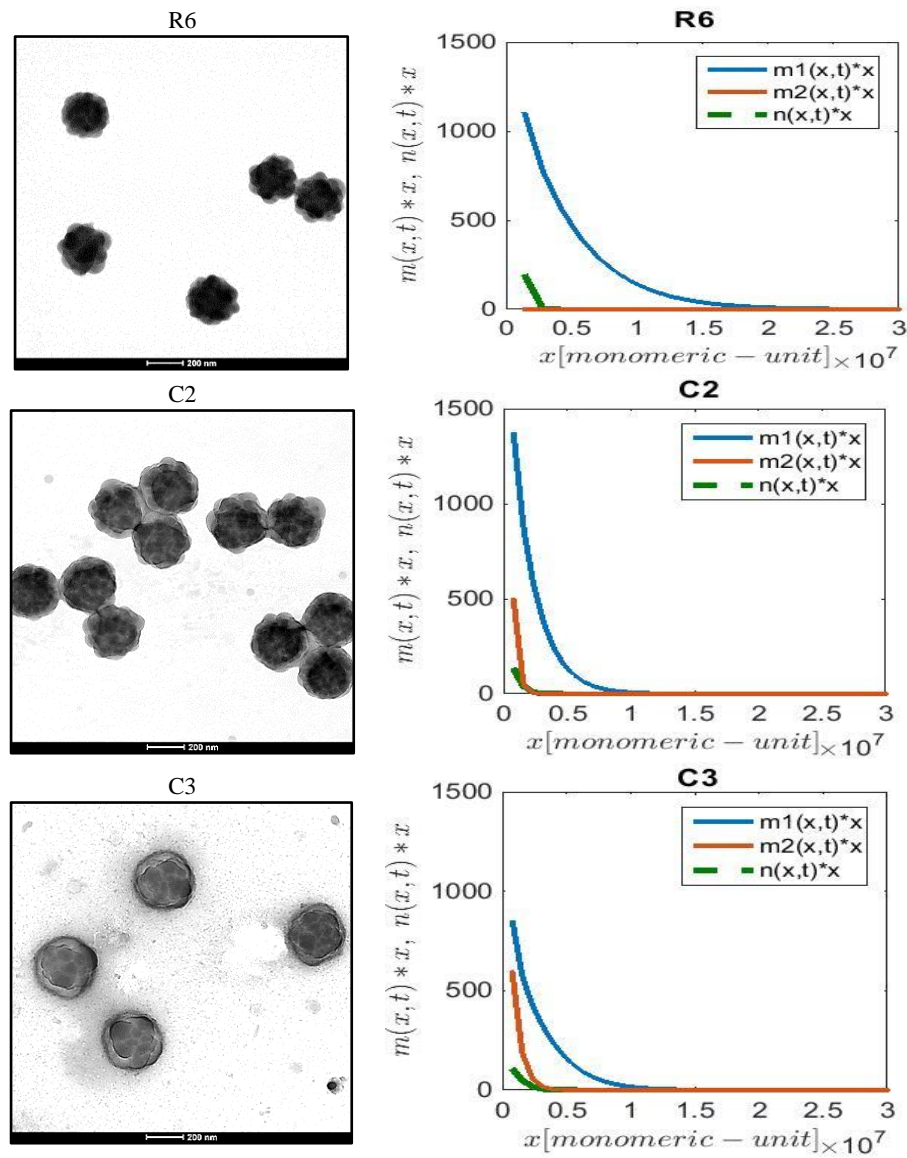


Figure 4. 7. TEM image of stained samples with the vapour of  $\text{RuO}_4$  for 1 hour compared to predicted continuous mass-cluster distributions using upgraded mathematical model from Chapter 3 for Run R6, C2 and C3. Images magnification is 25000.

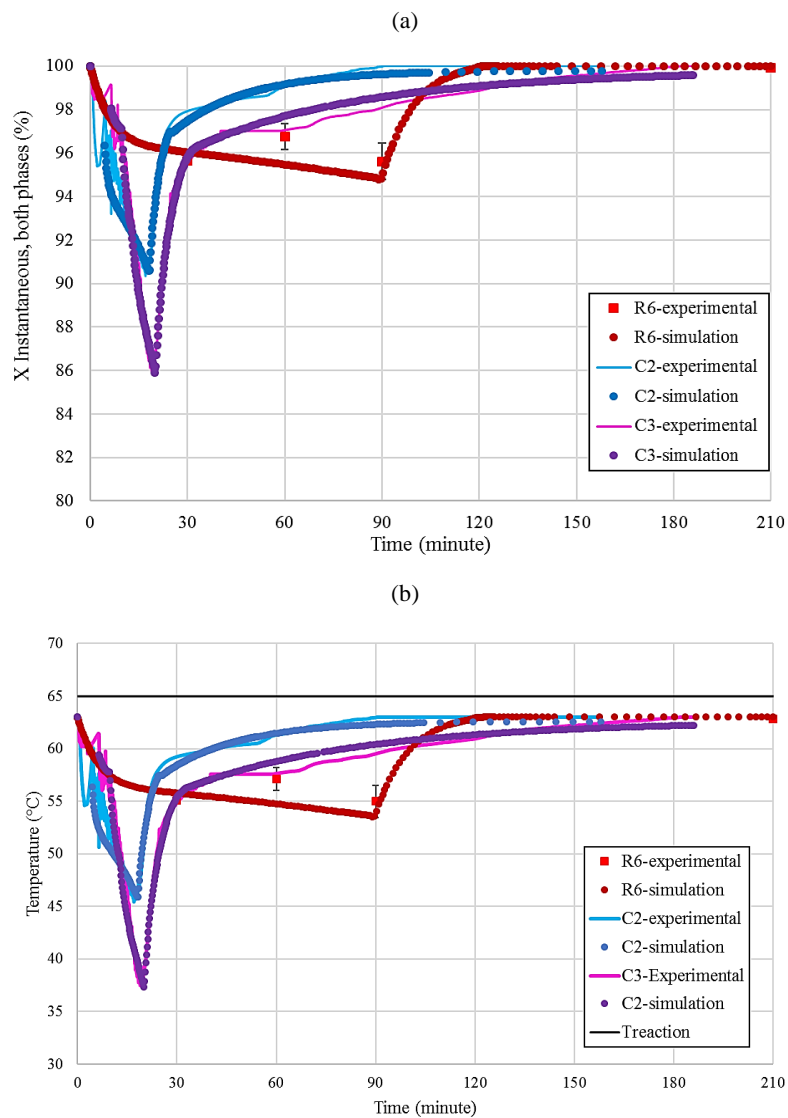


Figure 4. 8. Evolution of experimentally calculated instantaneous conversion based on polymer and monomer from both phases (a) and the  $T_{g\text{effective}}$  of matrix (b) compared to model simulated ones using equation 3.7 in Runs R6, C2 and C3.



#### 4.4. Conclusions

The discussed results in this chapter showed that, the unreacted monomers play a role similar to lowering the  $T_g$  of seed in the process. The higher the concentration of the un-reacted monomers in polymer particle, the lower the  $T_{g, \text{effective, matrix}}$  is achieved and because of softer matrix of polymerization, the clusters penetrate more in the particles. However, as the reactions were carried out using the same concentration of initiator, the higher monomer concentration led to higher polymerization rates and hence to shorter process times. The differences in process time partially compensated the effect of monomer plasticization and the effect on particle morphology was limited. The upgraded model was able to capture quite well the observed trends.

#### 4.5. References

- (1) Resources, N. O.; Oil, R.; Analyzers, B.; Chitinase, C. P. *World News*. **2007**.
- (2) Saenz de Buruaga, I.; Echevarha, A.; Armitage, P. D.; de la Cal, J.; Leiza, J. R.; Asua, J. M. On-Line Control of a Semibatch Emulsion Polymerization Reactor Based on Calorimetry. *AIChE J.* **1997**, *43* (4), 1069–1081.
- (3) Mehravar, E.; Leiza, J. R.; Asua, J. M. Synthesis and Characterization of Comb-like Acrylic-Based Polymer Latexes Containing Nano-Sized Crystallizable Domains. *Polymer*. **2016**, *84*, 167–177.
- (4) Fox, T. G. Influence of Diluent and of Copolymer Composition on the Glass Temperature of a Polymer System. *Bull. Am. Phys. Soc.* **1956**, *1*, 123–132.



## **Chapter 5. Effect of process disturbances on development of particle morphology**

### **5.1. Introduction**

As discussed in Chapter 1 the aim of this PhD is to pave the way to process optimization and on-line control of particle morphology in emulsion polymerization process as it is a long-term goal for latex industry. Currently, the production strategies used commercially are largely based on extensive experimental work guided by a rich literature on the effect of the operation variables on the final particle morphology.<sup>1-9</sup> However, it is open to discussion if this approach would be sufficient in a scenario of strong international competition. Thus, using a mathematical model for the process<sup>10</sup> it has been recently demonstrated *in silico* that the optimal strategies involved complex profiles of temperature and monomer feedings<sup>11</sup>, which are unlikely to be obtained by the currently used approach. Even if a suboptimal strategy is obtained based on extensive experimental work with the help of the qualitative guide, the practical implementation will be restricted to open loop control, which cannot cope with unexpected uncertainties often encountered in real practice. A closed-loop control

strategy would be preferable. Figure 5.1 shows a typical scheme for a model based closed-loop strategy of a polymerization process.

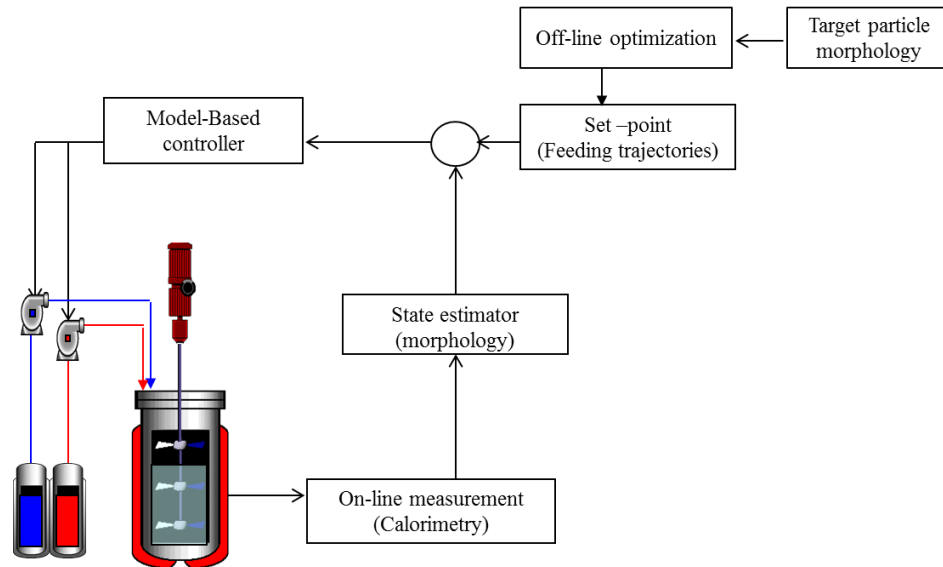


Figure 5. 1. Scheme of a closed-loop control strategy for a polymerization process with the target of particle morphology.

The strategy requires on-line measurements of the property to be controlled or a state estimation algorithm that with available measurements and a mathematical model of the process will infer the state variables and the property to be controlled. In addition, the mathematical model of the process should be used to obtain optimal trajectories of the state variables that would ensure the production of the desired polymer properties. The estimated states and the target values obtained from the optimization of the

mathematical model are used by a nonlinear model based controller to calculate the values of the manipulated variables (e.g., flow rates of monomers).

Unfortunately, there are no devices available for on-line monitoring of the particle morphology and particle morphology is not observable from other online available measurements. This situation is not new in polymer reaction engineering and ways to overcome it have been proposed. Thus, on-line control of copolymer composition monitoring the polymerization rate by calorimetry has been carried out.<sup>12</sup> With such a measurement, the instantaneous conversions (concentrations) of the individual monomers are not observable. Therefore, strict closed-loop control is not possible. However, the Mayo-Lewis equation (the mathematical model for such a system) can be used as state estimator/soft sensor because it provides a very good estimation of the conversions of the individual monomers, i.e. of the copolymer composition. This allowed achieving on-line control of the non-observable copolymer composition for different cases<sup>12,13</sup>. This idea has been extended to the on-line control of the molar mass distribution of linear polymers (another non-observable characteristic).<sup>14,15</sup>

Therefore, it is expected that both process optimization and on-line control would be possible if a mathematical model for the evolution of the particle morphology is available. The model can be directly used in optimization algorithms and as a “soft”

sensor in on-line monitoring. A model for the development of the morphology of composite particles has been recently proposed<sup>10</sup> and it has been upgraded and validated in this thesis, as it has been shown in Chapters 2-4 by comparing the model predictions with the experimental particle morphologies generated by modifying operation conditions of the conventional seeded semibatch emulsion polymerization used to produce composite polymer particles. Therefore, the validated mathematical model (with the adjusted parameters obtained in Chapter 3) can be used to determine optimal trajectories of monomers for the production of desired particle morphologies. Unfortunately, this was not possible in the limited time framework of this PhD and hence the on-line control of the particle morphology in an emulsion polymerization has not been demonstrated, but the necessary tools (e.g., the predictive mathematical model and experimental techniques to unambiguously determine composite particle morphology) to implement such strategy has been provided.

Despite not being able to implement such strategy, the effect that process disturbances might have on the development of particle morphology in emulsion polymerization was analyzed in this chapter in which a monomer feeding trajectory was tracked on-line using a calorimetry as a function of overall conversion (as in the experiments carried out in chapter 4). It was known from previous experiments that the tracked trajectory led to a multi-lobed particle morphology. The purpose of the study

was to analyse the effect of a disturbance (e.g., deliberately adding a shot of a solution of hydroquinone) on the final particle morphology under different trajectory tracking methods.

## **5.2. Experimental section**

The materials and the procedure used in the synthesis of the latexes are explained in Sections 4.2.1 and 4.2.2, respectively. The synthesized latexes are summarized in Table 5.1 that were characterized by TEM as explained in Appendix I. The experiments were carried out using the strategy explained in Chapter 4 to control the unreacted monomer concentration of the second stage of polymerization at a target value. In these experiments (Run D1-D3), the concentration of the unreacted monomers was chosen as to maintain the instantaneous conversion at 80%.

Table 5.2 summarizes the experiments. Run D1 is the reference experiment in which a target trajectory for the instantaneous conversion was sought. This trajectory is online tracked using the heat released during the polymerization as online measurement. The pre-emulsion and initiator solution streams used as manipulated variables to track the trajectory, were fed using the dosing loop control in the calorimeter reactor software. In Runs D2 and D3, the same trajectory was sought but a shot of (15 ml) hydroquinone solution (5 wt%) was injected to the reactor at an overall conversion of 50-55% to introduce a disturbance in the system.

Table 5. 1. Summary of composite polymer particle latexes synthesized in this chapter.

Run	Seed		Second stage				
	Monomer	T <sub>g,calculate</sub> (°C)	Monomer	T <sub>g,calculated</sub> (°C)	T <sub>reaction</sub> (°C)	Initiator	Instantaneous conversion <sup>*</sup>
D1	MMA/BA/AA/AM	60	S/BA/AA/AM	40	80	TBHP+ACBS	80
D2	MMA/BA/AA/AM	60	S/BA/AA/AM	40	80	TBHP+ACBS	80
D3	MMA/BA/AA/AM	60	S/BA/AA/AM	40	80	TBHP+ACBS	80

\*Based on polymer and monomer from second stage of process

Table 5. 2. Summary of operational trajectories used in the synthesis of latexes

Run	Feeding trajectory		HQ solution
	Pre-emulsion	Initiator solution	
D1	Equation 4.4	Linked to monomer feeding	No
D2	Equation 4.4	Linked to monomer feeding	Yes
D3	Equation 4.4	Constant feeding	Yes

In Run D2, the monomer and initiator feeding rates were lumped; namely, both feeding rates were a function of the heat generated during the polymerization. In Run D3, both feeding rates were decoupled; whereas the pre-emulsion feeding rate followed the output calculated online by equation 4.4; the flow rate of the ACBS solution was set on a constant flow rate. Particle morphology of the final latexes was measured for all experiments and the effect of the disturbance on the morphology achieved were analyzed.



### 5.3. Results and discussion

Figure 5.2 shows the target trajectory for the instantaneous conversion and the ones achieved during the three runs. The generated heat of polymerization vs process time for Run D1, D2 and D3 is shown in Figure 5.3. Figure 5.4 shows the time evolution of the amount of pre-emulsion fed to the reactor to follow the trajectory of Figure 5.2.

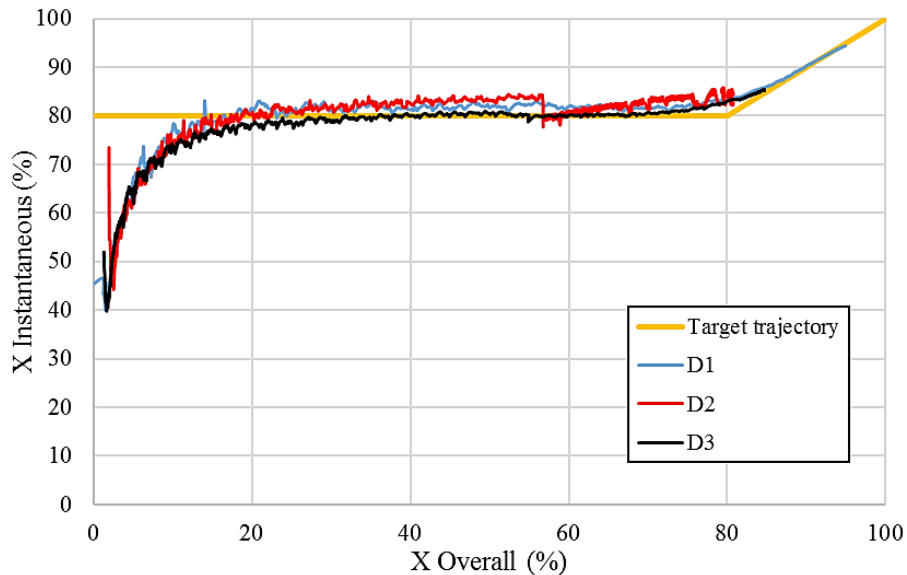


Figure 5. 2. Target trajectory for the instantaneous conversion and the experimentally measured evolution of instantaneous conversion over the overall conversion for Runs D1, D2 and D3.

It can be seen that in Run D2, after HQ injection, the  $Q_r$  decreased sharply and did not recover its value again, whereas in Run D3 upon the addition of the HQ solution,

the reaction rate sharply decreased initially, but it recovered to reach similar value of generated heat. The different behaviour of the evolution of the heat of reaction upon the introduction of the disturbance is due to the different control designs for the pre-emulsion and initiator solution in Runs D1 and D2 (lumped pre-emulsion and initiator dosing control) and Run D3 (decoupled dosing control loops for pre-emulsion and initiator solution). The dosing of pre-emulsion and initiator solution in Runs D1 and D2 was a function of the overall conversion, which is calculated on-line from the heat released by polymerization. Thus, the addition of HQ solution in Run D2 led to a strong decrease of polymerization rate, which was reflected in the very low amount of heat released and hence to a strong decrease of the feeding of the pre-emulsion (see the strong decrease of the slope in Figure 5.4). Since the initiator feeding was lumped to the monomer feeding, the amount of initiator could not compensate the scavenging effect of the added HQ and the polymerization reaction proceeded very slowly and only reached 80% of overall conversion after 210 minutes.

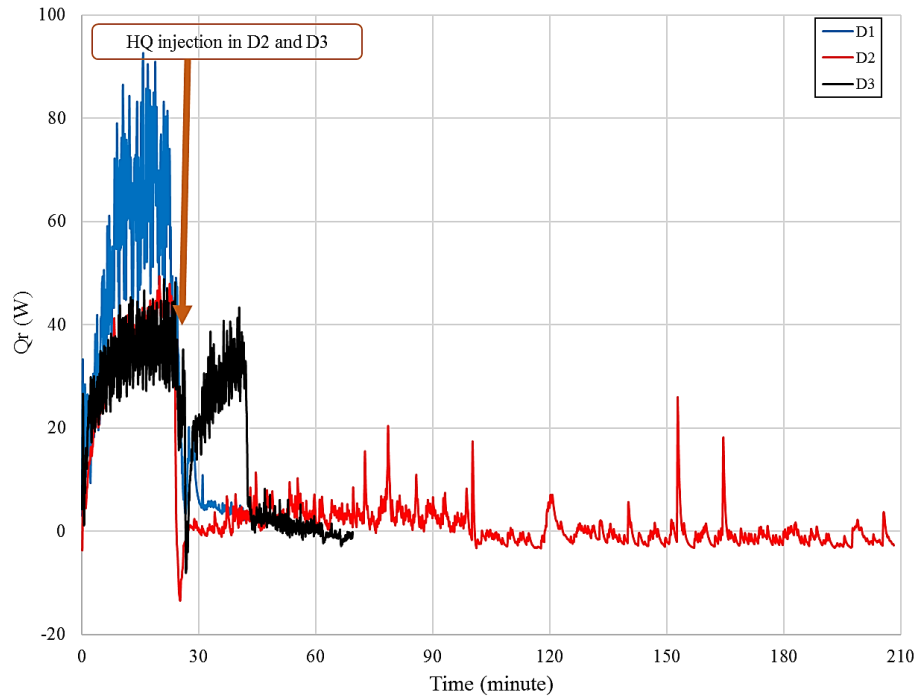


Figure 5. 3. Generated instantaneous heat of polymerization over process time for Run D1, D2 and D3.

In Run D3, the addition of the initiator solution was made using a constant flow rate from the beginning of the polymerization; namely the initiator solution feeding rate was independent of the monomer feeding rate, and hence not linked to the rate of polymerization. Therefore, upon introducing the disturbance, the heat released decreased sharply because radical concentration decreased, the monomer consumption lowered and consequently the monomer feeding rate decreased. However, since

initiator feeding rate was maintained, the initiator added did eventually compensated the effect of the HQ and polymerization rate was recovered and monomer feeding followed the target trajectory (that was based on overall conversion). Figure 5.4 shows this feature clearly. After the addition of HQ, the flow rate of pre-emulsion stopped (little plateau) for few minutes, but then it recovered although the slope is slightly smaller than before the disturbances. The polymerization was completed by the adding total amount of pre-emulsion after 70 minutes.

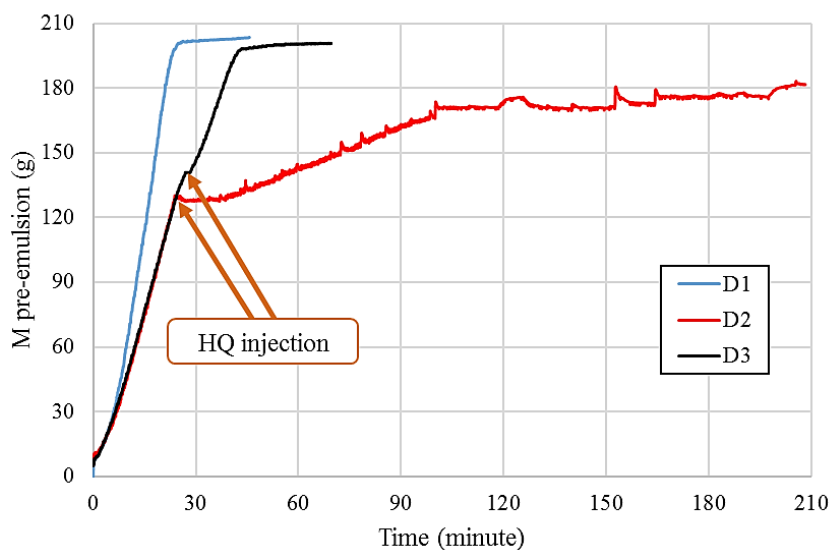


Figure 5. 4. Amount of fed pre-emulsion over time in Runs D1, D2 and D3.

Figure 5.5 shows the particle morphologies of the synthesized latexes in this chapter. As expected from previous experiments, particles with lobes partially

embedded in the matrix were obtained in Run D1. However, the morphology obtained in experiment D2 was noticeable different. The shape of the particle was almost spherical with lobes of the second stage polymer embedded in the matrix. This effect on the morphology is likely related to the longer time that the system remained at 80% conversion upon the addition of the HQ to the reactor. As it can be seen in Figure 5.4, the polymerization proceeded very slowly up to 210 minutes with a substantial amount of monomer in the polymer particles that plasticized the matrix and favoured movement/aggregation of the clusters. It may be argued that as the total amount of second stage monomer added to the reactor was less than in Run D1, the volume of clusters was not enough to protrude at the surface of the particles. However, the total amount of monomer added was about 90% of that in Run D1 and this difference is not enough to form large clusters protruding from the surface of the particle. Contrary to Run D2, the morphology of the particles produced in Run D3 is similar to that of Run D1. In run D3 as shown in Figures 5.3 and 5.4, the effect of the disturbances did only affect for some minutes and the polymerization was completed following the target trajectory. These results indicate the importance of the kinetics on the development of the particle morphology in emulsion polymerization. Although the conversion evolution of the unreacted monomer concentration in the polymer particles ( the trajectory tracked) was the same in the three experiments (see Figure 5.2) the

morphology achieved for the longer process was substantially different because cluster aggregation and movement is a kinetically controlled process.

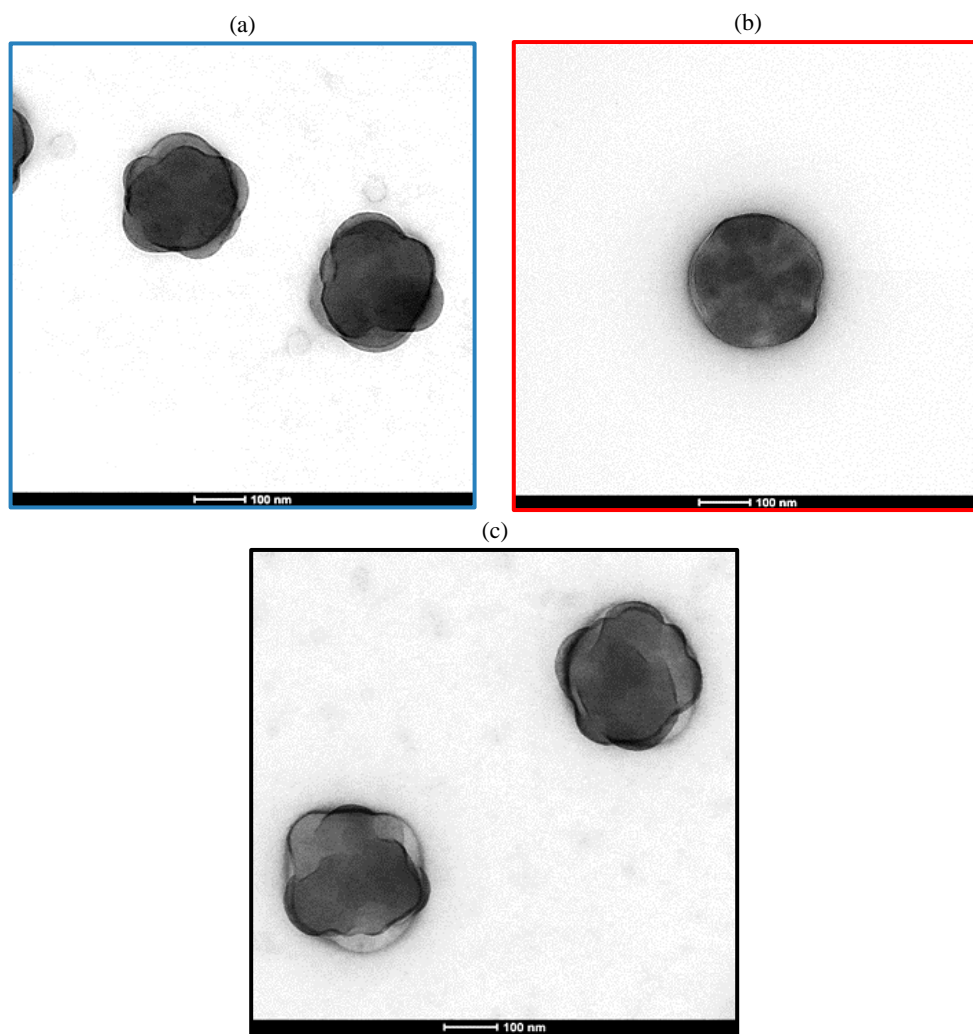


Figure 5. 5. TEM image of stained samples with the vapour of RuO<sub>4</sub> for 1 hour of Runs D1 (a), D2 (b) and D3 (c). Images magnification is 50000.

#### 5.4. Conclusion

In this chapter, the effect of process disturbances caused by addition of inhibitor on the particle morphology development was studied. In the cases studied, the value of instantaneous conversion was maintained constant (80%) as the overall conversion increased. However, the disturbances led to different process times. It was observed that the effect of the disturbances was closely related to the temporal profiles of the instantaneous conversion. As the instantaneous conversion was constant, the longer the process time, the more embedded were the clusters. On the other hand, when the disturbance lasted a short time, the morphology was not affected. Therefore, it is critical to design a control system able to follow closely the temporal track of the instantaneous conversion.

#### 5.5. References

- (1) Chen, Y. C.; Dimonie, V. L.; Shaffer, O. L.; El-Aasser, M. S. Development of Morphology in Latex Particles: The Interplay between Thermodynamic and Kinetic Parameters. *Polym. Int.* **1993**, *30* (2), 185–194.
- (2) Sundberg, D. C.; Durant, Y. G. Latex Particle Morphology, Fundamental Aspects: A Review. *Polym. React. Eng.* **2003**, *11* (3), 379–432.
- (3) Karlsson, L. E.; Karlsson, O. J.; Sundberg, D. C. Nonequilibrium Particle Morphology Development in Seeded Emulsion Polymerization. II. Influence of Seed Polymer Tg. *J. Appl. Polym. Sci.* **2003**, *90* (4), 905–915.
- (4) Stubbs, J. M.; Sundberg, D. C. Nonequilibrium Particle Morphology Development in Seeded Emulsion Polymerization. III. Effect of Initiator End Groups. *J. Appl. Polym. Sci.* **2004**, *91*, 1538–1551.

- (5) Stubbs, J. M.; Sundberg, D. C. Nonequilibrium Morphology Development in Seeded Emulsion Polymerization. IV. Influence of Chain Transfer Agent. *J. Appl. Polym. Sci.* **2006**, *102* (2), 945–957.
- (6) Stubbs, J. M.; Sundberg, D. C. Nonequilibrium Morphology Development in Seeded Emulsion Polymerization. V. The Effect of Crosslinking Agent. *J. Appl. Polym. Sci.* **2006**, *102* (3), 2043–2054.
- (7) Reyes, Y.; Akhmastkaya, E.; Leiza, J. R.; Asua, J. M. Particle Morphology. In *Chemistry and technology of emulsion polymerisation*; van Herk, A. M., Ed.; Wiley, UK, 2013; pp 145–167.
- (8) Blenner, D.; Stubbs, J.; Sundberg, D. Multi-Lobed Composite Polymer Nanoparticles Prepared by Conventional Emulsion Polymerization. *Polymer*. **2017**, *114*, 54–63.
- (9) Hamzehlou, S.; Leiza, J. R. Morphology of Composite Polymer Latexes: An Update on Synthesis and Applications, Modeling, and Characterization. In *Polymer Reaction Engineering of Dispersed Systems. Advances in Polymer Science, vol 281*; Pauer, W., Ed.; Springer, Cham, 2017; pp 105–141.
- (10) Hamzehlou, S.; Leiza, J. R.; Asua, J. M. A New Approach for Mathematical Modeling of the Dynamic Development of Particle Morphology. *Chem. Eng. J.* **2016**, *304*, 655–666.
- (11) Faust, J. M. M.; Hamzehlou, S.; Leiza, J. R.; Asua, J. M.; Mhamdi, A.; Mitsos, A. Dynamic Optimization of a Two-Stage Emulsion Polymerization to Obtain Desired Particle Morphologies. *Chem. Eng. J.* **2019**, *359*, 1035–1045.
- (12) Saenz de Buruaga, I.; Echevarha, A.; Armitage, P. D.; de la Cal, J.; Leiza, J. R.; Asua, J. M. On-Line Control of a Semibatch Emulsion Polymerization Reactor Based on Calorimetry. *AIChE J.* **1997**, *43* (4), 1069–1081.
- (13) Saenz de Buruaga, I.; Armitage, P. D.; Leiza, J. R.; Asua, J. M. Nonlinear Control for Maximum Production Rate of Latexes of Well-Defined Polymer Composition. *Ind. Eng. Chem. Res.* **1997**, *36* (1992), 4243–4254.
- (14) Vicente, M.; Benamor, S.; Gugliotta, L. M.; Leiza, J. R.; Asua, J. M. Control of Molecular Weight Distribution in Emulsion Polymerization Using On-Line Reaction Calorimetry. *Ind. Eng. Chem. Res.* **2001**, *40* (1), 218–227.



- (15) Vicente, M.; Leiza, J. R.; Asua, J. M. Simultaneous Control of Copolymer Composition and MWD in Emulsion Copolymerization. *AIChE J.* **2001**, *47* (7), 1594–1606.



## Chapter 6. Conclusions

This PhD aimed at paving the way to process optimization and on-line control of particle morphology in emulsion polymerization process. The bottleneck in achieving this goal is the lack of proper device for on-line monitoring of particle morphology. Therefore, the alternative is using a mathematical model as a soft sensor in on-line monitoring. The model needs to be capable of describing the evolution of the particle morphology during the polymerization as well as being sensitive to detect the effect of process variables on morphology changes. Experimental quantitative data of particle morphology is needed to validate the mathematical model. Different characterization techniques are required to characterize the particle morphology of the latexes and none of them does not provide quantitative information currently. This implies that there is the room for developing developing new techniques that can characterize particle morphology in quantitative mode. Moreover, the capability of the developed control strategies to cope with the unexpected uncertainties that often occur in a real system is important. Therefore, the implemented model can be used as state-estimator to track the optimal pathway in the process.

The composite polymer-polymer particle latexes were synthesized in a two-step seeded semi-batch emulsion polymerization. More hydrophobic co-monomers (Styrene/n-butyl acrylate) were polymerized in the second stage of polymerization using a more hydrophilic seed of poly (methyl methacrylate-co-n-butyl acrylate). According to thermodynamics, the equilibrium morphology for the studied cases was "inverted core-shell" while in all synthesized cases in this thesis; kinetically meta-stable morphologies were achieved due to determining effect of radical concentration profile on the development of the particle morphology. The effect of different reaction variables to alter the movement of synthesized clusters at the exterior zone of the particles toward to the equilibrium position in the center of the particles was studied.

In the studied cases for the effect of T<sub>g</sub> of seed on particle morphology, the evolution of the morphology was determined by Cryo TEM and TEM of samples stained with RuO<sub>4</sub>. It was found that in the second stage of the process many of small lobes were formed initially at the surface of the seed. The size of the lobes increased and their number decreased by the combined effect of polymerization and coagulation. Molar mass distribution of the seed increased by increasing in the amount of BA in the softer seed, likely because of increased probability of intermolecular chain transfer to polymer and therefore led to higher viscosity of the matrix. It was observed that lowering the T<sub>g</sub> of the seed was prominent on reducing the viscosity of the matrix than

its increase due to higher molar mass of polymer chains and the softer the seed, the higher extent of penetration of the clusters in the particles was achieved. The developed mathematical model by Hamzehlou *et al.*<sup>1</sup> was modified to account for the effect of radical concentration profile on the development of particle morphology. In agreement with the experimental observation, the mathematical model predicted higher extent of penetration of the clusters toward the equilibrium position at the center of the particle by softening the seed.

More spherical particles were synthesized changing the T<sub>g</sub> of second stage polymer from lower than reaction temperature to above it using a soft seed. It was difficult to conclude the position of the clusters inside the particles from conventional TEM images while the mathematical model predicted less cluster penetration toward the center of the particle and smaller clusters were captured in the interior non-equilibrium positions. The differences in the model predictions were due to the fact that in the model, the T<sub>g,effective</sub> that affected the coefficients controlling the movement of clusters was calculated taking into account the contribution of the polymers from seed and second stage and that of the monomer. On the other hand, increasing the T<sub>g</sub> of second stage polymer using a hard seed, spherical particles with small clusters was achieved instead of multi-lobed protruding one while the model predictions deviated from the experimental observations. The results suggested that contrary to the assumed

---

dependency of movement and coagulation of the clusters on the T<sub>g</sub> of seed and second stage polymer in the mathematical model, the size of the clusters was mainly determined by the T<sub>g</sub> of the second stage polymer, whereas the migration towards the equilibrium morphology was controlled by the T<sub>g</sub> of the matrix.

In the studied cases for the effect of reaction temperature in the second stage of polymerization, it was observed that at higher reaction temperature cluster coagulated more and the model predicted more cluster penetration toward the equilibrium position.

The nature of initiator in the second stage of polymerization, strongly affects the final morphology. Changing from water-soluble initiator to an oil soluble one, led to flatter radical concentration profile in the particles and the morphology changed from multi-lobed protruding morphology to the cluster occluded one. Although in that case, the inverted core-shell morphology was not achieved due to high viscosity of the matrix.

The effect of crosslinking of the seed on the morphology strongly depends on the reactivity of the double bonds in the crosslinking molecule compared to the used monomer. In a cross-linked seed, the elastic forces compete with van der Waals forces in the network of polymerization and result in the hindering of the cluster movements.

The predicted cluster distributions by mathematical model compared to experimental data revealed that the dependency of the parameters controlling the movement and coagulation of the clusters needed to be modified. Moreover, it was recognized that although the combination of different characterization techniques can provide reliable knowledge about the particle morphology development, it was difficult to reach the conclusion on the effect of process variables on the morphology changes in some cases. To overcome this limit, a method for the precise quantitative 3D characterization of polymer-polymer composite waterborne particles based on high angular dark field-scanning transmission electron microscopy (HAADF-STEM) coupled with image reconstruction was presented.

The potential of this technique was demonstrated in the study of the effect of process variables ( $T_g$  of both the seed and second stage polymer and type of initiator) on particle morphology development.  $T_g$  of the seed determines the viscosity of the particle, which in turn hinders the movement of the clusters. The driving forces for this movement are the van der Waals forces among the clusters (attractive) and between the clusters and the aqueous phase (repulsive). The latter force pushed the clusters toward the center of the particle (equilibrium morphology). Therefore, for the water-soluble initiator, the large clusters of poly(S-BA) formed lobes protruding from the surface of the particle when a hard seed ( $T_g = 86\text{ }^\circ\text{C}$ ) was used, and these clusters were more

embedded in the particle for lower  $T_g$  seeds. The presence of these large clusters at the outer region of the particle caused an unexpected effect on the position of the smaller inner clusters, which were affected by two opposite van der Waals forces. The repulsive force with the aqueous phase pushed the clusters toward the center of the particle and the attractive one with the large clusters that directed them toward the outer part of the particle. The detailed characterization shows that the attractive one was the predominant force, which suggests the introduction of backward movement in the model used. The observed small internal clusters from HAADF-STEM tomography suggests that among different aggregation mechanism (Ostwald ripening and coalescence due to van der Waals forces) involved in the coalescence of the clusters, the Ostwald ripening was not the main mechanism. Therefore, it could be concluded that the movement of the clusters was controlled by the  $T_g$  of the matrix and  $T_g$  of second stage polymer controlled the coalescence of the clusters located at the exterior of the particle. The mathematical model was upgraded including the backward movement and dependency of the cluster movement and coalescence on the  $T_g$ s of the matrix and the second stage polymer, respectively. The cluster size distributions predicted by the upgraded model for the effect of  $T_g$  of seed on the particle morphology development were in agreement with experimental observations.



Although the presented method is the only available characterization technique capable of providing accurate information about the morphology of complex polymer-polymer composite particle latexes, it is extremely time consuming and therefore it is worthy to have experimental cluster distribution statistically meaningful.

Nevertheless, the information about the morphology gathered by this technique revealed mechanistic features on the development of the particle morphology that could not be captured by the conventional TEM images and hence it allowed upgrading the mathematical model. All overall, the upgraded model provides a better prediction of the effect of process variables on the morphology of composite polymer particles and this opens the way to use the model in optimization and on-line control strategies.

It was shown that the unreacted monomers play a role similar to lowering the  $T_g$  of seed in the process. The higher the concentration of the un-reacted monomers in polymer particle, the lower the  $T_{g, \text{effective, matrix}}$  is achieved and because of softer matrix of polymerization, the clusters penetrate more in the particles. However, as the reactions were carried out using the same concentration of initiator, the higher monomer concentration led to higher polymerization rates and hence to shorter process times. The differences in process time partially compensated the effect of monomer plasticization and the effect on particle morphology was limited.

The effect of process disturbances caused by addition of inhibitor on the particle morphology development was studied. In the cases studied, the value of instantaneous conversion was maintained constant (80%) as the overall conversion increased. However, the disturbances led to different process times. It was observed that the effect of the disturbances was closely related to the temporal profiles of the instantaneous conversion. As the instantaneous conversion was constant, the longer the process time, the more embedded were the clusters. On the other hand, when the disturbance lasted a short time, the morphology was not affected. Therefore, it is critical to design a control system able to follow closely the temporal track of the instantaneous conversion.

### 6.1. References

- (1) Hamzehlou, S.; Leiza, J. R.; Asua, J. M. A New Approach for Mathematical Modeling of the Dynamic Development of Particle Morphology. *Chem. Eng. J.* **2016**, *304*, 655–666.

## List of Publication and conference presentations

Parts of this thesis have been presented in international conferences as well as in Industrial Liason Program (ILP) meeting.

- **XIV Meeting of the Group of Polymers of the Spanish Royal Chemistry and Royal Physics Societies (GEP 2016), Burgos, Spain, September 2016.**

Oral presentation: Study the effect of reaction condition on the morphology of structured polymer particles in latexes.

- **Workshop for process industry: Tackling the future of plant operation – How to integrate online data-analytics, process control, and PAT for optimal plant operation, Frankfurt, Germany, January 2017.**

Poster presentation: An innovative and fast mathematical model for prediction and control of dynamic development of latex particle morphology.

- **KoMSO challenging workshop: Challenges for mathematical modeling, simulation and optimization for advanced process control of batch processes, Heidelberg, Germany, February 2017.**

Poster presentation: An innovative and fast mathematical model for prediction and control of dynamic development of latex particle morphology.

- **International Polymer Colloids Group Conference (IPCG2017), Arantzazu, Spain, June, 25-30, 2017.**

Poster presentation: Effect of reaction variables on morphology of structured polymer nanoparticles via seeded emulsion polymerization.

- **Tackling the Future of Plant Operation -Jointly towards a Digital Process Industry, Barcelona, Spain, December 2017.**

Poster presentation: Modelling the dynamics of the particle morphology during the synthesis of structured polymer latex particles.

- **Bordeaux polymer conference, Bordeaux, France, May 2018.**

Oral presentation: Controlling the morphology of multiphase polymeric nanoparticles.

- **Polymer Reaction Engineering X (PRE 10), Punta Cana, Dominican Republic, May 2018.**

Oral presentation: Modelling and characterization of the morphology of multiphase polymeric nanoparticles.

- **23<sup>rd</sup> International Congress of Chemical and Process Engineering (CHISA 2018), Prague, Czech Republic, August 2018.**

Poster presentation: Quantitative characterization of the morphology of structured composite polymer particles by 3D TEM.

- **Working Party on Polymer Reaction Engineering, Prague, Czech Republic, September 2018.**

Oral presentation: Quantitative morphology characterization of synthesized structured polymer particles via seeded emulsion polymerization.

- **19<sup>th</sup> Industrial Liason Program (ILP) Meeting, University of the Basque country, San Sebastian, Spain.**

Oral presentation: Characterization of the morphology of composite polymer particles via tomographic analysis: towards a quantitative procedure

Parts of this thesis have been published or will be published soon. The list of papers that would be issued from this work is as follows:

- Gerlinger W., Asua J. M., Chaloupka T., Faust J. M. M., Gjertsen F., Hamzehlou S., Hauger S. O., Jahns E., Joy P. J., Kosek J., Lapkin A., Leiza J. R., Mhamdi A., Mitsos A., Naeem O., Rajabalinia N., Singstad P., Suberu J. Dynamic optimization and non-linear model-predictive control to achieve targeted particle morphologies in semi-batch emulsion polymerization, *Chemie Ingenieur Technik*, 2019, 91, No. 3, 1–14.
- Rajabalinia N., Hamzehlou S., Leiza J. R., Asua J. M. Experimental validation of a mathematical model for the evolution of the particle morphology of waterborne polymer-polymer hybrids: paving the way to the design and implementation of optimal polymerization strategies, *Chemical Engineering Journal*, 2019, 363, 259-269.
- Rajabalinia N., Hamzehlou S., Modin E, Chuvilin A, Leiza J. R., Asua J, Coupling HAADF-STEM tomography and image reconstruction for the precise characterization of particle morphology of composite polymer latexes (submitted to *Macromolecules*).

## **Resumen y conclusiones**

Este doctorado ha tenido como objetivo allanar el camino para la optimización del proceso y el control en línea de la morfología de las partículas en procesos de polimerización en emulsión. El cuello de botella para lograr este objetivo es la falta de un dispositivo adecuado para la monitorización en línea de la morfología de las partículas. Por lo tanto, la alternativa es utilizar un modelo matemático como sensor de software en el monitoreo en línea. El modelo debe ser capaz de describir la evolución de la morfología de la partícula durante la polimerización, además de ser sensible para detectar el efecto de las variables del proceso en los cambios morfológicos. Se necesitan datos cuantitativos experimentales de la morfología de partículas para validar el modelo matemático. Se requieren diferentes técnicas de caracterización para caracterizar la morfología de las partículas de los látex y ninguna de ellas proporciona información cuantitativa en la actualidad. Esto indica que hay lugar para el desarrollo de nuevas técnicas que pueden caracterizar la morfología de partículas de modo cuantitativo. Además, la capacidad de las estrategias de control desarrolladas para hacer frente a las incertidumbres inesperadas que a menudo ocurren en un sistema real es

importante. Por lo tanto, el modelo implementado se puede utilizar como estimador de estado para rastrear la ruta óptima en el proceso.

Los látex de partículas de polímero-polímero compuesto se sintetizaron en una polimerización de emulsión semicontinua sembrada en dos etapas. Los comonomeros más hidrófobos (estireno / acrilato de n-butilo) se polimerizaron en la segunda etapa de polimerización utilizando una semilla más hidrófila de poli (metacrilato de metilo-co-n- acrilato de butilo). Termodinámicamente, la morfología de equilibrio para los casos estudiados es "núcleo-corteza invertida", pero en todos los casos sintetizados en esta tesis se lograron morfologías cinéticamente meta-estables debido al efecto determinante del perfil de concentración de radicales en el desarrollo de la morfología de las partículas. Se estudió el efecto de diferentes variables de reacción para alterar el movimiento de los clúster sintetizados en la zona exterior de las partículas hacia la posición de equilibrio en el centro de las partículas.

En los casos estudiados sobre el efecto de la Tg de la siembra en la morfología de las partículas, la evolución de la morfología se determinó mediante Crio-TEM y TEM de muestras teñidas con RuO<sub>4</sub>. Se encontró que, en la segunda etapa del proceso, muchos de los lóbulos pequeños se formaron inicialmente en la superficie de la siembra. El tamaño de los lóbulos aumentó y su número disminuyó por el efecto



combinado de polimerización y coagulación. La distribución de masa molar de la siembra aumentó al aumentar la cantidad de BA en la siembra más suave, probablemente debido a la mayor probabilidad de transferencia de cadena intermolecular al polímero y, por lo tanto, condujo a una mayor viscosidad de la matriz. Se observó que la reducción de la Tg de la siembra era más importante a la hora de reducir la viscosidad de la matriz que el aumento debido a la mayor masa molar de las cadenas de polímero y cuanto más blanda era la semilla, se conseguía un mayor grado de penetración de los clúster en las partículas. El modelo matemático desarrollado por Hamzehlou et al.<sup>1</sup> se modificó para tener en cuenta el efecto del perfil de la concentración de radicales en el desarrollo de la morfología de las partículas. De acuerdo con las observaciones experimentales, el modelo matemático predijo un mayor grado de penetración de los grupos hacia la posición de equilibrio en el centro de la partícula al ablandar la siembra.

Se sintetizaron más partículas esféricas cambiando la Tg del polímero de la segunda etapa desde una más baja que la temperatura de reacción hasta una por encima de ella, usando una siembra blanda. Fue difícil concluir la posición de los grupos dentro de las partículas de las imágenes TEM convencionales, mientras que el modelo matemático predijo una menor penetración de los clúster hacia el centro de la partícula y se capturaron clúster más pequeños en las posiciones de no-equilibrio interior. Las

diferencias en las predicciones del modelo se debieron al hecho de que en el modelo, la  $T_g$  efectiva que afectó los coeficientes que controlan el movimiento de las agrupaciones se calculó teniendo en cuenta la contribución de los polímeros de la siembra, la segunda etapa y la del monómero. Por otro lado, al aumentar la  $T_g$  del polímero de segunda etapa utilizando una siembra dura, se lograron partículas esféricas con pequeños grupos en lugar de una protuberancia de múltiples lóbulos, mientras que las predicciones del modelo se desviaron de las observaciones experimentales. Los resultados sugirieron que, a diferencia de la supuesta dependencia del movimiento y la coagulación de los grupos en la  $T_g$  de la siembra y el polímero de la segunda etapa en el modelo matemático, el tamaño de los grupos se determinó principalmente por la  $T_g$  del polímero de la segunda etapa, mientras que la migración hacia la morfología de equilibrio fue controlada por la  $T_g$  de la matriz.

En los casos estudiados por el efecto de la temperatura de reacción en la segunda etapa de polimerización, se observó que, a mayor temperatura de reacción, los clúster se coagularon más y el modelo predijo una mayor penetración del grupo hacia la posición de equilibrio.

La naturaleza del iniciador en la segunda etapa de la polimerización afecta fuertemente la morfología final. El cambio de iniciador soluble en agua a uno soluble

en la fase orgánica, condujo a un perfil de concentración de radicales más plano en las partículas y la morfología cambió de morfología de múltiples lóbulos salientes a la del clúster ocluido. Aunque en ese caso, la morfología del núcleo-corteza invertida no se logró debido a la alta viscosidad de la matriz.

El efecto de la reticulación de la siembra sobre la morfología depende en gran medida de la reactividad de los dobles enlaces en la molécula de reticulación en comparación con el monómero usado. En una siembra reticulada, las fuerzas elásticas compiten con las fuerzas de van der Waals en la red de polimerización y dificultan los movimientos del clúster.

Las distribuciones de clúster predichas por modelo matemático en comparación con los datos experimentales revelaron que la dependencia de los parámetros que controlan el movimiento y la coagulación de los clúster debía modificarse. Además, se reconoció que, aunque la combinación de diferentes técnicas de caracterización puede proporcionar un conocimiento confiable sobre el desarrollo de la morfología de las partículas, fue difícil llegar a una conclusión sobre el efecto de las variables del proceso en los cambios de la morfología en algunos casos. Para superar este límite, se presentó un método para la caracterización cuantitativa precisa en 3D de partículas compuestas de polímero-polímero en base de agua mediante microscopía electrónica de transmisión

de barrido de alto ángulo angular (HAADF-STEM) junto a reconstrucción de imágenes.

El potencial de esta técnica se demostró en el estudio del efecto de las variables del proceso ( $T_g$  tanto de la siembra como del polímero de la segunda etapa y el tipo de iniciador) en el desarrollo de la morfología de las partículas. La  $T_g$  de la siembra determina la viscosidad de la partícula, lo que a su vez dificulta el movimiento de los grupos. Las fuerzas motrices para este movimiento son las fuerzas de van der Waals entre los grupos (atractivos) y entre los grupos y la fase acuosa (repulsiva). La última fuerza empuja los grupos hacia el centro de la partícula (morfología de equilibrio). Por lo tanto, para el iniciador soluble en agua, los grandes grupos de lóbulos formados de poli(S-BA) sobresalían de la superficie de la partícula cuando se usaba una siembra dura ( $T_g = 86\text{ °C}$ ), y estos grupos estaban más incrustados en la partícula en siembras de menor  $T_g$ . La presencia de estos grandes grupos en la región externa de la partícula causó un efecto inesperado en la posición de los grupos internos más pequeños, que se vieron afectados por dos fuerzas opuestas de van der Waals. La fuerza de repulsión con la fase acuosa empujó los grupos hacia el centro de la partícula y el atractivo con los grupos grandes los dirigían hacia la parte exterior de la partícula. La caracterización detallada muestra que la fuerza atractiva era la predominante, lo que sugiere la introducción de movimientos de retroceso en el modelo utilizado. Los pequeños grupos

internos observados en la tomografía HAADF-STEM sugieren que entre los diferentes mecanismos de agregación (maduración de Ostwald y coalescencia debida a las fuerzas de van der Waals) involucrados en la coalescencia de los grupos, la maduración de Ostwald no fue el mecanismo principal. Por lo tanto, se podría concluir que el movimiento de los grupos se controló mediante la Tg de la matriz y la Tg del polímero de la segunda etapa controló la coalescencia de los grupos ubicados en el exterior de la partícula. El modelo matemático se actualizó incluyendo el movimiento hacia atrás y la dependencia del movimiento del clúster y la coalescencia en las Tg de la matriz y el polímero de la segunda etapa, respectivamente. Las distribuciones de tamaño de clúster predichas por el modelo actualizado para el efecto de la Tg de la siembra en el desarrollo de la morfología de la partícula estuvieron de acuerdo con las observaciones experimentales.

Aunque el método presentado es la única técnica de caracterización disponible capaz de proporcionar información precisa sobre la morfología de los látex de partículas compuestas complejas de polímero-polímero, requiere mucho tiempo y, por lo tanto, merece la pena tener una distribución de agrupación experimental estadísticamente significativa.

Sin embargo, la información sobre la morfología recopilada por esta técnica reveló características mecanicistas sobre el desarrollo de la morfología de las partículas que las imágenes TEM convencionales no pudieron capturar y, por lo tanto, permitió actualizar el modelo matemático. En general, el modelo actualizado proporciona una mejor predicción del efecto de las variables del proceso en la morfología de las partículas de polímero compuesto y esto abre el camino para usar el modelo en estrategias de control en línea y optimización.

Se demostró que los monómeros sin reaccionar desempeñan un papel similar a la reducción de la Tg de la siembra en el proceso. Cuanto mayor sea la concentración de los monómeros no reaccionados en la partícula de polímero, menor será la Tg efectiva de la matriz, y debido a una matriz de polimerización más blanda, los grupos penetran más en las partículas. Sin embargo, como las reacciones se llevaron a cabo utilizando la misma concentración de iniciador, la mayor concentración de monómero condujo a mayores velocidades de polimerización y, por lo tanto, a tiempos de proceso más cortos. Las diferencias en el tiempo del proceso compensaron parcialmente el efecto de la plastificación de monómeros y el efecto sobre la morfología de las partículas fue limitado.

Se estudió el efecto de las perturbaciones del proceso causadas por la adición de un inhibidor en el desarrollo de la morfología de las partículas. En los casos estudiados, el valor de la conversión instantánea se mantuvo constante (80%) a medida que aumentaba la conversión global. Sin embargo, las perturbaciones llevaron a diferentes tiempos de proceso. Se observó que el efecto de las perturbaciones estaba estrechamente relacionado con los perfiles temporales de la conversión instantánea. Como la conversión instantánea era constante, cuanto más largo era el tiempo de proceso, más incrustados estaban los grupos. Por otro lado, cuando la alteración duró poco tiempo, la morfología no se vio afectada. Por lo tanto, es fundamental diseñar un sistema de control capaz de seguir de cerca el seguimiento temporal de la conversión instantánea.

### Referencias

- (1) Hamzehlou, S.; Leiza, J. R.; Asua, J. M. A New Approach for Mathematical Modeling of the Dynamic Development of Particle Morphology. *Chem. Eng. J.* **2016**, *304*, 655–666.





# Appendix I. Materials and characterization techniques

## I.1. Materials

Technical grade monomers, methyl methacrylate (MMA, Quimidroga), styrene (S, Quimidroga), butyl acrylate (BA, Quimidroga), acrylic acid (AA, Aldrich), acrylamide (AM, Aldrich), ethylene glycol dimethacrylate (EGDMA, Aldrich) and allyl methacrylate (AMA, Aldrich) were used as received. Sodium persulfate (NaPS, Fluka) as water-soluble thermal radical initiator, 2,2'-azobis (2-methylpropionitrile) (AIBN, Aldrich) as oil-soluble thermal radical initiator, tert-Butyl hydroperoxide (TBHP, Aldrich) and sodium acetone bisulfite (ACBS, BASF) as water-soluble redox pair radical initiator were used. Sodium lauryl sulfate (SLS, Aldrich) and Emulan-OG (BASF, Germany) were used as ionic and non-ionic emulsifiers, respectively. Deionized water (DI-water) was used throughout the work and hydroquinone (HQ, Aldrich) was used to stop the reaction in the samples withdrawn from the reactor. Tetrahydrofuran (GPC grade-THF, Aldrich) and ethanol (analytical standard grade, Aldrich) were used as solvent and internal standard in GC characterization,

respectively. EPoFix resin (Struers) was used as cold mounting system in sample preparation of cross-section characterization by TEM.

## **I.2. Characterization methods**

**Global conversion** of samples withdrawn from the reactor during first and second stage of polymerization were determined gravimetrically. The **instantaneous conversion** of samples withdrawn during second stage of polymerization was measured by gas chromatography (GC), using THF and ethanol as solvent and internal standard, respectively. A GC apparatus (HP 6890 series) equipped with a HP 7694E headspace sampler and a BP 20 capillary column was used. The summary of the method used in the characterization of the latex is shown in Table I.1.

**Polymer particle sizes of latexes** were measured by dynamic light scattering (DLS) using a Zetasizer Nano Series (Malvern Instrument). A few droplets of latex were diluted with deionized water to have a transparent solution. The equipment was operated at 20 °C and the reported z-average values are the average of three repeated measurements.

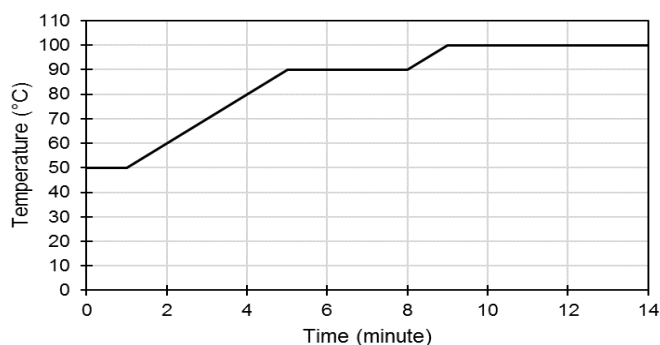
**Particle size distributions** of latexes were measured by capillary hydrodynamic fractionation (CHDF) using a CHDF 3000 apparatus (Matec applied science) with an operating flow of 1.4 ml/min at 35°C and detector wavelength at 220nm. Samples were

diluted to 0.5 wt% of solids content with the carrier (a mixture of surfactants in DI-water, 1X-GR500 from Matec) and were injected to the column. The samples were analyzed using the Matec software v.2.3.

**Table I.1.** Summary of the method used in GC analysis

Inlet flow temperature (°C)	170
Carrier gas	Helium
Detector temperature (°C)	250
Operation mode	Constant pressure

Temperature profile



**Gel fraction and swelling degree** of samples was measured by soxhlet extraction in THF<sup>1</sup>. The gel fraction is considered to be the insoluble part of polymer in a good solvent (in this work THF). A fiberglass piece of weight “ $w_f$ ” was impregnated with 2-3 droplets of latexes, dried overnight at 60 °C and weighted ( $w_p$ ). The extraction was carried out for 24 hours under reflux conditions (at about 75 °C). The gel (insoluble) fraction remained in the fiber glass and the sol part dissolved in the THF. The weight

of the fiberglass was measured in wet conditions ( $w_s$ ) and after drying overnight at 60°C ( $w_g$ ). The gel fraction and swelling degree were calculated as follows:

$$\text{gel (\%)} = \frac{w_g - w_f}{w_p - w_f} * 100 \quad (\text{I. 1})$$

$$\text{swelling degree} = \frac{w_s - (k + 1) * w_f}{w_g - w_f} \quad (\text{I. 2})$$

where  $k$  is the amount of THF (g) absorbed per gram of fiberglass itself . To measure  $k$ , four pieces of fiberglass of weight “ $w_f$ ” were kept for 24 hours under reflux conditions using THF (at about 75 °C) and then were weighted ( $w_a$ ). The amount of absorbed THF per gram of fiberglass was calculated as follows:

$$\text{THF absorbtion per gram of fiberglass} = \frac{w_a - w_f}{w_f} \quad (\text{I. 3})$$

and  $k$  was considered as the average of calculated values of the four samples.

Swelling is inversely proportional to the cross-linking density.

**The absolute molar mass distributions (MMD) of polymers** were measured by asymmetric flow field flow fractionation (AF4) equipped with a multi angle (18 angles ranging from 10° to 160°) light scattering laser photometer (MALS) (Dawn Heleos, Wyatt), a differential refractometer (RI) (Optilab Rex, Wyatt) and an Eclipse separation system AF4 (long channel, regenerated cellulose membrane, 10 KDa cut-off, Wyatt).

The chromatograms were obtained at room temperature with 1 ml/min flow rate of detector flow. The spacer was fixed at 490  $\mu\text{m}$ . A few droplets of latex were diluted with THF (to 8 or 16 mg/ml concentration) and the sample was injected to the channel after filtration (polyamide filter,  $\Phi=45 \mu\text{m}$ ). The data collection and treatment were carried out by ASTRA 6 software (Wyatt). The molar mass was calculated from the RI/MALS data using the Debye plot (with second-order Berry formalism) using weight average  $dn/dc$  value from the  $dn/dc$  values of the PS, PMMA and PBA which are 0.185, 0.084 and 0.064,<sup>2</sup> respectively.

The **morphology** of the particles was studied by transmission electron microscopy (TEM) in conventional and cryo modes, scanning electron microscopy (SEM) and environmental scanning electron microscopy (ESEM). TEM was carried out with a Tecnai™ G2 20 Twin device at 200 kV (FEI Electron Microscopes). The latexes were diluted with deionized water up to 0.05 wt% solids content, one drop of the dilution was placed on a carbon coated copper grid and dried at ambient temperature. TEM samples were stained with  $\text{RuO}_4$  vapor for 1 hour to increase the contrast of the images. Particle morphology was also determined by Cryo-TEM and for the preparation of the samples, one drop of the latex ( $\sim 3 \mu\text{l}$ ) was deposited in a copper grid (300 mesh, R QUANTIFOIL® R 2/2 EMS, Hat-field, PA, USA, hydrophilized by glow-discharged treatment just prior to use) within the environmental chamber of a FEI Vitrobot Mark

IV (Eindhoven, The Netherlands) and the excess liquid was blotted away. The sample was introduced into liquid nitrogen and transferred to a Single Tilt Cryo-Holder. The Cryo-Holder was previously prepared by 655 Turbo Pumping Station to maintain the sample at about  $-170\text{ }^{\circ}\text{C}$  and to minimize the thermal derive. Cross-section of the particles was studied by TEM of sample cross cut. Dried latexes at ambient temperature were embedded in epoxy resin and cured at room temperature in 12 hours. The cross cut slices with 70 nm thickness prepared by microtomy were collected on carbon coated copper grids and were stained with vapor of  $\text{RuO}_4$  for 1 hour to increase the image contrast.

Scanning electron microscopy (SEM) was carried out using a Hitachi S3030 SEM. The diluted sample (0.1 w%) was dry cast over double adhesive carbon tape put on 6 mm single aluminum stubs. The sample was dried over night at room temperature under vacuum and were metalized with gold with sputter coater before observation.

Environmental scanning electron microscopy (ESEM) images were obtained in a Quanta 250 FEG ESEM (FEI, Netherlands) equipped with a Peltier cooling stage and a gaseous secondary electron detector (GSED).<sup>3</sup> The characterization was carried out using the conditions reported by Gonzalez et al.<sup>4</sup> An aluminium stub of 10 mm in diameter and a height of 5 mm covered with mica was used as a substrate. To obtain

monolayer coverage of polymer particles on the substrate, the latex was diluted to 0.1 wt% solids content. A drop of the diluted latex was placed onto the substrate, which was mounted on the Peltier cooling stage using a eutectic metal alloy (Fusible Alloy 47, INNOVATOR Sp. Z o.o.) with a low melting temperature (47 °C) in order to ensure a good heat conductance. The sample was placed in the chamber at a pressure of 270 Pa. Water vapour was used to create pressure inside the chamber and thus the start-up humidity in the proximity of the sample was 42%. The pressure was kept constant during all the experiment. The temperature increased from 0°C with the ramp of 10 °C/min to 90 °C. After an increase of 5 °C or 10 °C of temperature, the samples were kept for 10 minutes and then images were taken.

**Modulated differential scanning calorimetry (M-DSC)** was used to estimate the extent of interpenetration of the two polymers.<sup>5</sup> For a completely phase separated system, the derivative of the heat capacity ( $dC_p/dT$ ) presents two peaks and the maxima are the glass transition temperature of the polymers and the  $dC_p/dT$  between the two peaks is close to the baseline. When intermixing occurs, the  $dC_p/dT$  in the region between the two peaks is higher than the baseline and the peaks are smaller and maybe closer to each other. The samples were dried at ambient temperature which is lower than the  $T_g$  of the softer phase in the polymer composite latex to prevent the film formation that can change particle morphology.<sup>6</sup> The measurements were carried out

in a Q2000 (TA instrument) equipment. The samples were characterized using the reported method by Jiang et al<sup>7</sup>: the scanning cycles consisted of sample equilibration at -30 °C and heating from -30 °C to the reaction temperature of latex. Then cooling to -30°C , heating from -30 °C to 150°C (marked as first heating cycle), isothermal at 150 °C for 60 minutes, again cooling to -30°C and finally heating from -30 °C to 150°C (marked as second heating cycle). An overall heating rate of 3 °C/min, an amplitude of  $\pm 2$  °C and a period of 60 seconds was applied to the heating cycles. The results of the first heating cycle were considered to represent the morphology of polymer particles as changes in the morphology are expected upon heating.

**Minimum film forming temperatures (MFFT)** were measured in an MFFT bar. A layer of latex with 90  $\mu\text{m}$  of thickness was formed on the metal bar that had a temperature gradient. MFFT was taken as the lowest temperature at which a transparent film with mechanical integrity was gained (proven by uniform knife cut).

### I.3. References

1. Bouvier-Fontes, L., Pirri, R., Asua, J. M. & Leiza, J. R. Cross-linking emulsion copolymerization of butyl acrylate with diallyl maleate. *J. Polym. Sci. Part A Polym. Chem.* **43**, 4684–4694 (2005).
2. Podzimek, S. in *Light Scattering, Size Exclusion Chromatography and Asymmetric Flow Field Flow Fractionation* 259–305 (John Wiley & Sons, Inc., 2011).
3. Baroni, T. C., Griffin, B. J., Browne, J. R. & Lincoln, F. J. Correlation between



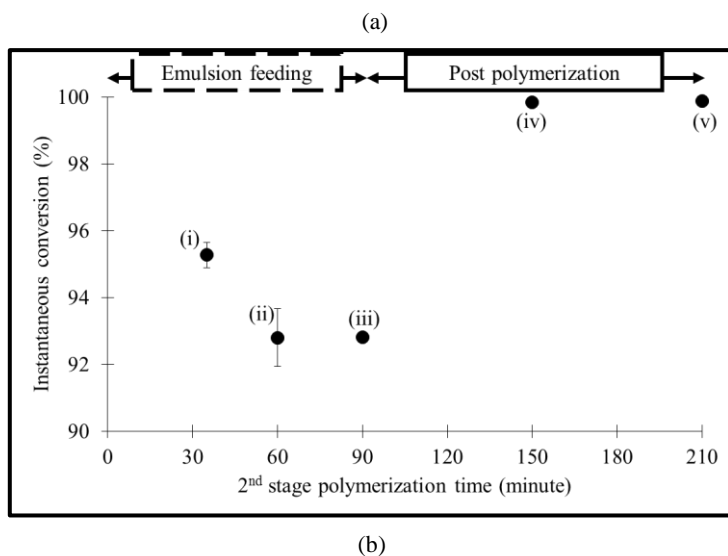
- Charge Contrast Imaging and the Distribution of Some Trace Level Impurities in Gibbsite. *Microsc. Microanal.* **6**, 49–58 (2000).
4. González-Matheus, K., Leal, G. P. & Asua, J. M. Film formation from Pickering stabilized waterborne polymer dispersions. *Polymer*. **69**, 73–82 (2015).
  5. Stubbs, J. M. & Sundberg, D. C. Measuring the Extent of Phase Separation During Polymerization of Composite Latex Particles Using Modulated Temperature DSC. *J. Polym. Sci. Part B Polym. Phys.* **43**, 2790–2806 (2005).
  6. Keddie, J. L. Film formation of latex. *Mater. Sci. Eng.* **21**, 101–170 (1997).
  7. Jiang, B., Tsavalas, J. & Sundberg, D. Measuring the Glass Transition of Latex-Based Polymers in the Hydroplasticized State via Differential Scanning Calorimetry. *Langmuir* **26**, 9408–9415 (2010).

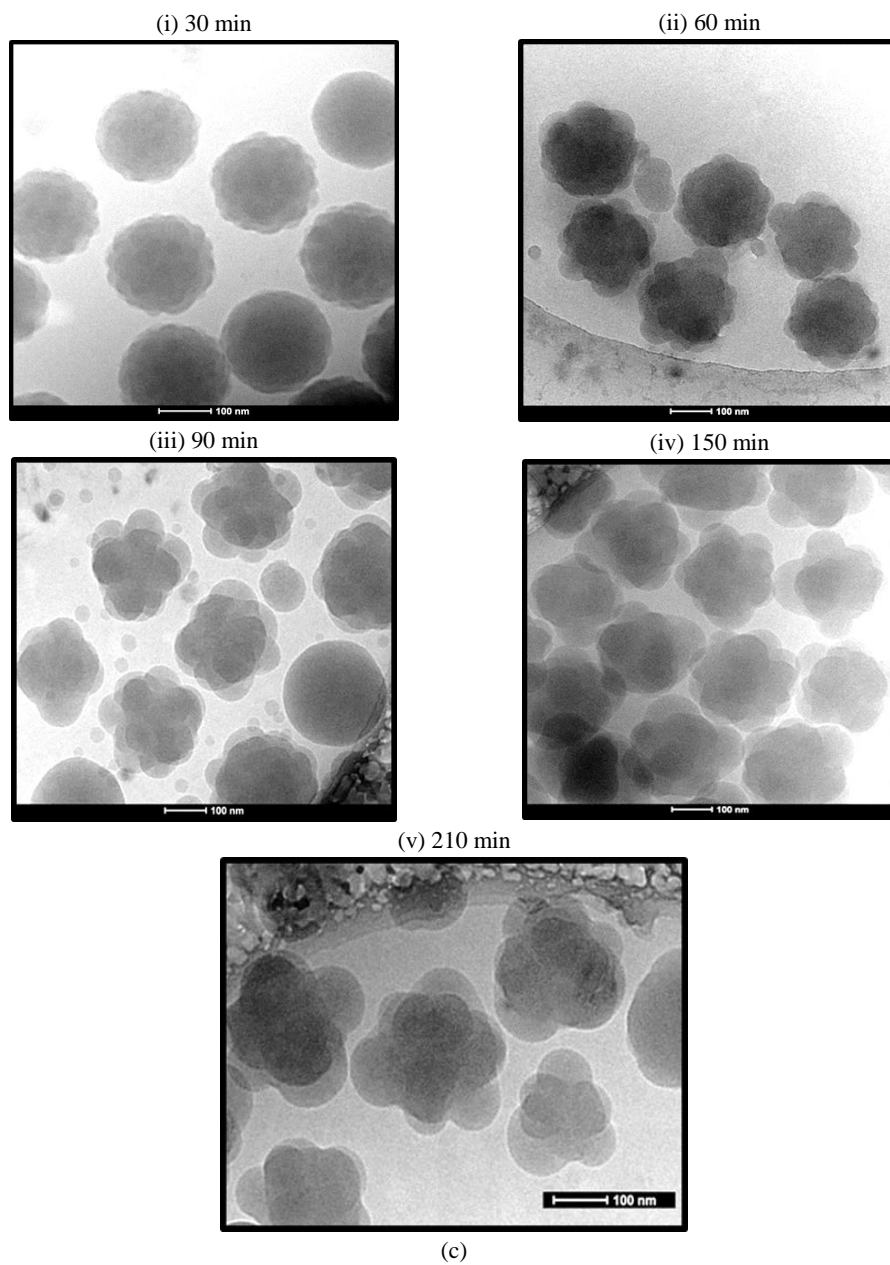


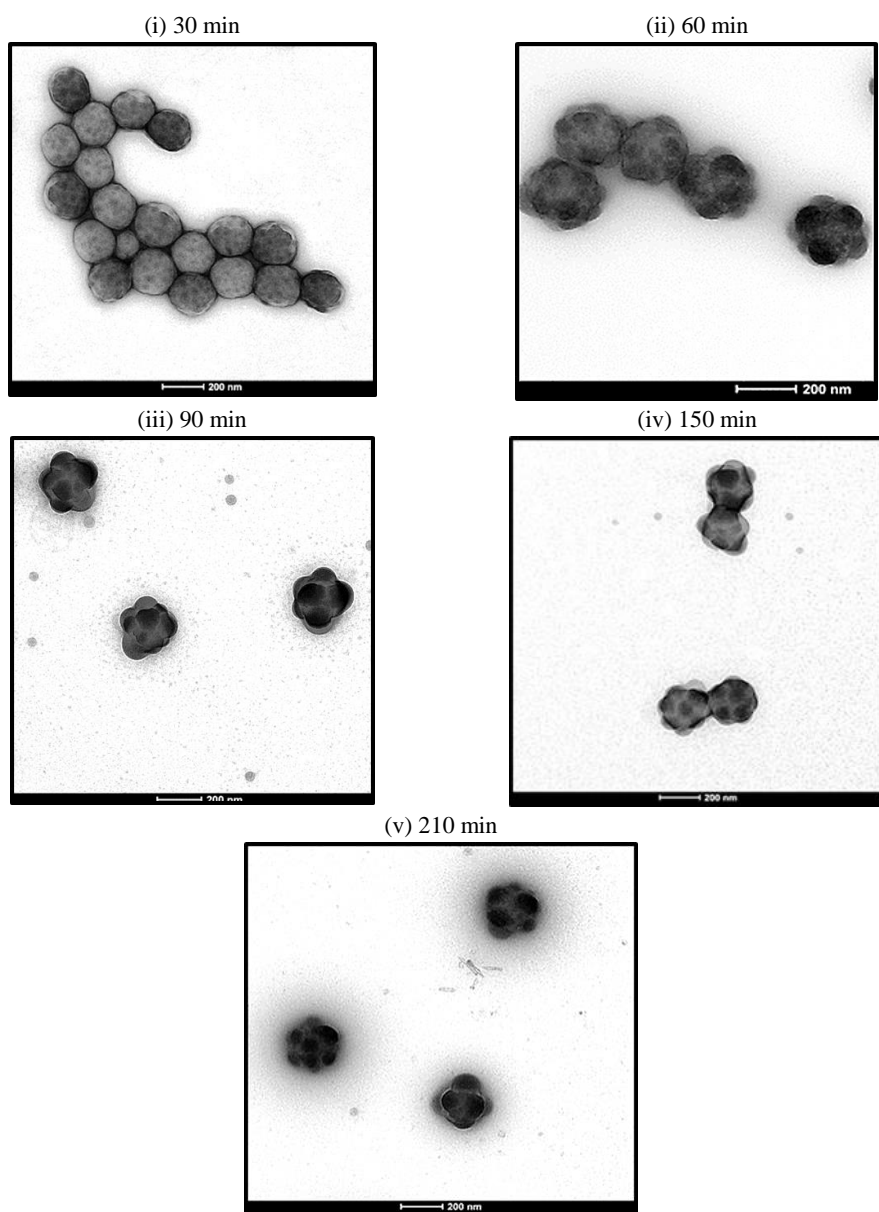
## Appendix II. Some Figures of Chapter 2 and Chapter 4

Figure 2.3, 2.8 and 2.9 of Chapter 2 are presented with larger images in this Appendix. Moreover, the cluster size distribution for Runs R1 and C1 of Chapter 4 are shown in Figure II.1

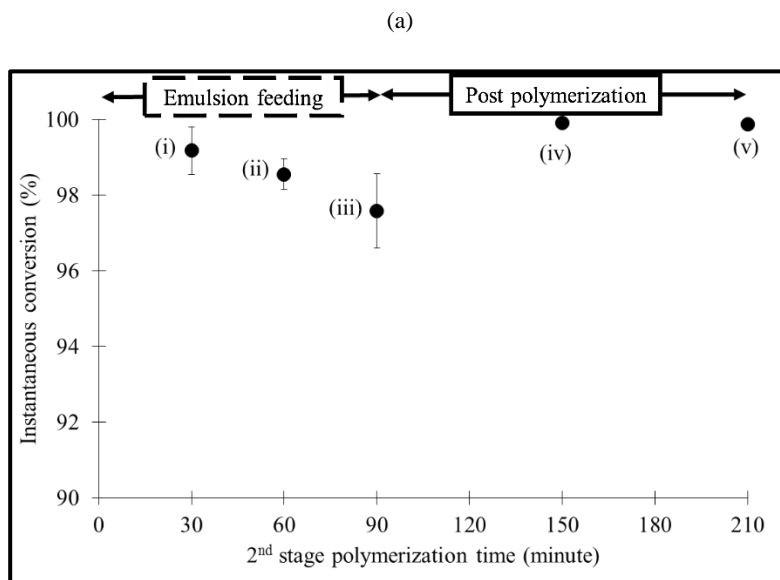
**Figure 2.3.** Evolution of (a) instantaneous conversion measured by GC and particle morphology during the 2<sup>nd</sup> stage of polymerization of Run R1 ( $T_{g_{seed}} = 86\text{ }^{\circ}\text{C}$ ): (b) Cryo-TEM images, images magnification: 50000 and (c) TEM images of stained sample with vapor of  $\text{RuO}_4$  for 1 hour, images magnification: 25000.

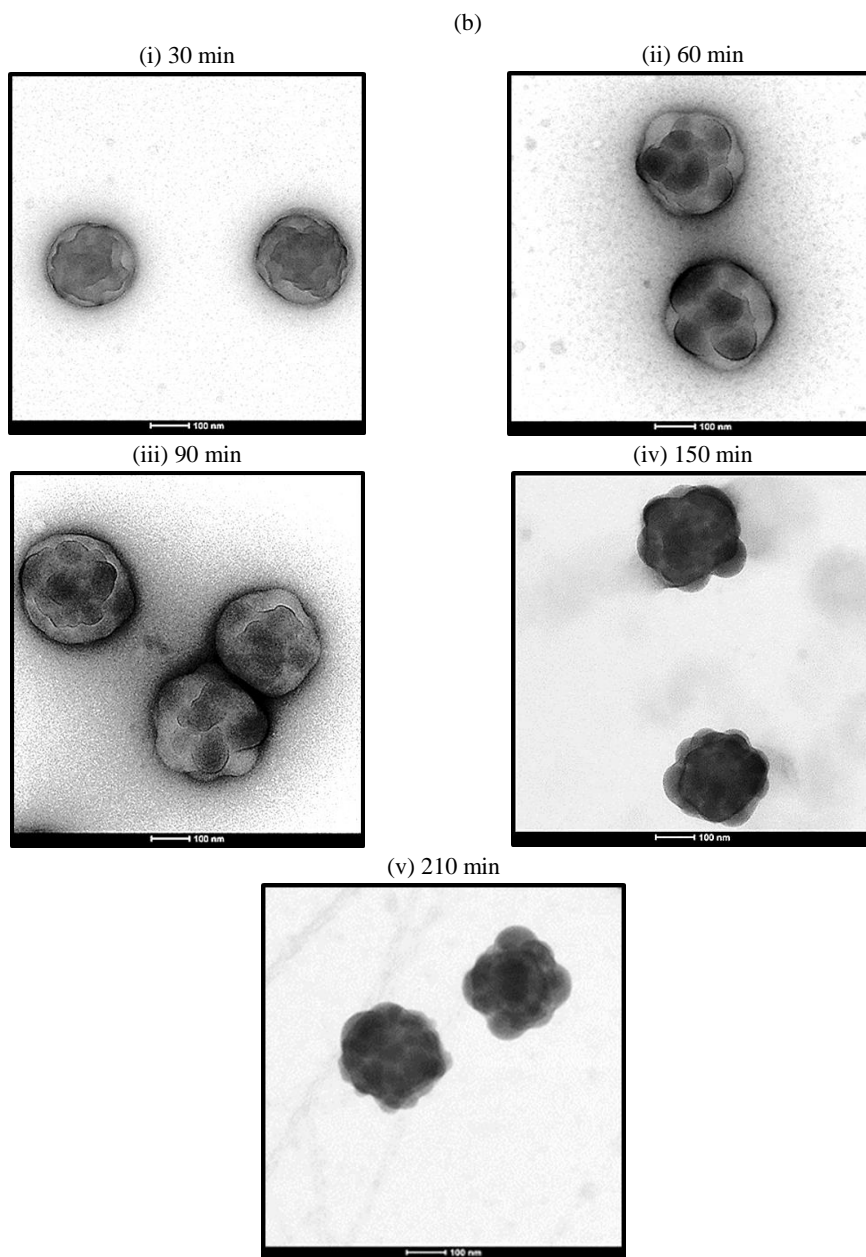




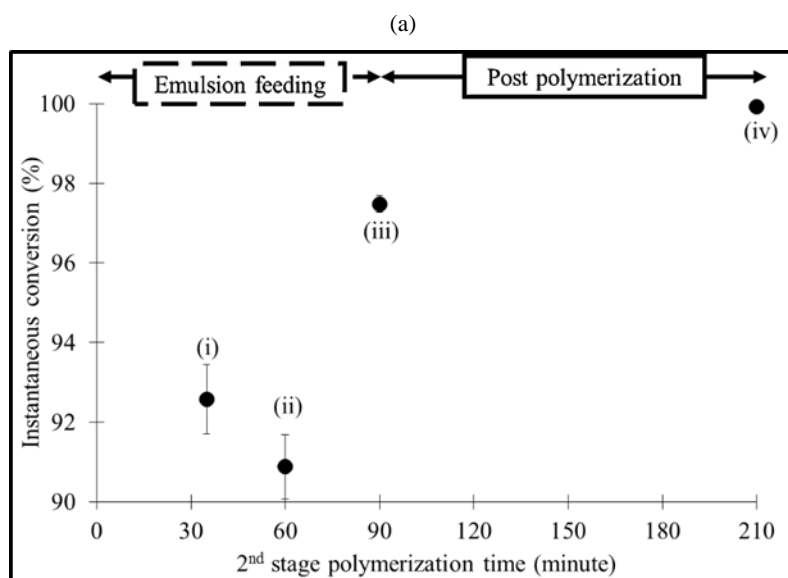


**Figure 2.8.** Evolution of (a) instantaneous conversion and (b) particle morphology (TEM images of stained sample with vapor of RuO<sub>4</sub>) during the second stage of polymerization of Run R2 (T<sub>g,seed</sub> = 63 °C). Images magnification: 50000.

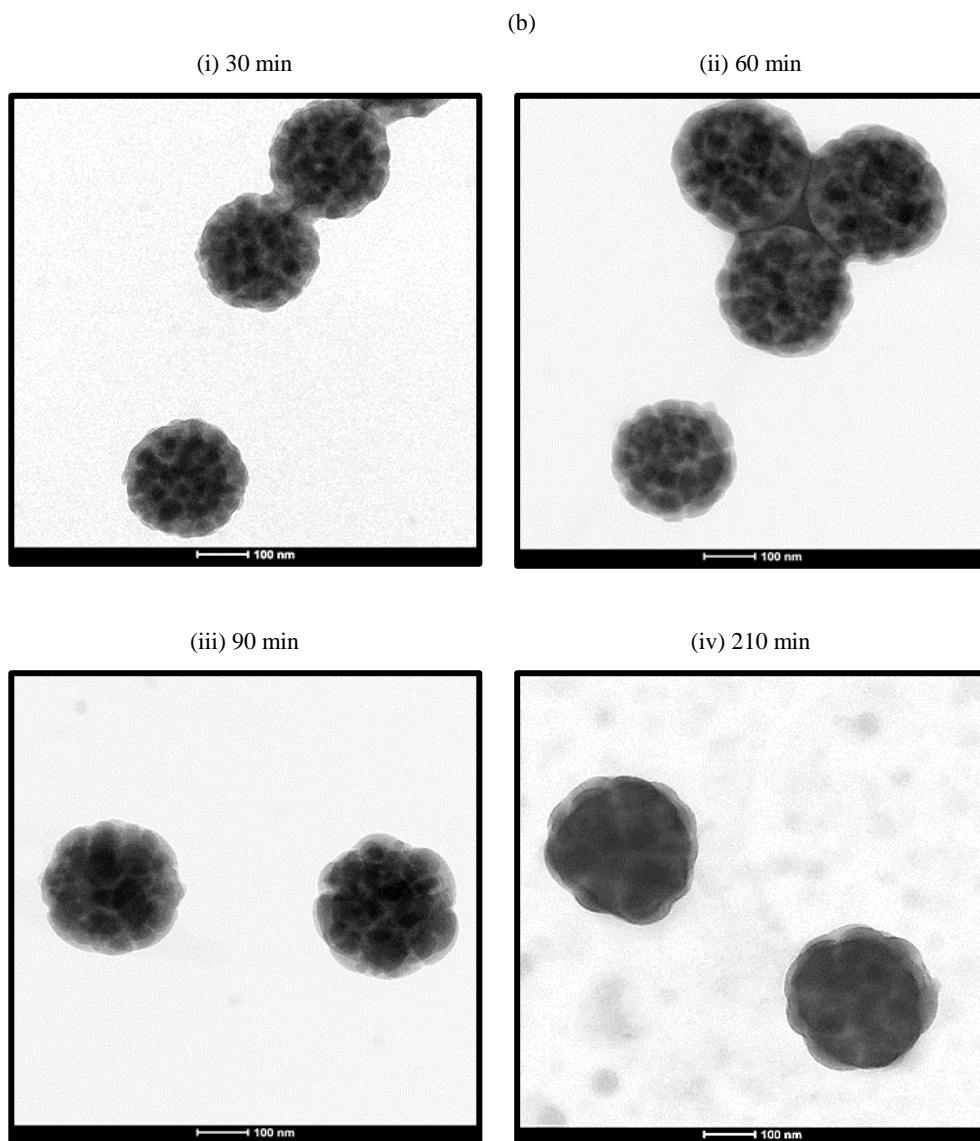




**Figure 2.9.** Evolution of (a) instantaneous conversion and (b) particle morphology (TEM images of stained sample with vapor of RuO<sub>4</sub>) during the second stage of polymerization of Run R3 ( $T_{g_{seed}} = 46\text{ }^{\circ}\text{C}$ ). Images magnification: 50000.







**Figure II.1.** Cluster size distributions for latexes of Runs R1 and C1: (a) sizes of external clusters calculated as diameters of equivalent sphere for the experimentally measured volumes; (b) sizes of internal clusters, calculated in the same way.

